Model Development and Investigations on Ion Homeostasis

by

Christina Helen Selstø

Thesis submitted in fulfillment of
the requirements for the degree of

PHILOSOPHIAE DOCTOR
(PhD)

University of
Stavanger

Faculty of Science and Technology
Department of Chemistry, Bioscience and Environmental Engineering
2023

University of Stavanger
N-4036 Stavanger
NORWAY
www.uis.no

ISBN 978-82-8439-167-0
ISSN 1890-1387

PhD Thesis UiS no. 702

Preface

This thesis is submitted as partial fulfillment of the requirements for the degree of *Philosophiae Doctor* at the University of Stavanger, Norway. The research of this work has been carried out at the Centre for Organelle Research (CORE) at the University of Stavanger.

The research has resulted in two published articles and one submitted manuscript. The thesis is written as a monography where published and unpublished materials are presented in a logical way for coherency. The material starts with the work on iron homeostasis, followed by the investigations on oscillatory conditions in homeostatic regulation by using cytosolic calcium (Ca^{2+}) as an example. My final work was the construction of a more detailed basic model of cytosolic Ca^{2+} homeostasis in non-excitable cells.

Christina Helen Selstø
Stavanger, 2023

Abstract

The environment surrounding an organism, a cell and an organelle is constantly changing. To keep organisms functioning there is an everlasting need to regulate and adapt in order to keep the internal environment relatively constant. Homeostasis is the term used to describe this ability of a system to regulate and stabilize its environment. Different processes and compensatory mechanisms are employed to do this. Homeostasis is also the overall theme binding this thesis together, spanning from iron regulation in plants to the regulation of calcium (Ca^{2+}) in humans. Ever since the term emerged, scientists have been searching for answers on how biological control mechanisms function and how they are able to maintain homeostasis. The work presented in this thesis is based on a computational approach using systems biology and control mechanisms like negative feedback and integral control. Controller motifs based on negative feedback loops between a controlled and manipulated/compensatory variable was previously identified by the research group, and has been used as a basis for the computational calculations and models.

Plants need iron for their growth and development, and even though this essential nutrient is difficult to access through the soil due to its availability. In the soil iron is strongly bound as Fe_2O_3, and plants have developed different strategies for iron uptake. Iron is also of great importance for human nutrition. Iron deficiency is one of the major causes of anaemia. Anaemia is a world wide problem and is a condition with too few red bloods cells or where the haemoglobin level within these is lower than usual. Iron regulation and homeostasis was modeled for non-graminaceous plants, with Arabidopsis thaliana as a model species. Since iron is toxic for plants at high levels it needs to be under homeostatic control. A model in agreement with experimental observations was developed. Iron-dependent degradation of the high-affinity transporter IRT1 was included in agreement with experimental findings, as well as the importance of the transcription factor FIT for the regulation of cytosolic iron. Auxiliary feedback was also introduced and investigated in the model. The role of such feedback is

to help improve adaptation kinetics without an influence to the set-point, resulting in a significant improvement of the system response time.

Homeostasis was also explored in order to see whether oscillatory conditions, which are common in biological systems, could show robust homeostasis. Homeostatic oscillators were identified, where compensatory frequency or amplitude levels lead to the average level corresponding to the set-point. This indicates that even during sustained oscillatory conditions homeostasis can be observed, suggesting an extension of the concept. Frequency control with the frequency being homeostatically regulated have also been described by us. Cytosolic calcium (Ca^{2+}) is a biological example of one of these conditions where oscillations, transients etc. take place even though Ca^{2+} is under strict homeostatic control. Dysregulation of cytosolic Ca^{2+} is critical as it will affect cellular signaling and promote apoptosis at high levels. A simple initial model of oscillating Ca^{2+} regulation was used as an example of oscillatory homeostats, which spiked the interest to investigate Ca^{2+} homeostasis on a cellular level.

Thus started the approach on building a model on cytosolic Ca^{2+} homeostasis and regulatory mechanisms in non-excitable cells. The work was started from an initial simple model based on erythrocytes with few organelles by studying the inflow and outflow mechanisms through the plasma membrane. Hysteretic properties in the plasma membrane Ca^{2+} ATPase (PMCA) was studied and identified, and compared well with experimental results. We also suggest that the inflow of Ca^{2+} could be inhibited by carboxyeosin which was used as an inhibitor in experimental research based on model calculations fitting well with these. For the Ca^{2+} induced Ca^{2+} release mechanism through the inositol 1,4,5-trisphosphate receptor (IP_3R) a dicalcic model has been presented. Comparing theoretical calculations with experimental bell-shaped curves of the Ca^{2+} dependency of the IP_3R channel at different IP_3 levels, a cooperativity of 2 has been suggested in the inhibition by Ca^{2+}. Cooperativity in the capacitative Ca^{2+} entry was also investigated and compared to experiments. Finally, even though oscillations was not the focus of this latest project, the cellular model can show sustained Ca^{2+} oscillations with period length ranging from a few seconds up to 30 hours!

Acknowledgements

I would like to start by expressing my deep gratitude to my supervisor Prof. Dr. Peter Ruoff for his guidance throughout my PhD work. His patience, encouragement and enthusiasm towards the research has assisted me throughout these years, and I am very grateful for all the hours of discussions, lectures, meetings and useful suggestions and feedback on my work. Thank you! My appreciation is also given to Prof. Dr. Tormod Drengstig for his collaboration and input as well as patience and understanding through many meetings introducing me to control engineering. I also wish to acknowledge my collaborator Dr. Kristian Thorsen for discussing control engineering principles and providing me with help during the initial stages of thesis writing and in discussions. I very much appreciate it. My deepest gratitude goes out to Dr. Oleg Agafonov, Dr. Xiang Ming Xu and Dr. Gunhild Fjeld which has been part of the Ruoff research group, for their time and great help. I would also like to give my sincere appreciation to friends and colleagues at the Centre for Organelle Research (CORE) for making it such a welcoming and friendly environment which I have been very sad to leave. I am also thankful for my time with the student organization MoBi2C which I hope will continue making CORE a great place for everyone. I would like to thank my family and friends for their support and continued interest in what I do. Especially my parents, for always being proud of me and for encouraging me into doing my best. Also the rest of my family for supporting me and staying curious with my work. My children, Marcus, Lilly and Noah, for always lighting up my day and helping me come back to my set-point. Last but not least, Øyvind, I could not have done this without you. Thank you for your continued support, encouragement, patience during these years, and always being there for me.

Chance throws peculiar conditions in everyone's way.
If we apply intelligence, patience and special vision,
we are rewarded with new creative breakthroughs.
—Walter Bradford Cannon.

List of publications

The main part of this dissertation is made up of the following published scientific papers:

- **Paper 1**

  Robust Concentration and Frequency Control in Oscillatory Homeostats
  K. Thorsen, O. Agafonov, **C. H. Selstø**, I. W. Jolma, X. Y. Ni, T. Drengstig, P. Ruoff
  PLoS One, vol. 9, no. 9, p. e107766, Sep. 2014.

- **Paper 2**

  The Organization of Controller Motifs Leading to Robust Plant Iron Homeostasis
  O. Agafonov, **C. H. Selstø**, K. Thorsen, X. M. Xu, T. Drengstig, P. Ruoff
  PLoS One, vol. 11, no. 1, p. e0147120, Jan. 2016.

- **Paper 3**

  A basic model of calcium homeostasis in non-excitable cells
  C. H. Selstø, P. Ruoff
  Manuscript submitted to PLoS Computational Biology, Dec. 2022.

List of other scientific communications

In addition to the published and submitted papers, results form the dissertation have also been communicated to the scientific community at:

(i) **A comprehensive model of cytosolic calcium homeostasis and associated oscillations.**
C.H. Selstø, T. Drengstig and P. Ruoff, *Poster presentation.* CSH Cellular Dynamics & Models meeting, Cold Spring Harbor, New York, USA. 2017.

(ii) **Cytosolic Ca^{2+} homeostasis. Why do we need it?**
C.H. Selstø, *Talk.* CORE Research Seminars, Stavanger, Norway. 2017.

(iii) **Modeling cytosolic calcium homeostasis in non-excitable cells.**
C.H. Selstø and P. Ruoff, *Talk.* Digital Life Annual Conference, Stiklestad, Norway. 2018.

List of Figures

List of Tables

Glossary

AA	Arachidonic Acid
AF	Auxiliary Feedback
AHA2/7	Arabidopsis H^+ ATPase 2/7
ApoCaM	Apocalmodulin (Ca^{2+} free calmodulin)
ARCC	Arachidonic acid Regulated Ca^{2+} Channel
AtbHLH	*Arabidopsis thaliana* basic Helix-Loop-Helix
B	Buffer
BAPTA	1,2-bis(o-aminophenoxy)ethane-N,N,N′,N′-tetraacetic acid (Ca^{2+} chelator)
bHLH	basic Helix-Loop-Helix
BHK-21	Baby Hamster Kidney 21 (cells)
Ca^{2+}	Calcium
CaM	Calmodulin
CICR	Ca^{2+} Induced Ca^{2+} Release
CRAC	Ca^{2+} Release Activated Channel
CV	Controlled Variable
e	Error (A_{set} - A)
EFSAM	EF Sterile Alpha Motif
EMT	Epithelial-Mesenchymal Transition
ER	Endoplasmic Reticulum
Fe	Iron
Fe-S	Iron-Sulfur
FIT	Fe-deficiency Induced Transcription factor
FPN	FerroPortiN
FRO	Ferric-chelate Reductase Oxidase
HeLa	Henrietta Lacks (human cancer cell line)
IP3	Inositol 1,4,5-TrisPhosphate
IP3R	Inositol 1,4,5-TrisPhosphate Receptor
IRT	Iron Regulated Transporter
IT	Information Technology
L	Lumen buffering protein
LOCC	Ligand Operated Ca^{2+} Channel
M	CaM (Calmodulin)

Mdm2	Mouse double minute 2 homolog
MM	Michaelis Menten
MV	Manipulated Variable
NA	Nicotinamine
NCX	Na^{+}/Ca^{2+} eXchanger
NRAMP	Natural Resistance-Associated Machrophage Protein
NSCC	Non-Spesific Ca^{2+} Channel
PIC	Permase In Chloroplasts
PLA	PhosphoLipase A
p53	Protein 53 (Tumor supressor protein)
PM	Plasma Membrane
PMCA	Plasma Membrane Ca^{2+} ATPase
RBL-1	Rat Basophilic Leukemia 1 (cells)
ROS	Reactive Oxygen Species
RyR	Ryanodine Receptor
SERCA	Sarco/Endoplasmic Reticulum Ca^{2+} ATPase
SOCC	Storage Operated Ca^{2+} Channel
SOCE	Storage Operated Ca^{2+} Entry
SR	Sarcoplasmic Reticulum
STAT3	Signal Transducer and Activator of Transcription 3
STIM	STromal Interaction Molecule
TF	Transcription Factor
VIT	Vacuolar Iron Transporter
VOCC	Voltage Operated Ca^{2+} Channel

Contents

Chapter 1

Aim of Thesis

The main objectives of this thesis is to

- Explore the regulation and homeostasis of iron in *Arabidopsis thaliana* by a computational approach using different controller motifs with negative feedback loops and reaction kinetic requirements that lead to robust homeostasis (integral control).
- Investigate, in general, the homeostatic regulation during oscillatory conditions, in addition to identifying compensating factors leading to a robust homeostasis.
- Build a mathematical model for cytosolic calcium (Ca^{2+}) homeostasis in non-excitable cells, and investigate the roles of different pumps, channels, transport proteins etc. which are involved in cytosolic Ca^{2+} regulation. Develop the cytosolic Ca^{2+} homeostasis model based on experimental results to provide new insights and novel aspects to the regulation of cytosolic Ca^{2+}.

Chapter 2

Introduction

2.1 Homeostasis

2.1.1 A brief history of the early conceptualization of homeostasis

The term "homeostasis" originates from Walter B. Cannon, who coined it in his 1929 paper "Organization for physiological homeostasis" [1, 2]. The word has its origin from the Greek words *homeo* and *stasis*, where homeo means *like* or *the same*, whereas stasis means *standing still*. Cannons definition of homeostasis as a tendency of a system to regulate itself back to a stable environment was largely based on ideas of Claude Bernards description of "Le Milieu Interieur" around 1854 [2]. However Cannon also describes that the stable conditions can include variations, although only within narrow limits [1, 3]. If these limits are exceeded it will result in severe consequences for the organism. Some of these consequences given by Cannon include incorrect regulation of glucose, water and sodium [1].

And even though Cannon and others' brilliant research and ideas have led to appreciate the concept of homeostasis, the search for answers to how our body works with the balances and equilibria that keeps us healthy, can be traced back to Greek philosophers BC. We can find that Alcmaeon had some thoughts on what maintained our health: "Alcmaeon said that what preserves health is the equilibrium of the powers - wet, dry, cold, hot, sweet and so forth - whereas the unchecked rule of any of them engenders disease: the rule of a single contrary is destructive.... Health is a balanced mixture of opposites" [4]. The well-known philosopher, Hippocrates, also referred to as the "father of modern medicine", agreed with Alcmaeon's view that health is a balance of forces. He thought this balance was between the four "humors": blood, phlegm, black bile and yellow bile/serum [5]. Equilibria and harmony were applied to understand health. Even though these ideas

are not identical to the homeostasis concept we use today, it is nevertheless some of the first "models" on how to understand health and how the body maintains its stability. Alcmaeon was in a very early sense describing the concept we now know as homeostasis.

In the 18th century Charles Blagden and John Hunter discovered that body temperature is conserved over a vast range of environmental conditions [2, 6]. Blagden did observational studies inside a room with increasingly high temperatures and observing what external temperature did to the body temperature. His conclusions were that the body destroys heat [2]. The stability of "Le Milieu Intériur" that Claude Bernard would in turn describe include the phenomena which Blagden and his fellows observed. Cannon finally summed up and categorized these and other findings as homeostasis [1, 2].

It is safe to say that the mysteries of the human body and the ability of a system to maintain its internal environment during external stress have been occupying the brilliant minds of all times. Bernard and Cannon laid the foundation which other researchers have based their hypotheses and work on when it comes to regulation and studies of systems. Cannon often used the phrase "not known" when it came to describing the regulatory aspect of his research [1]. At Cannon's time, many scientists had been researching the internal environment and the regulation of the steady state of several conditions such as thirst, blood sugar, calcium level, osmoregulation and the influences of pH and temperature etc. Even today much is still yet to be discovered and described when it comes to homeostatic mechanisms and how homeostasis is maintained in different systems. What Cannon contributed, other than of course the term homeostasis, is the progression of the concept to focus on the regulatory biological control factors as opposed to focus on the state itself. Cannon ends his important paper on the concept of homeostasis with "... further research into the operations of agencies for maintaining biological homeostasis is desirable" [1].

2.1.2 Homeostasis and regulation

Following Cannon and his definition of homeostasis several additions and adaptations of the concept have been introduced. New terms like "predictive" homeostasis, "rheostasis", "allostasis" and "homeodynamics" have emerged in order to describe considered shortcomings of the original concept, emphasizing biological systems as dynamic, and overlap somewhat [7, 8, 9, 10, 11]. The term rheostasis coined by Mrosovsky describes the

"physiology of change" where adaptation of systems and the change of set-points in cases like cyclic circadian changes and cases like fever are included [8]. Allostasis introduced by Sterling and Eyer also describes variation in states and is "the process of insuring viability in the face of challenge and change". Also allostasis describes the ability of a biological system to predict or anticipate what it needs to adapt to [7, 10]. Homeodynamics as a concept attempts to be a counterpart of homeostasis. Homeostasis is critiqued to describe the desire to regulate to a set level, compared to homeodynamics where there are intrinsic dynamic properties to the system that leads to shifting of the level it desires to reach. This is explained by the systems tendency of self-organization because of non-linear kinetic mechanisms, and dynamic interaction in its involved processes, also incorporating oscillations in its concept [11]. Nonetheless, as enlightening and well described these aspects are, others argue that these new concepts are just part of the overall homeostasis term and only give new insights into what homeostasis actually is about [7, 12].

Increasing interest in investigations of biological systems, pathways and regulatory networks with technological inventions gave way to the multidisciplinary nature of systems biology [13]. Ludwig von Bertalanffy suggested a common feature of all systems as being composed of interconnected constituents. General system theory is based upon the similarities between systems from different areas of science and society and aim to join them together in a way of understanding [13, 14]. In agreement with von Bertalanffy's ideas on how different systems share similar structures and control designs, new connections between homeostasis and control theory became apparent [14]. Cooperators of Cannon, such as Rosenbleuth and Wiener, introduced control theory to biological systems through the concept of homeostasis [3, 15, 16]. Hardy is reported to be the first to introduce the term "set-point" which is used to describe the desired level of regulation in the context of homeostasis [17]. Important aspects like feedback regulation in order to achieve homeostasis was suggested [3, 15, 16]. Generally, this can be arranged as negative feedback loops between a regulated species and its regulator(s). With feedback regulation and the development of computer science, computational methods for investigating homeostatic mechanisms, by means of mathematics, have emerged. Mathematical modeling of regulation in biological systems can be used as a tool for understanding homeostasis better. With the merge of control theory, one can look upon homeostatic regulation as any regulation of a controlled variable just like in an electrical system or water tank [2, 12, 18]. In his book

on *"Temporal organization in cells"* Goodwin underlines the importance of the discovery of molecular control mechanisms for understanding cell behavior. Goodwin further states that this must be the foundation upon which any future theory of cellular organization should be formed [19]. In order to compensate for the lack of dynamic properties of these systems by a mere qualitative approach, he writes *"It will be necessary to construct such a dynamics on the basis of what we know about the general kinetics of molecular activities in cells, and also on the basis of the dynamic behaviour of feed-back control devices such as those commonly used in engineering. This procedure will of necessity be rather approximate, but it is just at this point that a second consideration encourages the investigation of even crude kinetic models of cellular activity"* [19].

2.2 Applying Control Theory to Biological Systems

As mentioned, negative feedback has been thoroughly introduced to the homeostasis term and today it is a general conception that feedbacks are important in the regulation of biological systems. As control theory bases the regulation of a system to a certain desired set-point on feedback mechanisms, there is a natural correspondence between the concept of homeostasis in biology and systems control. In the next section I will focus on (some) concepts within control theory that have been applied in our research group. Especially, the concept of integral control has been essential to the work on robust homeostasis.

2.2.1 Controller motifs and feedback loops

Feedback can be described as a situation where two or more systems, or species, are connected and influence each other in order to either activate or inhibit the other in a dynamic way [20]. Åstrøm and Murray presented a quote in their book on feedback *"Feedback is a central feature of life. The process of feedback governs how we grow, respond to stress and challenge, and regulate factors such as body temperature, blood pressure and cholesterol level. The mechanisms operate at every level, from the interaction of proteins in cells to the interaction of organisms in complex ecologies"* [20, 21]. This short introduction gives an overview on the importance of feedback for life. The dynamic nature of life makes it necessary for compensating by feedback

regulation. Negative feedback has already been mentioned, as this is the most widespread and agreed upon regulatory mechanism for maintaining homeostasis. However, there are also cases of positive feedback and autocatalysis in regulation for homeostasis [20, 22], either reducing/accelerating the response time by the negative feedback, or taking itself part in the mechanism behind integral control [23, 24, 25, 26].

In order to identify reaction kinetic requirements and molecular mechanisms leading to robust homeostasis Drengstig and Ruoff, with coworkers, have reported a set of two component negative feedback loops termed controller motifs [27, 28, 29, 30]. The set consists of eight separate controller motifs, each illustrating a different set up in which two components are arranged in a feedback loop. Each controller motif consists of components A and E which are part of a negative feedback loop. The idea is that A is the controlled variable (CV), while E constitutes the manipulated variable (MV) or compensatory mediator species [27]. Dependent whether the compensatory flux adds or removes the controlled variable A, the eight motifs are separated into two categories, inflow and outflow controllers, as seen in Fig. 2.1.

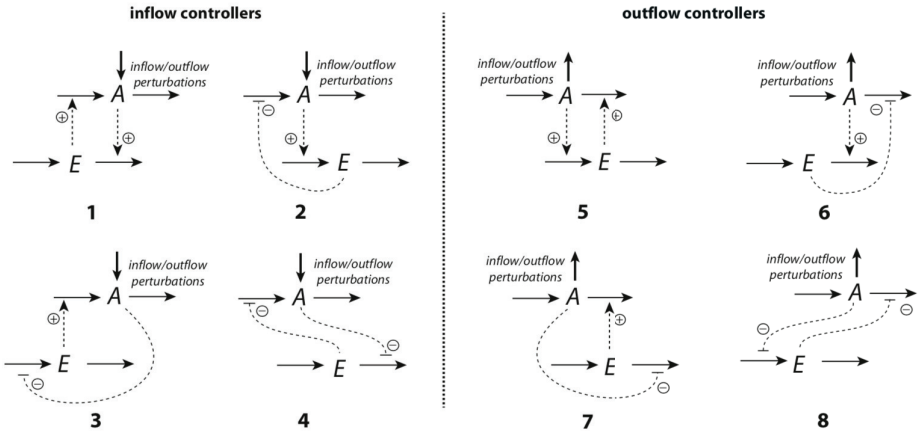

Figure 2.1: A basic set of controller motifs for robust homeostasis. Left panel shows inflow controller motifs 1-4, which uphold homeostasis by an additive compensatory flux to A, mediated by E. Right panel shows outflow controllers 5-8. In their case homeostasis is maintained by the outflow/removal of A mediated by E. Figure adapted from [27].

Common for the inflow controllers is the feature that E mediates the compensatory flux for the inflow of A, whereas E in the outflow controllers

aids the compensatory path in removal of excess A. Thus, negative feedback control adds more A to the system when the level of A is below its set-point, or removes A when the A level is above its set-point. The situation is illustrated in Fig. 2.2.

The objective of arranging molecular interactions and regulations networks in this way is to model molecular mechanisms and identify parameters leading to robust homeostasis. In investigating systems in terms of these controller motifs one can learn about the interaction between homeostatic controllers and which set-ups can describe specific mechanisms. Also, by perturbing and changing parameters of the system we can investigate homeostatic dysfunction, understand their origins and provide means to avoid controller breakdown.

2.2.2 Integral control and robust perfect adaptation

Negative feedback in itself however is not enough to ensure robust homeostasis. In order to be able to withstand perturbations and to keep the controlled variable at its set-point, robust control mechanisms can be employed, such as integral control [27, 29]. The concept of integral feedback control is well established in control engineering as a part in the negative feedback loop. The integral control scheme is illustrated in Fig. 2.3 [31].

2.2.3 Different adaptation types

As a process is perturbed, there are several modes of adaptation possible. These have been illustrated in Fig. 2.4. The aim of integral feedback control is of course to achieve perfect adaptation, where the value of the controled variable A is manipulated back to its set-point.

Alon et al. investigated the response and adaptation of bacterial chemotaxis and their results showed "exact adaptation" and robustness. They highlight the possibility of two functional properties of this adaption, either as fine-tuning of rate constants of parameters, or as robustness. As a finishing remark they posed the question whether systematic studies could yield "any *design principles* connected with robustness, perhaps analogous to those used in engineering" [32]. The following year, Yi et al. were the first to coin the term "robust perfect adaptation" while investigating the named *Barkai-Leibler* model, where they connected it to integral control from engineering [33]. In more recent time, Briat et al. describes what they call a stochastic antithetic integral controler in which they take noise into

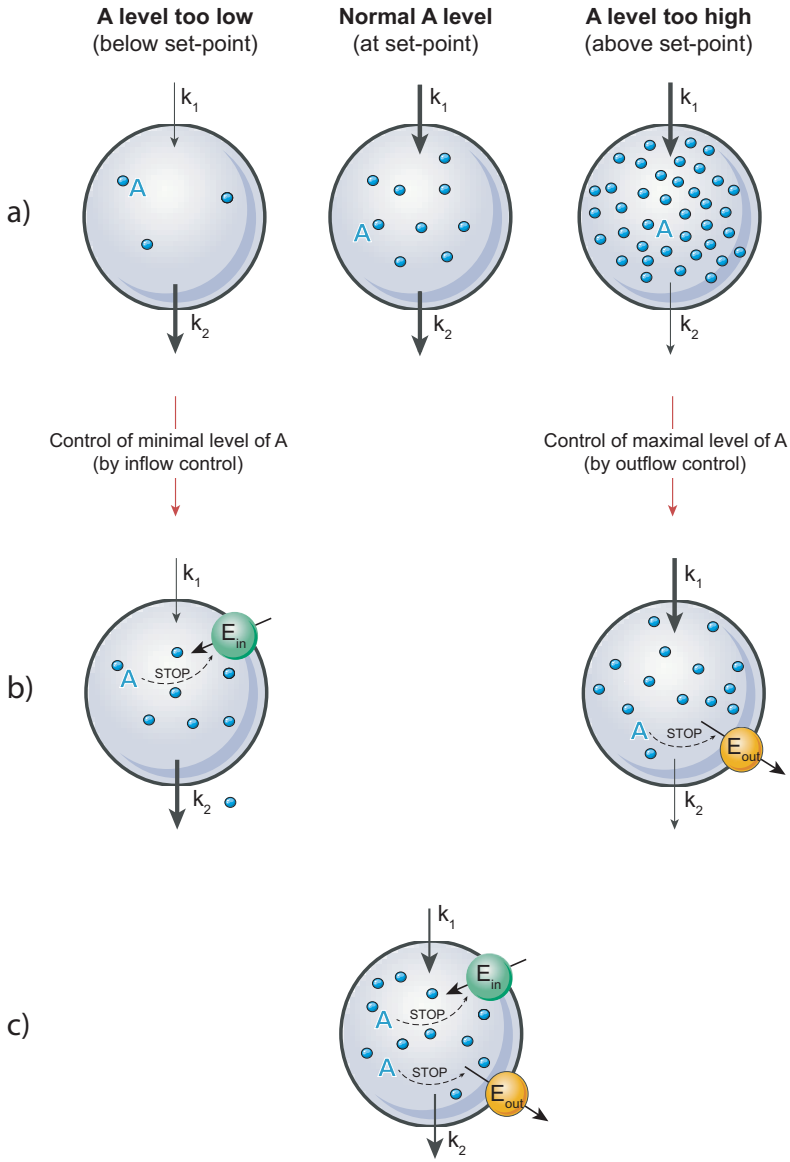

Figure 2.2: (Caption next page.)

Figure 2.2: (Continued from Previous page). **Function of negative feedback.** (a) If A levels decrease below or increase above its set-point, this could have severe consequences. In order to keep the A-level within acceptable limits, negative feedback can be invoked. (b) Left part of figure shows how an inflow controler will compensate, i.e., add A to the system whenever the A-level is below the inflow controller's set-point, $A_{set}{}^{in}$. The controller will be "silent" for A-levels above $A_{set}{}^{in}$. Right part of the figure shows an outflow controller, which on the other hand will remove A until A-levels are at the controller's set-point $A_{set}{}^{out}$. For A-levels below $A_{set}{}^{out}$ the outflow controller will not be operative. (c) Combining inflow and outflow controllers such that $A_{set}{}^{out} > A_{set}{}^{in}$ will define a homeostatic region of A with $A_{set}{}^{out}$ and $A_{set}{}^{in}$ as the upper and lower limits. Figure adapted from [27].

consideration, and can also be shown to exhibit robust perfect adaptation [34]. Previously, Saunders et al. described "integral rein control" based on the term "rein control" by Clynes (1969) for a dual-hormonal control which is evenly effective in either direction [35]. This is indeed the case in control of for instance blood sugar level and blood calcium level. El-Samad, however, critizises this view of integral control as one part of the control is too dependent on the other, and accomplishes to describe blood calcium homeostasis by a traditional integral control approach [36]. The homeostatic controler motifs described by Drengstig et al. can also be combined in such ways as to describe cases of blood calcium levels and blood glucose levels by means of integral control [27].

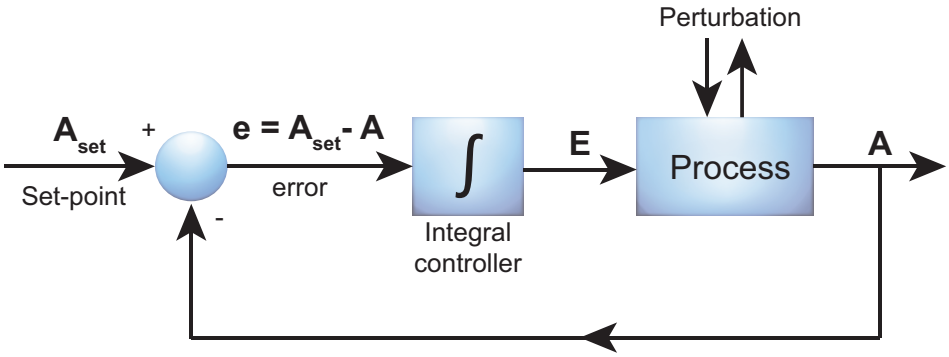

Figure 2.3: How an integral controller works. The diagram shows a negative feedback loop with A as the regulated variable. A is compared with its set-point and the error $e = A_{set}$ - A is calculated and then integrated. The integrated error E is then used to compensate for perturbations acting on the process which creates A. This procedure ensures that A will, at least for step-wise perturbations, attain A_{set}. Figure adapted from [29].

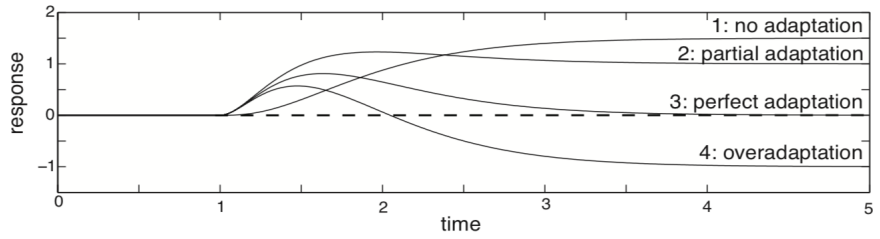

Figure 2.4: Adaptation modes following a step perturbation. Following a step perturbation at time=1, there are several modes of adaptation possible. The system responses can be 1: no adaptation, 2: partial adaptation, 3: perfect adaptation, and 4: overadaptation. Figure adapted from [28].

In order for integral control to be implemented in the controller motifs, E needs to be degraded by zero-order Michaelis Menten (MM) kinetics [27, 29]. Alternatively by using an antithetic feedback or positive feedback with first-order removal of E. This will lead to robust homeostasis with perfect adaptation. However, if the perturbation in the inflow controllers gets too large with regards to the perturbing inflow of A the controller will break down. However, this only happens when activation of compensatory flux E is E/(K_a+E) where K_a is an activation constant. The same happens with a large, uncontrolled outflow of A in the case of the outflow controllers as well [27, 37]. In kinetic and mathematical terms this can be described looking at the set-up of one controller motif, for instance outflow controller 5, Fig. 2.5.

In controller motif 5, A activates the formation of E, and E activates the degradation/inactivation of A. In this way, whenever the level of A increases, more E is available to activate the removal of A, adjusting A back to its set-point. Because of the zero-order degradation of E, by an enzyme, E_{set}, this is integral control. The zero-order degradation is achieved by Michaelis-Menten kinetics where the K_M of the enzymatic reaction by E_{set} is much lower than the concentration of E. This will lead to the set-point of A being independent of the perturbation.

The rate equations for species A and E are given as

$$\frac{dA}{dt} = \dot{A} = k_1 - k_{pert}^{out} \cdot A - \frac{k_3 \cdot A}{K_M + A} \cdot E \tag{2.1}$$

$$\frac{dE}{dt} = \dot{E} = k_5 \cdot A - \frac{V_{max}^{E_{set}} \cdot E}{K_M^{E_{set}} + E} \tag{2.2}$$

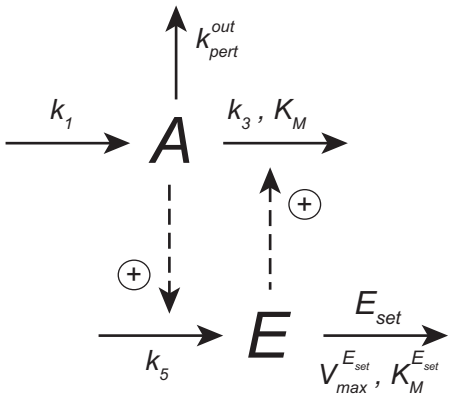

Figure 2.5: Outflow controller motif 5. A activates E, which in turn activates the compensatory flux (k_3A/K_M+A) · E. Integral control is achieved by enzyme E_{set}, which removes E by zero-order kinetics with respect to E. Details described in the main text.

Assuming steady state conditions of A and E, $\dot{A}$=0, $\dot{E}$=0 ,and that $K_M^{E_{set}}$ ≪ E, gives further the expression of E as

$$\frac{dE}{dt} = k_5 \cdot A - V_{max}^{E_{set}} = -k_5(\frac{V_{max}^{E_{set}}}{k_5} - A) = -k_5(A_{set} - A) = 0 \qquad (2.3)$$

Rearranging this to determine the set-point of A gives

$$\Rightarrow \boldsymbol{A_{set} = A_{ss} = \frac{V_{max}^{E_{set}}}{k_5}} \qquad (2.4)$$

In case the degradation of E had not been zero-order however, but a first-order degradation instead, the differential equation for E would look like this

$$\frac{dE}{dt} = \dot{E} = k_5 \cdot A - V_{max}^{E_{set}} \cdot E \qquad (2.5)$$

The set-point of A with a first-order degradation of E would therefore be dependent upon the concentration of E, and given as

$$\Rightarrow A_{set} = A_{ss} = \frac{V_{max}^{E_{set}} \cdot E}{k_5} \tag{2.6}$$

In the latter case, perturbations in A would also lead to fluctuations in E and therefore the level of A would not go back to its set-point and perfect adaptation can no longer be observed.

2.3 Biological signaling and oscillations

Biological systems can be defined as an organism as a whole, an organ system, an organ, or simply a cell. The common factor of biological systems is the existence of a network of several subunits which are connected and interacting. It has become popular to draw the connection between a biological system and a computer [15]. We have already seen that control engineering principles have been introduced in the association of biological regulation to analogous regulations of electrical devices, etc. From a systems theoretical perspective this fits well as all systems have similarities, and knowledge about one could benefit from learning more about another [13, 14].

The transfer of information within biological systems is called signaling, and could also be seen analogous to signals in information technology (IT). In IT information or signals can be given digitally and modulated in either frequency or amplitude in order to convey different interpretations of the signals. In biology, similarily, the amplitude or frequency of an analog signal can also be modified in order to give a different output of the signal [38]. As a result, transients and oscillations arise, and give different outcomes even from the same signaling transmitter. The most obvious example of this could be nerve signals. However, several biochemical reactions and phenomena in biological systems are oscillatory. Examples of biological oscillations include circadian rhythms [39, 40, 41], tumor supressor protein p53 [30, 42, 43], mechanical oscillations [41] and cytosolic calcium [44, 45, 46].

It is however important to note that for biological signals the receiver of the signal is just as important to give a meaning of the signal. A signal can be interpreted differently, depending on its receiver, and several different signals can convey the same message to the same receiver. It is rarely possible to look at the structure of the molecule, receptor etc. to analyze what meaning a signal holds [38]. Calcium (Ca^{2+}) is for instance one of the most important signaling ions, second messengers, in cell intrinsic signaling. The transfer of information through Ca^{2+} signaling is interpreted by its many recipients. The timing and readiness of the receiver (receptor) of a Ca^{2+} signal means everything for what information it conveys [47]. For instance, Ca^{2+} oscillations induced by the sperm cell can either initiate or terminate egg cell viability depending on the egg's age at the time of fertilization (Fig. 2.6 [48]).

Goodwin was interested in the rhythms in biological systems, for instance described in biological clocks [19]. In this context he characterized the occurrence of oscillations in a cell as the result of a negative feedback dynamic behavior for controlling cellular activites. Goodwin put together a mathematical model with two variables in which one of them inhibits the other thus creating a negative feedback. The model lead to oscillations due to the negative feedback and zero-order kinetics of the degradation rates [19, 49]. From a control engineering perspective oscillations are often considered a hindrance and an unwanted phenomenon to control a process; thus, control systems are usually designed to avoid them. In biology however, oscillations are quite common and often present in cellular events [19].

2.3.1 Types of oscillations

Oscillations can be described as periodic changes in a system. For oscillations to occur in a negative feedback loop generally either one of two separate conditions must exist. Oscillations can arise due to the presence of zero-order kinetics in the degradation step of the manipulated variable species (as we call E) and the controlled variable (called A), or as the result of autocatalysis [25, 50]. In order for oscillations to occur in a negative feedback system, non-linear kinetics need to be present. In biological models, this could be due to zero-order kinetics, or for instance cooperativity with the introduction of Hill-functions [51]. In the Goodwin oscillator with three intermediates for instance, degradation may follow first-order kinetics, but then the inhibition species need to have a very high cooperativity leading to

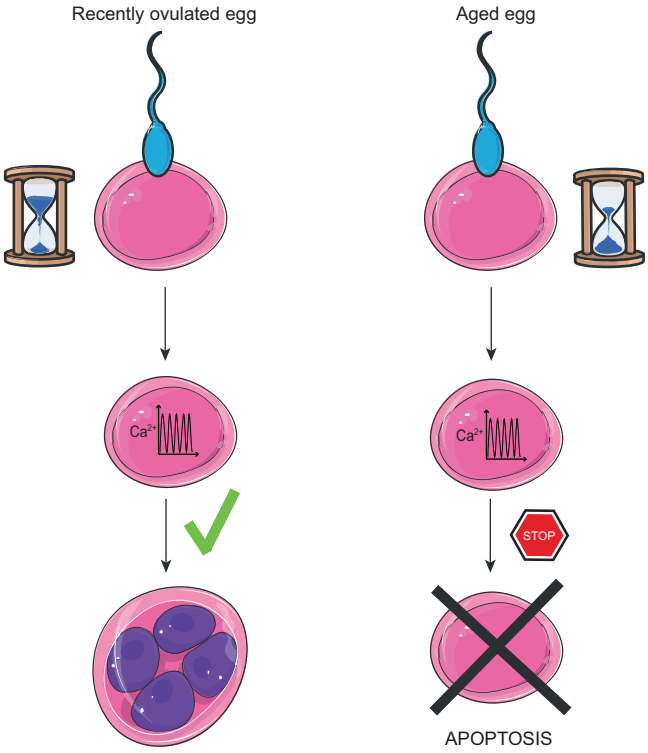

Figure 2.6: Different response to Ca^{2+} signaling following egg cell fertilization. In egg cells shortly after ovulation, Ca^{2+} oscillations initiated by the sperm leads to egg activation and the development of an embryo. In aged egg cells, however, the resulting Ca^{2+} following sperm interaction will lead to apoptosis and the termination of the egg cell. Redrawn from [48].

oscillatory behavior [25, 52]. Alternatively, degradations in A and E in one of the feedbacks shown in Fig. 2.1, for example motif 2, can be zero-order and then an inhibition cooperativity of 1 is sufficient. Oscillations can also be described by use of a combination of positive and negative feedback, called antagonistic feedback oscillations by Franck [23]. He also described a set of different feedback loops, similar to the basic set of feedback loops shown in Fig. 2.1. However, he did not make the connection to homeostasis and only considered them as different feedback alternatives between two components [23].

As previously addressed, zero-order degradation or autocatalysis are neccessary conditions for integral control leading to a robust homeostasis. This means, by meeting certain conditions, the feedback motifs are also

able to show oscillations. Oscillating homeostats will be presented and discussed in more detail in the results chapter.

Using the phase space, it is possible to distinguish between two classes of oscillations. *Limit-cycle oscillations* are represented in phase space by a simple closed curve. When perturbed for a short while, the trajectory will move towards the same limit cycle independent on the disturbance and initial conditions. This suggests strong stability in a limit-cycle oscillator, which corresponds well with biological and chemical oscillations, as a small perturbation from its set-point will lead to oscillations in increasing spirals until it reaches its limit-cycle. *Conservative oscillations* however, will be represented as several separate closed curves in the phase space due to the system's tendency to shift and stay in a new trajectory as perturbations or changes in initial conditions are applied. For conservative oscillations to persist there cannot be damping in the system. These type of oscillations are analogous to an ideal (mechanical) system following the Hamilton-Jacobi equations [25]. Due to their nature concervative systems are considered to have weak stability [19, 50].

Independently, Lotka & Volterra came up with a model (the "Lotka-Volterra model") that gives conservative oscillations. Lotka looked at chemical oscillations, while Voltera looked at oscillations in populations [50]. Goodwin is believed to be the first to propose a model for biochemical oscillatory behavior, describing gene-level control [51]. The Goodwin oscillator, or Goodwin model, is generally described as a three-component oscillator [52]. He did however, also describe a conservative oscillator a couple of years prior, which was formulated by only two variables [19]. This two-component oscillator has zero-order kinetics in the degradation terms, and show conservative oscillations [19]. In the three-component version from 1965 the degradation rates have first-order kinetics and were described to exhibit limit-cycle oscillations [52]. The latter version of limit-cycle oscillations based on a first order degradation, has undergone some critique since Goodwin did not address the cooperativity in the inhibitory step necessary for this result [51]. Following Goodwin, his results were indeed confirmed to give limit cycles nevertheless, though only with a Hill-coefficient (cooperativity) of 9 or higher for the inhibitory components [49, 51]. To achieve a response similar to that of cooperativity, several alternatives have been suggested. Instead of a Hill-type inhibition, the introduction of a critical inhibitor concentration with a "switching" or bistability mechanism could be possible to determine when the inhibition is turned on or off. Another alternative is the addition of several components, for instance multiple

phosphorylation steps in the inhibitory mechanism in order for the system to be appropriately delayed for the occurence of undampened, limit-cycle oscillations [49, 51, 53]. A three-component Goodwin oscillator with zero-order kinetics in the degradation rates exhibiting limit-cycle oscillations can also be shown with inhibitory cooperativity of 1 [25].

2.4 Iron homeostasis in plants

In plants as in humans, iron (Fe) is an essential and growth limiting nutrient. Fe is involved in major processes such as photosynthesis and chlorophyll synthesis [54]. High levels of Fe however are associated with toxicity due to the Fenton reaction. In the soil and rhizosphere Fe is fairly abundant, and both ferric iron (Fe^{III}) and ferrous iron (Fe^{II}) are present. Which Fe form is most abundant in the soil is dependent upon the soil condition. In anaerobic conditions in acidic soil Fe^{II} is found in high levels, and is readily taken up by plants [55, 56]. This could cause Fe overload of the plant which could lead to toxicity due to formation of reactive oxygen species (ROS). In order to prevent iron toxicity, formation of aerenchyma, spongy tissue with air channels, can happen. This leads to an increase in gas exchange which leads to oxygen diffusion to iron uptake regions [55, 56]. In aerobic soil however, Fe^{III} is present as low soluble iron-oxides/hydroxides [55, 57, 58]. Because of the importance of maintaining a supply of Fe to the plant as well as dealing with the risk of Fe toxicity, Fe needs to be kept homeostatically controlled.

During Fe deficiency plants utilize specific strategies for Fe uptake, which consist of Strategy I and II. Most flowering plants, angiosperms (both monocotyledoneous and dicotyledoneous), apply Strategy I. The plants using Strategy II are the graminaceous plants, grasses, including wheat, maize etc. The Strategy I plants are also commonly referred to as the non-graminaceous plants and include for instance the model organism *Arabidopsis thaliana* [57, 59, 60]. In the work performed for this thesis, the focus has been on the Fe-uptake in the model plant *Arabidopsis thaliana*.

As Fe^{III} in the soil has such a low solubility, the plant must somehow make the Fe^{III} more soluble, and reduce it to Fe^{II} in order to take it up efficiently during Fe deficiency. Strategy II plants release chelating substances called phytosiderophores which form the Fe^{III}-phytosiderophores that the plants have a highly specific uptake system for. In Strategy I plants, such as

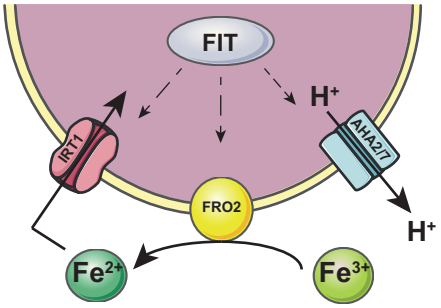

Figure 2.7: Iron uptake in *Arabidopsis thaliana*. In the occurence of iron deficiency, FIT1 will activate the gene expression of FRO2 and IRT1, leading to the response of iron uptake from the soil. Extrusion of protons from the plant root into the rhizosphere increases Fe^{III} (Fe^{3+}) solubility. The Fe^{III} is reduced by FRO2, and thereafter Fe^{II} (Fe^{2+}) can enter the cell through IRT1.

Arabidopsis thaliana, the solubility of Fe^{III} is increased in addition to the reduction of this to Fe^{II} [57, 59, 61].

The iron regulation in *Arabidopsis thaliana* has been well studied, and important regulatory components are identified. H^+ is released through ATPase AHA2 or AHA7 into the rhizosphere. This is followed by the reduction of Fe^{III} to Fe^{II} by the plasma membrane bound protein ferric-chelate reductase oxidase (FRO2) [57, 58]. Iron regulated transporter (IRT1) is essential and responsible for high affinity iron uptake to the root from the soil following reduction to Fe^{II} [56, 62, 63]. In studies done on *IRT1* knockout mutants, the mutant plant showed severe chlorosis, growth defects and death [56, 63]. The *IRT1* mutant also failed to accumulate radiolabeled ^{55}Fe after Fe starvation [56]. In plants containing IRT1, the level of IRT1 has also been discovered to be high at low external iron concentrations, and when the plant's supply of iron is adequate, the IRT1 level decreases. This could suggest a homeostasis-mediating mechanism where the degradation of IRT1 is iron-dependent [62].

In the case of low iron, "*Fe*-deficiency *I*nduced *T*rancription factor protein *1*" (FIT1) is required for the plant's response. FIT1 is a basic helix-loop-helix (bHLH) protein which has been found to interact with two other bHLH proteins, AtbHLH38 or AtbHLH39 (At = *Arabidopsis thaliana*), in order to control transcription of FRO2 and IRT1 [58, 64]. See an illustration of Strategy I in *Arabidopsis thaliana* in Fig. 2.7.

A couple of other bHLH transcription factor proteins, bHLH100 and bHLH101, have also been found to be upregulated during Fe deficiency.

These have been shown not to interact with FIT transcriptional targets such as FRO2 and IRT1. bHLH100 and bHLH101 have however been suggested to play a crucial role in the Fe-deficiency response due to mutant studies where the plants showed chlorosis and growth defects. Sivitz et al. [65] also suggest that bHLH100 and bHLH101 are part of the control of iron homeostasis by affecting the distribution of iron between tissues and organelles.

After Fe has entered the roots, it needs to be transported and distributed to the rest of the plant. The transport through the plant is associated with complexing/chelating molecules like nicotinamine (NA) and citrate [54, 57]. Once inside the cytosol, Fe needs to be distributed and sequestrated in order to facilitate its important functions in addition to avoiding toxicity [57, 61]. Two major storage mechanisms for Fe in plant cells are vacuoles and ferritins. Ferritins are iron storage proteins which can bind between 2500 and 4500 Fe^{3+} ions [61]. It has been reported that chloroplasts comprise up to 90 % of the total Fe concentration in leaf cells [54]. The "*P*ermease *I*n *C*hloroplasts" (PIC1) has been shown to regulate Fe entry into the chloroplast. The "Ferric Reductase Oxidase" 7 (FRO7) is also found in chloroplast membrane and facilitates the reduction of Fe^{III} to Fe^{II} in the cytosol. Studies of *FRO7*-lacking mutants have shown that sucrose is a limiting factor for growth. Without sucrose, plants rely on photosynthesis, and the results from the mutant experiment suggest that plants lacking FRO7 have reduced photosynthesis [54, 57]. In addition, Fe enters the mitochondria where it is involved in iron-sulfur (Fe-S) complex biosynthesis as well as Fe-mediated enzymatic reactions and electron-transport. The vacuole is a storage pool for Fe and other metals. The "*F*e-deficiency *I*nduced *T*ranscription factor protein 2" (FIT2), Ferroportin 2 (FPN2), and "*V*acuolar *I*ron *T*ransporter *1*" (VIT1) are responsible for the transport of Fe from the cytosol into the vacuole [57, 61]. The "Natural Resistance-Associated Macrophage Proteins 3 and 4" (NRAMP3/4) are responsible for the release of Fe from the vacuole into the cytosol during Fe-deficienty, and specially for germination purposes [57, 61, 66]. An overview of the involved species in plant iron homeostasis can be seen in Fig. 2.8.

2.5 Calcium

Ja Kalzium, das ist alles!
—Otto Loewi, 1959.

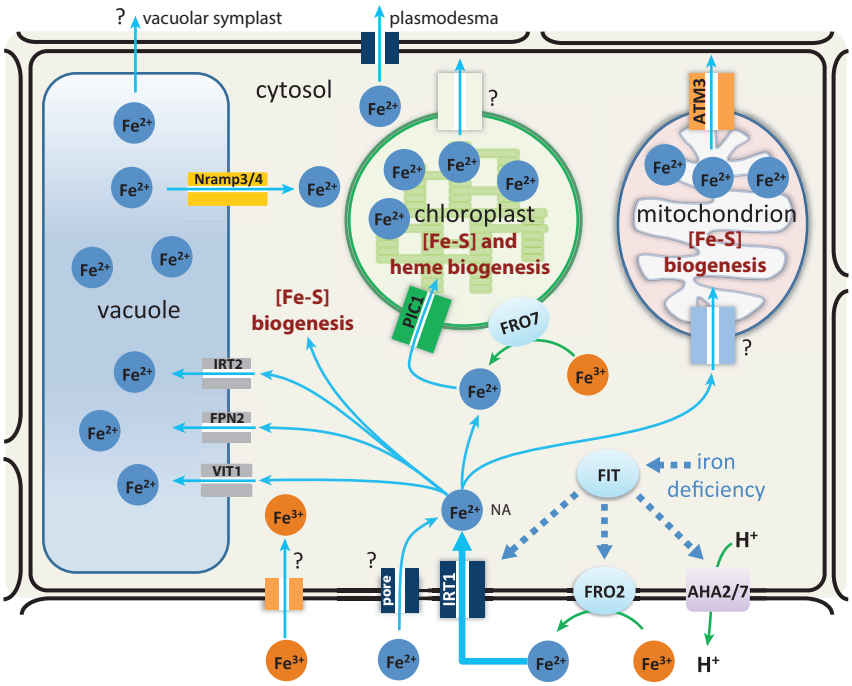

Figure 2.8: Iron homeostasis in Strategy I plants like *Arabidopsis thaliana*. In the case of iron-deficiency non-graminaceous plants utilize a strategy for iron uptake through the roots called Strategy I. FIT activates the transcription of involved proteins/-transporters AHA2/7 and IRT1 for iron uptake. Uptake of Fe involves protonic (H^+) release by AHA2/7 followed by the reduction of ferric iron (Fe^{3+}) to ferrous iron (Fe^{2+}) by FRO2 in the rhizosphere. The high-affinity transporter IRT1 transports Fe^{2+} through the plasma membrane (PM). Inside plant cells iron is transported into the vacuole for storage and into organelles like chloroplasts and mitochondria pending specific tasks. PIC1 is responsible for iron uptake into chloroplasts, and FIT2, FPN2 and VIT1 are responsible for iron storage in the vacuole. Remobilization of iron from the vacuole is achieved by the NRAMP3/4-based efflux. Figure from [67].

Calcium (Ca^{2+}) is one of the most abundant and important signaling ions in the body. Not only is it crucial for our bone health and the release of neurotransmitters, it is also involved in everything from fertilization, to gene expression, and cell death [38, 68, 69, 70]. As Campbell adresses, Ca^{2+} is generally thought of as a structural component in our body by most people. Ca^{2+} is commonly known as having something to do with our bones and teeth [69]. The discovery by Ringer in 1883 of the need for Ca^{2+} in heart contraction was pioneering in the history of discoveries concerning the role of Ca^{2+} [68, 69, 70, 71]. Prior to this Ca^{2+} had indeed only been considered a structural element, and that was the beginning of multiple pivotal discoveries following the next century on the importance of Ca^{2+} [68, 69, 70]. Table 2.1 summarizes some of the discoveries of Ca^{2+} function found in [68, 69, 70, 72]. Of course the discovery and invention of methods and technologies accelerate and aid these discoveries, but only findings concerning Ca^{2+} itself and not the technologies leading to these have been included in the table. Some of the first discoveries in the table concern Ca^{2+} in general and not necessarily only cytosolic Ca^{2+}. All are nevertheless important for the following pioneering and important discoveries that has lead the level of knowledge we have today on cytosolic Ca^{2+}.

Year	Ca^{2+} related discovery	Discovered by
1883	Necessary for heart contractions	Ringer
1894	Transmission of nerve impulses to muscle	Locke
1906	Needed for development of fertilized eggs	Loeb
1922	Cilia effects	Gray
1933	Adrenaline effect of increased paramecium motility due to cytosolic Ca^{2+} increase	von der Wense
1937	Ca^{2+} source in stimuli could be from either internal or external pool of bound Ca^{2+}	Heilbrunn
1947	Muscle contraction stimulated by injection of Ca^{2+} into the cell	Heilbrunn
1948	Diffusion of Ca^{2+} from outer membrane to inside the cell is to slow to account for rapid muscle contractions	Hill
1953-63	Discovery of Ca^{2+} storage in sarcoplasmic reticulum (SR)	Bennet & Porter, Kumagai, Hasselbach & Makinose, Ebashi
1964	Advent of Ca^{2+} buffers (Ca-EGTA)	Portzehl
1965	Determination of intracellular Ca^{2+} concentrations, resting ~ 0.1 μM	Portzehl

Year	Ca^{2+} related discovery	Discovered by
1966	Discovery of plasma membrane	
	Ca^{2+} ATPase (PMCA)	Schatzmann
1967-70	Discovery of calmodulin	Cheung, Kakiuchi
1968-70	Discovery of sarcoplasmic	
	Ca^{2+} ATPase (SERCA)	Martonosi, MacLennan
1971	Discovery of calsequestrin	MacLennan
1974/1989	Discovery and isolation of calreticulin	Ostwald& MacLennan, Fliegel
1979-83	Identification of the	
	inositol-4,5-trisphosphate reseptor (IP_3R)	Mikoshiba, Streb & Berridge
1986-88	Ca^{2+} oscillations in human cells	Woods, Berridge & Galione
1996	Discovery of arachidonic acid regulated	
	Ca^{2+} (ARC) entry	Shuttleworth

Table 2.1: Some calcium discoveries.

As Table 2.1 suggests, during the hundred years following Ringer [71], research did not only confirm the importance of Ca^{2+} for many cell and body functions, the level of detail also became enormous. From learning that Ca^{2+} had some kind of role in heart contractions, we have learned that signals arise from intracellular release from stores like the endoplasmic reticulum (ER)/sarcoplasmic reticulum (SR), and also characteristics of channels and molecules involved in this. As Portzehl and others following discovered when measuring the concentration of free cytosolic Ca^{2+}, its level is submicromolecular during resting conditions [69]. This huge difference in Ca^{2+} concentration between resting conditions, signaling events, and the extracellular concentration of around 1 mM highlights the importance of robust and reliable regulation mechanisms.

2.5.1 Cytosolic calcium homeostasis

The cytosolic Ca^{2+} concentration is regulated to around 100 nM [69]. Compared to the external environment of approximately 1 mM, the cytosolic concentration is very low. Due to the involvement of Ca^{2+} for signaling purposes and that high concentrations of Ca^{2+} are associated with apoptosis, the maintenance of cytosolic Ca^{2+} homeostasis is highly important. Dysregulation of cytosolic Ca^{2+} homeostasis has been linked to various cancers, neurodegenerative diseases, and heart disease [73, 74].

In order to achieve homeostasis, cytosolic Ca^{2+} needs to be regulated by a vast machinery of channels, pumps, receptors, buffering proteins, etc. These components function as compensatory factors by regulating the cytosolic resting level of Ca^{2+}. However, since large Ca^{2+} transients and oscillations also occur in the cytosol, these have to be considered as they disrupt the low resting level repeatedly. We have proposed in Paper 2 of the thesis that cytosolic Ca^{2+} oscillations could indeed be described as homeostatic, and this will be adressed in the results section.

Even though Ca^{2+} can leak through the plasma membrane (PM), this is not a very efficient way of entering the cell. The way extracellular Ca^{2+} can enter the cytosol, is through different types of PM channels. These are mainly the voltage operated Ca^{2+} channels (VOCCs), ligand operated Ca^{2+} channels (LOCCs) - like the arachidonic acid regulated Ca^{2+} channel (ARCC), non-specific Ca^{2+} channels (NSCCs), and the store operated Ca^{2+} channels (SOCCs). Since the focus of my work performed during this thesis addresses non-excitable cells, the VOCCs are not considered, as they are only found in excitable cells [38, 69, 70]. Once Ca^{2+} has entered the cell, it can be bound to buffering proteins in the cytosol, taken up into organelles for storage, or removed from the cytosol through the plasma membrane Ca^{2+} ATPase (PMCA) or the Na^{+}/Ca^{2+} exchanger (NCX). A similar pump to the PMCA is found in the ER/SR called the sarco-endoplasmic reticulum Ca^{2+} ATPase (SERCA) [38, 69, 70, 75].

An overview of the components involved in the cytosolic Ca^{2+} homeostasis is portrayed in Fig. 2.9.

Ca^{2+} entry through the plasma membrane

In non-excitable cells, the ARCC and SOCC make up the main Ca^{2+} inflow channels. In comparison they are quite similar in some ways yet very different in the way they function. Both ARCC and SOCC are Orai channels, which mean they are made up of Orai protein subunits [76]. Some SOCCs can also be transient receptor potential (TRP) channels [38]. The type of activation is quite different between the ARCCs and the SOCCs, as SOCC inflow is activated by ER store depletion, whereas PM-bound ARCC is activated by lower agonist stimuli of arachidonic acid, $\sim$2–4 μM, to the PM [72]. After signal stimuli to a PM bound receptor, phospholipase A_2 (PLA_2) hydrolyzes phospholipids in the PM leading to release of arachidonic acid (AA). AA then activates the ARCC [38]. It is suggested that the

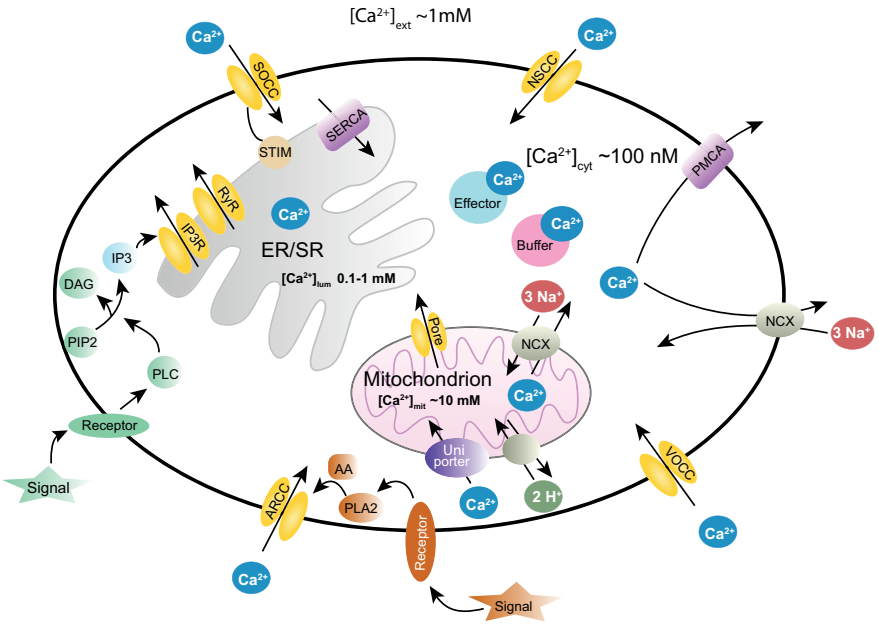

Figure 2.9: Cytosolic calcium homeostasis in human cells. Cytosolic calcium is kept under tight control by the interconnected machinery of channels, pumps, receptors, organelles, etc. Extracellular Ca^{2+} enters the cell through voltage operated Ca^{2+} channels (VOCCs), arachidonic acid regulated Ca^{2+} channels (ARCCs), store operated Ca^{2} channels (SOCCs), and non-specific cation channels (NSCC). Inside the cell, Ca^{2+} is stored and reacquired from organelles: sarco/endoplasmic reticulum (SR/ER), mitochondria and buffering proteins through various transporters involved. Removal of Ca^{2+} from the cytosol to the extracellular space is performed by plasma membrane Ca^{2+} ATP-ases (PMCA), and Na^{+}/Ca^{2+} exchangers (NCX).

main purpose of the SOCCs is to refill the depleted ER with Ca^{2+} during sustained elevated Ca^{2+} signaling, also termed capacitative Ca^{2+} entry. The non-capacitative entry of Ca^{2+} through ARCC is believed to modulate the frequency of Ca^{2+} signals/oscillations [72]. Both types of channels are regulated by stromal interaction molecule (STIM). For the activation of SOCC, STIM1 and STIM2 function as Ca^{2+} sensors in the ER lumen where Ca^{2+} binds to an EF-hand. When the Ca^{2+} concentration in the ER drops, STIM locates into puncta near the PM and connects to SOCC to activate it. The difference between the STIM1 and STIM2 lies in the level of decrease in luminal Ca^{2+}. STIM2 is assumed to regulate basal Ca^{2+} concentrations and small decreases in luminal concentration. STIM1 activates Ca^{2+} influx through SOCC following ER depletion, and is sensitive to larger changes

in the luminal Ca^{2+} concentration than STIM2 [77, 78]. ARCC is also regulated by STIM, only the mechanism is unclear. It has been suggested that STIM plays a role in the activation by arachidonic acid, as STIM is believed to be permanently connected to the ARCC Orai3 subunit [76]. There has been suggested a relationship between the two inflow channels in function by inhibitory effects. The ARC channel has been found to be inhibited by sustained increase in the cytosolic Ca^{2+} concentration. This indicates that when ER is depleted and the SOCC is activated resulting in a sustained Ca^{2+} signal, this will inhibit the ARCC. However, this inhibition is a slow process, revealing that oscillatory signals will not affect the ARCC. This means that the two channels have non-overlapping roles for Ca^{2+} entry, where ARCC is believed to modulate the frequency of oscillatory Ca^{2+} signals, while the SOCCs predominantly determine the amplitude of sustained Ca^{2+} signals [38, 72].

Ca^{2+} extrusion through the plasma membrane

In non-excitable cells, the plasma membrane Ca^{2+} (PMCA) is the most important outflow path for Ca^{2+}. Though mostly present in excitable cells, the Na^+/Ca^{2+} exchanger (NCX) has also been found in non-excitable cells, and has been suggested to play a role in the removal of Ca^{2+} from the cytosol [75, 79]. The difference in function between the two extrusion pathways is that the PMCA is a high affinity and low throughput Ca^{2+} pump, while the NCX is a low affinity but high throughput exchanger. The PMCA is an ATPase that hydrolyses 1 ATP and exchanges 1 H^+ per Ca^{2+} ion transported. It is more efficient than the NCX at lower concentration ranges, and is likely to work as a fine tuner of the cytosolic Ca^{2+} concentration. The NCX exchanges one Ca^{2+} ion for 3 external Na^+ ions [75, 80, 81]. Cytosolic Ca^{2+} has been shown to activate both the PMCA and NCX. Calmodulin (CaM) which is a Ca^{2+} binding protein found in the cytosol, is known to modulate and bind to the PMCA in order to relieve the PMCA from autoinhibition, see Fig. 2.10 [75, 82]. By binding to the PMCA, CaM decreases the dissociation constant, K_d, for Ca^{2+} from 10-20 μM in resting state to 1 μM. The pump can also be activated by acidic phospholipids in the PM, but only to about 50 % of its maximal activation [75, 83]. CaM binding is therefore of great importance to the efficiency and function of the PMCA and overall Ca^{2+} regulation in the cytosol.

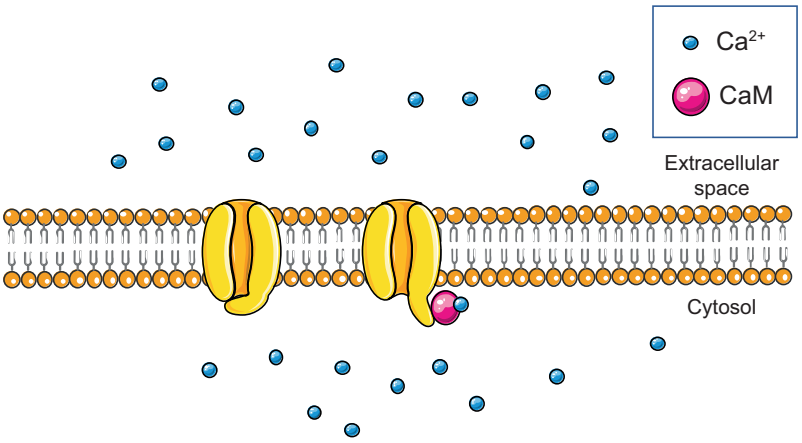

Figure 2.10: PMCA pump with and without autoinhibition. Binding of calmodulin (CaM) to the CaM-binding site of PMCA relieves the pump from autoinhibition allowing it to be activated by Ca^{2+} in order to remove Ca^{2+} from the cytosol.

Ca^{2+} regulation inside the cell

Once Ca^{2+} has entered the cytosol from outside the cell, its level can be regulated by its removal through the PM, by transport to the ER or mitochondria, or by binding to buffering proteins in the cytosol. Some of the intracellular roles of regulation have already been addressed, like the STIM proteins in the ER membrane activating the capacitative Ca^{2+} entry, and the activation by calmodulin (CaM) on the PMCA.

The Ca^{2+}-binding proteins, sometimes refered to as Ca^{2+} buffers can be divided into two categories. One category envelopes the "true" buffers, that bind Ca^{2+} as its concentration increases leading to a buffering effect, while the other consists of the Ca^{2+} sensors (or effectors) that bind to Ca^{2+} in order to excert some sort of function. The sensors can also work as buffers, if found in large concentrations [84]. Examples of Ca^{2+} buffers are parvalbumin, calbindin and calretinin. Calmodulin (CaM) is probably the best known Ca^{2+} effector/sensor. CaM is involved as a modulating factor in many signaling events and enzymes, which also includes the cytosolic Ca^{2+} regulation machinery [84]. It contains 4 binding sites for Ca^{2+}, where only Ca^{2+} binding to two of these have shown to elicit a conformational change in order for activation of its targets. However, it is believed that its fully liganded form binding 4 Ca^{2+} is the most common functional form [85, 86].

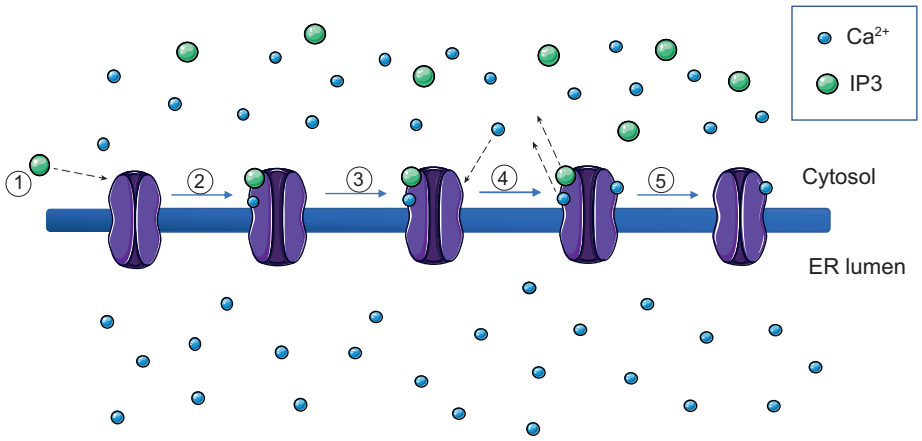

Figure 2.11: Activation and inhibition of the IP_3R. 1: IP_3 binds to IP_3R, 2: Ca^{2+} binds to IP_3R at a concentration below 300 nM activating the channel and enabling Ca^{2+} release, 3: Ca^{2+} concentration reaches a high level of above 300 nM and another Ca^{2+} binds to an inhibitory site, 4: IP_3R get less sensitive to IP_3 with Ca^{2+} bound to its inhibitory site, 5: IP_3R closes and stops the Ca^{2+} release through the ER.

Sequestration of Ca^{2+} into the endoplasmic reticulum (ER) and mitochondria also happens in order to maintain a low cytosolic Ca^{2+} concentration. The uptake pump in the ER is the PMCA-equivalent sarco/endoplasmic reticulum Ca^{2+} ATPase (SERCA), which requires 1 ATP per 2 Ca^{2+} ions transported [80]. The ER is believed to hold around 0.1–1mM Ca^{2+}, and is also highly important in the formation of cytosolic Ca^{2+} signals [87]. The inositol 1,4,5-trisphosphate receptor (IP_3R) and the ryanodine receptor (RyR) in the ER membrane are responsible for releasing Ca^{2+} from the ER into the cytosol. This Ca^{2+} release from the ER is important in signaling events. In non-excitable cells, the IP_3R is most prominant, and an interesting aspect of the IP_3R is that in addition to its activation by ligand IP_3, Ca^{2+} itself both activates and inhibits its activity [88]. This Ca^{2+} dependency follows a bell-shaped curve, where the Ca^{2+} induced Ca^{2+} release (CICR) has a peak at around 300 nM. If the Ca^{2+} concentration rises above 300 nM it will inhibit the IP_3R [88, 89]. The proposed activation and inhibition of the IP_3R can be seen in Fig. 2.11.

2.5.2 Calcium oscillations

The Ca^{2+} concentration in the cell can oscillate in order to convey a specific signal to a receiver. This signal is interpreted by its receiver by means of

amplitude and frequency of the signal, as this is relevant for affinities and possible Ca^{2+} binding-proteins that bind Ca^{2+} first. Ca^{2+} have in some cases been considered a digital intracellular messenger, as multiple cellular events initialized by Ca^{2+} is an all or nothing response. Such "on"/"off" responses like should the cell die or not, or will the neuron fire or not, can be considered as digital signals as they follow a binary pattern [69]. This strengthens the idea that a biological system is comparable in their workings as computers.

Woods et al. [90] were one of the first groups to observe Ca^{2+} oscillations as repetitive transients in hepatocytes. Berridge has had an important part in describing cytosolic Ca^{2+} oscillations, as well as the role that the IP_3R in the ER membrane play in this phenomenon [44, 91]. SOCC is believed to have a frequency modulating control of Ca^{2+} oscillations, while the ARCC has been shown to have a amplitude modulating role [72]. The strength of the signal and the ligand concentration can also play a role in what the nature of the resulting Ca^{2+} signal and perhaps oscillations will be. Different cells can also display different forms of oscillations [44, 69]. The Ca^{2+} release through IP_3R is believed to be one of the most important mechanisms for Ca^{2+} oscillations. It is believed that the described bell-shaped Ca^{2+} dependency of the channel is of fundamental importance in the generation of the oscillations. Whether Ca^{2+} oscillations are dependent on IP_3 or not is under debate [46, 92]. Since the IP_3R channel is activated at lower concentrations of Ca^{2+}, it will open channels, and as one channel opens it can trigger a cascade of the next channels opening too as they are activated by the adjacent Ca^{2+} concentration. However, as the Ca^{2+} increases above 300 nM or more, an inhibition occurs which closes the channel and lets the Ca^{2+} concentration decrease to its resting state before the channel is able to be activated and opened again [44].

As both Ca^{2+} oscillations and the cytosolic Ca^{2+} homeostasis are such important concepts, with great influence to many vital cell functions - as well as linked to various diseases, it is essential to learn more about how Ca^{2+} is regulated. Through the work presented in this thesis the aim has been to learn more about how Ca^{2+} acts homeostatically, and on the other hand also as a signal and regulator.

Chapter 3

Materials and Methods

The work performed for this thesis has been entirely computational. Computational methods have been used for developing mathematical models to describe biological systems. The models consist of a set of rate equations based on reaction kinetics and control engineering principles. FORTRAN 77 was used for programs, and computations were performed by solving rate equations numerically with the subroutine Livermore Solver of Ordinary Differential Equations (LSODE) [93]. The compiler Absoft Pro 16.0 Fortran compiler (absoft.com) was used for compilations. Gnuplot (www.gnuplot.info) and Adobe Illustrator (adobe.com) was used for plots, and GraphClick 79 for extracting experimental data from graphs (https://graphclick.en.softonic.com/mac). Gnuplot/Kaleidagraph (www.synergy.com) and Excel was used for analysis of experimental data from graphs. Figures were made in Adobe Illustrator. Some cellular biology illustrations provided from Servier Medical Art by Servier have been used in some of the figures (https://smart.servier.com). For structural analysis and figures, the program Cn3D was used (https://www.ncbi.nlm.nih.gov/Structure/CN3D/cn3d.shtml). For simplicity of annotations, concentrations of compounds are denoted by compound names without square brackets.

3.1 Iron homeostasis

Arbitrary units (au) have been used for parameters in model calculations because the cellular concentrations and associated rate constants from the experimental results are unknown.

3.2 Calcium homeostasis

For the model we have chosen a deterministic approach. In model calculations, all concentrations concerning initial conditions and rate constants of the kinetic parameters are given in their respective figures and the text. Initial conditions are overall given in μM, while the rate constants are given as different units like s^{-1}, μM, s^{-1} μM^{-1} and μM/s. The time unit is seconds.

Chapter 4

Results and Discussion

In this part of the thesis, the results from my research will be presented and discussed. The order of the following sections will begin with iron homeostasis, followed by oscillatory homeostats, and finally Ca^{2+} regulation and homeostasis, which has been the major part of my thesis work. The common theme has been homeostasis and mainly the regulation of ions, iron and calcium. The novel approach has been the incorporaction of integral control into negative feedback loops to describe how robust homeostasis can be achieved in these systems.

4.1 Iron regulation

Iron (Fe) is an essential nutrient for plants. It is also an important nutrient for humans, as Fe is part of enzymatic cofactors like hemoglobin, iron-sulfur (Fe-S) clusters, catalase etc. In general heme-iron is found to be the better option as an iron source for human consumption, compared to non-heme iron found in plants [94, 95, 96]. People living in developing countries for instance, and those having diet restrictions towards meat, depend upon plant based Fe. It is a fact that anaemia is closely linked to iron deficiency as it is a condition with too few red blood cells and/or the haemoglobin level is below a critical level. Anaemia is a major health problem world wide. In some developing countries it has been estimated by the WHO that over half the children under 5 and pregnant women are affected by anaemia. Surprisingly close to 40 % of the same group is affected also in industrialized countries, and an estimate of one third of the entire global population appears affected [94, 97, 98]. It is therefore of great value to learn more about the iron regulation in plants and to investigate possibilities of increased bioavailability of iron from dietary plants.

4.1.1 Iron homeostasis in *Arabidopsis thaliana*

The purpose of making this plant iron model was to study iron homeostasis during high-affinity iron uptake, and to investigate how different components could be interconnected. As still much of the feedback, reaction kinetics and connections between the iron homeostatic machinery in plants are unknown, this led to the choice of using arbitrary units in order to focus on the response kinetics and the qualitative comparison to experimental findings.

4.1.2 IRT1 in iron homeostasis

IRT1, as described in section 2.4.1, is the high-affinity transporter for iron under iron-deficient conditions. It is essential for the growth and development of plants. When starting out developing a model for iron homeostasis in *A. thaliana*, the negative feedback set-up of the involved components needed to be sorted out. As a starting point, external and cytosolic iron (Fe) was of course included in an initial model, as well as the *IRT1*-mRNA and IRT protein. Iron is bound as Fe-oxides, and because of the difficulty in sequestration of iron under such conditions, plants have a high demand for iron supply, in agreement with the need of an inflow controller. This harmonizes with the observation that when Fe is low and needs to increase, the E-species, here represented by IRT1, needs to activate. As the focus is on the iron homeostasis during iron uptake under iron deficient conditions, the iron assimilation flux that maintains the cell's need for iron, has been represented by the single flux $j_{\text{Fe-assim}}$ (Fig. 4.1):

$$j_{Fe-assim} = k_2 \cdot Fe_{cyt} \tag{4.1}$$

At first a model where IRT1 activates the transport of external Fe into the cytosol, and cytosolic Fe inhibits the transcription of *IRT1* was formulated. In this model, Fig. 4.1, the transcriptional control of *IRT1* (representing mRNA) is iron dependent, and the level of IRT1 protein is regulated by this mechanism during iron deficiency.

The rate equations for the model in Fig. 4.1 are given as:

$$\dot{Fe_{cyt}} = k_1 \cdot \text{IRT1} \cdot Fe_{ext} - k_2 \cdot Fe_{cyt} \tag{4.2}$$

$$\dot{\text{IRT1}} = k_5 \cdot IRT1 - \frac{V_{max} \cdot \text{IRT1}}{K_M + \text{IRT1}} \tag{4.3}$$

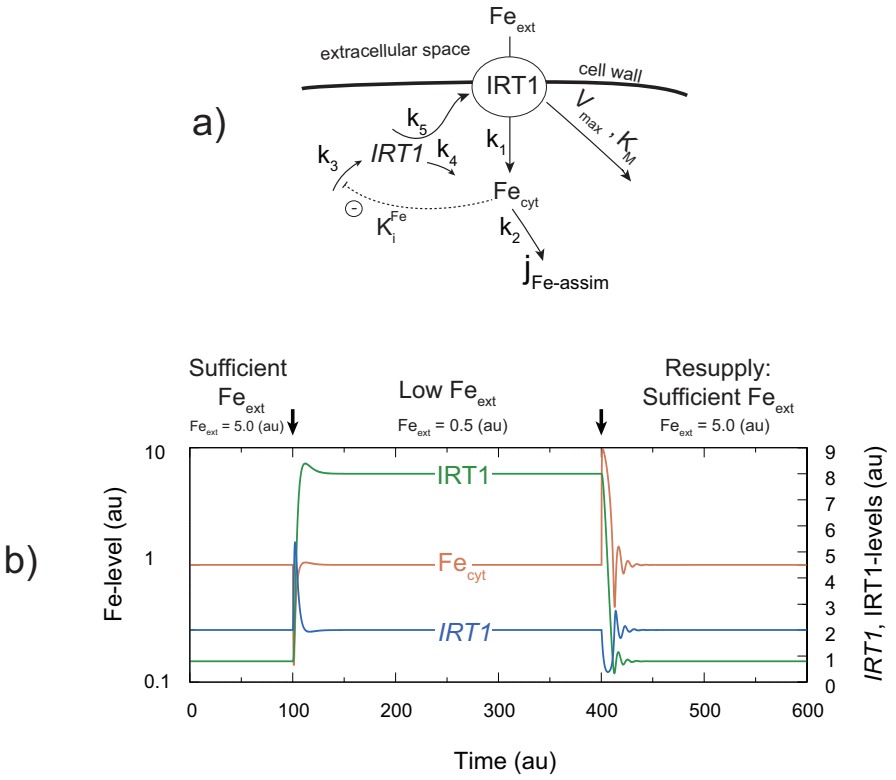

Figure 4.1: Model of iron homeostasis with iron-dependent *IRT1* transcriptional control. (a) Model reaction scheme, where Fe_{cyt} inhibits the transcription of *IRT1*-mRNA by the inhibition constant K_i^{Fe}. Inhibition is represented by the expression Fe_{cyt} / (K_i^{Fe} + Fe_{cyt}) in the rate equation for *IRT1*. (b) Graph showing modeled iron *IRT1*, and IRT following changes in external iron. The calculation has three phases where the arrows represent the start of a new phase. Phase 1 has a sufficient level of external iron (Fe_{ext}=5.0); phase 2 has a low external iron concentration (Fe_{ext}=0.5); in phase 3 external iron is resupplied in order to give sufficient amounts of external iron (Fe_{ext}=5.0). The set-point for Fe_{cyt} is arbitrarily set to 1.0. Rate parameters are as following during the three phases: $k_1 = 1.0$, $k_2 = 4.0$, $k_3 = 1.1$, $k_4 = 5.0 \cdot 10^{-1}$, $k_5 = 5.0 \cdot 10^{-1}$, $V_{max}^{E_{set}}$ = 1.0, $K_M^{E_{\text{set}}} = 1.0 \cdot 10^{-6}$, and $K_i^{Fe} = 1.0 \cdot 10^{-1}$. Initial concentrations are set to: Fe_{cyt} = 1.0, IRT1 = 0.8, *IRT1* = 2.0. IRT1 levels rise as Fe_{ext} decrease in order to maintain cytosolic Fe homeostasis.

$$\dot{IRT1} = \frac{k_3 \cdot K_i^{Fe}}{K_i^{Fe} + Fe_{cyt}} - k_4 \cdot IRT1 \tag{4.4}$$

Assuming $K_M \ll$ IRT1 gives a steady state expression of *IRT1* as V_{max}/k_5. Setting both $\dot{\text{IRT1}}$ and $\dot{IRT1} = 0.0$ given steady state conditions, a set-point expression for Fe_{cyt} can be written as:

$$Fe_{cyt,set} = \frac{k_3 \cdot k_5 \cdot K_i^{Fe}}{V_{max} \cdot k_4} - K_i^{Fe} \tag{4.5}$$

The model simulation gives a qualitative agreement with experimental findings that IRT1 levels increase when external Fe is low, and decreases when external Fe is higher [56, 62, 63, 99]. However, considering the work by Connolly et al. showing that IRT1 levels are increased in iron-deficient conditions and decrease as Fe levels rise, their results suggest that IRT1 is degraded in an iron-dependent manner [62]. Taking this into consideration, a modification of the model was made, where Fe_{cyt} is now activating the degradation of IRT1 instead of inhibiting the synthesis of *IRT1*-mRNA. The model, shown in Fig. 4.2, still has the structure of an inflow controller, which leads to iron replenishment when iron-levels are low and below the cytosolic set-point. The main difference between this model and the model in Fig. 4.1 is the way cytosolic iron regulates the level of IRT1. The mRNA *IRT1* level does not change as all.

The degradation of IRT1 is iron-dependent, where K_a^{Fe} represents an activation constant. K_a^{Fe} activating the degradation/removal or internalization in an iron-dependent manner. The E_{set} enzyme degrading IRT1 is active when bound to iron. The iron dependency can be described by the Fe activation factor f_a^{Fe}:

$$f_a^{Fe} = \frac{Fe_{cyt}}{K_a^{Fe} + Fe_{cyt}} \tag{4.6}$$

The rate equations for the model given in Fig. 4.2 are given as:

$$\dot{Fe_{cyt}} = k_1 \cdot \text{IRT1} \cdot Fe_{ext} - k_2 \cdot Fe_{cyt} \tag{4.7}$$

$$\dot{\text{IRT1}} = k_5 \cdot IRT1 - \frac{V_{max} \cdot \text{IRT1}}{K_M + \text{IRT1}} \cdot \frac{Fe_{cyt}}{K_a^{Fe} + Fe_{cyt}} \tag{4.8}$$

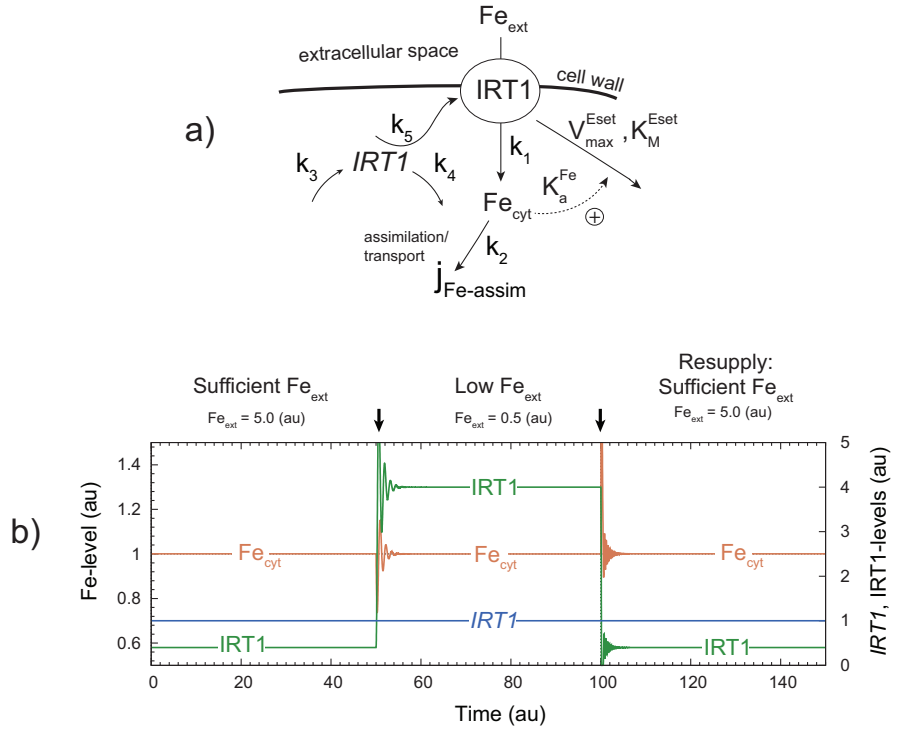

Figure 4.2: Model of iron homeostasis with iron-dependent IRT1 degradation. (a) *IRT1* represents mRNA, and IRT1 the protein. Fe_{ext} denotes the external level of iron, and Fe_{cyt} is the cytosolic iron level. K_a^{Fe} represent the activation constant for the iron-dependent degradation of IRT1, and $j_{Fe\text{-}assim}$ is the assimilation flux and transport of Fe to the rest of the plant. (b) Response of Fe_{cyt}, *IRT1*, and IRT following changes in external iron. The shift to the next phase of the calculation is represented by an arrow. Phase 1 has a sufficient external iron level (Fe_{ext}=5.0); in phase 2 the external iron concentration is lowered (Fe_{ext}=0.5); in phase 3 external iron is resupplied to sufficient amounts of external iron once again as in phase 1(Fe_{ext}=5.0). The set-point for Fe_{cyt} is arbitrarily set to 1.0. Rate parameters are as following during the three phases: $k_1 = 1.0$, $k_2 = 2.0$, $k_3 = 1.0 \cdot 10^2$, $k_4 = 1.0 \cdot 10^2$, $k_5 = 1.0 \cdot 10^2$, $V_{max}^{E_{set}} = 2.0 \cdot 10^2$, $K_M^{E_{\text{set}}} = 1.0 \cdot 10^{-4}$, and $K_a^{Fe} = 1.0$. Initial concentrations are set to: $Fe_{cyt} = 1.0$, *IRT1* = 1.0, and IRT1 = 0.4. The graph represents the responses in *IRT1*-mRNA, IRT1, and cytosolic Fe at different external Fe concentrations. The level of IRT1 increases when the demand for iron is high, as observed by experiments. Figure adapted from [67].

$$\dot{IRT1} = k_3 - k_4 \cdot IRT1 \tag{4.9}$$

The iron-dependent degradation, can also be considered as an iron sensing mechanism. The iron sensor may function in a way where the IRT1 level reflect the cytosolic Fe level and this could influence other regulatory mechanisms. The nature of the f_a^{Fe} equation reveals that it has saturation properties, that means it reaches its maximum at high Fe concentrations. When f_a^{Fe} saturates the feedback loop breaks. Also the degradation of IRT1 follows Michaelis-Menten kinetics, with a relatively strong binding of E_{set} to its substrate IRT1, i.e. assuming that $K_M^{E_{set}} \ll$ IRT1. This condition is an idealization in modeling, and ensures that Fe_{cyt} is kept homeostatically regulated at its set-point. As can be seen in Fig. 4.2b, IRT1 increases during Fe-limiting conditions to keep the cytosolic Fe level at its set-point, given as 1.0 in this simulation. The set-point of Fe_{cyt} is given from the steady state expression of Eq. 4.8

$$Fe_{cyt,set} = \frac{k_3 \cdot k_5 \cdot K_a^{Fe}}{k_4 \cdot V_{max}^{E_{set}} - k_3 \cdot k_5} \tag{4.10}$$

The modelled results of the IRT1 response to external Fe conditions compare well with the experimental results of Connolly et al., as well as others [56, 62, 99, 100]. This is given as an indication that the degradation of IRT1 is indeed iron-dependent, like Connolly et al. suggested. Compared to the previous model in Fig. 4.1, this set-up gives a faster response time of both IRT1 and thus the Fe_{cyt} level. Also, the regulation of IRT1 through its degradation by iron is also corroborated by the experimental findings.

Interestingly, Barberon et al. also studied the degradation of IRT1, and during IRT1-overexpression experiments they observed that this condition lead to iron-*in*dependent degradation of IRT1 [99]. Barberon et al. used *irt1-1* mutants, *IRT1* knockouts, where overexpression of *IRT1* by 35S::IRT1 gave accumulation of IRT1, strong overload of metals, and oxidative stress. Also the degradation rates of IRT1 did not seem to correlate with the amount of external Fe applied [99]. This discrepancy was investigated by the model, and the model has also resulted in an explanation of why Barberon et al. might have observed this presumed iron-independent degradation of IRT1 during overexpression studies.

The same model, Fig. 4.2, was used to investigate the observations by Barberon et al. In order to model the overexpression of *IRT1* the k_3

parameter was increased. The increase in k_3 also increases the set-point of cytosolic Fe, see expression 4.10. The experimentally observed iron overload [99] can be explained by the set-point change leading to a build up of cytosolic iron. Since there is simply a new set-point, the homeostatic property is kept, however considering Eq. 4.6 as the synthesis rate of IRT1 increases, f_a^{Fe} is nearly saturated at high k_3 values. When f_a^{Fe} approaches saturation ($f_a^{Fe} \to 1$), the signaling pathway from cytosolic Fe to IRT1 degradation reaches its capacity limit and the degradation becomes independent of iron. An illustration of the effect of IRT1 overexpression can be seen in Fig. 4.3

4.1.3 FIT as an iron regulator during iron deficiency

The transcription factor FIT has been found to be upregulated during Fe deficient conditions in *A. thaliana*. In addition, other important proteins in the iron-uptake machinery like FRO2 and IRT1 have been found to require the presence of FIT [58, 64]. As the previous model was quite simple, in addition not allowing for a dynamic rensponse in the *IRT1*-mRNA level, some additions were included in order to allow comparison with experimental results for low and sufficient iron conditions.

As the FIT transcription factor protein does not work on its own, but in complex with AtBHLH 38/39 [64],they have been added to the model as a joined component TF (transcription factor). FIT itself has been found to be regulated by iron [58], therefore this has also been added to this extended model. Since there has been reported increase in both *IRT1* and *FIT*-mRNAs due to iron-deficiency [56, 58, 62], the regulation of FIT by Fe_{cyt} was added as an inhibition of its transcription of *FIT*-mRNA. This will in turn lead to both an increase in FIT and IRT1 levels. In this model, the findings of an additional negative feedback [58], where FIT prevents IRT1 protein turnover through inhibition has been added. The extended model can be seen in Fig. 4.4.

Model calculations with the addition of a FIT-dependent inhibition of IRT1 degradation suggest that this leads to a significant decrease in response time of the homeostasis of cytosolic Fe. This regulation however, was added as a negative feedback with no influence on the set-point of Fe_{cyt}. In our paper, we suggest that this type of negative feedback could be termed "auxiliary feedback". See model calculations comparing regulation with and without this auxiliary feedback in Fig. 4.5. Rate equations can be found in the publication [67].

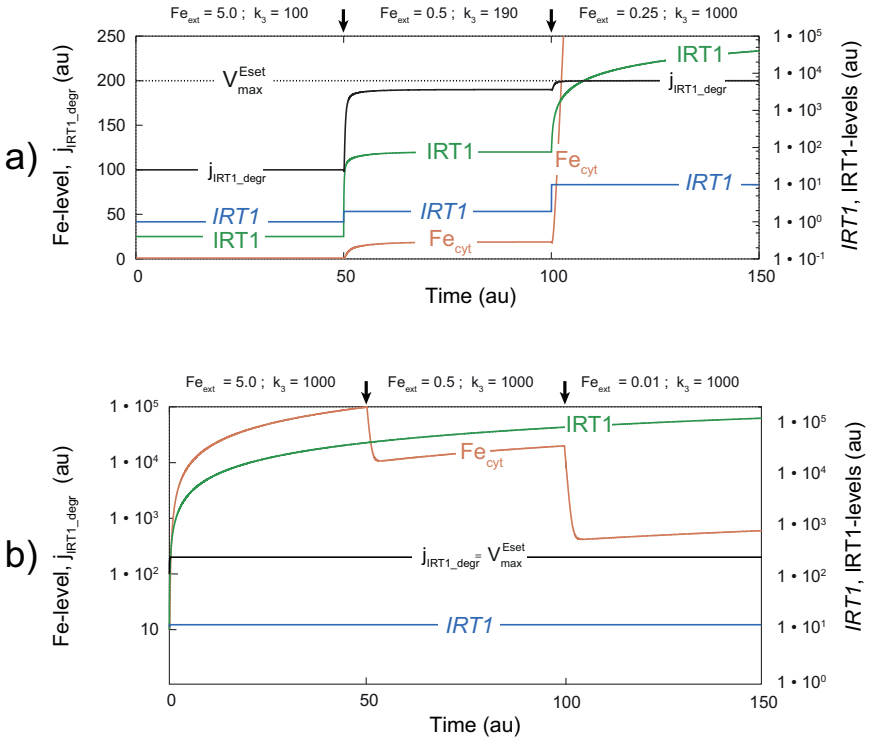

Figure 4.3: Model results for IRT1 overexpression. (a) Increase in k_3 leads to IRT1 overexpression. At t=0, $k_3 = 100$, k_3 value increased at t = 50 to $k_3 = 190$. At t = 100 k_3 is further increased to 1000. *IRT1*, IRT1 and iron levels all increase in response to the changes, however Fe_{cyt} is homeostatically regulated to its set-point as long as the IRT1 synthesis rate is lower than its degradation rate (j_{IRT1_degr}). At t=100, with a k_3 value of 1000, the Fe_{cyt} homeostasis is no longer kept because now the synthesis rate of IRT1 is greater than its degradation rate leading to saturation in j_{IRT1_degr} as it reaches the level of $V_{max}^{E_{set}}$. (b) Iron-independent degradation of IRT1 during IRT1 overexpression. IRT1 synthesis rate $k_3 = 1000$ through the whole simulation and the external iron level is varied (5.0, 0.5 and 0.01). The j_{IRT1_degr} is at its maximum value $V_{max}^{E_{set}}$, leading to *IRT1* being independent of the concentration of iron. Figure adapted from [67].

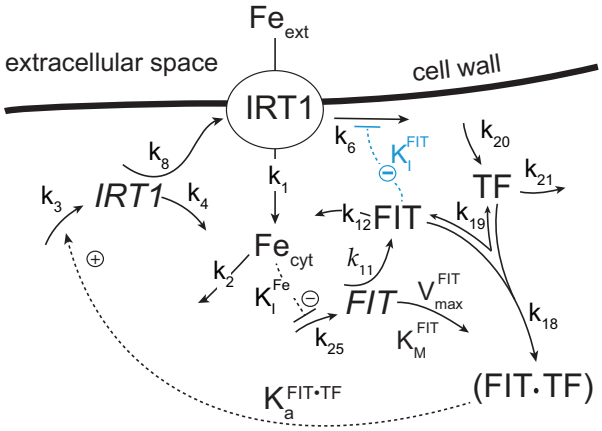

Figure 4.4: Extended iron homeostasis model. New additions to the model comprises *FIT*-mRNA and FIT protein, K_I^{Fe} representing the iron-dependent inhibition of *FIT* synthesis, blue colored K_I^{FIT} representing the FIT-dependent auxiliary feedback as an inhibition of IRT1 degradation, and TF which is an abbreviation of transcription factor. Also FIT·TF illustrating the complex of FIT with the TF, and $K_a^{FIT \cdot TF}$ which is the activation constant of the FIT·TF dependent activation of *IRT1*-mRNA synthesis. Figure adapted from [67], rate equations can be found in the supporting material of this paper.

The results in Fig. 4.5 are in good agreement with experimental results compared to results of levels of both mRNA transcripts and proteins [58].

The set-point of this model is determined in a different way than in the previously given models, and is dependent on *FIT*. The rate equation of *FIT* is given as

$$\dot{FIT} = \frac{k_{25} \cdot K_I^{Fe}}{K_I^{Fe} + Fe_{cyt}} - \frac{V_{max}^{FIT} \cdot FIT}{K_M^{FIT} + FIT} \tag{4.11}$$

When the rate equation for *FIT* is set to zero, as well as using the assumption that $K_M^{FIT} \ll FIT$, the set-point of Fe_{cyt} is

$$Fe_{cyt,set}^{FIT} = K_I^{Fe} \left(\frac{k_{25}}{V_{max}^{FIT}} - 1 \right) \tag{4.12}$$

In this extended model FIT is involved in both transcriptional and post-translational control mechanisms. The model shows some similarity to the first introduced model, but instead of Fe_{cyt} inhibiting the synthesis of *IRT1* mRNA, the FIT·TF complex activates the synthesis of *IRT1*-mRNA in accordance to findings by Colangelo and Guerinot [58].

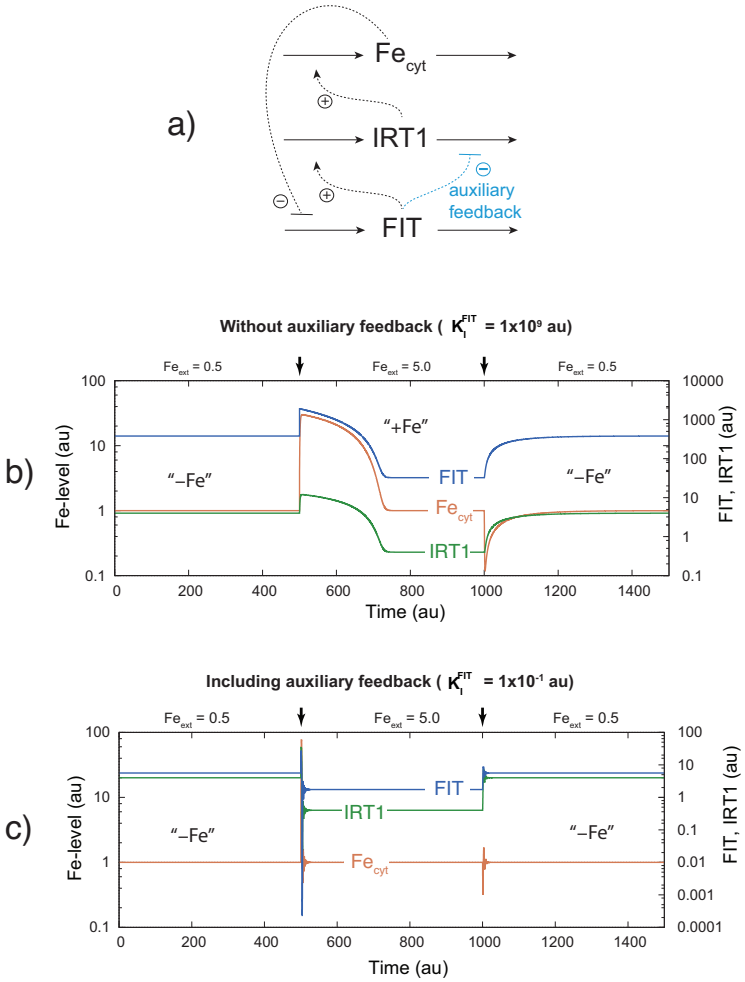

Figure 4.5: Regulation of cytosolic iron homeostasis with and without auxiliary feedback. (a) Feedback mechanisms included in the extended iron homeostasis model. Auxiliary feedback is outlined in blue. (b) Regulation of Fe homeostasis, and levels of IRT1 and FIT through changes in external Fe without auxiliary feedback. First and third phases have low $\mathrm{Fe_{ext}}$ (= 0.5), while the second phase have a higher $\mathrm{Fe_{ext}}$ level (5.0). Rate constants: $k_1 = 1.0$, $k_2 = 2.0$, $k_3 = 1.0 \cdot 10^2$, $k_4 = 1.0$, $k_6 = 4.0 \cdot 10^2$, $k_8 = 1.0 \cdot 10^2$, $K_I^{FIT} = 1.0 \cdot 10^9$, $k_{11} = 1.0 \cdot 10^3$, $k_{12} = 1.0 \cdot 10^3$, $K_a^{FIT \cdot TF} = 1.0 \cdot 10^4$, $k_{18} = 1.0 \cdot 10^2$, $k_{19} = 10.0$, $k_{20} = 1.0 \cdot 10^4$, $k_{21} = 2.0 \cdot 10^4$, $K_I^{Fe} = 1.0$, $k_{25} = 4.0$, $V_{max}^{FIT} = 2.0$, $K_M^{FIT} = 1.0 \cdot 10^{-4}$. Initial concentrations: $\mathrm{Fe_{cyt}} = 1.0$, *IRT1* = 16.0, IRT1 = 4.0, *FIT* = 381.0, FIT = 381.0, TF = 0.5, FIT·TF = 1905.0. (c) Same as in b but including auxiliary feedback. Same rate constants except $K_I^{FIT} = 1.0 \cdot 10^{-1}$ and initial concentrations: $\mathrm{Fe_{cyt}} = 1.0$, *IRT1* = 0.3, IRT1 = 4.0, *FIT* = 5.6, FIT = 5.6, TF = 0.5, FIT·TF = 28.0. Regulation with auxiliary feedback shows a much more rapid response time. Figure adapted from [67].

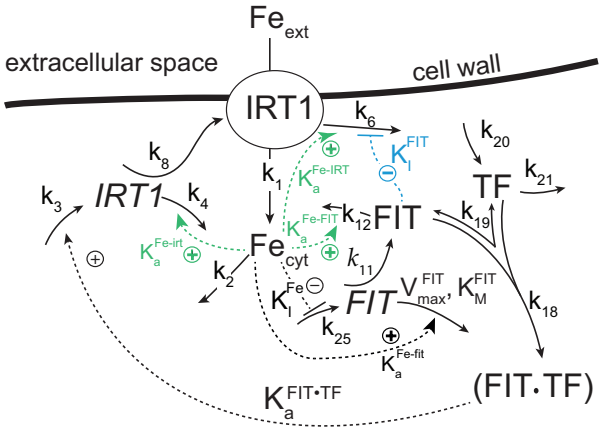

Figure 4.6: Extended iron homeostasis model with alternative auxiliary feedback. The auxiliary feedback (AF) from earlier is still shown in blue, while the suggested alternative AFs are shown in green. The alternative potential AFs all arise from Fe_{cyt}. The Fe-dependent degradation of *IRT1*, IRT1, and FIT, are given as K_a^{Fe-irt}, K_a^{Fe-IRT}, and K_a^{Fe-FIT}, respectively. The alternative feedback of the *FIT* degradation is given as a black dashed line and with the activation constant K_a^{Fe-fit}. Figure adapted from [67].

Iron dependent auxiliary feedback

Auxiliary feedback (AF) was termed in the last section as a sort of helper or assisting negative feedback. A characteristic is that it does not influence the set-point, but rather helps improve the controller's adaption kinetics to the set-point [67]. In addition to the AF presented in Fig. 4.4, of FIT-dependent inhibition of IRT1 degradation, several additional feedbacks were in turn tested to see whether they would improve the response kinetics. These include Fe determined AFs leading to Fe-dependent degradation of *IRT1*, IRT1, and FIT, see Fig. 4.6. In addition an Fe-dependent degradation of *FIT* was added, however this feedback affects the set-point of Fe_{cyt} because the set-point is given by *FIT* in this model. Since this last feedback affects the set-point it does not qualify as an AF, and is instead considered an alternative regular feedback for the model.

The AFs were added one at a time separately and then in combination with the existing AF of the extended model. The existing AF (FIT-dependent degradation of IRT1) was still present while adding the alternative, however its inhibition constant, K_I^{FIT}, was $K_I^{FIT} = 1.0 \cdot 10^9$ like in Fig. 4.5b where it can be considered inactive. The addition of the AFs to *IRT1*, IRT1, or FIT, are given as activation factors f_a which are

multiplied to the existing corresponding rate equations. These are given in the following expressions representing the fraction of activated enzyme in the respective feedback mechanism

$$f_a^{Fe-irt} = \frac{Fe_{cyt}}{K_a^{Fe-irt} + Fe_{cyt}} \tag{4.13}$$

$$f_a^{Fe-IRT} = \frac{Fe_{cyt}}{K_a^{Fe-IRT} + Fe_{cyt}} \tag{4.14}$$

$$f_a^{Fe-FIT} = \frac{Fe_{cyt}}{K_a^{Fe-FIT} + Fe_{cyt}} \tag{4.15}$$

The expression added to the *FIT* rate equation when adding the alternative Fe-dependent degradation, was added by the given expression

$$f_a^{Fe-fit} = \frac{Fe_{cyt}}{K_a^{Fe-fit} + Fe_{cyt}} \tag{4.16}$$

One hypothesis was that a combination might improve the response time even further. However the combination of two AFs did not show any significant improvement, and in some cases the opposite. A few of the other auxiliary feedbacks showed promising results on their own however, well comparable to the effect of the FIT-induced auxiliary feedback. See an overview of some AF simulations in addition to the Fe-dependent degradation of *FIT* in Fig. 4.7.

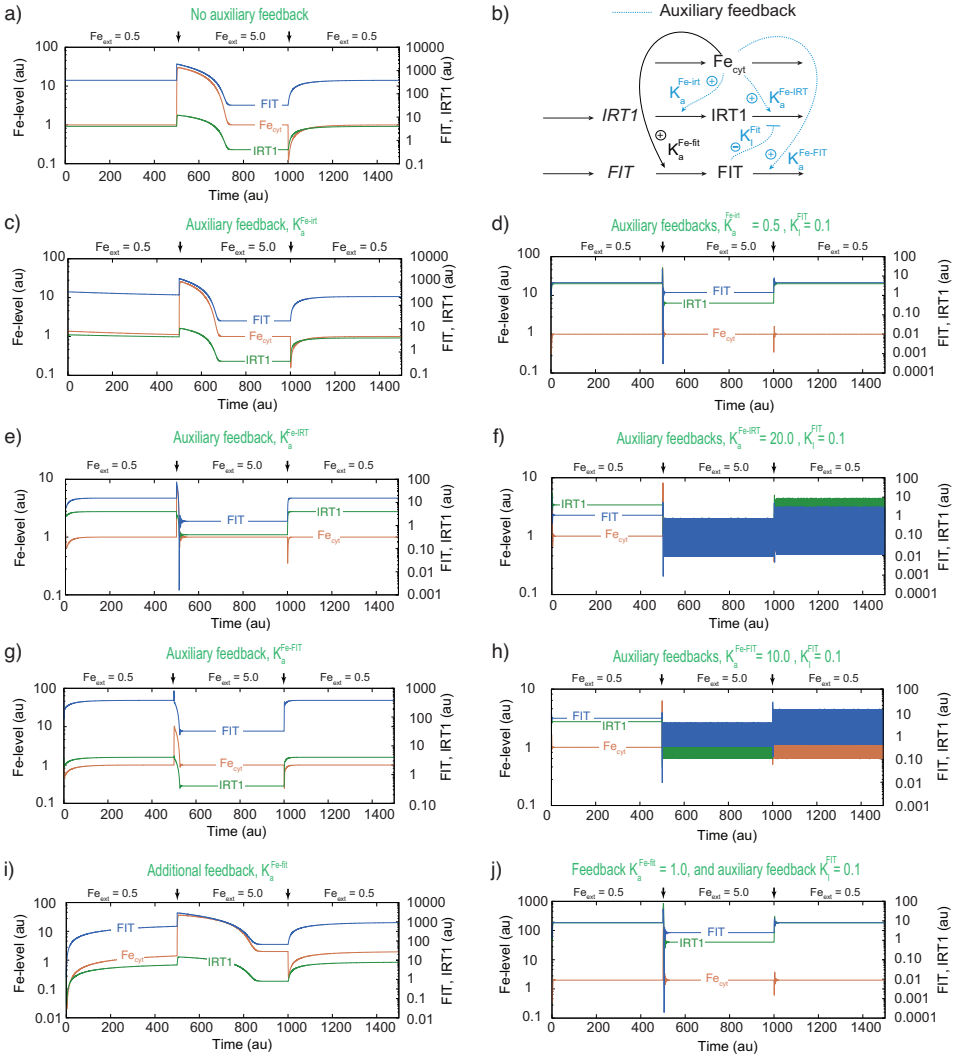

Figure 4.7: Alternative and auxiliary feedback mechanisms. (a) Graph with no added auxiliary feedback in model as given in Fig. 4.5b. (b) Scheme showing an overview of the added auxiliary feedbacks and alternative feedback, all Fe-dependent degradations of another reaction species. (c) K_a^{Fe-irt} is added alone, achieved by setting the k_9 level extremely low eliminating the auxiliary feedback effect. When K_a^{Fe-irt} is added alone the response time decreases. Rate constants: $k_1 = 0.5$, k_1 phase 2 = 5.0, k_1 phase 3 = 0.5, $k_2 = 2.0$, $k_3 = 1.0 \cdot 10^2$, $k_4 = 400.0$, $k_6 = 1.0$, $k_8 = 1.0 \cdot 10^2$, $K_I^{FIT} = 1.0 \cdot 10^9$, $k_{11} = 1.0 \cdot 10^3$, $k_{12} = 1.0 \cdot 10^3$, $K_a^{FIT \cdot TF} = 1.0 \cdot 10^4$, $k_{17} = 1.0$, $k_{18} = 1.0 \cdot 10^2$, $k_{19} = 10.0$, $k_{20} = 1.0 \cdot 10^4$, $k_{21} = 2.0 \cdot 10^4$, $k_{22} = 1.0 \cdot 10^{-4}$, $K_I^{Fe} = 1.0$, $k_{25} = 4.0$, $V_{max}^{FIT} = 2.0$, $K_M^{FIT} = 1.0 \cdot 10^{-4}$, $K_a^{Fe-irt} = 0.5$. Initial concentrations: $\mathrm{Fe_{cyt}} = 1.0$, $IRT1 = 16.0$, IRT1 = 4.0, $FIT = 381.0$, FIT = 381.0, TF = 0.5, FIT·TF = 1905.0. Unless stated, rate constants remain unchanged for following calculations.

(d) Both K_a^{Fe-irt} and K_I^{FIT} AFs added, well comparable to only K_I^{FIT} added as seen in Fig. 4.5c. Same now $K_I^{FIT} = 0.1$. Initial conditions: $Fe_{cyt} = 1.0$, *IRT1* = 0.34, IRT1 = 4.0, *FIT* = 0.9, FIT = 4.6, TF = 0.5, FIT·TF = 22.9. (e) K_a^{Fe-IRT} added alone, gives nearly as fast response as for only K_I^{FIT}. $K_a^{Fe-IRT} = 20.0$ ($K_a^{Fe-irt} = 0.0$). Initial conditions: $Fe_{cyt} = 1.0$, *IRT1* = 1.45, IRT1 = 4.0, *FIT* = 5.9, FIT = 29.5, TF = 0.5, FIT·TF = 147.6. (f) Both K_a^{Fe-IRT} and K_I^{FIT} ($K_I^{FIT} = 0.1$) gives oscillations. Initial conditions: $Fe_{cyt} = 1.0$, *IRT1* = 0.5, IRT1 = 4.0, *FIT* = 2.1, FIT = 10.4, TF = 0.5, FIT·TF = 51.9. (g) Only K_a^{Fe-FIT} added, gives shorter response time. $K_a^{Fe-FIT} = 10.0$ (K_a^{Fe-IRT}=0.0). Initial conditions: $Fe_{cyt} = 1.0$, *IRT1* = 0.28, IRT1 = 4.0, *FIT* = 1.1, FIT = 5.6, TF = 0.5, FIT·TF = 28.1. (h) Both K_a^{Fe-FIT} and K_I^{FIT} gives oscillations. Same initial conditions as previous. (i) Additional feedback K_a^{Fe-fit} ($K_a^{Fe-fit} = 1.0$) is added, has a higher response time than without this. (j) Addition of $K_I^{FIT} = 0.1$ AF gives nearly the same result as only K_I^{FIT}, however the set-point is changed because this feedback affects the determination of the set-point.

As Fig. 4.7 shows, addition of other feedbacks can also reduce response time for cytosolic Fe to return to its set-point similarily to the original AF given by K_I^{FIT}. The most promising additional feedback is the Fe-dependent degradation of *IRT*, where Fe_{cyt} activates *IRT* degradation, Fig. 4.7c. When combining with the original AF, which inhibits the degradation of IRT, this combination leads to a well comparable response to K_I^{FIT} alone. The combination also leads to a slight increase in the IRT concentration, in addition to increased FIT/*FIT*-mRNA levels, meaning that the regulator level is increased. Any of the potential AFs alone will again lead to a decreased overall FIT-level. The addition of the Fe-dependent activation of the IRT degradation does not combine well with the existing K_I^{FIT} AF, Fig. 4.7f. Both AFs affect the same reaction in opposite directions. This could potentially balance, however, in combination it does not seem stable. On its own, the effect of the response time is positive nevertheless as the response time is improved. The third alternative AF which is the activation of FIT degradation by Fe_{cyt}, Fig. 4.7g, also decrease the response time, however this combination also leads to an oscillatory response. It is not presently known if Fe_{cyt} regulates any of these degradations. Experiments have intrestingly shown that proteasomal degradation of FIT is required for the plant response during iron deficient conditions [101]. Whether this regulation is attributed Fe_{cyt} or not is as stated currently unknown. In addition to the given potential AFs that were introduced, an alternative feedback, an activation of *FIT* degradation, was also added. The higher the K_a^{Fe-fit} rate constant is set, the higher the response time gets. However, with the addition of K_I^{FIT}, the response time drastically decreases again

to around the same as when only K_I^{FIT} is there. Still, this alternative feedback actually influences the set-point of Fe_{cyt} since its expression is dependent upon the rate equation of *FIT*.

4.1.4 Iron homeostasis during iron storage and remobilization

Until this point, the model has described a high-affinity uptake of iron during low Fe_{ext} conditions. But what about the cases where there are higher amounts of readily available Fe in the soil? This is the case in more acidic soil where more iron is becoming soluble as opposed to normal neutral soil where due to the pH ($\approx$7) iron is bound as low-soluble $Fe(OH)_3$ or Fe_2O_3. In this condition the plant requires some additional mechanisms to avoid the toxicity of high iron concentrations. A combined model integrating both the low-affinity uptake during high Fe_{ext} and the high-affinity uptake during Fe-deficiency is presented in Fig. 4.8. The model also includes intracellular storage and its remobilization.

The model is a further extension of the previously described model of Fig. 4.4. In conditions of high/sufficient Fe_{ext}, the plant still takes up iron though no longer through the FIT-IRT1 pathway [61, 102]. FIT has been found in overexpression studies to be produced in both Fe-deficient and Fe-sufficient plant conditions. However, IRT1 and FRO2 production is not induced during Fe-sufficient conditions, and are constrained to Fe-deficient conditions [102]. This, together with the fact that iron is allowed to enter the plant even in *IRT1* knockout plants that are supplied with Fe in the water, suggests that iron has an alternative inflow-path, i.e. a low affinity transporter [56]. In order to avoid iron toxicity due to build-up of Fe_{cyt}, there are storage mechanisms like Fe_{cyt} binding to ferritins and nicotianamine (NA). NA is also important for Fe transport within the plant, and during conditions of high Fe concentrations, NA is synthesized correspondingly. During high loading of iron to the plant, NA is mostly found to be localized in vacuoles indicating an importance of vacuoles in Fe storage in order to avoid toxicity [103]. Under Fe-deficient or normal Fe-levels, NA is generally found in the cytosol, meaning that iron is not stored in the vacuole during those conditions [103]. A common transporter representing IRT2 and FPN2 is responsible for the iron-uptake into the vacuole in the model [57, 61]. NRAMP3/4 has been found to be resposible for the remobilization of Fe_{store} into the cytosol [57, 61, 66].

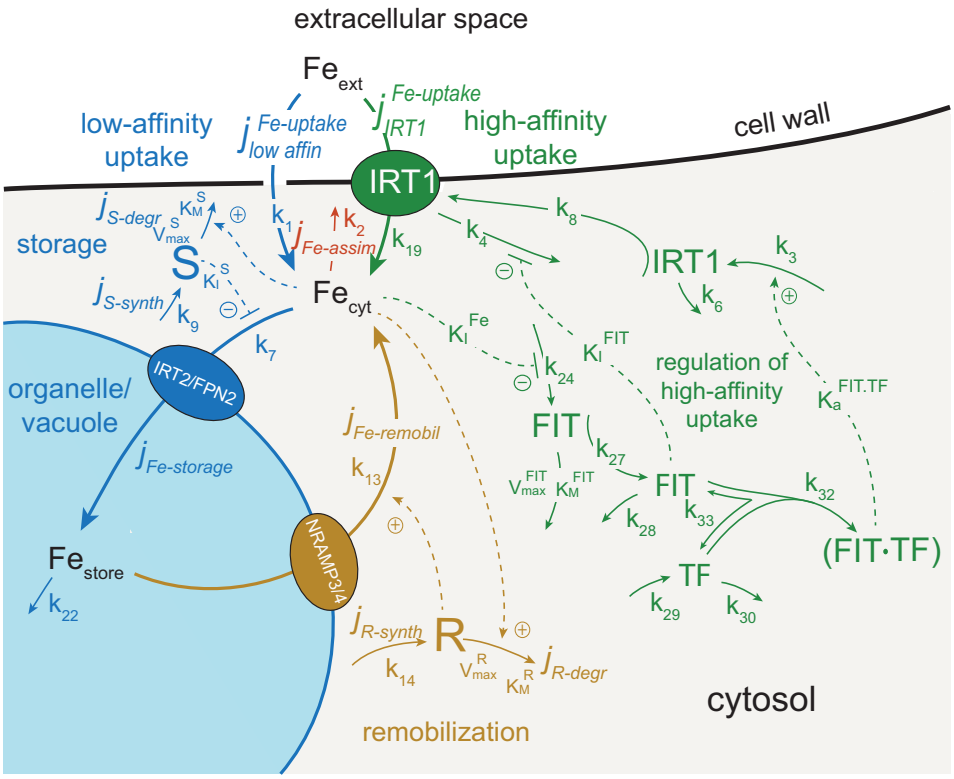

Figure 4.8: Integrative iron uptake model including high and low affinity uptake of iron. Low-affinity uptake mechanism combined with uptake of iron storage is highlighted in blue. The derepression of an unknown repressor S leads to iron storage into the vacuole/store. The low-affinity uptake is not dependent upon S, however, the set-point (outflow control) is. The model also includes remobilization of Fe_{store} to the cytosol (highlighted in ochre). The mechanism representing the assimilation and transport to other plant parts is shown in red color. Note some changes in rate constant notations, described in supporting material from [67].

The rate of the high-affinity uptake described in the extended model from Fig. 4.4, is given by the following $j_{IRT1}^{Fe-uptake}$ expression

$$j_{IRT1}^{Fe-uptake} = k_{19} \cdot \text{IRT1} \cdot Fe_{ext} \tag{4.17}$$

The low-affinity uptake rate is assumed to be proportional to the Fe_{ext} concentration, and is given by the expression for $j_{la}^{Fe-uptake}$

$$j_{la}^{Fe-uptake} = k_1 \cdot Fe_{ext} \tag{4.18}$$

The expression for $\text{j}_{\text{Fe-assim}}$ is still the same as in Eq. 4.1. Finally, the rate of the storage flux, is described as $j_{Fe-storage}$

$$j_{Fe-storage} = k_7 \cdot Fe_{cyt} \cdot \frac{K_I^S}{K_I^S + S} \tag{4.19}$$

The mechanism for Fe_{cyt} transport into storage, is based on an inhibitor S, which inhibits the entry of Fe_{cyt} into vacuole/storage during iron-deficient conditions. When Fe_{cyt} is high, it activates the degradation of S, which leads to derepression, and Fe_{cyt} is stored. This corresponds well with the findings on ferritin activation [104]. K_I^S represent the inhibition constant for the S inihibiton of $j_{Fe-storage}$. For simplicity the flux of Fe_{cyt} into the vacuole/storage is considered proportional to the concentration of Fe_{cyt}, as the transporter concentration is regarded as constant (and thereby also k_7). Similarily, for the remobilization of Fe_{store}, the rate constant representing the NRAMP13/14 (k_{13}) is also considered constant. The rate of the remobilization flux is given as

$$j_{Fe-remobil} = k_{13} \cdot Fe_{store} \cdot R \tag{4.20}$$

A set-point for Fe_{cyt} in this model can be determined from the remobilization equations with respect to the inflow controller R. The rate equation for R is given as:

$$\dot{R} = j_{R-synth} - j_{R-degr} = k_{14} - Fe_{cyt} \cdot \left(\frac{V_{max}^R \cdot R}{K_M^R + R} \right) \tag{4.21}$$

Assuming that $K_M^R \ll \text{R}$, this gives the set-point at remobilization:

$$Fe_{cyt,set}^R = \frac{k_{14}}{V_{max}^R} \tag{4.22}$$

The set-point of Fe_{cyt} determined during low affinity uptake and for the storage of iron can be found from the rate equation for S:

$$\dot{S} = j_{S-synth} - j_{S-degr} \tag{4.23}$$

$j_{S-synth}$ is the constant k_9 in the model, Fig. 4.8, and j_{S-degr} is iron-dependent and activated by Fe_{cyt}, and can be described by Michaelis-Menten kinetics:

$$j_{S-degr} = Fe_{cyt} \cdot \left(\frac{V^S_{max} \cdot S}{K^S_M + S} \right) \tag{4.24}$$

By setting $\dot{S} = 0$, this leads to the $Fe_{cyt,set}$ during low affinity uptake

$$Fe^S_{cyt,set} = \frac{j_{S-synth}}{V^S_{max}} \tag{4.25}$$

Since there are several set-points for Fe_{cyt} in this model, they need to be arranged in a hierarchical way in order to avoid wind-up and to ensure correct function in the model to avoid that controllers work against each other [27]. In this context, the different set-points have the following values based on the chosen rate parameters in the program; $Fe^S_{cyt,set} = 1.5$, $Fe^{FIT}_{cyt,set} = 1.0$, $Fe^R_{cyt,set} = 0.8$. The difference in set-points also allows the differentiation between storage, high-affinity and remobilization phases to be easily identified; see calculations presented in Fig. 4.9.

In the beginning of the simulation, there is a high concentration of Fe_{ext} which means that the Fe-uptake is through the low-affinity transporter. From the development of the graph in both Fig. 4.9a and Fig. 4.9b, the Fe_{ext} is observed to be proportional to the Fe-uptake during low-affinity uptake. At the same time as the low-affinity uptake happens, there is a flux of Fe_{cyt} into the storage which is represented by the $j_{Fe-storage}$ curve. At about t $\approx$ 1250, the Fe_{ext} concentration is no longer sufficient to maintain the homeostasis by the S-controller and the Fe_{cyt} concentration drops below the S-determined set-point of 1.5. As the low-affinity influx of Fe_{ext} decrease, the need for iron is now compensated and satisfied by the increase in Fe_{ext} by the high-affinity uptake mechanism through IRT1. At this time, there is a set-point of 1.0 which is maintained by the high-affinity uptake. In combination, the $j^{Fe-uptake}_{low-affinity}$ and the $j^{Fe-uptake}_{IRT1}$ compensate the assimilatory flux represented by $j_{Fe-assim}$, in order to

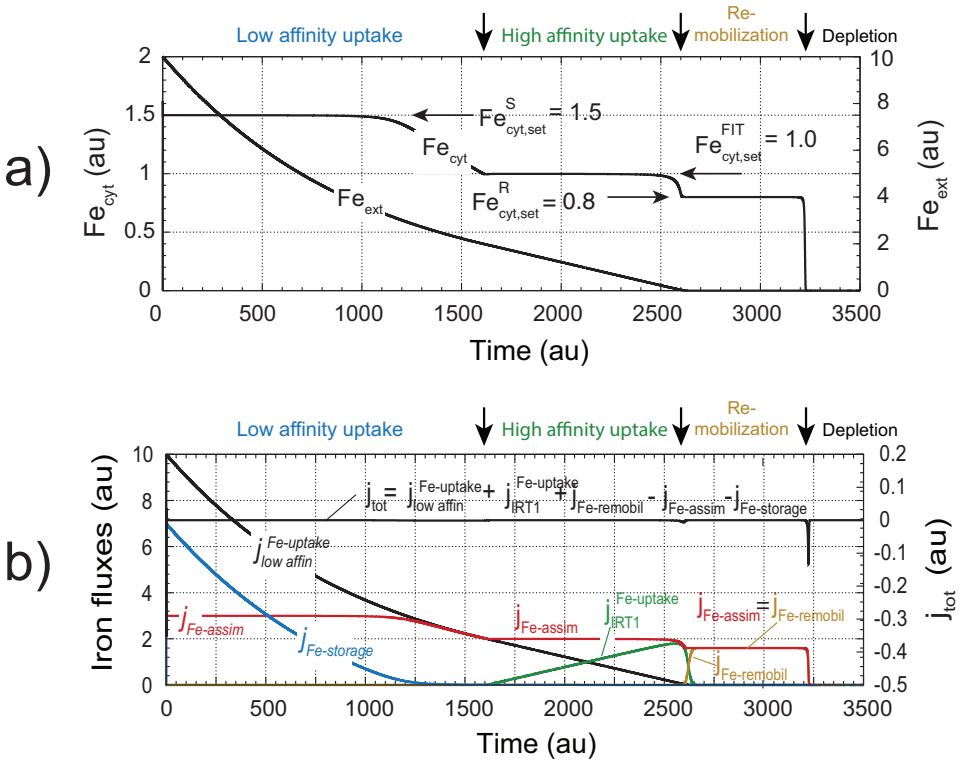

Figure 4.9: Iron regulation during storage, high-affinity uptake and remobilization conditions. (a) Iron regulation during low-affinity uptake/storage conditions in phase 1, high-affinity uptake in phase 2, iron re-mobilization in phase 3, and iron-depletion conditions during the last 4th phase. Rate constants: $k_1 = 1.0$, $k_2 = 2.0$, $k_3 = 1.0 \cdot 10^2$, $k_4 = 1.0$, $k_6 = 4.0 \cdot 10^2$, $k_7 = 1.0 \cdot 10^2$, $k_8 = 1.0 \cdot 10^2$, $V^S_{max} = 10.0$, $K^S_M = 1.0 \cdot 10^{-4}$, $K^S_I = 0.1$, $k_{13} = 0.5$, $k_{14} = 0.8$, $V^R_{max} = 1.0$, $K^R_M = 1.0 \cdot 10^{-6}$, $k_{19} = 0.5$, $k_{22} = 5.0 \cdot 10^{-4}$, $K^{Fe}_I = 1.0$, $k_{24} = 4.0$, $V^{FIT}_{max} = 2.0$, $K^{FIT}_M = 1.0 \cdot 10^{-4}$, $k_{27} = 1.0 \cdot 10^3$, $k_{28} = 1.0 \cdot 10^3$, $k_{29} = 1.0 \cdot 10^4$, $k_{30} = 2.0 \cdot 10^4$, $k_{32} = 1.0 \cdot 10^2$, $k_{33} = 10.0$, $K^{FIT \cdot TF}_a = 1.0 \cdot 10^4$, $K^{FIT}_I = 0.01$. Initial concentrations: $\mathrm{Fe_{ext}} = 10.0$, all other initial conditions are 0.0. (b) Same calculation and phases as in (a), but showing the different fluxes of iron. Same rate constants as in (a). Figure adapted from [67].

maintain Fe_{cyt} homeostasis. This relationship can be represented by the following expression

$$j_{Fe-assim} = j_{low-affinity}^{Fe-uptake} + j_{IRT1}^{Fe-uptake} \tag{4.26}$$

Eventually the Fe_{ext} concentration is exhausted at around t $\approx$ 2600. At this point, remobilization of Fe_{store} occurs represented by the $j_{Fe-remobil}$ flux. During these conditions, a new set-point is again reached, this time determined by the R-controller at 0.8. At t $\approx$ 3250, all iron in the system both in external and internal reservoirs is depleted. At this point the R-controller also fails to maintain Fe_{cyt} homeostasis. The set-up of controller motifs in this model, see Fig. 4.8, allows the system to respond to the external Fe concentration in a way that maintains Fe_{cyt} homeostasis.

Biofortification strategies for iron

Iron biofortification is of great interest to the health of the global population. There are several possible processes for increasing the bioavailability in food crops. Traditionally this has been done through conventional breeding or agronomic practices, however genetic engineering and modification can be used to predict and enhance the improvement at another level. Different transgenic approaches in for instance rice have been identified and shown to yield 1-6 fold of iron increase [105]. The model presented in this work is a computational approach used to identify and model mechanisms for robust iron homeostasis in comparison with experimental results. The overall interest in this is to increase the understanding of plant iron homeostasis. In the context of biofortification, the understanding of iron homeostasis, iron localization and the mechanisms involved are helpful in order to develop better strategies [61, 106].

During low external concentrations of iron, vacuolar iron storage does not occur. The mechanisms involved seem to only lead to iron storage in the vacuole when large amounts of iron enters the cell. This has been the mechanism in the iron model presented here, in agreement with experimental findings [103]. We suggest a possibility of increased vacuolar storage of iron also during conditions where external iron concentrations are low. This strategy is based on placing an inflow controller within the vacuolar membrane and having the controller molecule inside the vacuole. Based on the negative feedback structure of the controller molecule this will lead

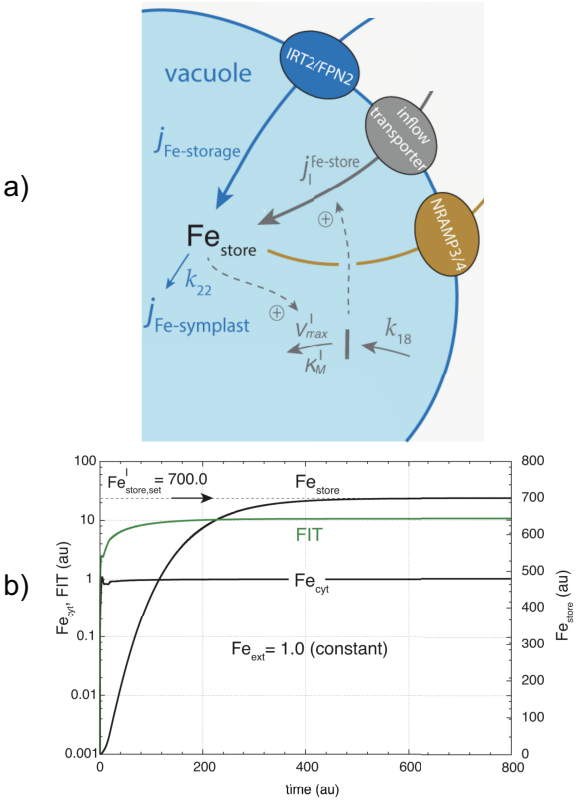

Figure 4.10: Iron storage in vacuole as a biofortification strategy. (a) Close up view of the vacuole, but otherwise the same model as in Fig. 4.8. The addition to the model is done in the vacuole where a controller molecule "I" is present. This controller molecule activates an inflow transporter in the vacuolar membrane, but is also subject to an iron-dependent degradation. $\dot{I}$= k_{18} - $Fe_{store} \cdot V^I_{max} \cdot I/(K^I_M + I)$. Iron flux through the inflow transporter is given as $j_I^{Fe-store} = k_{17} \cdot Fe_{cyt} \cdot I$. (b) Plot shows how iron increases in the vacuole, Fe_{store}, while cytosolic Fe levels are maintained. Assuming $K_M \ll I$, the set-point inside the vacuole is given as $Fe^I_{store,set} = k_{18}/V^I_{max}$, and is set to 700.0 here. Rate constants: $k_{17} = 1.0 \cdot 10^{-3}$, $k_{18} = 700.0$, $V^I_{max} = 1.0$, $K^I_M = 1.0 \cdot 10^{-4}$. Initial concentration of I = 0.0. Figure adapted from [67].

to the maintanance of a defined iron homeostatic set-point of the vacuole. Illustration of this addition to the iron model is shown in Fig. 4.10a.

Fig. 4.10b shows how the concentration of iron inside the vacuole increase to the given set-point as a function of time. The set-point, $Fe^{I}_{store,set}$, is defined as 700.0. This set-up is purely theoretical, but illustrates a potential possibility of manipulating mechanisms involved in iron-storage. There are experimental reports of incorporation of synthesized transporters like putative ferric reductase 2 (FRP2) to the vacuolar membrane, as well as overexpression of the vacuolar iron transporter (VIT1) to increase and redirect vacuolar storage [61].

4.2 Homeostatic oscillations

4.2.1 Extending the concept of homeostasis

As previously stated, homeostasis is defined by Cannon "as a tendency of a system to regulate itself back to a stable environment". Homeostasis of a system is therefore traditionally interpreted and confined as the system returning to a set value within narrow limits. We want to extend the concept to include sustained oscillatory and pulsatile conditions, as we show that robust homeostasis can be maintained based on the set of controller motifs shown in Fig. 2.1 in the Introduction. With the emergence of alternative terminologies such as rheostasis, allostasis and homeodynamics, our attempt is not the first to add to the concept of homeostasis. We do not wish to make a new term altogether but to expand the definition by our approach using integral control un an oscillatory regime. The findings from this study have biological significance to the oscillatory signaling of calcium and p53, in addition to the regulatory involvement of circadian rhythms concerning homeostasis. Specifically, calcium will be discussed with a preliminary model demonstrating an outflow homeostatic controller showing oscillations in intracellular Ca^{2+}.

4.2.2 Oscillatory controllers

The eight controller motifs of Fig. 2.1 represent negative feedback of the controlled variable A where the species E will either activate or inhibit its compensatory flux. These controller motifs can be used as oscillatory homeostats to illustrate the ability to maintain robust homeostasis during

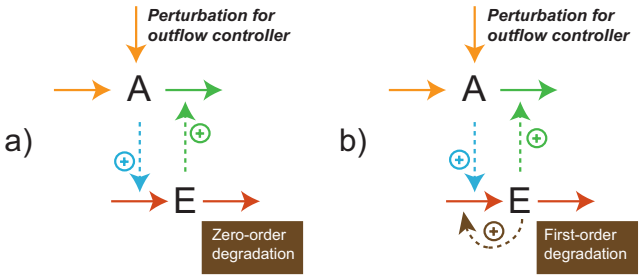

Figure 4.11: Outflow controller 5 with two different integral control implementations. (a) Shows outflow controller 5 with integral control represented through the zero-order degradation of E. The red arrows represent the set-point, given by the ratio between the removal and synthesis rates of E. The blue arrow illustrates the negative feedback by A to the activation of E. The green arrows show the compensatory flux, which is the concentration of E regulating the process that makes A. Orange color indicates the perturbations that affect the level of A. (b) This figure shows the same outflow controller 5, however with a different implementation of integral control. The integral controller is now represented by an autocatalytic formation of E, as well as a first-order removal with respect to E. The color scheme still represents the same as in panel a.

oscillatory conditions. Fig. 4.11 shows how a two-component homeostatic controller motif can implement integral control in two different ways.

Both conservative and limit-cycle versions of the motifs can be shown and can be compared with homeostatic mechanisms such as cytosolic Ca^{2+} oscillations. Motif 2 and 5 have been chosen as representative examples of this because they portray both an inflow and outflow controller respectively. The two motifs also represent differences in the way species E controls the compensatory flux (j_{comp}), where in motif 2 E inhibits the j_{comp}, whereas E in motif 5 is activating the j_{comp}. Outflow controller 6 in its limit-cycle version has also been used in the Ca^{2+} oscillatory model.

Conservative oscillatory controllers

For a system to be considered conservative its energy (or Hamiltonian function/H-function) can be found, and the H-value remain constant in time. In phase space, conservative oscillators show periodic motions that occur as closed paths in phase space for each H-value. The H-function can derive the dynamics of a two-component conservative oscillator, and is given as the following equations

$$\frac{\partial H}{\partial E} = -\dot{A} \tag{4.27}$$

$$\frac{\partial H}{\partial A} = \dot{E} \tag{4.28}$$

These equations are analogous to the Hamilton-Jacobi equations from classical mechanics. They also show time independency and the system can thus be considered conservative.

The negative feedback oscillators based on motif 1 and 5 of Fig. 2.1 can represent the Lotka-Volterra oscillator. In this case integral control is implemented by autocatalysis in the formation of species A and the following degradation of A by a first-order process with respect to A [24]. By changing the implementation of integral control to zero-order kinetics in the removal of A, the same motifs now show harmonic oscillations. See Fig. 4.11 for an illustration of how this difference is implemented schematically. Motif 2 can be used to represent the Goodwin oscillator of two components from 1963. Early on, Goodwin actually drew attention to the analogy between the dynamics of a set of cellular two-component negative feedback oscillators and classical mechanics [19]. As an example, motif 2 is represented in the following figure Fig. 4.12.

The graph in Fig. 4.12c shows an increase in frequency as the perturbation k_2 is increased from 1.0 to 3.0 after 50 time units. As another example of perturbation response, a harmonic oscillator based on motif 5, is also modeled. Typical for the harmonic oscillator is the constancy of the frequency upon changing k_1 (perturbation) values. This can be observed in the following representation in Fig. 4.13.

By comparing motif 2 and 5 as conservative oscillators, one can see the difference in responce of the frequency and mean values <E> and <A> of an inflow-type and outflow-type controller respectively. This can be seen in Fig. 4.14.

In the inflow-type controller (motif 2), the increased outflow perturbation is compensated by a decrease in the average amount of E. This leads to an increased compensatory flux which in turn neutralizes the increased removal of A. This is given as

$$j_{comp} = \frac{k_3 \cdot K_I^E}{K_I^E + E} \tag{4.29}$$

Rate equations for both A and E can be seen in Fig. 4.12b. The average amount of A (<A>) is kept at its set-point given as

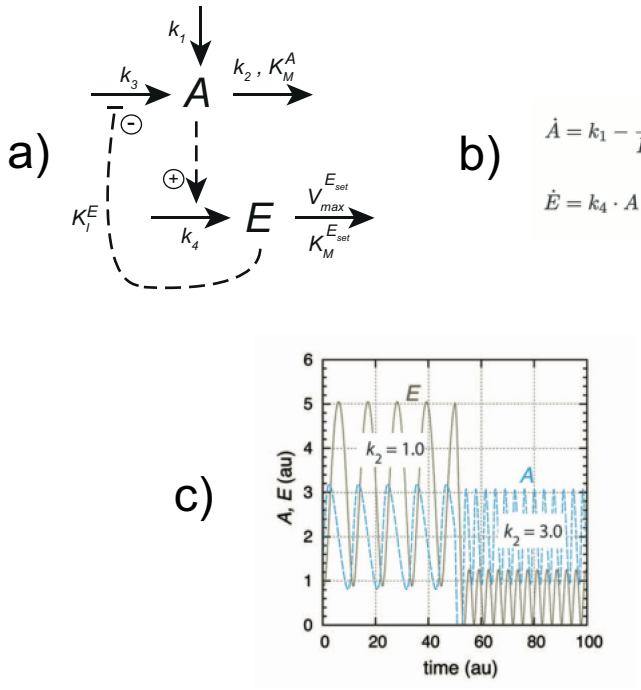

$$\dot{A} = k_1 - \frac{k_2 \cdot A}{K_M^A + A} + \frac{k_3 \cdot K_I^E}{K_I^E + E}$$

$$\dot{E} = k_4 \cdot A - \frac{V_{max}^{E_{set}} \cdot E}{K_M^{E_{set}} + E}$$

Figure 4.12: Representation of conservative oscillator based on motif 2. (a) Reaction kinetic representation of "Goodwin's oscillator" based on motif 2. When $K_M^A \ll$ A and $K_M^{Eset} \ll$ E conservative oscillations occur. Integral feedback and thereby robust homeostasis is introduced by the latter condition [27, 29]. (b) Rate equations for the controlled variable A and manipulated variable E. (c) Conservative oscillations in A and E. Initial conditions are given as: $k_1 = 0.0$, $k_2 = 1.0$, $K_M^A = 1 \cdot 10^{-6}$, $k_3 = 6.0$, $K_I^E = 0.5$, $k_4 = 1.0$, $V_{max}^{E_{set}} = 2.0$, $K_M^{E_{set}} = 1 \cdot 10^{-6}$. Initial concentrations: $A_0 = 1.5$, $E_0 = 1.0$. At time $t = 50.0$, k_2 is changed from 1.0 to 3.0.

$$< A_{set} >= \frac{V_{max}^{E_{set}}}{k_4} \tag{4.30}$$

assuming $K_M^{E_{set}} \ll$ E.

By using an harmonic approximation, the frequency, ω, of oscillations can be estimated, with the assumption of $k_1 = 0$. For motif 2 this can be written as

$$\omega = \frac{\sqrt{k_3 \cdot k_4 \cdot K_I^E}}{K_I^E + E_{ss}} \tag{4.31}$$

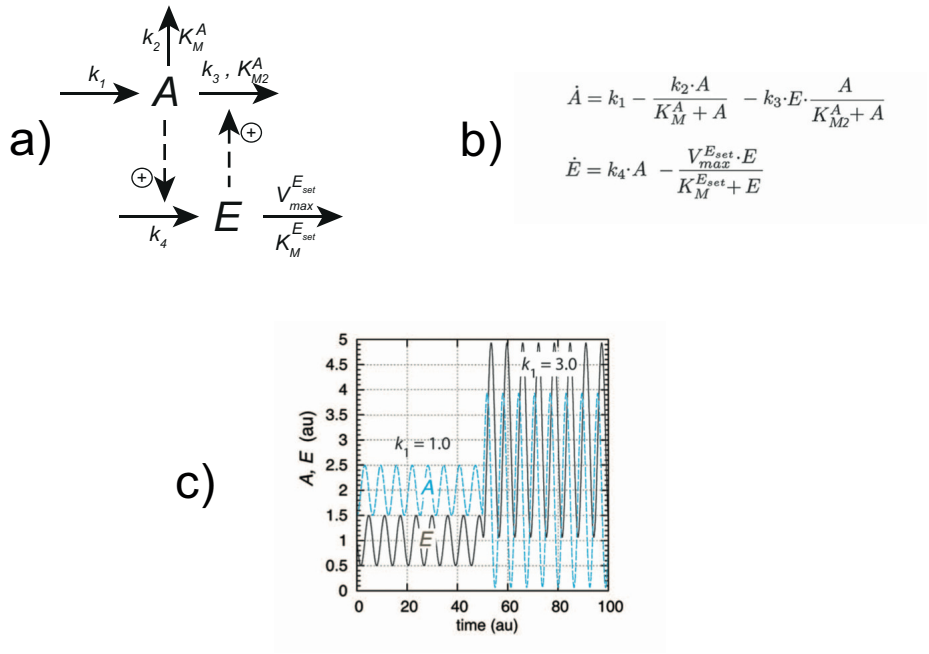

Figure 4.13: Representation of conservative oscillator based on motif 5. (a) Reaction kinetic representation of an harmonic oscillator based on motif 5. $K_M^A \ll$ A (or $k_2 = 0$) and $K_M^{Eset} \ll$ E. (b) Rate equations for the controlled variable A and manipulated variable E. (c) Conservative oscillations in A and E. Initial conditions are given as: $k_1 = 1.0$, $k_2 = 0.0$, $k_3 = 1.0$, $K_{M2}^A = 1 \cdot 10^{-6}$, $k_4 = 1.0$, $V_{max}^{E_{set}} = 2.0$, $K_M^{E_{set}} = 1 \cdot 10^{-6}$. Initial concentrations: $A_0 = 1.5$, $E_0 = 1.0$. At time $t = 50.0$, k_1 is changed from 1.0 to 3.0. Figure adapted from Paper I [25].

where E_{ss} is the steady state of E, which can be calculated when $\dot{A} = 0$

$$E_{ss} = \frac{k_3 \cdot K_I^E}{k_2} - K_I^E \tag{4.32}$$

Based on the indications from equation 4.31 and the modeled results in Fig. 4.14a, the frequency is observed to increase as the perturbation k_2 increases in motif 2. When k_2 increases to a point that the E level is lower than K_I^E, the compensatory flux, j_{comp}, approaches its maximum value of k_3. When this occurs the homeostatic capacity of the controller is reached and further increase of k_2 leads to a breakdown of the controller. The breakdown happens because the k_2 increase cannot be met by an increase in j_{comp}. For outflow controller 5, the compensatory flux

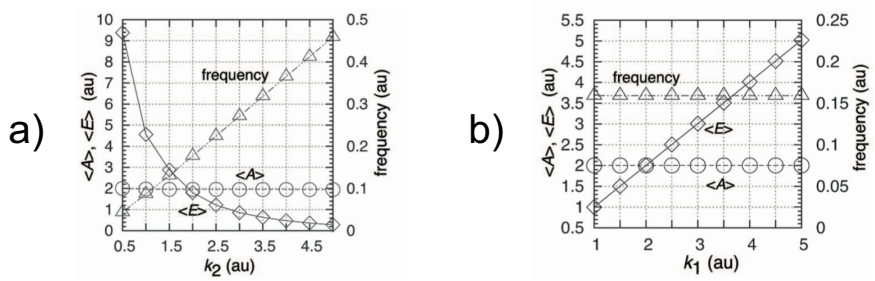

Figure 4.14: Frequency changes in conservative oscillators based on inflow controller 2 and outflow controller 5. (a) Frequency, <A> and <E> as a function of the perturbation k_2. The frequency increases and <E> decreases with the increase of k_2, while <A> is kept at its set-point $V_{max}^{E_{set}}$ / k_4 = 2.0. (b) Frequency, <A> and <E> as a function of the perturbation k_1. The frequency is in this case constant as k_1 increases. <E> increases with the increase of k_1, while <A> is kept at its set-point $V_{max}^{E_{set}}$ / k_4 = 2.0.

$$j_{comp} = k_3 \cdot E \tag{4.33}$$

will compensate any inflow perturbations (k_1 changes) of A by increasing. When $K_M^A \ll$ A and $K_M^{Eset} \ll$ E the oscillations are harmonic around the set-point $< A_{set} > = V_{max}^{E_{set}}/k_4$. The frequency, ω, for motif 5 is

$$\omega = \sqrt{k_3 \cdot k_4} \tag{4.34}$$

The oscillation period is

$$T = \frac{2\pi}{\sqrt{k_3 \cdot k_4}} \tag{4.35}$$

With an increase in perturbation strength (increased k_1), the frequency of harmonic oscillator 5 is unchanged, see Fig. 4.14b. With the increase in j_{comp}, an increase in <E> will occur, thus keeping the homeostasis of <A>. This behavior can also be observed for the corresponding inflow controller motif 1.

Limit-cycle oscillatory controllers

As previously described, the idea of making limit-cycle oscillations is based on conservative oscillations where an intermediate is added to the controller

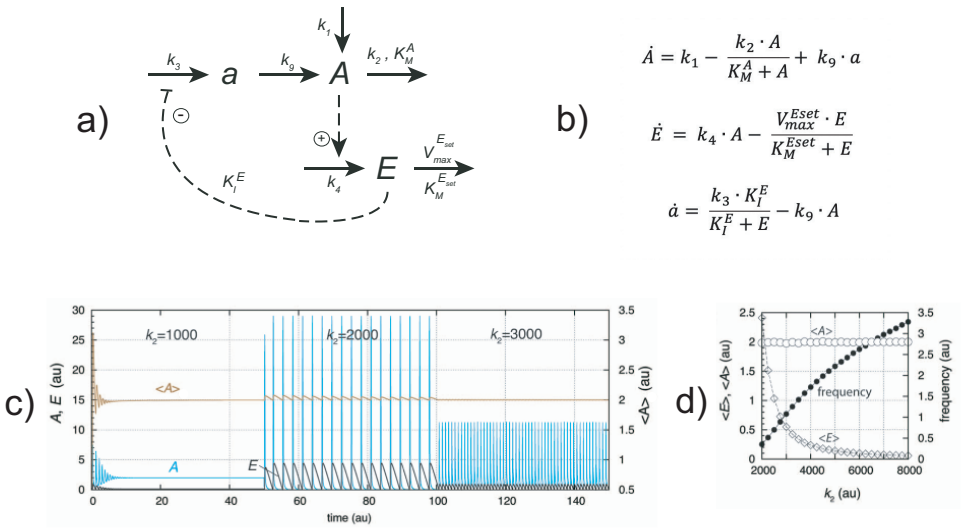

Figure 4.15: Representation of limit-cycle oscillator based on motif 2. (a) Reaction kinetic representation of a limit-cycle oscillator based on motif 2 where an intermediate a is added upstream of A. (b) Rate equations for the controlled variable A, manipulated variable E and intermediate variable a. (c) Limit-cycle oscillations in A and E. <A>, the average of A, is kept under homeostatic control despite pulsatile oscillations in A. Initial conditions are given as: $k_1 = 1.0$, $K_M^A = 1.0$, $k_3 = 1.0 \cdot 10^5$, $K_I^E = 1.0 \cdot 10^{-3}$, $k_4 = 1.0$, $V_{max}^{E_{set}} = 2.0$, $K_M^{E_{set}} = 1.0 \cdot 10^{-6}$, $k_9 = 2.0$. Degradation kinetics with respect to A are no longer strictly zero-order as compared to motif 2 in the conservative case. Initial concentrations: $A_0 = 1.5$, $E_0 = 0.3$, $a_0 = 166.17$. At time t = 50.0, k_2 is changed from $1.0 \cdot 10^3$ to $2.0 \cdot 10^3$, and at t = 100.0, k_3 is changed to $3.0 \cdot 10^3$. (d) Frequency, <A> and <E> given as a function of the change in k_2 perturbation.

either upstream of A or E [24]. In Fig. 4.15 a representation of motif 2 as a limit-cycle oscillator can be seen. In this model an intermediate a is added upstream of the controlled variable A. E feeds back to the formation of the intermediate a, and the degradation of A is no longer strictly zero-order.

Compared to the conservative case in Fig. 4.12, the limit-cycle case also displays an increase in the frequency as the pertubation (k_2) strength increases. As in the conservative case, the limit-cycle oscillator also keeps <A> at its setpoint at all times during perturbation changes, where <x> is the average calculated as

$$\frac{1}{\tau} \int_0^\tau X(t) dt \tag{4.36}$$

Motif 5 has also been converted into a limit-cycle oscillator by adding

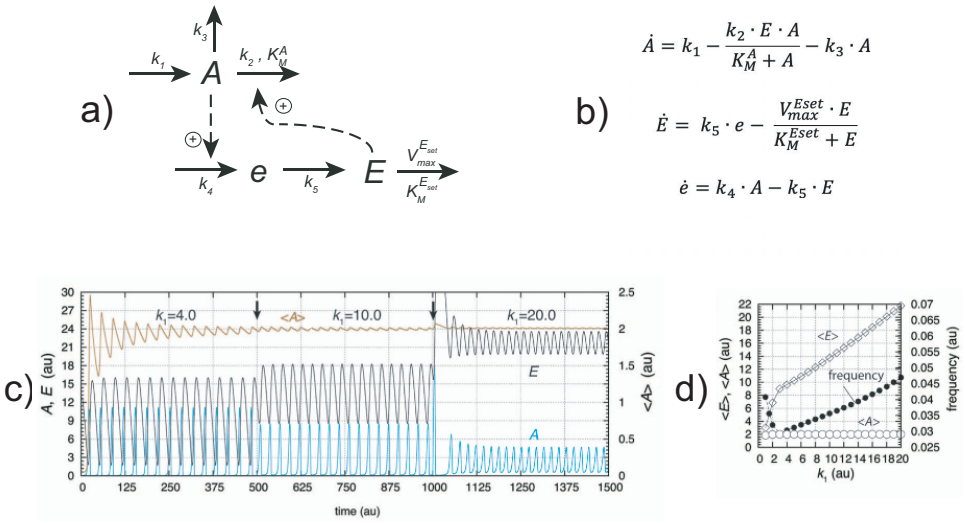

Figure 4.16: Representation of limit-cycle oscillator based on motif 5. (a) Reaction kinetic representation of a limit-cycle oscillator based on motif 5. (b) Rate equations for the controlled variable A, manipulated variable E and intermediate variable e. (c) Limit-cycle oscillations in A and E. Initial conditions are: $k_2 = 1.0$, $K_M^A = 0.1$, $k_3 = 0.0$, $k_4 = 0.5$, $k_5 = 0.2$, $V_{max}^{E_{set}} = 1.0$, $K_M^{E_{set}} = 1.0 \cdot 10^{-6}$. Initial concentrations: $A_0 = 1.9964 \cdot 10^{-2}$, $E_0 = 12.0258$, $e_0 = 8.0983$. At time t = 500.0, k_1 is changed from 4.0 to 10.0, and at t = 1000.0, k_1 is changed to 20.0. (d) Frequency, <A> and <E> given as a function of k_1.

the intermediate e upstream to the variable E. This set-up can be seen together with its behavior following an increased pertubation in Fig. 4.16.

<A> homeostasis is kept by increasing <E> in both the conservative and limit-cycle cases. Frequency changes (both decrease and increase) is observed for the limit-cycle oscillator, however overall the frequency changes are not as large as for motif 2. This observation indicates that the limit-cycle motif 5 oscillator has a kind of intrinsic frequency compensation on k_1 perturbations similar to the harmonic one.

Considering the limit-cycle oscillations here, one can show, [25], that the same controller motifs can also show homeostasis in <A> like in the case of the conservative oscillators.

4.2.3 Robust frequency control in oscillatory homeostats

Several biological oscillators, such as the temperature compensation of the circadian clock and the p53-Mdm2 system, show a homeostatic regulation of

frequency/period [42, 107]. The temperature compensation of the circadian period holds a nearly constant period length of 24 hours at different but constant temperatures [107]. Also the P53-Mdm2 system has a nearly constant period where the oscillation number might be indicative to the strength of DNA damage within the cell [42, 108]. We are able to show robust frequency control in two different ways. The first one is by the presence of quasi-conservative kinetics in a limit cycle oscillator and the second way is to have E regulated by additional inflow/outflow controllers I_1,I_2.

Robust frequency control based on quasi-conservative kinetics

In order to achieve quasi-conservative behavior in a limit-cycle oscillator, the intermediate species, a or e, needs to obey approximately the steady state assumption $\dot{a} \approx 0$ and $\dot{e} \approx 0$. The result is called quasi-conservative or quasi-harmonic due to the system still having a limit-cycle however behaving more as a conservative system. p53 is a transcription factor with tumor suppressor properties, which is upregulated in response to stress signals such as DNA damage [42]. The p53-Mdm2 system is a negative feedback loop where p53 activates Mdm2 transcriptionally, and Mdm2 will in turn negatively regulate p53 both by inhibition of its activity and by enhancing its degradation rate. It is found that this system exhibits oscillatory behavior, where the amplitude varies widely, however the frequency is less variable [42]. This description matches well with the behavior of the quasi-harmonic oscillator. When motif 1 or 5 is used as a basis for this, the system is quasi-harmonic, and the resulting oscillations and frequency can be described by a harmonic oscillator, a single sine function. $\dot{e} \approx 0$ is achieved in the motif 5 limit-cycle oscillator by an increased k_5 value. The practically perfect fit of the numeric simulation to a single sine function can be seen in Fig. 4.17a.

The presence of zero-order degradation in A is needed to obtain conservative oscillations and will promote oscillatory conditions also for limit-cycle oscillations. In order to have limit-cycle strict zero-order degradation is no longer necessary, because of the intermediate species. However, rate constants also need to be matched in order to have oscillations in that case. Changing these may lead to the loss of oscillations. By the introduction of a first-order degradation of A the oscillations in the quasi-harmonic system can be effectively quenched. This has been done in the simulation shown in Fig. 4.17b, where the quenching effect can be seen as k_3 is changed to 0.1.

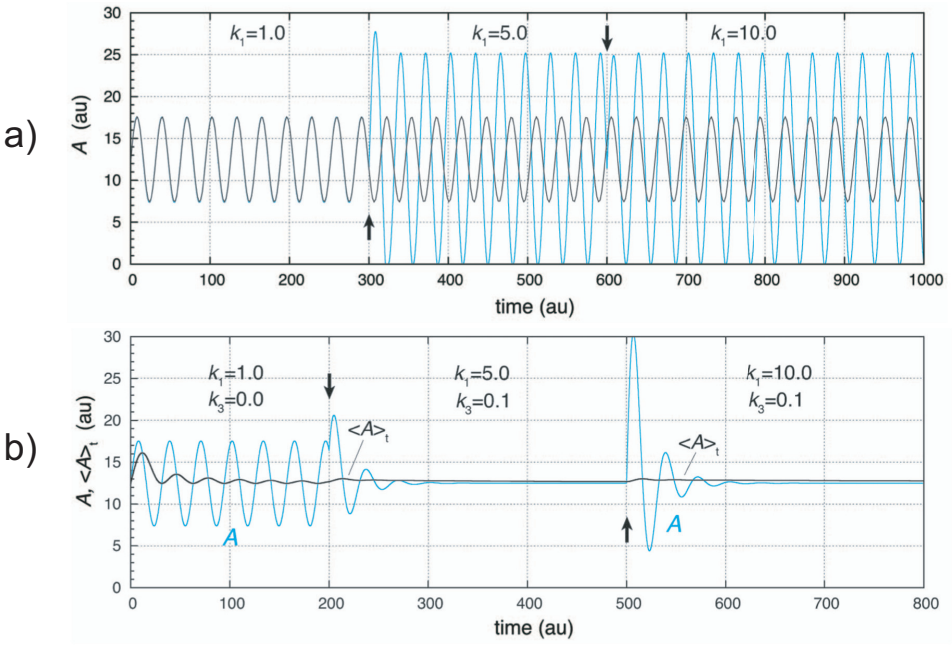

Figure 4.17: Limit cycle oscillator based on motif 5 with quasi-harmonic behavior. (a) Oscillations of A with different perturbation strength (k_1). For t < 300 au, the numerical calculation of A shown in blue overlaps perfectly with the single harmonic $A_{(fit)}(t) = A_{(ampl)} \cdot \sin(2\pi t/P + \phi) + <A>_{set}$ given in black. $k_1 = 1.0$, $A_{(ampl)} = 5.0791$, $P = 31.44$, ϕ = -0.05, and $<A>_{set} = V_{max}^{E_{set}}/k_4 = 12.5$. $A_{(ampl)}$ is the numerically calculated amplitude and P is the numerically calculated period length. Parameter values: $k_2 = 5.0 \cdot 10^{-2}$, $K_M^A = 1.0 \cdot 10^{-6}$, $k_3 = 0.0$, $k_4 = 0.8$, $k_5 = 20.0$, $V_{max}^{E_{set}} = 10.0$, $K_M^{E_{set}} = 1.0 \cdot 10^{-6}$. Initial concentrations: $A_0 = 12.4290$, $E_0 = 1.0139$, $e_0 = 0.4952$. At time t = 0.0, k_1 is changed from 1.0 to 5.0, and at t = 600.0, k_1 is changed to 10.0. (b) In this simulation, the same conditions as in panel a applies, but in addition the parameter k_3 is varied. At t= 200 and t=500, k_3 is changed from 0.0 to 0.1, which effectively quenches the oscillations in the system, but <A> is still kept under homeostatic control.

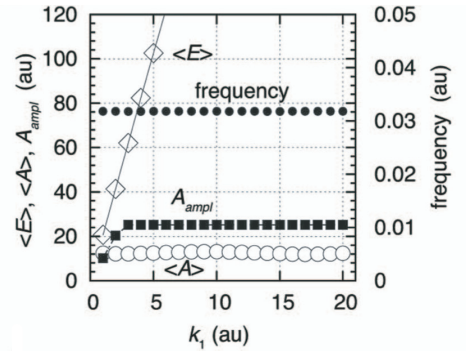

Figure 4.18: Concentration, frequency and amplitude homeostasis. <A>, A_{amp}, <E> and the frequency are shown as a function of k_1.

An increase in the k_1 value causes the oscillations to shift, however the frequency stays the same. This can be observed in Fig. 4.18. With high k_1 values the amplitude of A gets saturated, which is a secondary effect of the oscillator's homeostatic property.

Robust frequency control based on the control of <E>

Another way to achieve robust frequency control is to control <E>, because there is a correspondence between <E> and the frequency of the oscillator. This can be done by adding two extra inflow and outflow controllers, I_1 and I_2, to the limit-cycle oscillator. These extra controllers will have their own inflow and outflow set-points for <E>, in order to obtain control of <E>. In this type of oscillator (I_1- and I_2-controlled oscillator) the set-point of <E> determines the frequency. In Fig. 4.19a, a possible set-up with the extra controllers I_1 and I_2 is presented for motif 5. The set-points for <E> are given by the rate equations for I_1 and I_2 in Paper I, [25], and are written as:

$$< E >_{set}^{I_1} = \frac{k_6}{V_{max}^{I_1}} \tag{4.37}$$

$$< E >_{set}^{I_2} = \frac{V_{max}^{I_2}}{k_7} \tag{4.38}$$

a)

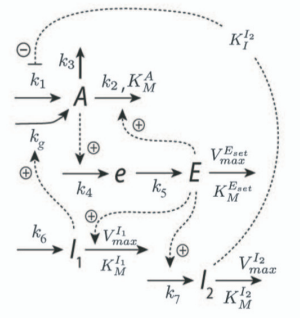

b)

$$\dot{A} = \frac{k_1 \cdot K_I^{I_2}}{K_I^{I_2} + I_2} + k_g \cdot I_1 - \frac{k_2 \cdot E \cdot A}{K_M^A + A} - k_3 \cdot A$$

$$\dot{E} = k_5 \cdot e - \frac{V_{max}^{Eset} \cdot E}{K_M^{Eset} + E}$$

$$\dot{e} = k_4 \cdot A - k_5 \cdot E$$

$$\dot{I_1} = k_6 - \frac{E \cdot V_{max}^{I_1} \cdot I_1}{K_M^{I_1} + I_1}$$

$$\dot{I_2} = k_7 \cdot E - \frac{V_{max}^{I_2} \cdot I_2}{K_M^{I_2} + I_2}$$

Figure 4.19: Robust frequency control based on control of <E> in a limit-cycle oscillator of motif 5. (a) Reaction kinetic representation of a limit-cycle oscillator based on motif 5 with additional control variables I_1 and I_2 added in order to control <E>. (b) Rate equations for the controlled variable A, manipulated variable E, intermediate variable e, control variable I_1 and control variable I_2.

I_1 and I_2 have the same set-point of 20.0 au, and in the absence of I_1 and I_2 the frequency varies like in the limit-cycle model of motif 5 from figure Fig. 4.16.

With I_1 and I_2 both active, <E> shows robust homeostasis at 20.0 with an essentially constant frequency. When one controller, I_1, is knocked out (not present), <A> is still homeostatically controlled but <E> is not, Fig. 4.20b. <E> approaches its set-point at high k_1 values, however the frequency is no longer under control. When the other controller, I_2, is knocked out, Fig. 4.20b, control of both <E> and the frequency is still observed, but is lost at higher k_1 values.

4.2.4 Homeostatic regulation during cytosolic Ca^{2+} oscillations

The previous sections have shown how it is possible to have robust homeostasis in <A> during oscillatory conditions. In physiological terms there are several examples where homeostatic regulation is needed in conditions where oscillations occur, for instance in the case of cytosolic calcium (Ca^{2+}).

Inside the cytosol Ca^{2+} is regulated at a very low level, ≈ 100 nM, whereas the extracellular concentration is several orders of magnitude higher at ≈ 1 mM [69]. As Ca^{2+} is important for cellular signaling, as well as a signal for apoptosis, it is crucial that cytosolic Ca^{2+} levels are kept under homeostatic

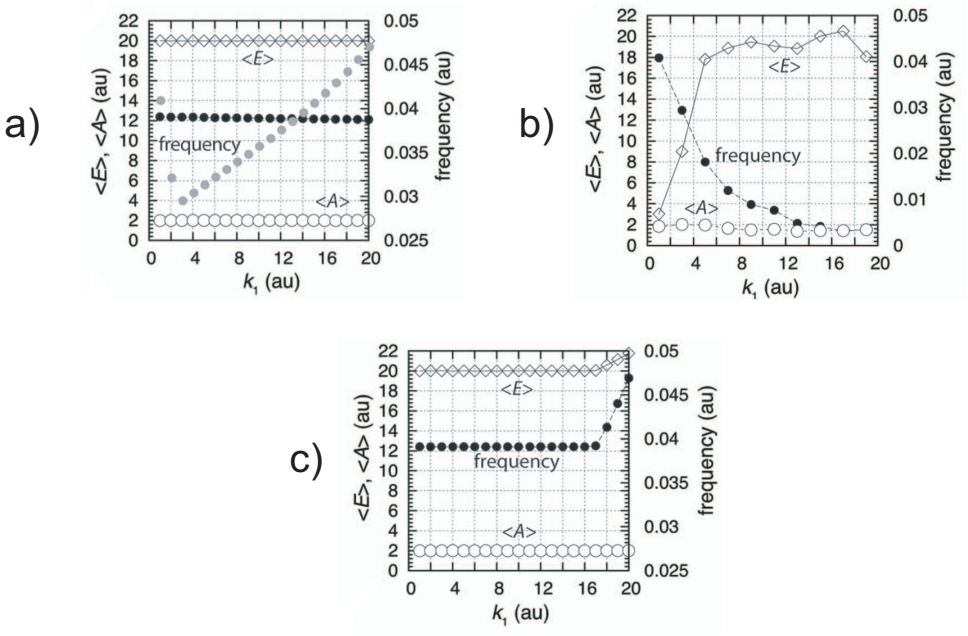

Figure 4.20: Frequency changes in conservative oscillators based on inflow controller 2 and outflow controller 5. (a) Frequency, <A> and <E> as a function of the perturbation k_1. Rate constants: k_1 = variable, $k_2 = 1.0$, $K_M^A = 0.1$, $k_3 = 0.0$, $k_4 = 0.5$, $k_5 = 0.2$, $V_{max}^{E_{set}} = 1.0$, $K_M^{E_{set}} = 1.0 \cdot 10^{-6}$, $k_6 = 20.0$, $V_{max}^{I_1} = 1.0$, $K_M^{I_1} = 1.0 \cdot 10^{-6}$, $k_7 = 1.0$, $V_{max}^{I_2} = 20.0$, $K_M^{I_2} = 1.0 \cdot 10^{-6}$. Initial concentrations: $A_0 = 0.7638$, $E_0 = 18.8155$, $e_0 = 1.6887$, $I_{1,0} = 1.6695 \cdot 10^3$, and $I_{2,0} = 2.7657 \cdot 10^2$. Black dots show frequency with I_1 and I_2, while grey dots show frequency without I_1 and I_2 control over E. (b) Same as in a), but I_1 is knocked out. (c) Same as in a), but I_2 is knocked out.

control. To a cell Ca^{2+} signals can be presented as Ca^{2+} oscillations, and the cytosolic concentration can reach much higher levels than the resting 100 nM level. As cytosolic Ca^{2+} oscillations may be under homeostatic regulation, we investigated Ca^{2+} oscillations in terms of oscillatory homeostats. In response to increased stimulation of a cell, cytosolic Ca^{2+} oscillations have been found to increase in frequency [44, 90, 109]. The very information conveyed by the Ca^{2+} signal lays in both the amplitude and frequency of the Ca^{2+} spikes [109]. In order to control the intracelluar Ca^{2+} concentration, a large amount of different channels, pumps and buffers are involved, and some even hold a role in modulation of the frequency and amplitude of the oscillations. The storage operated Ca^{2+} channel (SOCC) is believed to

have control of frequency modulation of Ca^{2+} oscillations [72]. Relating to the oscillatory signaling of cytosolic Ca^{2+} as well as it being under solid homeostatic regulation, the possibility arises of oscillatory homeostats being functional also during signaling.

The simple model suggested here in relation to the homeostatic regulation of cytosolic Ca^{2+}, Fig. 4.21a, is based on outflow controller 6. Rate equations in Fig. 4.21b. The model considers a non-excitable cell under stationary conditions which is stimulated. The model shows oscillations as well as the removal of excess cytosolic Ca^{2+}. Inflow of extracellular Ca^{2+} is activated by an external signal, while increased cytosolic Ca^{2+} levels induce an additional inflow from internal Ca^{2+} stores (Calcium-Induced Calcium Release - CICR). For simplicity, both inflows have been considered as one in the represented k_1 rate constant. In order to maintain the CICR flux, cytosolic Ca^{2+} is pumped into the ER to keep its internal level of Ca^{2+} high. The ER is used as a representative storage unit for Ca^{2+} in the cytosol, and is considered for this models purpose to have a constant concentration of Ca^{2+}. The only included removal of cytosolic Ca^{2+} is therefore the pumping through the plasma membrane (PM) to the extracellular space.

Considering different inflow rates (k_1), which could biologically represent different external Ca^{2+} levels and/or a variation of activation levels of the cell, this gives diverse oscillation patterns. Cytosolic Ca^{2+} oscillations at three different k_1 levels can be seen in Fig. 4.21c. An increase in the Ca^{2+} inflow affects the oscillations in terms of increased frequency. At a low k_1 level and increased K_M value the oscillations are quenched. The correlation between period length and inflow rate is shown in Fig. 4.21d, where the oscillation period decreases with an increased inflow rate. This relationship has been observed experimentally by Berridge and Galione where the period of oscillations vary based on external conditions like Ca^{2+} concentration and stimuli [44]. As both Fig. 4.21c and d illustrate, the average level of cytosolic Ca^{2+} ($<Ca^{2+}>$) is kept at its set-point indicating that robust cytosolic Ca^{2+} homeostasis is maintained. Also at the third scenario where oscillations are quenched, the cytosolic Ca^{2+} level is still kept at its homeostatic set-point.

This simple homeostatic model of cytosolic Ca^{2+} demonstrates how cytsolic Ca^{2+} oscillations could be seen as an example of oscillatory homeostasis. An oscillatory homeostat, as have been presented during the previous sections, allows the maintantance of homeostatic conditions through a more dynamic system where there are periodic changes in the controlled variable. Oscillatory Ca^{2+} signals are important for cellular signaling, and without

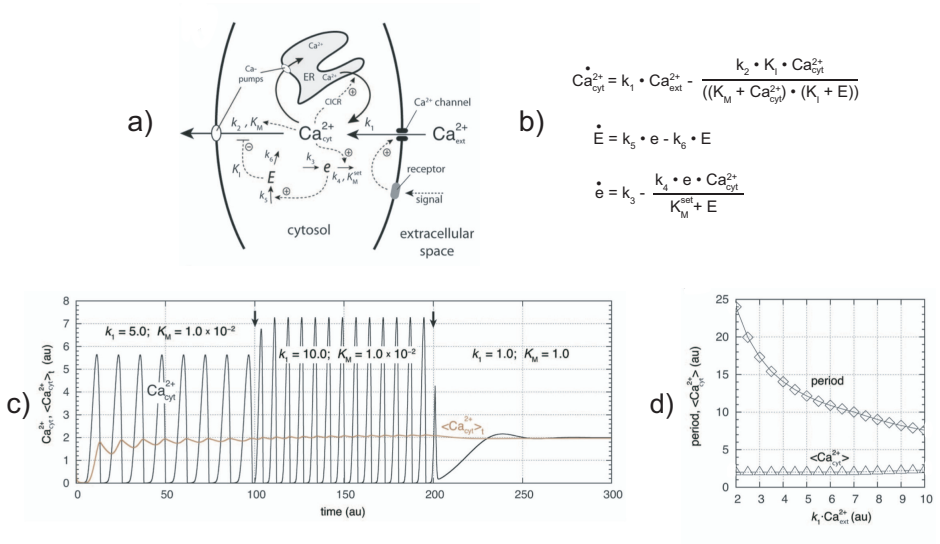

Figure 4.21: Homeostatic model of cytosolic Ca^{2+} oscillations. (a) Simple model with reaction scheme of cytosolic Ca^{2+} in a non-excitable cell. The set-up is based on an extended version of outflow controller 6 with an intermediate e to have limit-cycle oscillations. k_1 as a combined inflow from extracellular space and the ER is considered a measure reflecting the stimulation strength. (b) Rate equations for $<Ca^{2+}_{cyt}>$, E and e. (c) Cytosolic Ca^{2+} oscillations and average concentration $<Ca^{2+}_{cyt}>$ with different stimulation strength represented by k_1-values. Set-point for $Ca^{2+}_{cyt} = k_3 / k_4 = 2.0$. Rate constants: k_1 phase 1 = 5.0, k_1 phase 2 = 10.0, k_1 phase 3 = 1.0, k_2 = 500.0, K_M^{set} phase 1 and 2 = $1.0 \cdot 10^{-2}$, K_M^{set} phase 3 = 1.0, $K_M^{set} = 1.0 \cdot 10^{-6}$, k_3 = 2.0, k_4 = 1.0, k_5 = 1.0, K_I = 0.1. Initial concentrations: $Ca^{2+}_{cyt,0} = 1.772$, $E_0 = 1.643$, $e_0 = 2.908 \cdot 10^{-3}$. Ca^{2+}_{ext} is considered constant = 1.0. At $k_1 = 1.0$ at t= 200, the K_M value is increased leading to quenching of oscillations. (d) Period length and $<Ca^{2+}_{cyt}>$ calculated after 2000 time units for increasing k_1 values representing increasing stimulation strength. Rate constants as in b) and $K_M = 1.0 \cdot 10^{-2}$. Initial concentrations for each calculated data point: $Ca^{2+}_{cyt,0} = 6.126 \cdot 10^{-2}$, $E_0 = 30.693$, $e_0 = 28.806$.

these oscillations the value of cytosolic Ca^{2+} as a signaling tool would be a lot more limited than it is. As the purpose of this Ca^{2+} model did not include adding the more complex characteristics of the Ca^{2+} regulatory network of the cell, more work is needed in order to understand more about the complexity of Ca^{2+} homeostasis as well as Ca^{2+} signaling.

4.3 Cytosolic calcium homeostasis in non-excitable cells

As the previous section shows, an interest in cytosolic Ca^{2+} emerged, with a simple model in which oscillatory homeostats were investigated. In order to learn more about the homeostasis and regulation of cytosolic Ca^{2+}, the need for a more detailed model became apparent. The following section will present a systematic development from a minimal model to a gradually more complex basic mathematical model, including regulatory and kinetic requirements which lead to the regulation and homeostasis of cytosolic Ca^{2+}. Investigations of several mechanisms and kinetic requirements of cytosolic Ca^{2+} regulation as well as the role of cytosolic Ca^{2+} as a regulator has also been done. Although the focus in the previous section was oscillatory homeostatic conditions, the main focus in this following work has not been on oscillations. We did, however, observe that the model is capable of showing oscillations and that Ca^{2+} homeostasis can still be maintained during these conditions.

4.3.1 Starting to make a Ca^{2+} model

The aim for building this cytosolic Ca^{2+} model was to describe and increase the understanding of how cytosolic Ca^{2+} is regulated including homeostatic mechanisms. The resulting basic model in this work is based on cytosolic Ca^{2+} homeostasis in non-excitable cells. It was developed by using negative feedback loops with integral control with molecular interactions and kinetic requirements known from experimental data found in litterature. The roles and functions of Ca^{2+} are complex. The vast number of Ca^{2+} fluxes, paths, etc., in cells, and the body in general, makes it necessary to limit the model to some extent.

The initial minimal model included only the dynamics of Ca^{2+} and the plasma membrane Ca^{2+} ATPase (PMCA). The only elements were Ca^{2+} (both extracellular and intracellular), the outflow path of PMCA, as well

as two different buffers; one general buffer (B) and calmodulin (CaM), the latter being an important Ca^{2+} modulator. Fig. 4.22 shows the initial model including a flow diagram with the concept of integral control and illustrations of the negative feedback loops between cytosolic Ca^{2+} and PMCA with and without integral control.

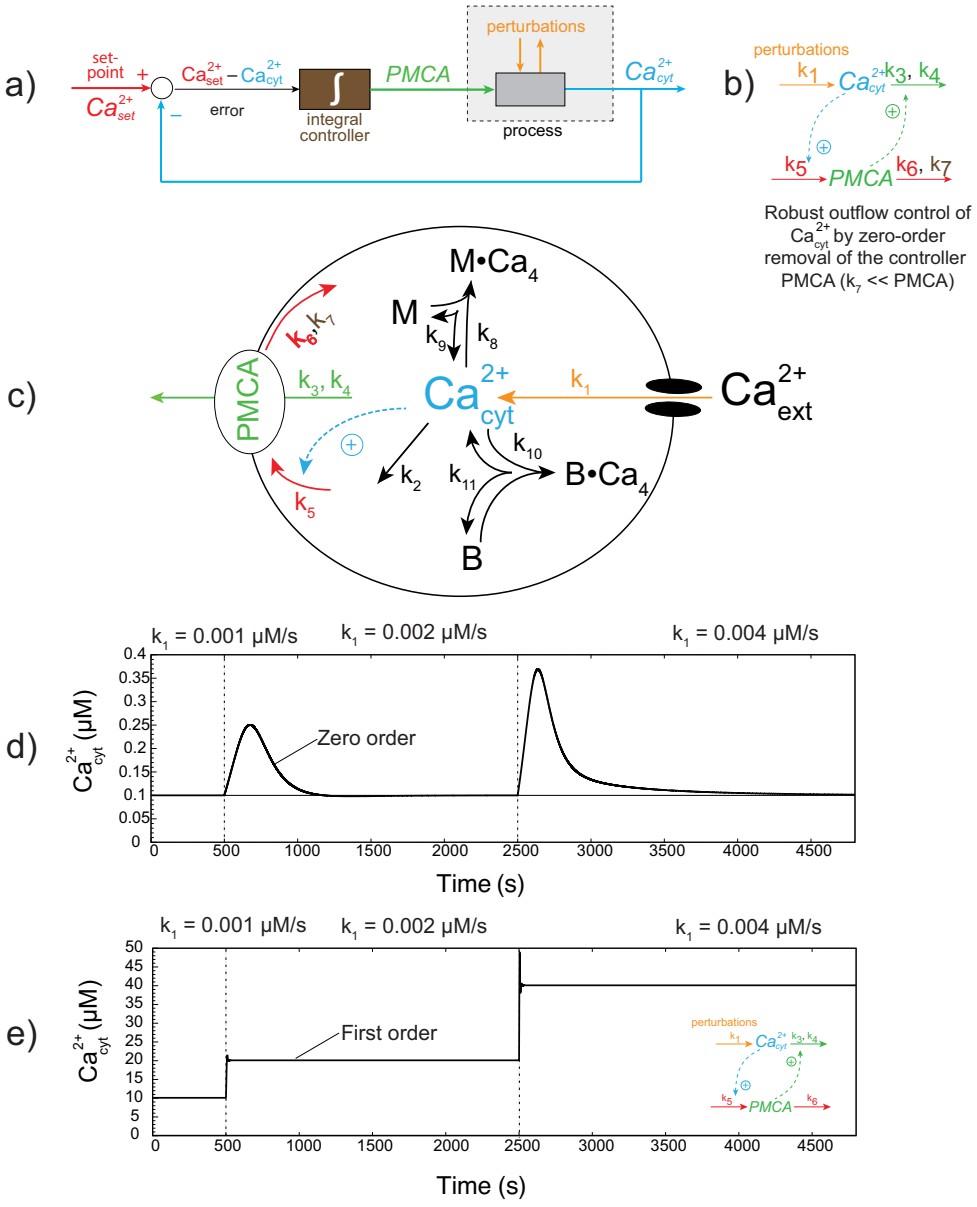

Figure 4.22: (Caption next page.)

Figure 4.22: (Continued from Previous page). **Initial minimal model of the negative feedback loop between cytosolic Ca^{2+} and PMCA.** (a) Integral control scheme with Ca^{2+}. The concept of integral control is illustrated with Ca^{2+} being the regulated species. The actual Ca^{2+} value is compared to its set-point, resulting in an error which is integrated in time. The integrated error E is proportional to the concentration of PMCA which removes excess Ca^{2+} coming into the cell. (See Eqs. 4.39-4.45) (b) Scheme of an outflow controller, a negative feedback loop, between Ca^{2+} and PMCA. The compensatory flux generated by PMCA removes Ca^{2+}. Integral control introduced by Michaelis-Menten kinetics in the internalization of PMCA, where k_7 is much lower than the cytosolic Ca^{2+} concentration. (c) Overview of the simple initial model. The model has an arbitrary inflow of Ca^{2+} with PMCA as the only extrusioncompensating mechanism. Steady state condition d(PMCA)/dt = 0 is assumed, giving the setpoint of the controller as Ca^{2+}_{set} = k_6 / k_5. (d) Graph showing robust homeostasis in cytosolic Ca^{2+} for 3 different constant k_1 inflow values during three phases (indicated by dotted lines). Rate constants: $k_{1phase1} = 1.0 \cdot 10^{-2}$ s^{-1}, $k_{1phase2} = 2.0 \cdot 10^{-2}$ s^{-1}, $k_{1phase3} = 4.0 \cdot 10^{-2}$ s^{-1}, $k_2 = 0.0$ s^{-1}, $k_3 = 1.0 \cdot 10^{-1}$ s^{-1}, $k_4 = 1.0 \cdot 10^{-1}$ μM, $k_5 = 5.0$ s^{-1} μM^{-1}, $k_6 = 5.0 \cdot 10^{-1}$ μM/s, $k_7 = 1.0 \cdot 10^{-5}$ μM, $k_8 = 2.5$ s^{-1} μM^{-1}, $k_9 = 5.0$ s^{-1}, $k_{10} = 3.0 \cdot 10^{2}$ s^{-1} μM^{-1}, $k_{11} = 5.0 \cdot 10^{1}$ s^{-1}. Initial conditions: $Ca^{2+}_{cyt} = 9.9991 \cdot 10^{-2}$ μM, PMCA = $1.9995 \cdot 10^{2}$ μM, $Ca^{2+}_{ext} = 1.0 \cdot 10^{3}$ μM, M = 9.5239μM, $(M \cdot Ca_4) = 4.7615 \cdot 10^{-1}$ μM, B = $6.2502 \cdot 10^{2}$ μM, $(B \cdot Ca_4) = 3.7498 \cdot 10^{2}$ μM. (e) Graph showing the same feedback loop but without integral control. In this version the Michaelis Menten kinetics in the internalization of PMCA is replaced with first order kinetics. Otherwise same initial conditions and rate equations as in d.

The comparison of Fig. 4.22d and Fig. 4.22e, shows that integral control gives a perfect adaptation in the perturbed system, while the lack of integral control leaves the system without the ability of showing Ca^{2+} homeostasis. The rate equations are given as:

$$\dot{Ca^{2+}_{cyt}} = k_1 \cdot Ca^{2+}_{ext} - k_2 \cdot Ca^{2+}_{cyt} - k_3 \cdot \frac{PMCA \cdot Ca^{2+}_{cyt}}{k_4 + Ca^{2+}_{cyt}} \tag{4.39}$$

$$-4 \cdot k_8 \cdot M \cdot Ca^{2+}_{cyt} + 4 \cdot k_9 \cdot (M \cdot Ca_4) - 4 \cdot k_{10} \cdot B \cdot Ca^{2+}_{cyt} + 4 \cdot k_{11} \cdot (B \cdot Ca_4)$$

$$\dot{PMCA} = k_5 \cdot Ca^{2+}_{cyt} - k_6 \cdot \frac{PMCA}{k_7 + PMCA} \tag{4.40}$$

$$\dot{M} = -k_8 \cdot M \cdot Ca^{2+}_{cyt} + k_9 \cdot (M \cdot Ca_4) \tag{4.41}$$

$$\dot{(M \cdot Ca_4)} = -\dot{M} \tag{4.42}$$

$$\dot{B} = -k_{10} \cdot B \cdot Ca^{2+}_{cyt} + k_{11} \cdot (B \cdot Ca_4) \tag{4.43}$$

$$(B \cdot \dot{Ca}_4) = -\dot{B} \tag{4.44}$$

With zero-order kinetics, assuming $k_7 \ll$ PMCA and the steady state condition $P\dot{M}CA = 0$, the set-point of the controller is given as

$$Ca^{2+}_{set} = \frac{k_6}{k_5} \tag{4.45}$$

$P\dot{M}CA$ is proportional to the integrated error, i.e. $\int_0^t (Ca^{2+}_{set}$ - $Ca^{2+}_{cyt})$dt $\approx P\dot{M}CA$.

The set-up described in this section is a very simple overview of the function of PMCA. PMCA has been found to remove Ca^{2+} on its own in the presence of acidic phospholipids in the plasma membrane, but only to a limited degree [83, 110]. In the presence of calmodulin (CaM) activation of PMCA is at its maximum. Without CaM present, PMCA is only activated to about half of its maximum activity [75, 111]. The addition of CaM would therefore be a natural step in further developing the model.

Erythrocytes as a starting point

The regulatory dynamics in this initial model system consisting of Ca^{2+} and the PMCA is comparable to that of erythrocytes. In non-excitable cells, the PMCA is found to be the most abundant and functional pump [75]. Erythrocytes are non-excitable cells which have no nucleus, mitochondria, or other organelles when they are mature making them a good choice as the starting point for the model.

4.3.2 The Plasma Membrane Ca^{2+} ATPase

In order to transport Ca^{2+} out of the cell, the PMCA needs ATP and hydrogen with the ratio of 1 ATP and 1 H^+ per 1 Ca^{2+}. For simplicity, the assumption of the availability of enough ATP and H^+ is made. To build upon the simple model shown in Fig. 4.22, the binding of PMCA-CaM is added as a complex given as (PMCA·M) and as (PMCA·M^*) after a first-order activation by cytosolic Ca^{2+}. The (PMCA·M^*) complex removes Ca^{2+} more efficiently. The PMCA is considered a high affinity pump with

a K_d of 0.1-1 μM with CaM, and with a K_d of 10-20 μM at rest. PMCA without CaM is still part of the model, but with only a minor effect on the Ca^{2+} removal from the cytosol.

The extended model is seen in Fig. 4.23 where the set-point for cytosolic Ca^{2+} can now be determined from:

$$\frac{d(PMCA \cdot M^*)}{dt} = k_5 \cdot Ca^{2+}_{cyt} \cdot (PMCA \cdot M) - \frac{k_6(PMCA \cdot M^*)}{k_7 + (PMCA \cdot M^*)} \quad (4.46)$$

With zero-order kinetics for the inactivation of (PMCA·M^*) and considering the steady state condition for (PMCA·M^*) where $k_7(=K_M) \ll$ (PMCA·M^*):

$$\frac{d(PMCA \cdot M^*)}{dt} = k_5 \cdot Ca^{2+}_{cyt} \cdot (PMCA \cdot M) - k_6 = 0 \quad (4.47)$$

$$k_5 \cdot Ca^{2+}_{cyt} \cdot (PMCA \cdot M) = k_6$$

the set-point and steady state value of cytosolic Ca^{2+} is:

$$Ca^{2+}_{set} = Ca^{2+}_{ss} = \frac{k_6}{k_5(PMCA \cdot M)} \quad (4.48)$$

The set-point of Ca^{2+} in Eq. 4.48 is now dependent upon the (PMCA·M) complex, which leads to the possibility of a variable set-point. Ca^{2+} induced increases in the steady state of cytosolic Ca^{2+} was demonstrated by Russel et al. [112]. This change in Ca^{2+} steady state value was shown as immediate and sustained following rapid additions of Ca^{2+} to bovine parathyroid cells when preincubated in 0.5 mM Ca^{2+}. As with our model the set-point steady-state of Ca^{2+} can be variable.

As stated, the PMCA is a high affinity pump, however with low throughput. This is characterized by a low transport turnover number (k_6). In order to obtain experimental values for input-data to the model, V_{max} and K_M values were determined from analysis of experimental data. BRENDA, the enzyme database, reports entries for both turnover numbers and K_M values for PMCA with respect to Ca^{2+}. 12 reports found in BRENDA of K_M values range betwen 0.13 - 20 μM, and values around 0.1 have also been reported [113, 114]. Turnover numbers range widely from 9.5-149 s^{-1} found in BRENDA entries, and have also been reported from other sources

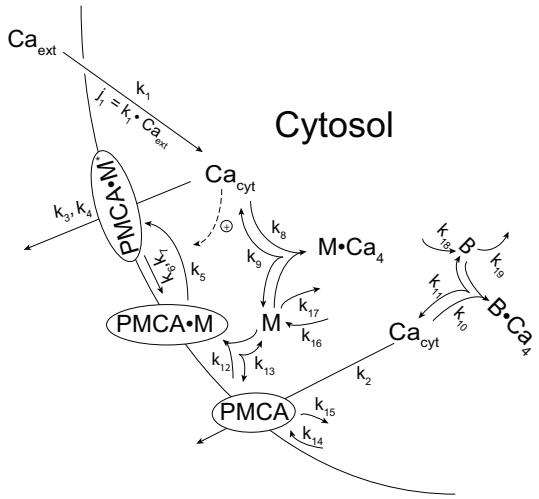

Figure 4.23: Model of Ca^{2+} removal through the PMCA with CaM activation. Based on erythrocytes, the illustration shows the regulation of cytosolic Ca^{2+} through the removal of a PMCA-CaM complex activated by Ca^{2+} itself. Leak channels for entry and low-rate removal of Ca^{2+} are also included.

from 30 to 200 s^{-1} [113, 115]. K_M was determined to be 1.2 μM based on research by Niggli et al. which fits well with these reports [110]. V_{max} was also determined both from different sets of experimental data in addition to analysis of extrusion rates in experimental plots. Calculations based on Scharff and Foder's experimental data gave a V_{max} of 300 μM/s [116]. This is a good match with the calculations based on the experiments on cochlear hair cells by Chen et al., where the extrusion rate was estimated to be about 200 Ca^{2+} ions per second [115]. However, calculations based on Vanagas et al. yielded values as low as 25 and 96 μM/s [117]. Dagher and Lew found the zero-order kinetic extrusion rate of PMCA in erythrocytes by using an ionophore, A23187, for loading the cells with massive amounts of Ca^{2+}[118]. V_{max} was determined based on the plots of the extrusion rates from these experimental data, by finding the slope of the linear zero-order extrusion. Michaelis-Menten kinetics are assumed, with $K_M \ll Ca^{2+}$, leading to v = V_{max}. A theoretical plot for Ca^{2+} extrusion through the PMCA was obtained by model calculations and compared to the experimental plots adapted from Dagher and Lew. Both plots can be seen in Fig. 4.24.

V_{max} derived from the slope of the straight line in the plots give a value around 260 μM/s which compares well with the results from the other experimental data.

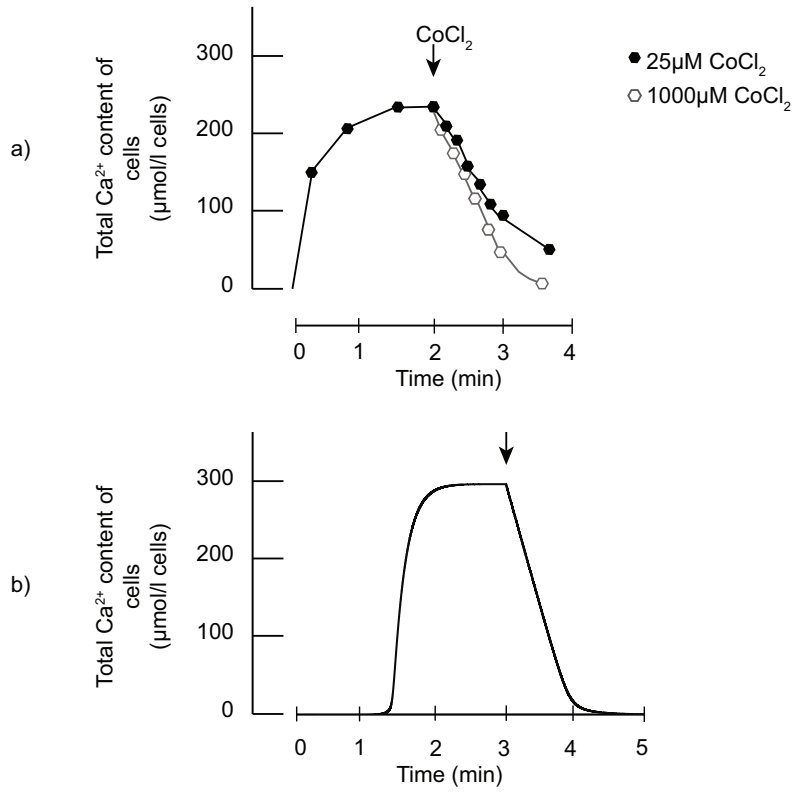

Figure 4.24: Ca^{2+} extrusion by PMCA in erythrocytes. (a) Plot showing changes in Ca^{2+} concentration over time for extrusion rate determination adapted from results by Dagher and Lew [118]. An ionophore was added to the cells to load Ca^{2+} into the cytosol. $CoCl_2$ was then added at different concentrations in order to block the ionophore at the times indicated by the arrow in the plots. White and black dots in the plot show concentration based on different concentrations of the inhibitor. (b) Graph shows theoretical plot based on model calculations. Inflow of Ca^{2+} was blocked after 3 minutes indicated by the arrow to mimic the same effect as in the experiment in a. Theoretical plot shows similar shape and result from the experimental results. Rate constants: $k_1 = 1.5 \cdot 10^{-5}$ s^{-1}, $k_2 = 0.0$ s^{-1}, $k_3 = 7.0 \cdot 10^2$ s^{-1}, $k_4 = 1.0 \cdot 10^{-2}$ μM, $k_5 = 1.6 \cdot 10^2$ μM^{-1} s^{-1}, $k_6 = 8.0 \cdot 10^{-2}$ μM/s, $k_7 = 1.0 \cdot 10^{-6}$ μM, $k_8 = 2.5$ s^{-1}, $k_9 = 5.0$ s^{-1}, $k_{10} = 1.0 \cdot 10^2$ μM^{-1} s^{-1}, $k_{11} = 80.0$ s^{-1}, $k_{12} = 1.0 \cdot 10^{-2}$ μM^{-1} s^{-1}, $k_{13} = 1.0 \cdot 10^{-1}$ μM^{-1} s^{-1}, $k_{14} = 0.0$ μM/s, $k_{15} = 0.0$ μM/s, $k_{16} = 0.0$ μM/s, $k_{17} = 0.0$ s^{-1}, $k_{18} = 0.0$ μM/s, $k_{19} = 0.0$ s^{-1}, k_1 phase 2 $= 6.5 \cdot 10^{-1}$ s^{-1}, k_2 phase 2 $= 1.0 \cdot 10^{-1}$ s^{-1}, k_3 phase 2 $= 7.0 \cdot 10^2$ s^{-1}, k_1 phase 3 $= 1.5 \cdot 10^{-5}$ s^{-1}, k_2 phase 3 $= 0.0$ s^{-1}, k_3 phase 3 $= 7.0 \cdot 10^2$ s^{-1}. Initial conditions: ${Ca^{2+}}_{cyt} = 9.8506 \cdot 10^{-2}$ μM, (PMCA $\cdot$ M*) $= 2.3606 \cdot 10^{-5}$ μM, ${Ca^{2+}}_{ext} = 56.0$ μM, M $= 9.5354$ μM, (M $\cdot$ Ca^4) $= 4.6965 \cdot 10^{-1}$ μM, B $= 1.7943 \cdot 10^2$ μM, (B $\cdot$ Ca^4) $= 22.094$ μM, (PMCA $\cdot$ M) $= 4.8695 \cdot 10^{-3}$ μM, PMCA $= 5.1068 \cdot 10^{-3}$ μM.

Dynamics of the PMCA and hysteretic behavior

By comparison with experimental data, the model was used to investigate properties of the PMCA pump. Specifically the activation of the PMCA as Ca^{2+} enters the cell has been examined. Observations of the Ca^{2+} concentration inside the cell show that Ca^{2+} levels have a tendency to rise before they decrease, even with an active PMCA pump. Sedova and Blatter looked at the concentration of Ca^{2+} in endothelial cells as the PMCA was active and then inhibited [119]. They performed this by adding 2 mM of $Ca^{2+}{}_{ext}$ followed by washing of Ca^{2+} and then inhibiting PMCA by carboxyeosin before again adding 2mM of $Ca^{2+}{}_{ext}$, see Fig. 4.25. This procedure was done in order to observe how inhibition of PMCA would affect the concentration of Ca^{2+}.

The findings of Sedova and Blatter was explored by comparing model calculations with their experimental data. The conditions of their experiment were mimicked and parameters identified in order to find what requirements are needed to obtain these results. A comparison between experiment and calculations are shown in Fig. 4.25.

In order to keep Ca^{2+} at the same level during phase 4 as in phase 2, our model calculations show that the inflow rate k_1 needs to be lower during this phase. The assumption by Sedova and Blatter was that the PMCA is fully inhibited during phase 3, however the inhibition is ended before the phase is over following the readdition of 2 mM $Ca^{2+}{}_{ext}$ in phase 4. We suspect that the PMCA is not fully inhibited, and also that the inhibitor carboxyeosin might have an effect on the inflow of $Ca^{2+}{}_{ext}$. Experimental results in rat myocytes by Choi and Eisner indicate an inhibition of Ca^{2+} inflow through the plasma membrane by carboxyeosin [120].

An alternative explanation could be that the Na^+/Ca^{2+} exchanger (NCX) can bring Ca^{2+} down to its set-point when PMCA is inactive [119]. This is a controversial view as NCX has a lower affinity of Ca^{2+} and is generally believed to be active at higher Ca^{2+} concentrations than the PMCA [79, 81]. This alternative is not supported by the experiments of Parekh on RBL-1 cells which contain both PMCA and NCX [109]. In their experiment PMCA was blocked by La^{3+} to investigate oscillatory conditions. The Ca^{2+} release activated channel (CRAC) was also blocked. Both oscillations and the Ca^{2+} induced Ca^{2+} release activity continued after blockage of PMCA. In the case of that experiment, if the NCX was able to compensate for the removal of Ca^{2+} in the absence of the PMCA, it would most likely have halted the oscillations as this will happen if PMCA is active.

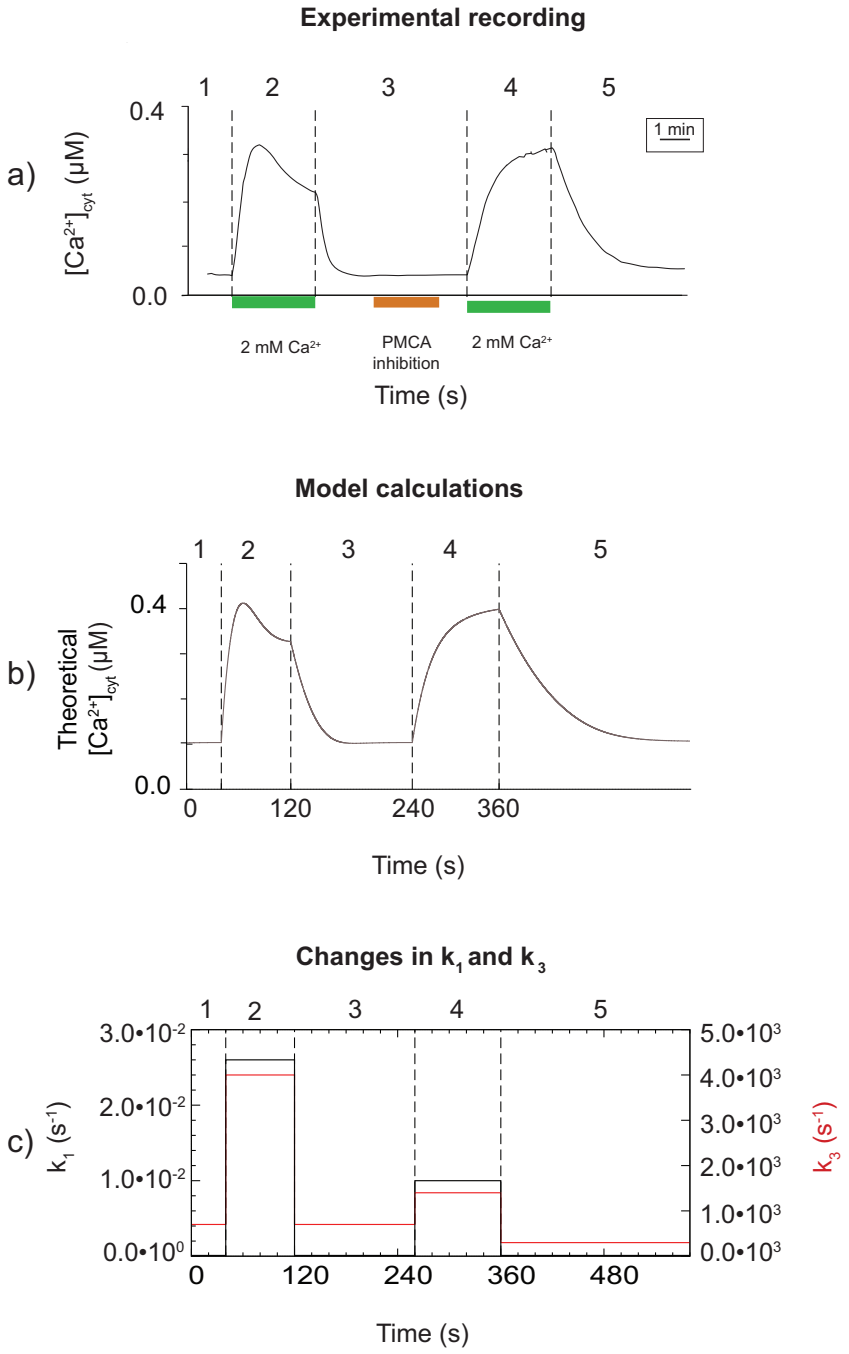

Figure 4.25: (Caption next page.)

Figure 4.25: (Continued from Previous page.) **Ca^{2+} extrusion through the PMCA in erythrocytes.** (a) Replot of the experimental data from Sedova and Blatter [119]. The cytosolic Ca^{2+} concentration is shown as a result of different treatments. The experiment is divided into five phases, where each new phase is indicated by a dashed vertical line. Phase 1: No Ca^{2+} is added. Phase 2: 2 mM extracellular Ca^{2+} is added. Phase 3: Extracellular Ca^{2+} is washed out. PMCA is inhibited by carboxyeosin. Phase 4: 2 mM extracellular Ca^{2+} is added. Phase 5: Extracellular Ca^{2+} is washed out. (b) Plot based on model calculations of the events in panel a. Parameter input is set to match experimental conditions. Phases represent the equivalent to that of the experimental. Rate constants: $k_1 = 1.0 \cdot 10^{-4}$ s^{-1}, $k_2 = 0.0$ s^{-1}, $k_3 = 7.0 \cdot 10^2$ s^{-1}, $k_4 = 0.01$ μM, $k_5 = 16.0$ μM^{-1} s^{-1}, $k_6 = 8.0 \cdot 10^{-3}$ μM/s, $k_7 = 1.0 \cdot 10^{-6}$ μM, $k_8 = 2.5$ s^{-1}, $k_9 = 5.0$ s^{-1}, $k_{10} = 100.0$ μM^{-1} s^{-1}, $k_{11} = 80.0$ s^{-1}, $k_{12} = 0.01$ μM^{-1} s^{-1}, $k_{13} = 0.1$ μM^{-1} s^{-1}, $k_{14} = 0.0$ μM/s, $k_{15} = 0.0$ s^{-1}, $k_{16} = 0.0$ μM/s, $k_{17} = 0.0$ s^{-1}, $k_{18} = 0.0$ μM/s, $k_{19} = 0.0$ s^{-1}, k_1 phase 2 $= 0.026$ s^{-1}, k_2 phase 2 $= 0.0$ s^{-1}, k_3 phase 2 $= 4.0 \cdot 10^3$ s^{-1}, k_1 phase 3 $= 1.0 \cdot 10^{-4}$ s^{-1}, k_2 phase 3 $= 0.0$ s^{-1}, k_3 phase 3 $= 7.0 \cdot 10^2$ s^{-1}, k_1 phase 4 $= 0.01$ s^{-1}, k_2 phase 4 $= 0.0$ s^{-1}, k_3 phase 4 $= 1.4 \cdot 10^3$ s^{-1}, k_1 phase 5 $= 1.0 \cdot 10^{-4}$ s^{-1}, k_2 phase 5 $= 0.0$ s^{-1}, k_3 phase 5 $= 3.0 \cdot 10^2$ s^{-1}. Initial conditions: ${Ca^{2+}}_{cyt} = 0.10247$ μM, PMCA $\cdot$ M* $= 1.0973 \cdot 10^{-4}$ μM, ${Ca^{2+}}_{ext} = 1.0 \cdot 10^3$ μM, M $= 9.5161$, M $\cdot {Ca^4} = 0.48886$ μM, B $= 178.59$ μM, B $\cdot$ $Ca^4 = 22.936$ μM, PMCA $\cdot$ M $= 4.8225 \cdot 10^{-3}$ μM, PMCA $= 5.0677 \cdot 10^{-3}$ μM. (c) Changes in k_1 and k_3 during the five phases. As can be seen from the plot, both k_1 and k_3 values are lower in phase 4 in order to achieve a similar curve in the model calculations compared to the experimental observations given in panels b and a respectively. For discussion, see main text.

The Ca^{2+} concentration curve from the experiments by Sedova and Blatter in comparison to the model calculations in Fig. 4.25 indicate that hysteresis (slow changing effects) may play a role in Ca^{2+} regulation. The nature of the curves show similarities with that of hysteretic enzymes and slow activation [119, 121, 122]. There are several rate limiting factors in enzymatic reactions. These could be at the stages of either substrate binding or product release, or more commonly at the stage of conformational change after substrate binding. Kinetic properties in a conformationally changed enzyme can cause slowness in the activation of the catalyzed reaction. This phenomenon was studied by Carl Frieden and was termed hysteretic behavior [122]. Hysteretic enzymes respond slowly to changes in ligand concentrations. The manifestation of this property in the PMCA is shown as a transient of Ca^{2+} even without changes in the levels of ${Ca^{2+}}_{\text{ext}}$ or PMCA. Scharff et al. reported this reaction in PMCA and reached the conclusion that this is a necessary attribute in enabling the occurence of transients [121]. In the case of signaling, transients are important and variations in their amplitude and frequency are interpreted as different signals. The slow activation in PMCA allows the Ca^{2+} concentration to

reach relevant concentrations for signaling purposes. A subsequent slow deactivation leaves the PMCA enough time to bring down the levels of cytosolic Ca^{2+} to its set-point again.

In order to incorporate this into the model, we have used CaM binding as the limiting factor. It is included in the model in addition to PMCA in an active state. It is widely agreed upon that CaM binding is notoriously slow, and that its binding to the PMCA can vary for different pump isoforms. In non-excitable cells, the PMCA isoforms predominantly present are characterized as "slow pumps", whereas the PMCA isoforms mainly found in excitable cells are "fast pumps" due to rapid and varying levels of Ca^{2+} [123, 124, 125]. Corresponding to the model set up, ApoCaM[1] has been found to bind to proteins, receptors etc. in the cell membrane for the purpose of local activation by thereafter binding to Ca^{2+} [126]. By assuming such a binding arrangement, the target (PMCA) already bound to CaM can immediately be activated by Ca^{2+}. With the other scenario possible, PMCA without bound effector molecules first has to bind to Ca^{2+}-CaM competing with other targets as well. As the total concentration of CaM with bound Ca^{2+} has been found to be quite low, as low as approximately 1 %, we find it likely that CaM would bind to PMCA as ApoCaM [127]. In the model, Fig. 4.23, Ca^{2+}-CaM is represented as $M \cdot Ca_4$. The total concentration of CaM is 10 μM, whereas the model representation $M{\cdot}Ca_4$ makes up between 4 to 10 % of the total CaM concentration depending on rate constants applied. In line with values found in literature, the k_8 value and k_9 value, representing the on- and off-rate constants of the binding/dissociation of Ca^{2+} to CaM respectively, is set to 2.5 $\mu M^{-1} \cdot s^{-1}$ and 5.0 s^{-1} respectively. In this way the K_d is kept at a defined value of 2 μM [127, 128]. Hysteresis is applied in the model by a change in k_3. The PMCA channel with both an immediate and slow activation is shown in Fig. 4.26.

Comparing peak shapes the hysteretic curve looks similar to the experimental results in Fig. 4.25. As can be seen from Fig. 4.27, this characteristic peak shape can also be represented by overshooting under non-hysteretic conditions in the activation of the PMCA pump. The peak shape varies for different k_3 values where a higher k_3 value gives overshooting before decreasing to the steady state. Lower k_3 values give a more gradual increase towards a steady state. However, with this overshooting the steady state is quickly reached, compared to the case when k_3 changes hysteretically

[1] Calcium-free calmodulin

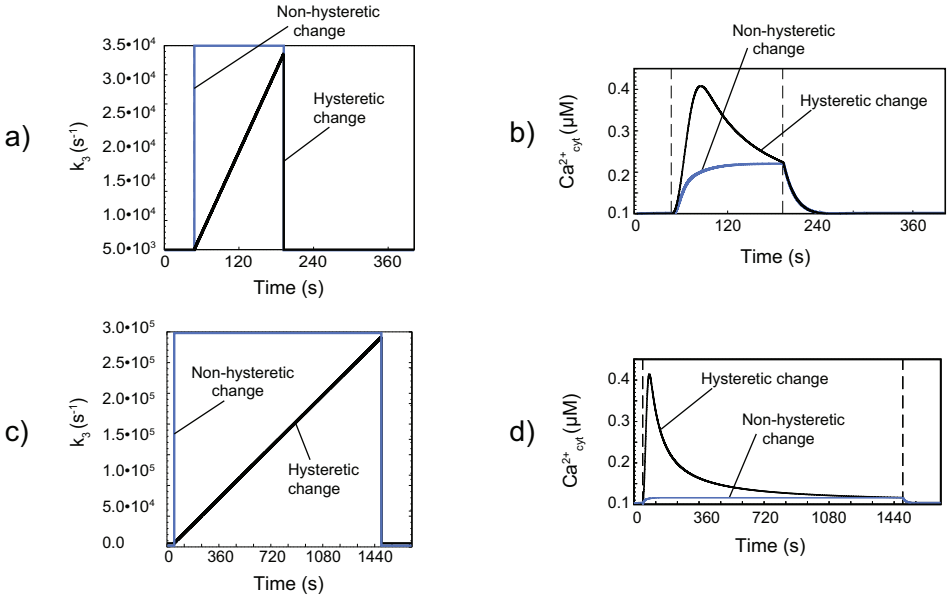

Figure 4.26: Hysteretic vs. non-hysteretic PMCA activation. (a) Change in k_3 is shown, where the k_3 value is increased linearly in the calculation representing a hysteretic behavior of the PMCA pump. In the non-hysteretic activation of PMCA the k_3 value is increased immediately in a step-wise manner. (b) The plot shows the concentration of calculated cytosolic Ca^{2+} with slow activation of PMCA with CaM via k_3 compared to a non-hysteretic, or immediate, activation of PMCA. (c) Change in k_3 is shown, where the k_3 value is increased linearly over time representing a hysteretic behavior in the PMCA pump. Compared to the condition in panel a, this panel shows change over a longer time period. When PMCA is instantaneously activated, k_3 undergoes a step-wise change. (d) Plot based on same calculation as in plot b, however with an extended phase 2 to illustrate what will happen over time with the Ca^{2+} concentration here. The concentration will decrease and approach its set-point over time with a linear increase in k_3. The concentration of Ca^{2+} for the non-hysteretic condition will, as the plots shows quickly reach the steady state.

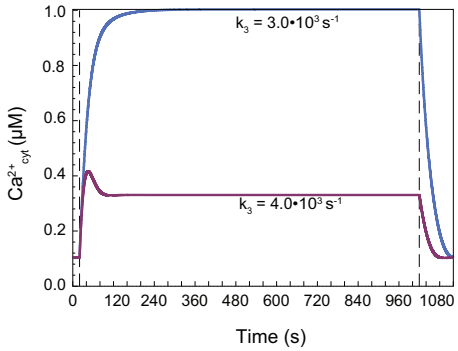

Figure 4.27: Ca^{2+} concentration with immediate activation of PMCA with different k_3 values. The plot shows a comparison of the peak shape given for the Ca^{2+} with an immediate, non-hysteretic, activation of PMCA. One curve (purple) shows an overshooting condition before it stabilizes at its steady state, $k_3 = 4.0 \cdot 10^3$ s^{-1}. The other curve (blue) shows a more gradual increase towards its steady state, $k_3 = 3.0 \cdot 10^3$ s^{-1}.

(Fig. 4.26c). This behavior is comparable to findings by Scharff et al. on hysteretic behavior in PMCA [121]. The linear increase is an approximation for an increase towards steady state that takes longer time. When it takes some time for the pump to achieve its optimal capacity this can be described in the model as k_3 being a time function as incorporated here as it will take longer to reach its steady state.

4.3.3 Expanding the model - including NCX

As mentioned in the previous section, the Na^+-Ca^{2+} exchanger (NCX) also plays a role in the removal of Ca^{2+} from the cytosol. We added NCX to the existing model in order to investigate some of the findings and suggested behavior of NCX by Sedova and Blatter [119]. As shown from the plots in Fig. 4.25, hysteretic behavior and unsatisfactory inhibition of the PMCA could explain the plot characteristics given. To investigate further and compare our results to other cell types, we added NCX to the model and explored its role. In the work done by Sedova and Blatter, using epithelial cells, La^{3+} was used to inhibit PMCA [119]. This inhibition was shown to be effective. Combined with the results by Sedova and Blatter that the Ca^{2+} level decreases to its resting values in the presence of Na^+ suggests that NCX is involved in the extrusion of Ca^{2+} out of the cytosol [109, 119]. As supported by the findings by Chou et al. [129], CaM was, like for PMCA,

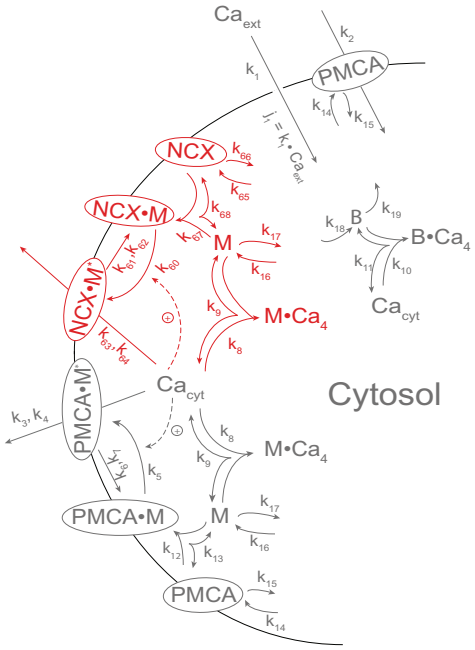

Figure 4.28: Model of Ca^{2+} removal by both PMCA and NCX. Model with the additional Ca^{2+} removal by NCX (outlined in red).

added as a regulator of NCX activity.The expanded model including the NCX can be seen in Fig. 4.28. The set-point of Ca^{2+} when only NCX is present can be calculated in an analogous way as for PMCA, i.e.

$$Ca^{2+}_{set,NCX} = \frac{k_{61}}{k_{60}} \tag{4.49}$$

Where k_{61} is the maximum velocity of the Michaelis-Menten type of (NCX·M*) deactivation and k_{60} is the rate constant of the Ca_{cyt}-induced activation of (NCX·M), Fig. 4.28.

Fig. 4.29 show a recalculation of Sedova and Blatter's work when both PMCA and NCX are included into the model, in addition to the inhibition by La^{3+} [119]. The plots adapted from the experiments and theoretical calculations compare well, and indicate that removal through NCX alone could get Ca^{2+} down to its set-point, albeit at a slower rate than with PMCA active. To improve peak shape in the experiments by Sedova and Blatter we have also added a slow hysteretic inflow of Ca^{2+} into the cytosol

(by k_1), in addition to the hysteretic change of PMCA by k_3. The hysteretic changes in k_1 and k_3 parameters are shown in Fig. 4.29c.

The equations for the increase in k_1 and linear increase in k_3 for both phase 2 and 4, are:

$$k_{1phase2} = k_{1,ph1} + k_{1,ph2}^{max} \cdot (1 - e^{-\alpha(t-t_{ph1})}) \tag{4.50}$$

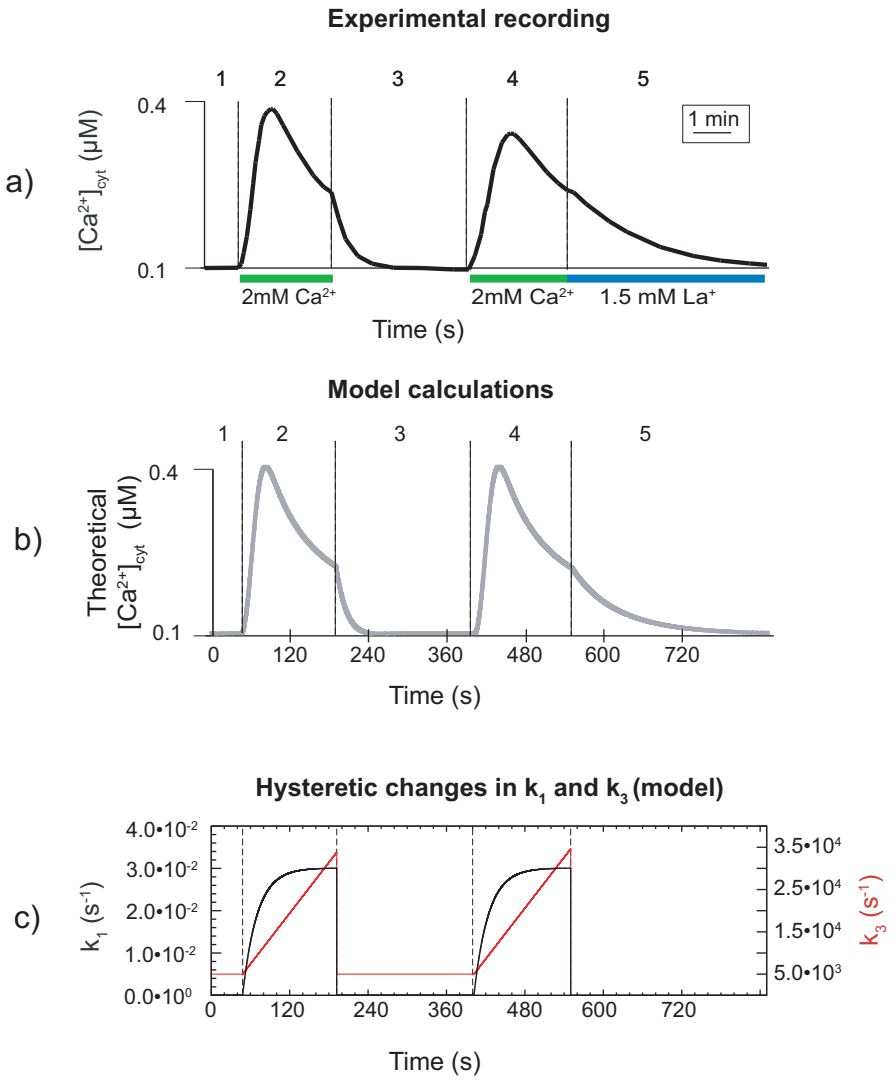

Figure 4.29: (Caption next page.)

Figure 4.29: (Continued from Previous Page.) **Ca^{2+} dynamics with model including both PMCA and NCX in endothelial cells.** (a) Experimental record redrawn from Sedova and Blatter (Figure 6A in [119]). Phase 1: No Ca^{2+} entry. Both PMCA and NCX are active. Phase 2: 2 mM Ca^{2+} is added. Phase 3: Wash out of extracellular Ca^{2+}. Both PMCA and NCX are active for removal of cytosolic Ca^{2+}. Phase 4: 2 mM extracellular Ca^{2+} is added again. Phase 5: 1.5 mM La^{3+} is added to inhibit PMCA. Only NCX is active for removal of Ca^{2+} from the cytosol. (b) Plot based on model calculations of the events in panel a. Increase in k_1 in phases 2 and 4 simulates entry of extracellular Ca^{2+} into the cytosol. In phase 5, k_3 is set to 0 in order to model an inhibition of PMCA by La^{2+}. The time step in the calculation is given as $1.0 \cdot 10^{-2}$ s, with 5 phases and the intervals given as 48 s, 144 s, 210 s, 148 s and 300 s. Rate constants: $k_1 = 1.5 \cdot 10^{-5}$ s^{-1}, $k_2 = 0.0$ s^{-1}, $k_3 = 7.0 \cdot 10^2$ s^{-1}, $k_4 = 1.0 \cdot 10^{-2}$ μM, $k_5 = 1.6 \cdot 10^2$ μM^{-1} s^{-1}, $k_6 = 8.0 \cdot 10^{-2}$ μM/s, $k_7 = 1.0 \cdot 10^{-6}$ μM, $k_8 = 2.5$ s^{-1}, $k_9 = 5.0$ s^{-1}, $k_{10} = 1.0 \cdot 10^2$ μM^{-1} s^{-1}, $k_{11} = 80.0$ s^{-1}, $k_{12} = 1.0 \cdot 10^{-2}$ μM^{-1} s^{-1}, $k_{13} = 1.0 \cdot 10^{-1}$ μM^{-1} s^{-1}, $k_{14} = 0.0$ μM/s, $k_{15} = 0.0$ s^{-1}, $k_{16} = 0.0$ μM/s, $k_{17} = 0.0$ s^{-1}, $k_{18} = 0.0$ μM/s, $k_{19} = 0.0$ s^{-1}, $k_{60} = 16.0$ μM^{-1} s^{-1}, $k_{61} = 8.0 \cdot 10^{-3}$ μM/s, $k_{62} = 1.0 \cdot 10^{-6}$ μM, $k_{63} = 1.0 \cdot 10^5$ s^{-1}, $k_{64} = 1.0 \cdot 10^2$ μM, $k_{65} = 0.0$ μM/s, $k_{66} = 0.0$ s^{-1}, $k_{67} = 1.0 \cdot 10^{-2}$ μM^{-1} s^{-1}, $k_{68} = 1.0 \cdot 10^{-1}$ s^{-1}, k_1 phase 2 $= 3.0 \cdot 10^{-2}$ s^{-1}, α, phase 2 $= 4.5 \cdot 10^{-2}$ s^{-1}, k_3 phase 2 $= 5.0 \cdot 10^3$ s^{-1}, β, phase 2 $= 2.0 \cdot 10^2$ s^{-1}, k_1 phase 3 $= 1.0 \cdot 10^{-4}$ s^{-1}, k_3 phase 3 $= 5.0 \cdot 10^3$ s^{-1}, k_1 phase 4 $= 3.0 \cdot 10^{-2}$ s^{-1}, α, phase 4 $= 4.5 \cdot 10^{-2}$ s^{-1}, k_3 phase 4 $= 5.0 \cdot 10^3$ s^{-1}, β, phase 4 $= 2.0 \cdot 10^2$ s^{-1}, k_1 phase 5 $= 0.0$ s^{-1}, k_3 phase 5 $= 0.0$ s^{-1}. Initial conditions: ${Ca^{2+}}_{cyt} = 1.0247 \cdot 10^{-1}$ μM, PMCA·M* $= 1.0973 \cdot 10^{-4}$ μM, ${Ca^{2+}}_{ext} = 1.0 \cdot 10^3$ μM, M = 9.5161 μM, M·Ca4 $= 4.8886 \cdot 10^{-1}$ μM, B $= 1.7859 \cdot 10^2$ μM, B·Ca4 = 22.936 μM, PMCA·M $= 4.8225 \cdot 10^{-3}$ μM, PMCA $= 5.0677 \cdot 10^{-3}$ μM, NCX·M* $= 1.0973 \cdot 10^{-4}$ μM, NCX·M $= 4.8225 \cdot 10^{-3}$ μM, NCX $= 5.0677 \cdot 10^{-3}$ μM. (c) Changes in k_1 and k_3 during the five phases. Increase in k_1 is hyperbolic and approaches an upper limit, and increase in k_3 is linear.

$$k_{1phase4} = k_{1,ph3} + k^{max}_{1,ph4} \cdot (1 - e^{-\alpha(t - t_{ph3})}) \tag{4.51}$$

$$k_{3phase2} = k_{3,ph1} + \beta(t - t_{ph1}) \tag{4.52}$$

$$k_{3phase4} = k_{3,ph3} + \beta(t - t_{ph3}) \tag{4.53}$$

The $k_{1,ph1}$ and $k_{1,ph3}$ values are constant at $1.0 \cdot 10^{-4}$ s^{-1}, while the maximum values for k_1 in phase 2 (${k^{max}}_{1,ph2}$) and phase 4 (${k^{max}}_{1,ph4}$) are both $1.4 \cdot 10^{-2}$ s^{-1}. The parameter α is given as $4.5 \cdot 10^{-2}$ s^{-1}, and describes how fast k_1 increases during the phase, which also makes it possible to adapt the increase in k_1 to the corresponding peak shape in the experimental plots of Ca^{2+}. Parameters t_{ph1} and t_{ph3} represent end times for phases 1 and 3. Variations in the behavior in cytosolic Ca^{2+} concentration for

different k_1 values and α values are given in Fig. 4.30. In order to get the desired peak shape from the experiment shown in Fig. 4.30b this was obtained by decreasing k_1 and increasing α. This gives the same maximum concentration of Ca^{2+} while altering the change in its removal and thereby the property of its peak. Hysteretic changes in k_3 are described in the equations 4.52 and 4.53. Also $k_{1,ph1}$ and $k_{1,ph3}$ are constant with a value of $5.0 \cdot 10^3$ s^{-1}, and the parameter β is given as 200 s^{-2}.

Another experiment by Sedova and Blatter described how the Ca^{2+} efflux was affected with only PMCA active and with an active NCX present [119]. This is interesting in order to see if NCX could be responsible for the removal of Ca^{2+}. The comparison between experimental and modeled results also gives us a good example in how model calculations can differ from biological experiments in the shape of the resulting curves. A comparison of Ca^{2+} efflux with La^{3+} inhibition of PMCA with and without NCX activated in experimental recording and corresponding model calculation can be seen in Fig. 4.31.

In phase 1 cells are at resting conditions with no Ca^{2+} entering the cytosol. In phase 2 extracellular Ca^{2+} is added (2 mM), while PMCA is active and NCX is inactive due to Na^+ free conditions. During phases 3 and 4 PMCA is inhibited by the addition of La^{3+}, while in phase 4 Na^+ is resupplied leading to the activation of NCX, which drives the cytosolic Ca^{2+} down to its resting level of 0.1 μM. In the model calculations, NCX is inactive or activated by changing the k_{63} parameter from 0 to $1.0 \cdot 10^5$ s^{-1}. Calculations simulate a complete inactivation of PMCA activity by setting the turnover number $k_3 = 0$ s^{-1}. Comparing with the experimental results the removal of Ca^{2+} does not completely stop during phase 3, suggesting an incomplete inhibition of PMCA even with La^{3+}. There can also be other aspects in the biological experiment such as leaking, buffering etc., because there are so many more variables involved in a biological system than in a model.

4.3.4 Complete model overview

The model was further expanded in order to incorporate more of the important components in the regulation of cytosolic Ca^{2+} and its dynamics. Different focus areas will be presented and discussed further in the following sections. Fig. 4.32 shows the full complete model. The grey areas are regulatory mechanisms and pathways that have been included to the program, they have, however not been explicitely explored. The ER has

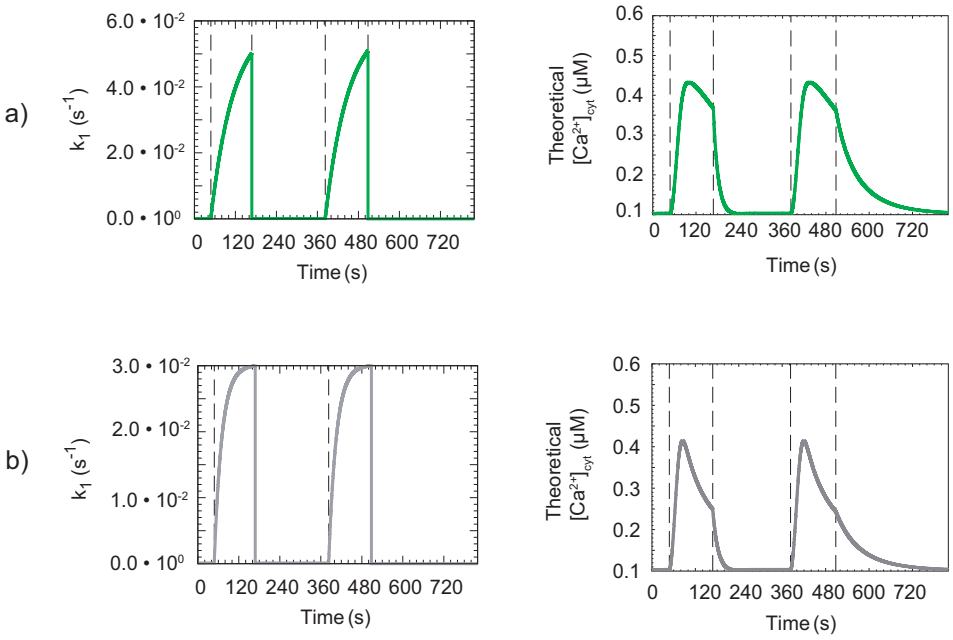

Figure 4.30: Change in Ca^{2+} concentration due to hysteretic variation in k_1. (a) Left panel shows hysteretic change in k_1 during phase 2 and 4 as in plots in Fig. 4.29. $k_1 = 0.06$, $\alpha = 0.015$. Right panel shows changes in Ca^{2+} concentration given these values. Variations in k_1 is given as: k_1 phase 1 = $1.0 \cdot 10^{-4}$ s^{-1}, k_1 phase 2 = $6.0 \cdot 10^{-2}$ s^{-1}, α, phase 2 = $1.5 \cdot 10^{-2}$ s^{-1}, k_1 phase 3 = $1.0 \cdot 10^{-4}$ s^{-1}, k_1 phase 4 = $6.0 \cdot 10^{-2}$ s^{-1}, α, phase 4 = $1.5 \cdot 10^{-2}$ s^{-1}, k_1 phase 5 = 0.0 s^{-1}. Time step is given as $1.0 \cdot 10^{-2}$ s, with 5 phases and the intervals given as 48 s, 120 s, 215 s, 125 s and 311 s. Rate constants are given as $k_1 = 1.0 \cdot 10^{-4}$ s^{-1}, $k_2 = 0.0$ s^{-1}, $k_3 = 5.0 \cdot 10^3$ s^{-1}, $k_4 = 1.2$ μM, $k_5 = 16.0$ μM^{-1} s^{-1}, $k_6 = 8.0 \cdot 10^{-3}$ μM/s, $k_7 = 1.0 \cdot 10^{-6}$ μM, $k_8 = 2.5$ s^{-1}, $k_9 = 5.0$ s^{-1}, $k_{10} = 1.0 \cdot 10^2$ μM^{-1} s^{-1}, $k_{11} = 80.0$ s^{-1}, $k_{12} = 1.0 \cdot 10^{-2}$ μM^{-1} s^{-1}, $k_{13} = 1.0 \cdot 10^{-1}$ μM^{-1} s^{-1}, $k_{14} = 0.0$ μM/s, $k_{15} = 0.0$ s^{-1}, $k_{16} = 0.0$ μM/s, $k_{17} = 0.0$ s^{-1}, $k_{18} = 0.0$ μM/s, $k_{19} = 0.0$ s^{-1}, $k_{60} = 16.0$ μM^{-1} s^{-1}, $k_{61} = 8.0 \cdot 10^{-3}$ μM/s, $k_{62} = 1.0 \cdot 10^{-6}$ μM, $k_{63} = 1.0 \cdot 10^5$ s^{-1}, $k_{64} = 1.0 \cdot 10^2$ μM, $k_{65} = 0.0$ μM/s, $k_{66} = 0.0$ s^{-1}, $k_{67} = 1.0 \cdot 10^{-2}$ μM^{-1} s^{-1}, $k_{68} = 1.0 \cdot 10^{-1}$ s^{-1}, k_3 phase 2 = $5.0 \cdot 10^3$ s^{-1}, α phase 2 = $2.0 \cdot 10^2$ s^{-1}, k_3 phase 3 = $5.0 \cdot 10^3$ s^{-1}, k_3 phase 4 = $5.0 \cdot 10^3$ s^{-1}, α phase 4 = $2.0 \cdot 10^2$ s^{-1}, k_3 phase 5 = 0.0 s^{-1}. Initial conditions: $Ca^{2+}{}_{cyt} = 1.0247 \cdot 10^{-1}$ μM, PMCA·M* = $1.0973 \cdot 10^{-4}$ μM, $Ca^{2+}{}_{ext} = 1.0 \cdot 10^3$ μM, M = 9.5161 μM, M·Ca4 = $4.8886 \cdot 10^{-1}$ μM, B = $1.7859 \cdot 10^2$ μM, B·Ca4 = 22.936 μM, PMCA·M = $4.8225 \cdot 10^{-3}$ μM, PMCA = $5.0677 \cdot 10^{-3}$ μM, NCX·M* = $1.0973 \cdot 10^{-4}$ μM, NCX·M = $4.8225 \cdot 10^{-3}$ μM, NCX = $5.0677 \cdot 10^{-3}$ μM. (b) Left panel shows a difference in hysteretic behavior in k_1 with values $k_1 = 0.03$ and $\alpha = 0.045$. Right panel shows Ca^{2+} with corresponding shape of peaks due to change in values illustrating the role of hysteretic behavior in k_1 on Ca^{2+} dynamics. Variations in k_1 is given as: k_1 phase 1 = $1.0 \cdot 10^{-4}$ s^{-1}, k_1 phase 2 = $3.0 \cdot 10^{-2}$ s^{-1}, α phase 2 = $4.5 \cdot 10^{-2}$ s^{-1}, k_1 phase 3 = $1.0 \cdot 10^{-4}$ s^{-1}, k_1 phase 4 = $3.0 \cdot 10^{-2}$ s^{-1}, α phase 4 = $4.5 \cdot 10^{-2}$ s^{-1}, k_1 phase 5 = 0.0 s^{-1}. Same rate constants as a.

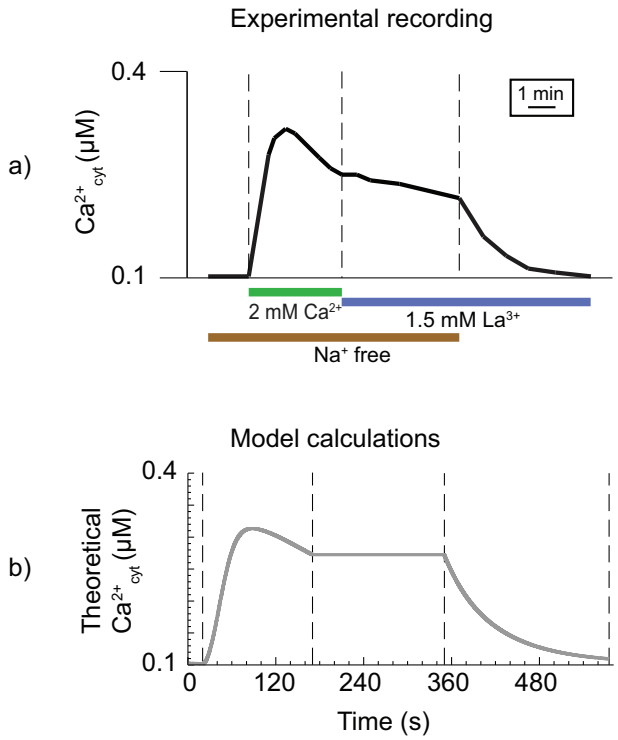

Figure 4.31: Removal of Ca^{2+} following La^{3+} inhibition of PMCA. Experimental recording and model calculations are compared in order to investigate the role of NCX in the removal of Ca^{2+} from the cytosol. In the experiment NCX is not active until phase 4 as a result of unavailable Na^+ in the first three phases [119]. In the model this is achieved by setting $k_{63} = 0$. Experimental graph in panel a was redrawn from Sedova and Blatter (Figure 6B) [119]. Phase 1: No Ca^{2+} entry. Phase 2: Extracellular Ca^{2+} is added in the experiment, k_1 is increased in the model to simulate this. Phase 3: La^{3+} inhibition of PMCA halts the removal of Ca^{2+} from the cytosol, in the model $k_3 = 0$ which completely inactivates PMCA. Phase 4: PMCA is still inhibited, but now NCX is active due to Na^+ availability. In the model, $k_{63} = 1.0 \cdot 10^5$ s^{-1} in model calculations, other rate constants and initial conditions are as in Fig. 4.30. Time step is given as $1.0 \cdot 10^{-2}$ s, with 5 phases and the intervals given as 20 s, 150 s, 180s and 225 s. Hysteretic change in k_1 is given as: k_1 phase 1 = 0.0 s^{-1}, k_1 phase 2 = $3.0 \cdot 10^{-2}$ s^{-1}, α, phase 2 = $1.3 \cdot 10^{-2}$ s^{-1}, k_1 phase 3 = 0.0 s^{-1}, k_1 phase 4 = 0.0 s^{-1}. Hysteretic change in k_3: k_3 phase 2 = $5.0 \cdot 10^3$ s^{-1}, α, phase 2 = $2.0 \cdot 10^2$ s^{-1}, k_3 phase 3 = $5.0 \cdot 10^3$ s^{-1}, k_3 phase 4 = $5.0 \cdot 10^3$ s^{-1}, α, phase 4 = $2.0 \cdot 10^2$ s^{-1}, k_3 phase 5 = 0.0 s^{-1}. Changes in k_{63} parameter through the phases: $k_{63,phase2}$ = 0.0 s^{-1}, $k_{63,phase3}$ = 0.0 s^{-1}, $k_{63,phase4}$ = $1.0 \cdot 10^5$ s^{-1}.

now been added, which plays important roles in the regulation of cytosolic Ca^{2+} concentration and also signaling events. The capacitative Ca^{2+} entry through the store operated Ca^{2+} channels (SOCCs) which is connected to the Ca^{2+} levels in the ER. Investigations of the IP_3R channel and the bellshaped Ca^{2+} dependency of the Ca^{2+} induced Ca^{2+} release through the IP_3R channel in the ER was also performed.

In the following sections each new component of the model is described and discussed. First, the possibility of change in cytosolic Ca^{2+} is discussed based on previous parts of the model in this new integrated model, followed by the addition of the capacitative Ca^{2+} entry and the dynamics of IP_3R in the ER.

Changes in Ca^{2+} steady state

As seen in the previous section, the set-point for cytosolic Ca^{2+} can be variable as it is dependent upon the (PMCA·M) complex [112]. Russel et al. [112] showed that with a sudden increase in extracellular Ca^{2+} the resting levels of Ca^{2+} in the cytosol increased. They also saw that with a gradual increase in extracellular Ca^{2+} the cytosolic Ca^{2+} levels did not change, however spikes did occur in some cases before going back to the original steady-state level [112]. This matches with model calculations shown in previous figures where an increase of extracellular Ca^{2+} leads to higher cytosolic Ca^{2+} levels. Fig. 4.33 gives a representation of the change in cytosolic Ca^{2+} at different levels of total PMCA with increasing inflow of extracellular Ca^{2+} (increase in k_1).

What the plot in Fig. 4.33 shows is that there is an increase in steady state of cytosolic Ca^{2+} with increase in inflow of extracellular Ca^{2+}, and that the change is more notable if the total amount of PMCA in the plasma membrane is smaller. That the steady state can change with increases in extracellular Ca^{2+} is in qualitative agreement with the experimental observations by Russel et al. [112].

4.3.5 Capacitative Ca^{2+} entry and the endoplasmic reticulum (ER) as important factors in Ca^{2+} dynamics of the cell

The connection between the store-operated Ca^{2+} channel (SOCC) and the ER was the next to be introduced to the model. This relationship is important in the dynamic of the capacitative Ca^{2+} entry and the function of

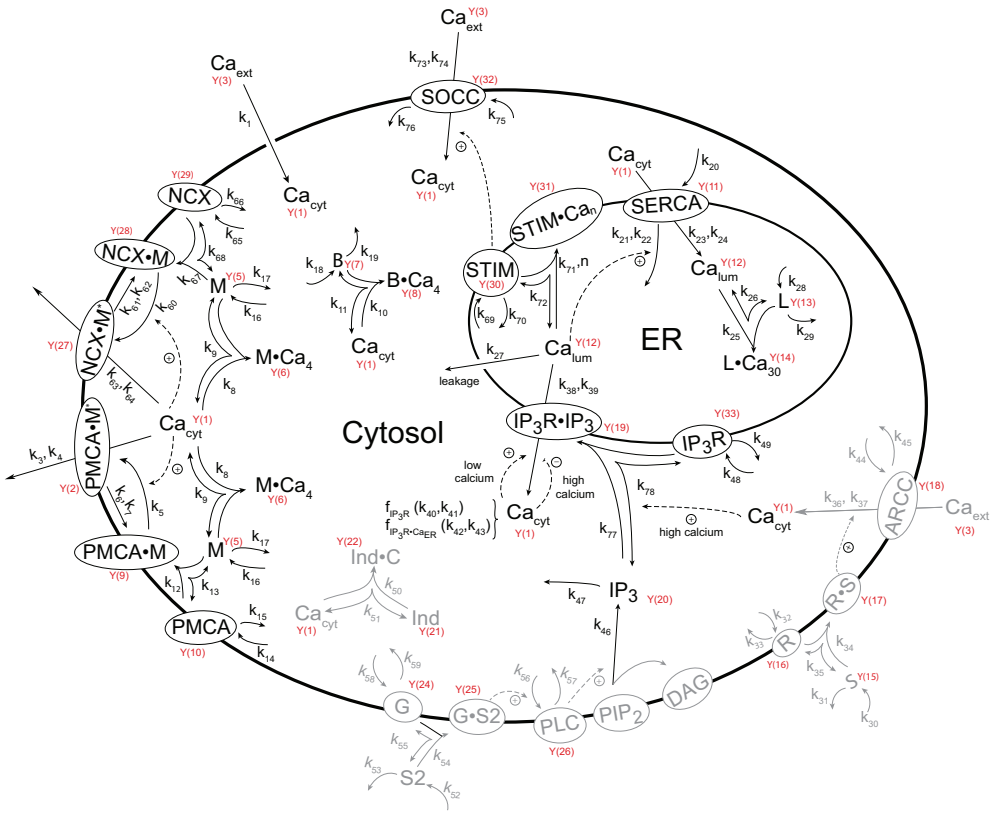

Figure 4.32: Complete model of cytosolic Ca^{2+} regulation. The model represents a non-excitable cell with inflow and outflow mechanisms in the plasma membrane, in addition to intracellular buffering and storage with the mechanisms involved in this. The leak inflow channel, described by k_1, and the PMCA and the NCX have already been added before this point, in addition to CaM (M) and buffer proteins (B). An additional inflow path through the plasma membrane, the store operated Ca^{2+} channel (SOCC) has been included. The ARCC inflow pathway is colored grey as it does not have a functional part in the model at this point. The endoplasmic reticulum (ER) with its sarco/endoplasmic Ca^{2+} ATPase (SERCA), leak outflow channel, lumic buffering proteins represented by L, Ca^{2+} sensor STIM and outflow channel inositol 1,4,5-trisphosphate receptor (IP_3R) have also been added. The processes in grey are added to the model but have not been explored and implemented. The red Y-values represent the LSODE Y vector components for each dynamic variable. Arrows show reactions involving the different biochemical species. Dashed arrows represent activating or inhibiting signaling events.

the ER in its regulation. Not only is the ER important as a Ca^{2+} store, but channels like the inositol 1,4,5-trisphosphate receptor (IP_3R) and ryanodine receptor (RyR) located in the ER-membrane are involved in Ca^{2+} signaling. In order to replenish the ER with Ca^{2+} the capacitative Ca^{2+} entry, or store operated Ca^{2+} entry (SOCE), is initiated with the help of stromal interaction molecule (STIM). Including the capacitative Ca^{2+} entry also gives a more realistic inflow mechanism to the model compared to only having the more simplistic parameter k_1 from before. The model section for SOCE is shown in Fig. 4.34.

Store operated Ca^{2+} channels (SOCCs) are comprised of Orai-protein channels in the plasma membrane, and are also sometimes called Ca^{2+} release activated channel (CRAC). SOCCs are responsible for the inflow of Ca^{2+} through the capacitative Ca^{2+} entry. In order to identify the requirements for the mechanism in SOCC, its flux j_{SOCC} was compared to the j_1 flux of the plasma membrane leak channel. If the rate of synthesis for STIM is three orders of magnitude larger than its degradation, than the influx and Ca^{2+} profile was identical to the leak channel. Fig. 4.35 shows the same model calculation as in Fig. 4.29 and the same conditions only with SOCC responsible for the inflow of extracellular Ca^{2+}. The two graphs in Fig. 4.35 show identical behavior.

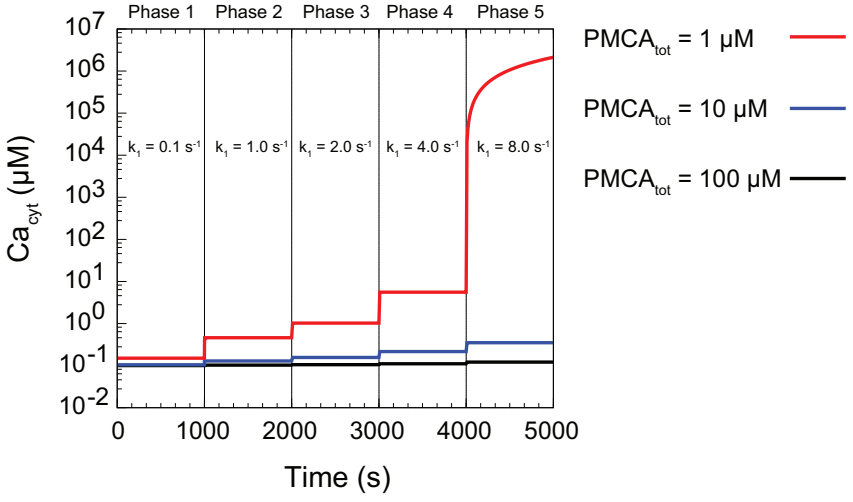

Figure 4.33: (Caption next page.)

Figure 4.33: (Continued from Previous Page.) **Influence of total amount of PMCA on the steady state of cytosolic Ca^{2+} at increasing Ca^{2+} inflow.** Plot shows changes in steady state of cytosolic Ca^{2+} at different total concentrations of PMCA. The value of k_1 is also changed during the five phases shown in the graph. Black line represents $PMCA_{tot}$ = 100 μM ($k_6 = 2.0 \cdot 10^3$ μM/s), blue line represents $PMCA_{tot}$ = 10 μM ($k_6 = 2.0 \cdot 10^2$ μM/s), and red line represents $PMCA_{tot}$ = 1 μM ($k_6 = 2.0 \cdot 10^1$ μM/s). With theoretical set-point of cytosolic Ca^{2+} depends on PMCA·M with the equation: $Ca^{2+}_{set} = Ca^{2+}_{ss} = k_6/(k_5 \cdot (\text{PMCA·M})$. Variations in k_1 is given as: k_1 phase 1 = $1.0 \cdot 10^{-1}$ s^{-1}, k_1 phase 2 = 1.0 s^{-1}, k_1 phase 3 = 2.0 s^{-1}, k_1 phase 4 = 4.0 s^{-1}, k_1 phase 5 = 8.0 s^{-1}. Time step is given as $1.0 \cdot 10^{-2}$ s, with 5 phases of $1.0 \cdot 10^3$ s. Rest of rate constants are given as k_2 = 0.0 s^{-1}, $k_3 = 5.0 \cdot 10^3$ s^{-1}, k_4 = 1.2 μM, $k_5 = 2.0 \cdot 10^2$ μM^{-1} s^{-1}, $k_6 = 2.0 \cdot 10^3$ μM/s, $k_7 = 1.0 \cdot 10^{-3}$ μM, k_8 = 2.5 s^{-1}, k_9 = 5.0 s^{-1}, $k_{10} = 1.0 \cdot 10^2$ μM^{-1} s^{-1}, k_{11} = 80.0 s^{-1}, $k_{12} = 1.0 \cdot 10^2$ μM^{-1} s^{-1}, $k_{13} = 1.0 \cdot 10^{-4}$ μM^{-1} s^{-1}, k_{14} = 0.0 μM/s, k_{15} = 0.0 s^{-1}, k_{16} = 0.0 μM/s, k_{17} = 0.0 s^{-1}, k_{18} = 0.0 μM/s, k_{19} = 0.0 s^{-1}, $k_{20} = 1.0 \cdot 10^3$ μM/s, k_{21} = 1.0 s^{-1}, $k_{22} = 1.0 \cdot 10^{-4}$ μM, $k_{23} = 1.0 \cdot 10^{-2}$ s^{-1}, $k_{24} = 1.3 \cdot 10^{-5}$ μM, $k_{25} = 5.0 \cdot 10^2$ μM^{-1} s^{-1}, $k_{26} = 1.0 \cdot 10^7$ s^{-1}, $k_{27} = 4.0 \cdot 10^{-1}$ s^{-1}, k_{28} = 0.0 μM/s, k_{29} = 0.0 s^{-1}, k_{30} = 0.0 μM/s, $k_{31} = 1.0 \cdot 10^2$ s^{-1}, k_{32} = 0.0 μM/s, k_{33} = 0.0 s^{-1}, $k_{34} = 1.0 \cdot 10^2$ μM^{-1} s^{-1}, $k_{35} = 1.0 \cdot 10^2$ s^{-1}, k_{36} = 0.0 μM^{-1} s^{-1}, $k_{37} = 1.0 \cdot 10^{-2}$ μM, $k_{38} = 5.0 \cdot 10^{-1}$ s^{-1}, $k_{39} = 1.0 \cdot 10^{-2}$ μM, $k_{40} = 2.26 \cdot 10^{-1}$, $k_{41} = 7.94 \cdot 10^{-1}$, $k_{42} = 2.26 \cdot 10^{-1}$, $k_{43} = 7.94 \cdot 10^{-1}$, k_{44} = 1.0 μM/s, k_{45} = 1.0 s^{-1}, k_{46} = 50.0 μM^{-1} s^{-1}, k_{47} = 1.0 s^{-1}, k_{48} = 2.0 μM/s, k_{49} = 1.0 s^{-1}, k_{50} = 84.0 μM^{-1} s^{-1}, k_{51} = 8.4 s^{-1}, $k_{52} = 1.0 \cdot 10^1$ μM/s, k_{53} = 1.0 s^{-1}, $k_{54} = 1.0 \cdot 10^1$ μM^{-1} s^{-1}, k_{55} = 1.0 s^{-1}, $k_{56} = 1.0 \cdot 10^{-3}$ μM^{-1} s^{-1}, $k_{57} = 1.0 \cdot 10^1$ s^{-1}, $k_{58} = 1.0 \cdot 10^1$ μM/s, k_{59} = 1.0 s^{-1}, k_{60} = 16.0 μM^{-1} s^{-1}, $k_{61} = 8.0 \cdot 10^{-3}$ μM/s, $k_{62} = 1.0 \cdot 10^{-6}$ μM, $k_{63} = 1.0 \cdot 10^5$ s^{-1}, $k_{64} = 1.0 \cdot 10^2$ μM, k_{65} = 0.0 μM/s, k_{66} = 0.0 s^{-1}, $k_{67} = 1.0 \cdot 10^{-2}$ μM^{-1} s^{-1}, $k_{68} = 1.0 \cdot 10^{-1}$ μM^{-1} s^{-1}, k_{69} = 0.0 μM/s, k_{70} = 0.0 s^{-1}, k_{71} = 1.0 μM^{-1} s^{-1}, $k_{72} = 9.6 \cdot 10^1$ s^{-1}, $k_{73} = 1.0 \cdot 10^1$ μM^{-1} s^{-1}, $k_{74} = 1.0 \cdot 10^{-7}$ μM, k_{75} = 1.0 μM/s, k_{76} = 1.0 s^{-1}, k_{77} = 1.0 μM^{-1} s^{-1}, k_{78} = 1.0 μM^{-1} s^{-1}, cooperativity phase 1 = 1.0. Initial conditions (all in μM): $Ca^{2+}{}_{cyt} = 1.00047 \cdot 10^{-1}$, PMCA·M* = $4.89568 \cdot 10^{-2}$, $Ca^{2+}{}_{ext} = 1.0 \cdot 10^3$, M = 8.58555, M·Ca4 = $4.29479 \cdot 10^{-1}$, B = $8.88844 \cdot 10^2$, B·Ca4 = $1.11158 \cdot 10^2$, PMCA·M = $9.99510 \cdot 10^1$, PMCA = $1.16418 \cdot 10^5$, NCX·M* = $1.20225 \cdot 10^{-5}$, NCX·M = $4.61388 \cdot 10^{-3}$, NCX = $5.37401 \cdot 10^{-3}$, SERCA = $4.00550 \cdot 10^4$, $Ca^{2+}_{lum} = 1.0 \cdot 10^3$, L = $2.38096 \cdot 10^3$, L·Ca30 = $1.19048 \cdot 10^2$, STIM = 8.83782, STIM·Ca = $9.20606 \cdot 10^1$, SOCC = 1.0, S = 0.0, R = $1.0 \cdot 10^2$, R·S = 0.0, ARCC = 1.0, IP3R·IP3 = 9.09052, IP3R = 2.0, IP3 = 5.0.

Ca^{2+} leakage from the ER

We have investigated the kinetic properties of the leak channel from the ER in addition to the mechanisms of SOCC and SERCA. A decline in Ca^{2+} was shown to correspond to an increase in SOCE in experimental results by Luik et al. [130]. Data points from experimental data by Luik et al. and Camello et al. [130, 131] were extracted from their graphs presenting Ca^{2+} leak from the ER following SERCA inhibition in order to compare to theoretical calculations. A representation of these data with a fitted line is

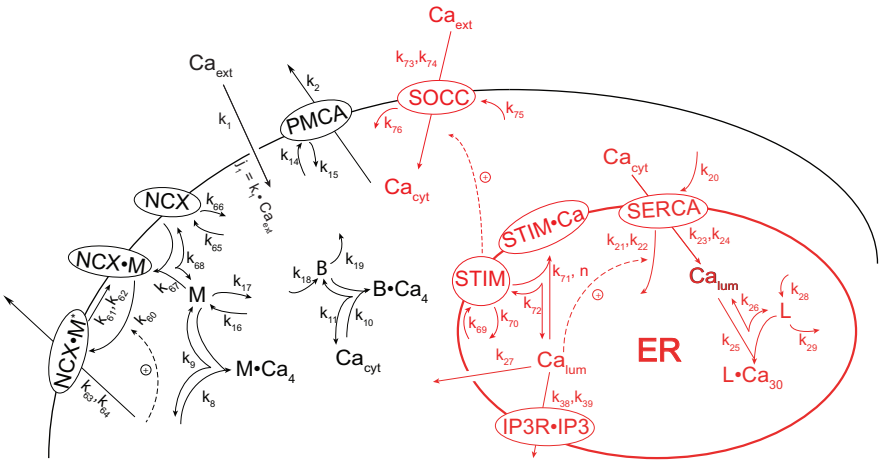

Figure 4.34: Model with capacitative Ca^{2+} entry. The involved components in capacitative Ca^{2+} entry are given in red. The ER is used as a Ca^{2+} store to replenish the cytosol with Ca^{2+}. The Ca^{2+} level inside the ER is regulated by "capacitative Ca^{2+} entry", which, by using STIM, activates the store operated Ca^{2+} channel (SOCC) and the inflow of Ca^{2+} into the cytosol. IP_3R represents the outflow path from the ER in addition to a passive leak channel described by first-order rate constant k_{27}. SERCA is the channel in the ER membrane involved in moving cytosolic Ca^{2+} into the ER, and functions in the model as an inflow controller for $Ca^{2+}{}_{lum}$.

given in Fig. 4.36.

The exponential fit, Fig. 4.36a, was employed by gnuplot's fit function. The initial leak rate (t=0) was estimated by

$$v_0 = 465.947 \cdot 0.01181 \frac{\mu M}{s} = 5.5 \frac{\mu M}{s} \tag{4.54}$$

where $Ca_0 = 465.947$ and $k_{exp} = 0.0118101\ s^{-1}$. At t = 230 s the leak rate is reduced to

$$v_{230} = 5.5 \frac{\mu M}{s} \cdot e^{-0.01181 \cdot 230} = 0.364 \frac{\mu M}{s} \tag{4.55}$$

Datapoints from experimental results by Camello et al. [131] were presented as fitting monoexponential kinetics, however we find that it is better fitted to Michaelis-Menten kinetics. The curve fit to Michaelis-Menten kinetics was best approached by applying hysteretic change in V_{max} as shown in the inset of Fig. 4.36b.The estimate of the average leak rate was calculated by the following equation

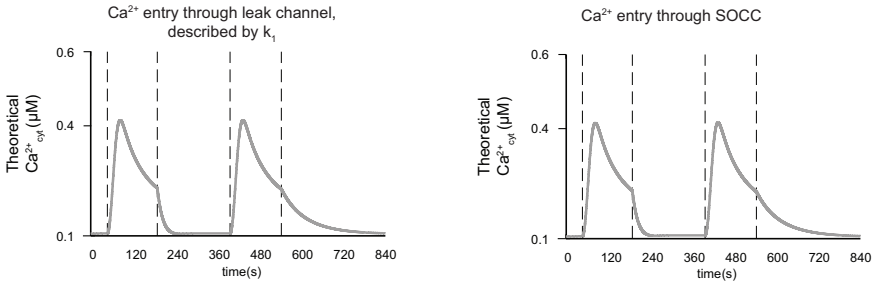

Figure 4.35: Plots of model calculations comparing Ca^{2+} inflow through plasma membrane leak channel (k_1) vs. SOCC. Left graph shows the same model calculations as presented in Fig. 4.29b, whereas the right side shows the same conditions with the difference being that Ca^{2+} is now through SOCC. The time step is given as $1.0 \cdot 10^{-2} s$, with 5 phases and the intervals given as 48 s, 144 s, 210 s, 148 s and 300 s. Rate constants for the model calculations where SOCC has replaced the leak channel are given as: $k_1 = 0.0\ s^{-1}$, $k_2 = 0.0\ s^{-1}$, $k_3 = 5.0 \cdot 10^3\ s^{-1}$, $k_4 = 1.2\ \mu M$, $k_5 = 16.0\ \mu M^{-1}\ s^{-1}$, $k_6 = 8.0 \cdot 10^{-3}\ \mu M/s$, $k_7 = 1.0 \cdot 10^{-6}\ \mu M$, $k_8 = 2.5\ s^{-1}$, $k_9 = 5.0\ s^{-1}$, $k_{10} = 1.0 \cdot 10^2\ \mu M^{-1}\ s^{-1}$, $k_{11} = 80.0\ s^{-1}$, $k_{12} = 1.0 \cdot 10^{-2}\ \mu M^{-1}\ s^{-1}$, $k_{13} = 1.0 \cdot 10^{-1}\ \mu M^{-1}\ s^{-1}$, $k_{14} = 0.0\ \mu M/s$, $k_{15} = 0.0\ s^{-1}$, $k_{16} = 0.0\ \mu M/s$, $k_{17} = 0.0\ s^{-1}$, $k_{18} = 0.0\ \mu M/s$, $k_{19} = 0.0\ s^{-1}$, $k_{20} = 1.0 \cdot 10^2\ \mu M/s$, $k_{21} = 1.0 \cdot 10^{-1}\ s^{-1}$, $k_{22} = 1.0 \cdot 10^{-6}\ \mu M$, $k_{23} = 0.0\ s^{-1}$, $k_{24} = 1.0 \cdot 10^{-2}\ \mu M$, $k_{25} = 1.25 \cdot 10^3\ \mu M^{-1}\ s^{-1}$, $k_{26} = 1.0 \cdot 10^6\ s^{-1}$, $k_{27} = 1.0 \cdot 10^{-1}\ s^{-1}$, $k_{28} = 0.0\ \mu M/s$, $k_{29} = 0.0\ s^{-1}$, $k_{30} = 0.0\ \mu M/s$, $k_{31} = 1.0 \cdot 10^2\ s^{-1}$, $k_{32} = 0.0\ \mu M/s$, $k_{33} = 0.0\ s^{-1}$, $k_{34} = 1.0 \cdot 10^2\ \mu M^{-1}\ s^{-1}$, $k_{35} = 1.0 \cdot 10^2\ s^{-1}$, $k_{36} = 1.0 \cdot 10^2\ \mu M^{-1}\ s^{-1}$, $k_{37} = 1.0 \cdot 10^{-2}\ \mu M$, $k_{38} = 10.0\ s^{-1}$, $k_{31} = 1.0 \cdot 10^{-2}\ \mu M$, $k_{40} = 2.24 \cdot 10^{-1}$, $k_{41} = 7.94 \cdot 10^{-1}$, $k_{42} = 2.24 \cdot 10^{-1}$, $k_{43} = 7.94 \cdot 10^{-1}$, $k_{44} = 1.0\ \mu M/s$, $k_{45} = 1.0\ s^{-1}$, $k_{46} = 50.0\ \mu M^{-1}\ s^{-1}$, $k_{47} = 1.0\ s^{-1}$, $k_{48} = 1.0$, $k_{49} = 1.0\ s^{-1}$, $k_{50} = 84.0\ \mu M^{-1}\ s^{-1}$, $k_{51} = 8.4\ s^{-1}$, $k_{52} = 0.0\ \mu M/s$, $k_{53} = 0.0\ s^{-1}$, $k_{54} = 10.0\ \mu M^{-1}\ s^{-1}$, $k_{55} = 1.0\ s^{-1}$, $k_{56} = 0.0\ \mu M^{-1}\ s^{-1}$, $k_{57} = 10.0\ s^{-1}$, $k_{58} = 0.0\ \mu M/s$, $k_{59} = 0.0\ s^{-1}$, $k_{60} = 16.0\ \mu M^{-1}\ s^{-1}$, $k_{61} = 8.0 \cdot 10^{-3}\ \mu M/s$, $k_{62} = 1.0 \cdot 10^{-6}\ \mu M$, $k_{63} = 1.0 \cdot 10^5\ s^{-1}$, $k_{64} = 1.0 \cdot 10^2\ \mu M$, $k_{65} = 0.0\ \mu M/s$, $k_{66} = 0.0\ s^{-1}$, $k_{67} = 1.0 \cdot 10^{-2}\ \mu M^{-1}\ s^{-1}$, $k_{68} = 1.0 \cdot 10^{-1}\ s^{-1}$, $k_{69} = 1.0 \cdot 10^3\ \mu M/s$, $k_{70} = 1.0\ s^{-1}$, $k_{71} = 1.0$, $k_{72} = 1.0\ s^{-1}$, $k_{73} = 1.0 \cdot 10^{-4}\ \mu M^{-1}\ s^{-1}$, $k_{74} = 1.0 \cdot 10^{-7}\ \mu M$, $k_{75} = 1.0\ \mu M/s$, $k_{76} = 1.0\ s^{-1}$. Changes in the following phases are given as: k_3 phase 2 $= 5.0 \cdot 10^3\ s^{-1}$, β, phase 2 $= 2.0 \cdot 10^2\ s^{-1}$, k_{73} phase 2 $= 3.0 \cdot 10^{-2}$, α, phase 2 $= 4.5 \cdot 10^{-2}\ s^{-1}$, k_3 phase 3 $= 5.0 \cdot 10^3\ s^{-1}$, k_{73} phase 3 $= 1.0 \cdot 10^{-4}$, k_3 phase 4 $= 5.0 \cdot 10^3\ s^{-1}$, β, phase 4 $= 2.0 \cdot 10^2\ s^{-1}$, k_{73} phase 2 $= 3.0 \cdot 10^{-2}$, α, phase 4 $= 4.5 \cdot 10^{-2}\ s^{-1}$, k_3 phase 5 $= 0.0\ s^{-1}$, k_{73} phase 5 $= 0.0$. In the model calculation for the leak channel, the input-values for the rate constants are identical, however SOCC and STIM are not included, and the changes in the k_{73} in the values above are the values used for k_1. Initial conditions (in μM): $Ca^{2+}{}_{cyt} = 1.0247 \cdot 10^{-1}$, PMCA·M* $= 1.0973 \cdot 10^{-4}$, $Ca^{2+}{}_{ext} = 1.0 \cdot 10^3$, M $= 9.5161$, M·Ca4 $= 4.8886 \cdot 10^{-1}$, B $= 1.7859 \cdot 10^2$, B·Ca4 $= 22.936$, PMCA·M $= 4.8225 \cdot 10^{-3}$, PMCA $= 5.0677 \cdot 10^{-3}$, NCX·M* $= 1.0973 \cdot 10^{-4}$, NCX·M $= 4.8225 \cdot 10^{-3}$, NCX $= 5.0677 \cdot 10^{-3}$, SERCA $= 8.1888 \cdot 10^4$, $Ca^{2+}_{lum} = 0.0$, L $= 2.5 \cdot 10^3$, L·Ca30 $= 0.0$, S $= 0.0$, NCX·M $= 4.8225 \cdot 10^{-3}$, NCX $= 5.0677 \cdot 10^{-3}$, STIM $= 10.0$, STIM·Ca $= 0.0$, SOCC $= 1.0$.

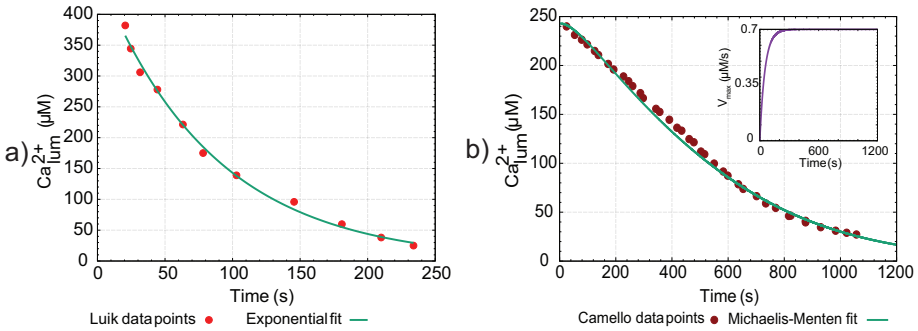

Figure 4.36: Representation of experimental data of Ca^{2+} leak from ER. (a) Shows datapoints given in red extracted from experimental results from Luik et al. [130]. Green line is an exponential fit, following the function $f_{exp}(x)=A_0 \cdot e^{(-k_{exp} \cdot x)}$ to the datapoints. (b) Red dots represent datapoints extracted from experimental results from Camello et al. [131]. Green line is a fit following zero-order Michaelis-Menten kinetics with a hysteretic change in V_{max} for a better fit. Change in V_{max} is shown in the upper right corner of the plot for reference. The rate equation is given as $dCa^{2+}_{lum}/dt = V_{max} \cdot Ca^{2+}_{lum}/(K_M + Ca^{2+}_{lum})$, where V_{max} increases towards a maximum value fitting hysteretic behavior. Hysteretic change in V_{max} is given by $V_{max}(t)=V^{final}_{max} \cdot (1.0\text{-}e^{(-K_{hys} \cdot t)})$. Where $V^{final}_{max} = 0.7$ μM/s, $K_M = 215.0$ μM, and the hysteretic factor $K_{hys} = 0.019$ s^{-1}. $t = t(0) + \Delta t$, $\Delta t = 0.1$. Initial conditions: $Ca^{2+}_{lum} = 243.0$ μM, $Ca^{2+}_{cyt} = 0.0$ μM.

$$v_{leak} = \frac{V_{max}(t) \cdot Ca^{2+}_{lum}}{K_M + Ca^{2+}_{lum}} \tag{4.56}$$

where $V_{max}(t)$ is the hysteretic change in V_{max} with time in the following way

$$V_{max}(t) = V^{final}_{max}(1 - e^{-Khys \cdot t}) \tag{4.57}$$

The change in V_{max} from the insert in Fig. 4.36b, is shown by applying the following parameter values $V^{final}{}_{max} = 0.7$ μM/s, $K_M = 215$ μM, $K_{hys} = 0.019$ s^{-1}, and initial concentration of $Ca^{2+}{}_{lum} = 243$ μM. The leak rate derived from the Camello data points was determined to be

$$v_{leak} = \frac{(250 - 30)\mu M}{1000 s} = 0.22 \frac{\mu M}{s} \tag{4.58}$$

These leak rates compare to reported leak rates of 19 μM to a few tens of μM per minute in pancreatic acinar cells, or and BHK-21 cells, even

though there has also been reports of higher values in sensory neurons and HeLa-cells [131].

Similar to experiments done by Luik et al. SERCA was inhibited in the leak calculations from the ER [130]. Experimenting with rate constants involved in the leak itself as well as in the buffering of Ca^{2+} in the ER lumen, different decay kinetics were observed. In Fig. 4.37 response in SOCC activity as well as Ca^{2+} concentration in the ER is compared by changing the level of Ca^{2+}_{lum} that is buffered and the rate constant for the leak.

From the plots in Fig. 4.37 it is seen that the leak rate increases as k_{27} (rate constant for Ca^{2+}_{lum} leak to the cytosol) increases, as does the SOCC activity. The same effect can also be seen with a decrease in buffering of Ca^{2+} in the ER lumen, where Fig. 4.37c shows a similar behavior as in Fig. 4.37a.

SERCA as an inflow controller

SERCA is reponsible for replenishing the ER with Ca^{2+} and is an ATPase similar to PMCA. Ca^{2+} activates the degradation of SERCA from the ER lumen. In the model we constructed SERCA as an inflow controller meaning that it will maintain the level of luminal Ca^{2+} in the ER by adding Ca^{2+} from the cytosol. The set-up of SERCA and Ca^{2+} involved in an inflow controller fits inflow controller 1 previously presented [27]. With zero-order kinetics, and the assumption that $k_{22} \ll Ca^{2+}_{lum}$ the set-point of luminal Ca^{2+} by SERCA is

$$Ca^{2+}_{lum,set} = \frac{k_{20}}{k_{21}} \tag{4.59}$$

In the model k_{21} is set to 1.0, meaning that the value of k_{20} determines the set-point for Ca^{2+} in the ER here. This is done as a tool to lock Ca^{2+} levels in the ER at a certain level. The systems behavior through changes in this k_{20} parameter is shown in Fig. 4.38.

The plots in Fig. 4.38 shows that as the level of Ca^{2+} in the ER decreases, the SOCC flux increases. The level of available STIM as Ca^{2+} is released correlates with the activity of SOCC. Also the level of bound Ca^{2+} to buffering proteins in the ER lumen follow an expected behavior compared of decreasing level of Ca^{2+} as shown in Fig. 4.38a. Since the set-point of luminal Ca^{2+} is determined by the parameter k_{20} alone, we see that even as

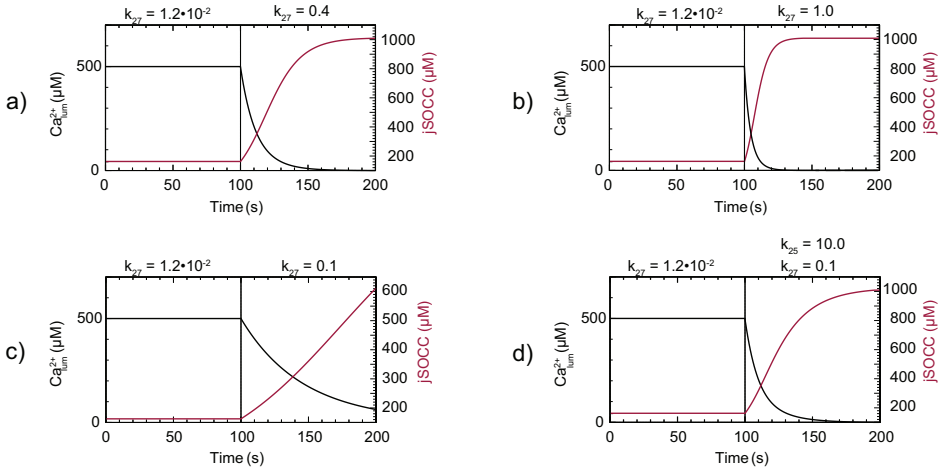

Figure 4.37: Influences of Ca^{2+} leak out of ER and Ca^{2+} buffering in ER. (a) Plot shows concentration of Ca^{2+}_{lum} and jSOCC in two phases where SERCA is inhibited in phase 2 as well as a change in k_{27} (rate constant for the Ca^{2+} leak from ER). The time step is given as $1.0 \cdot 10^{-2}$ s, with 2 phases and the intervals given as 100 s each. Rate constants are given in phase 1 as: $k_1 = 1.0 \cdot 10^{-1}$ s^{-1}, $k_2 = 0.0$ s^{-1}, $k_3 = 5.0 \cdot 10^4$ s^{-1}, $k_4 = 1.2$ μM, $k_5 = 16.0$ μM^{-1} s^{-1}, $k_6 = 8.0 \cdot 10^{-3}$ μM/s, $k_7 = 1.0 \cdot 10^{-6}$ μM, $k_8 = 2.5$ μM^{-1} s^{-1}, $k_9 = 5.0$ s^{-1}, $k_{10} = 1.0 \cdot 10^2$ μM^{-1} s^{-1}, $k_{11} = 80.0$ s^{-1}, $k_{12} = 1.0 \cdot 10^{-2}$ μM^{-1} s^{-1}, $k_{13} = 1.0 \cdot 10^{-1}$ s^{-1}, $k_{14} = 0.0$ μM/s, $k_{15} = 0.0$ s^{-1}, $k_{16} = 0.0$ μM/s, $k_{17} = 0.0$ s^{-1}, $k_{18} = 0.0$ μM/s, $k_{19} = 0.0$ s^{-1}, $k_{20} = 5.0 \cdot 10^2$ μM/s, $k_{21} = 1.0$ s^{-1}, $k_{22} = 1.0 \cdot 10^{-4}$ μM, $k_{23} = 1.0 \cdot 10^{-2}$ s^{-1}, $k_{24} = 1.3 \cdot 10^{-5}$ μM, $k_{25} = 5.0 \cdot 10^2$ μM^{-1} s^{-1}, $k_{26} = 1.0 \cdot 10^7$ s^{-1}, $k_{27} = 1.2 \cdot 10^{-2}$ s^{-1}, $k_{28} = 0.0$ μM/s, $k_{29} = 0.0$ s^{-1}, $k_{30} = 0.0$ μM/s, $k_{31} = 1.0 \cdot 10^2$ s^{-1}, $k_{32} = 0.0$ μM/s, $k_{33} = 0.0$ s^{-1}, $k_{34} = 1.0 \cdot 10^2$ μM^{-1} s^{-1}, $k_{35} = 1.0 \cdot 10^2$ s^{-1}, $k_{36} = 0.0$ μM^{-1} s^{-1}, $k_{37} = 1.0 \cdot 10^{-2}$ μM, $k_{38} = 5.0 \cdot 10^{-1}$ s^{-1}, $k_{39} = 1.0 \cdot 10^{-2}$ μM, $k_{40} = 2.26 \cdot 10^{-1}$, $k_{41} = 7.94 \cdot 10^{-1}$, $k_{42} = 2.26 \cdot 10^{-1}$, $k_{43} = 7.94 \cdot 10^{-1}$, $k_{44} = 1.0$ μM/s, $k_{45} = 1.0$ s^{-1}, $k_{46} = 50.0$ μM^{-1} s^{-1}, $k_{47} = 1.0$ s^{-1}, $k_{48} = 2.0$ μM/s, $k_{49} = 1.0$ s^{-1}, $k_{50} = 84.0$ μM^{-1} s^{-1}, $k_{51} = 8.4$ s^{-1}, $k_{52} = 10.0$ μM/s, $k_{53} = 1.0$, $k_{54} = 10.0$ μM^{-1} s^{-1}, $k_{55} = 1.0$ s^{-1}, $k_{56} = 1.0 \cdot 10^{-3}$ μM^{-1} s^{-1}, $k_{57} = 10.0$ s^{-1}, $k_{58} = 10.0$ μM/s, $k_{59} = 1.0$ s^{-1}, $k_{60} = 16.0$ μM^{-1} s^{-1}, $k_{61} = 8.0 \cdot 10^{-3}$ μM/s, $k_{62} = 1.0 \cdot 10^{-6}$ μM, $k_{63} = 1.0 \cdot 10^5$ s^{-1}, $k_{64} = 1.0 \cdot 10^2$ μM, $k_{65} = 0.0$ μM/s, $k_{66} = 0.0$ s^{-1}, $k_{67} = 1.0 \cdot 10^{-2}$ μM^{-1} s^{-1}, $k_{68} = 1.0 \cdot 10^{-1}$ s^{-1}, $k_{69} = 0.0$ μM/s, $k_{70} = 0.0$ s^{-1}, $k_{71} = 1.0$ μM^{-1} s^{-1}, $k_{72} = 96.0$ s^{-1}, $k_{73} = 10.0$ μM^{-1} s^{-1}, $k_{74} = 1.0 \cdot 10^{-7}$ μM, $k_{75} = 1.0$ μM/s, $k_{76} = 1.0$ s^{-1}, $k_{77} = 1.0$ μM^{-1} s^{-1}, $k_{78} = 1.0$, cooperativity phase 1 = 1.0. Phase 2: Same as above except $k_3 = 5.0 \cdot 10^3$ s^{-1}, $k_{23} = 0.0$ s^{-1}, $k_{27} = 4.0 \cdot 10^{-1}$ s^{-1}, $k_{71} = 1.0 \cdot 10^1$ μM^{-1} s^{-1}, $k_{73} = 1.0$ μM^{-1} s^{-1}. Initial conditions (in μM): $Ca^{2+}{}_{cyt} = 6.88358 \cdot 10^{-3}$, PMCA·M* = $9.20553 \cdot 10^{-1}$, $Ca^{2+}{}_{ext} = 1.0 \cdot 10^3$, M = $1.06641 \cdot 10^2$, M·Ca4 = $3.67037 \cdot 10^{-1}$, B = $9.91471 \cdot 10^2$, B·Ca4 = 8.53109, PMCA·M = $7.26366 \cdot 10^{-2}$, PMCA = $6.81131 \cdot 10^{-3}$, NCX·M* = $1.43989 \cdot 10^{-7}$, NCX·M = $9.14246 \cdot 10^{-3}$, NCX = $8.57311 \cdot 10^{-4}$, SERCA = $6.05347 \cdot 10^2$, $Ca^{2+}_{lum} = 4.99994 \cdot 10^2$, L = $2.43903 \cdot 10^3$, L·Ca30 = $6.09751 \cdot 10^1$, S = 0.0, R = $1.0 \cdot 10^2$, R·S = 0.0, ARCC = 1.0, IP3R·IP3 = 9.93163, IP3R = 2.0, IP3 = 5.0, STIM = $1.62523 \cdot 10^1$, STIM·Ca = $8.46461 \cdot 10^1$, SOCC = 1.0. (b) Same rate constants as in a, however in phase 2 $k_{27} = 1.0$ s^{-1}. (c) Same rate constants as in a, however in phase 2 $k_{27} = 1.0 \cdot 10^{-1}$ s^{-1}.(d) Same rate constants as in c, however in phase 2 rate constant of L·Ca_{30} formation (binding of Ca^{2+}_{lum} to buffers in ER) is decreased from $k_{25} = 5.0 \cdot 10^2$ μM^{-1} s^{-1} to $k_{25} = 10.0$ μM^{-1} s^{-1}.

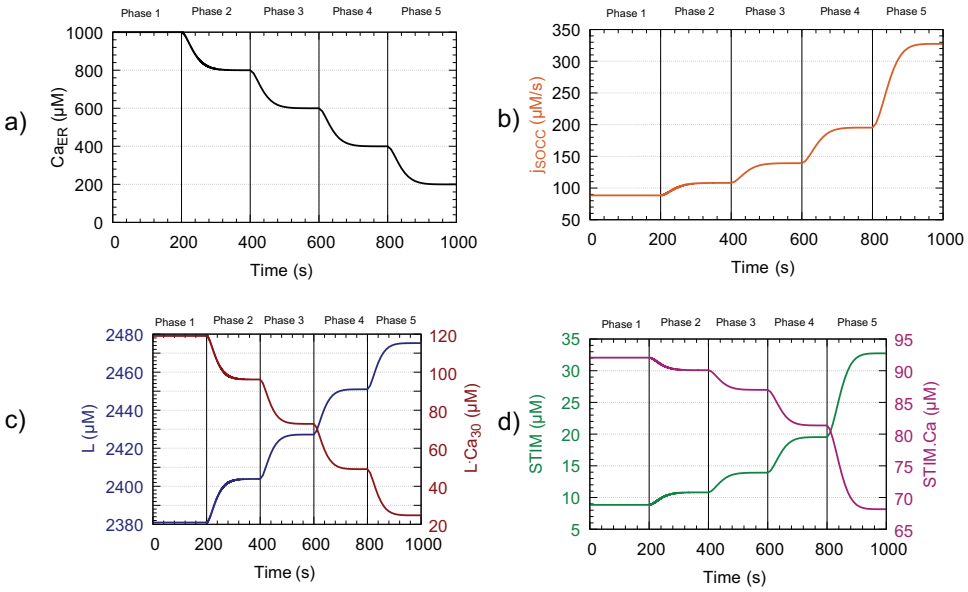

Figure 4.38: Influence of locked Ca^{2+}_{lum} concentrations on j_{SOCC}, L and STIM levels. (a) Plot shows the level of Ca^{2+} in the ER given a change in k_{20} through 5 phases. Phase 1 k_{20} = 1000.0 μM/s, phase 2 k_{20} = 800.0 μM/s, phase 3 k_{20} = 600.0 μM/s, phase 4 k_{20} = 400.0 μM/s, and phase 5 k_{20} = 200.0 μM/s. As given by the set-point, k_{20} determines the set-point of luminal Ca^{2+}. The time step is given as $1.0 \cdot 10^{-2}$ s, with 5 phases and the intervals given as 200 s each. Rate constants are the same as in Fig. 4.37, except for k_{20} given above and $k_{1phase3-5} = 0.0$ s^{-1}. Initial conditions (in μM): $Ca^{2+}{}_{cyt}$ = $5.08708 \cdot 10^{-3}$, PMCA·M* = $8.92504 \cdot 10^{-1}$, $Ca^{2+}{}_{ext}$ = $1.0 \cdot 10^{3}$, M = $1.06739 \cdot 10^{2}$, M·Ca4 = $2.71495 \cdot 10^{-1}$, B = $9.93683 \cdot 10^{2}$, B·Ca4 = 6.31869, PMCA·M = $9.82881 \cdot 10^{-2}$, PMCA = $9.20827 \cdot 10^{-3}$, NCX·M* = $1.02566 \cdot 10^{-7}$, NCX·M = $9.14322 \cdot 10^{-3}$, NCX = $8.56596 \cdot 10^{-4}$, SERCA = $4.01054 \cdot 10^{4}$, Ca^{2+}_{lum} = $1.0 \cdot 10^{3}$, L = $2.38096 \cdot 10^{3}$, L·Ca30 = $1.19048 \cdot 10^{2}$, S = 0.0, R = $1.0 \cdot 10^{2}$, R·S = 0.0, ARCC = 1.0, IP3R·IP3 = 9.94939, IP3R = 2.0, IP3 = 5.0, STIM = 8.837872, STIM·Ca = $9.20606 \cdot 10^{1}$, SOCC = 1.0. (b) As the luminal Ca^{2+} level decreases, the flux through SOCC, j_{SOCC}, increases. (c) Plot shows how decreasing Ca^{2+} levels in the ER affects the level of Ca^{2+} bound by buffers in the ER lumen. (d) STIM-level bound and unbound to Ca^{2+} is given, and is clearly following the level of Ca^{2+} in the ER and fits well with the activation of SOCC represented in the j_{SOCC} plot in panel b.

SOCC flux increase etc. as a response to this, there is no refilling of Ca^{2+} in the ER to the physiological resting level as would be expected under these conditions. Since Ca^{2+}_{lum} is locked, the filling of the ER by Ca^{2+} is dependent on the ER Ca^{2+} set-point.

STIM and its activation of capacitative Ca^{2+} entry

In the model STIM activates the PM bound SOCC, whereas STIM·Ca is inactive. STIM is a Ca^{2+} sensor located in the ER membrane, and activates the capacitative Ca^{2+} entry mainly by binding to the Orai1 protein when Ca^{2+} in the ER is depleted [132, 133]. Though there are two isoforms of STIM, only one STIM form is included in the model for the sake of simplicity.There are still questions about the differences between the two STIM forms and their role in SOCE. They differ in their regulation, but have been found to have similar affinities to Ca^{2+}. The K_D of STIM1 being 0.2-0.6 mM and the K_D of STIM2 is 0.5 mM. The different regulatory roles are suggested to be due to properties in their structure [134, 135]. Both K_D values fit well with STIM1 Ca^{2+} sensing in the range of $\sim$ 100 - 400 μM [130, 136, 137]. STIM1 is suggested to be the main active sensor during Ca^{2+} depletion from the ER in order to activate capacitative Ca^{2+} entry. STIM2 seems to respond to smaller changes in luminal Ca^{2+} concentrations. Research differ between proposing only a minor role for STIM2 in the capacitative Ca^{2+} entry to indicating that it too is a feedback regulator of both cytosolic and luminal Ca^{2+} however during smaller decreases in Ca^{2+} from the ER [78, 134, 138]. Cooperativity in STIM1 in the activation of the capacitative Ca^{2+} entry by SOCC has been suggested with a Hill coefficient of $\sim$ 4 - 8 [130, 136]. Since only an EF-hand binding site in STIM has been known, oligomerization has been suggested by some to be a suitable and possible explanation for this cooperativity. However, more recent studies suggest that several more binding sites, perhaps 5-6, located in the EFSAM part of STIM, could be involved [136, 137]. It is also believed that the EF-hand site must first bind to Ca^{2+} in order for STIM to undergo conformational changes so that other sites can become available [136]. Depletion of the ER Ca^{2+} can be from either release through the IP_3R (or RyR) channel, which will be discussed more later, or leak channels.

Further we wanted to investigate the cooperativity of STIM since that has been a question in terms of the activation of the capacitative Ca^{2+} entry. Luik et al. has estimated a Hill coefficient of $\sim$ 3.8 and 4.2 based on experimental findings [130].

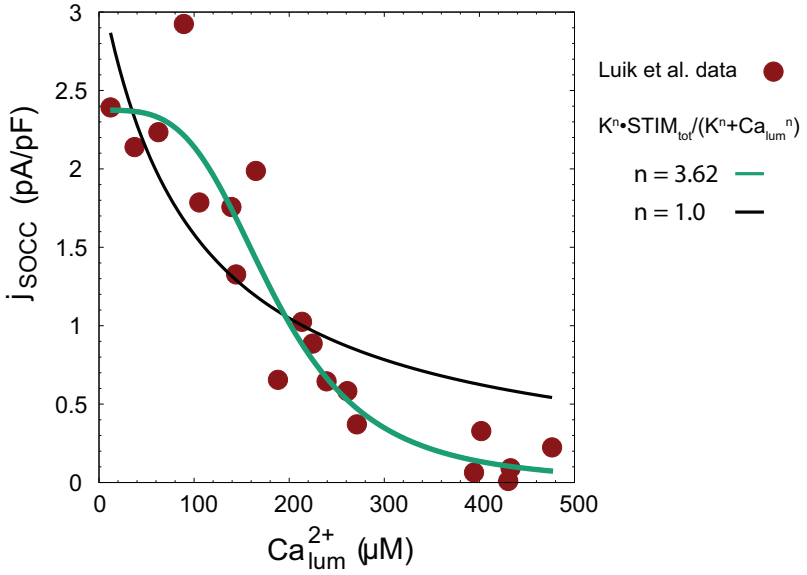

Figure 4.39: Capacitative Ca^{2+} entry (j_{SOCC}) with different cooperativity in STIM. Red data points show extracted data by Luik et al. [130]. Green and black fitted lines show fitted Eq. 4.60 with adjustable parameters n and K, according to a cooperativity of 3.62 and 1.0 respectively. Data is analyzed according to the equation: $K_I^n \cdot STIM_{tot}/K_I^n + Ca_{lum}^n$. For n=1.0, α = 310.28 ± 73 μM and K = 96.0 μM ± 37 μM. For n=3.62459, α = 2.37719 ± 0,171 μM and K = 184.527 μM ± 14 μM.

From the experimental data by Luik et al. [130] we analyzed and compared different cooperativities by using the relationship in Eq. 4.60.

$$j_{SOCC} = \frac{K_I^n \cdot STIM_{tot}}{K_I^n + Ca_{lum}^n} = \frac{\alpha}{\beta + Ca_{lum}^n} \tag{4.60}$$

n represents the cooperativity (Hill-coefficient) of j_{SOCC} by luminal Ca^{2+}, K_I^n is the inhibition constant and $STIM_{tot}$ is the total concentration of STIM. The coefficients α and β were fitted to the Luik et al. [130] data points, where $\beta = K_I^n$. The black line in Fig. 4.39 represents a condition where STIM only binds one Ca^{2+} (n = 1.0), and the green line shows a cooperativity of 3.62 (n = 3.62) that was found to be the optimum value.

We analyzed the Hill equation presented by Luik et al. [130] in their supporting info concerning their Fig. 1c. We were not able to verify their stated fitting function, which was supposed to be inhibitory with respect to calcium, but the stated expression of fitting function actually

shows a calcium activation of j_{SOCC} (pA/pF). We believe an equivalent expression to the one we use, Eq. 4.60, was also used by them. The Hill-coefficient of 4.2 found by Luik et al. was interpreted by them as a result of STIM oligomerization [130]. Even though Fig. 4.39 shows a good fit of Eq. 4.60 with a cooperativity of 3.62, we interpret this result as potentially misleading. The result of high Hill-coefficient could be misleading due to the indication of the green line in Fig. 4.39 should reach a plateau at low $Ca^{2+}{}_{\mathrm{lum}}$ concentrations. Also Eq. 4.60 indicates a mechanism of derepression where luminal Ca^{2+} inhibits j_{SOCC}, but only done indirectly by STIM binding. STIM cooperativity was investigated more thoroughly, and different scenarios for cooperativity is presented in Fig. 4.40.

Plot shapes were compared to experimental data represented by the red data points. Different values for n (cooperativity) were applied, and the different colored plots in Fig. 4.40a represent cooperativities from 0.8 to 1.5. The plots show the higher values for cooperativity agree well with higher concentrations of Ca^{2+}_{lum}, but the smaller n values agree better with a lower concentration of Ca^{2+}_{lum}. As a result, in Fig. 4.40b we started with a cooperativity of 1.3 and decreased n linearly to 0.8 as Ca^{2+}_{lum} concentration from higher to lower concentrations. Considering the relatively high experimental uncertainty in the data, this model seems to be the best fit with the experimental data by Luik et al. [130].

IP_3R

IP_3R was chosen as the only channel for the release of Ca^{2+} from the ER. Although RyR also have this function, it is mainly located in the sarcoplasmic reticulum (SR) of excitable cells [139]. IP_3R has been found to produce agonist-induced oscillations of Ca^{2+} on its own, however some contradicting research has been published on the subject mainly in excitable cells [140, 141]. Also, for modeling purposes, only one form is used, even though the channel has three isoforms. All isoforms of IP_3R have a biphasic regulation by Ca^{2+} giving them a bell-shaped curve, with a maximum at around 300 nM cytosolic Ca^{2+}, and they are also regulated by IP_3 [88, 89, 142, 143]. Kaftan et al. [143], however, found that at lower or higher IP_3 presence the bell-shaped curve shifted its maximum to the left or right respectively due to changes in the Ca^{2+} dependent inhibition. This activation and subsequent release of Ca^{2+} from the ER by cytosolic Ca^{2+} has been named Ca^{2+} induced Ca^{2+} release (CICR) [38, 88, 144].

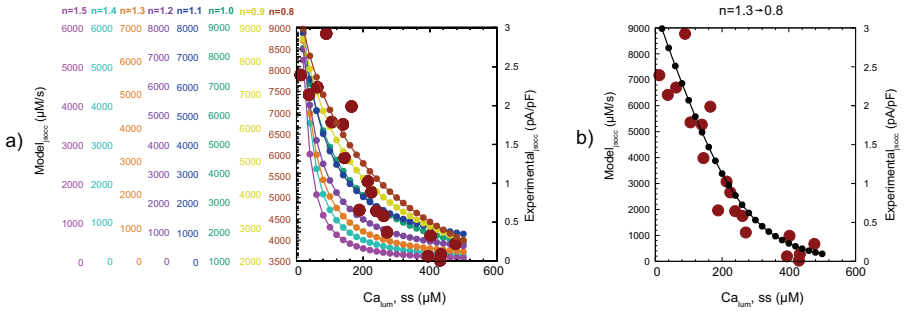

Figure 4.40: Model calculations vs. experimental data with different cooperativities. (a) Red large data points adapted from Luik et al. like in previous figure Fig. 4.39 [130]. Incorporation of different STIM cooperativities into the current model were compared to the experimental data. Different n values for cooperativity were applied to the calculations, and the different colored plots represent cooperativity from 0.8 to 1.5. The time step is given as $5.0 \cdot 10^{-3}$. Rate constants are given as: $k_1 = 0.0\ s^{-1}$, $k_2 = 0.0\ s^{-1}$, $k_3 = 5.0 \cdot 10^4\ s^{-1}$, $k_4 = 1.2\ \mu M$, $k_5 = 16.0\ \mu M^{-1}\ s^{-1}$, $k_6 = 8.0 \cdot 10^{-3}\ \mu M/s$, $k_7 = 1.0 \cdot 10^{-6}\ \mu M$, $k_8 = 2.5\ \mu M^{-1}\ s^{-1}$, $k_9 = 5.0\ s^{-1}$, $k_{10} = 1.0 \cdot 10^2\ \mu M^{-1}\ s^{-1}$, $k_{11} = 80.0\ s^{-1}$, $k_{12} = 1.0 \cdot 10^{-2}\ \mu M^{-1}\ s^{-1}$, $k_{13} = 1.0 \cdot 10^{-1}\ s^{-1}$, $k_{14} = 0.0\ \mu M/s$, $k_{15} = 0.0\ s^{-1}$, $k_{16} = 0.0\ \mu M/s$, $k_{17} = 0.0\ s^{-1}$, $k_{18} = 1.0 \cdot 10^3\ \mu M/s$, $k_{19} = 1.0 \cdot 10^{-2}\ s^{-1}$, $k_{20} = 5.0 \cdot 10^2\ \mu M/s$, $k_{21} = 1.0\ s^{-1}$, $k_{22} = 1.0 \cdot 10^{-6}\ \mu M$, $k_{23} = 1.0 \cdot 10^{-4}\ s^{-1}$, $k_{24} = 1.3 \cdot 10^{-5}\ \mu M$, $k_{25} = 1.25 \cdot 10^3\ \mu M^{-1}\ s^{-1}$, $k_{26} = 1.0 \cdot 10^6\ s^{-1}$, $k_{27} = 1.0 \cdot 10^{-1}\ s^{-1}$, $k_{28} = 0.0\ \mu M/s$, $k_{29} = 0.0\ s^{-1}$, $k_{30} = 0.0\ \mu M/s$, $k_{31} = 1.0 \cdot 10^2\ s^{-1}$, $k_{32} = 0.0\ \mu M/s$, $k_{33} = 0.0\ s^{-1}$, $k_{34} = 1.0 \cdot 10^2\ \mu M^{-1}\ s^{-1}$, $k_{35} = 1.0 \cdot 10^2\ s^{-1}$, $k_{36} = 0.0\ \mu M^{-1}\ s^{-1}$, $k_{37} = 1.0 \cdot 10^{-2}\ \mu M$, $k_{38} = 1.0\ s^{-1}$, $k_{39} = 1.0 \cdot 10^{-2}\ \mu M$, $k_{40} = 2.26 \cdot 10^{-1}$, $k_{41} = 7.94 \cdot 10^{-1}$, $k_{42} = 2.26 \cdot 10^{-1}$, $k_{43} = 7.94 \cdot 10^{-1}$, $k_{44} = 1.0\ \mu M/s$, $k_{45} = 1.0\ s^{-1}$, $k_{46} = 50.0\ \mu M^{-1}\ s^{-1}$, $k_{47} = 1.0\ s^{-1}$, $k_{48} = 2.0\ \mu M/s$, $k_{49} = 1.0\ s^{-1}$, $k_{50} = 84.0\ \mu M^{-1}\ s^{-1}$, $k_{51} = 8.4\ s^{-1}$, $k_{52} = 10.0\ \mu M/s$, $k_{53} = 1.0\ s^{-1}$, $k_{54} = 10.0\ \mu M^{-1}\ s^{-1}$, $k_{55} = 1.0\ s^{-1}$, $k_{56} = 1.0 \cdot 10^{-3}\ \mu M^{-1}\ s^{-1}$, $k_{57} = 10.0\ s^{-1}$, $k_{58} = 10.0\ \mu M/s$, $k_{59} = 1.0\ s^{-1}$, $k_{60} = 16.0\ \mu M^{-1}\ s^{-1}$, $k_{61} = 8.0 \cdot 10^{-3}\ \mu M/s$, $k_{62} = 1.0 \cdot 10^{-6}\ \mu M$, $k_{63} = 1.0 \cdot 10^5\ s^{-1}$, $k_{64} = 1.0 \cdot 10^2\ \mu M$, $k_{65} = 0.0\ \mu M/s$, $k_{66} = 0.0\ s^{-1}$, $k_{67} = 1.0 \cdot 10^{-2}$, $k_{68} = 1.0 \cdot 10^{-1}\ s^{-1}$, $k_{69} = 0.0\ \mu M/s$, $k_{70} = 0.0\ s^{-1}$, $k_{71} = 1.0\ \mu M^{-1}\ s^{-1}$, $k_{72} = 96.0\ s^{-1}$, $k_{73} = 10.0\ \mu M^{-1}\ s^{-1}$, $k_{74} = 1.0 \cdot 10^{-7}\ \mu M$, $k_{75} = 1.0\ \mu M/s$, $k_{76} = 1.0\ s^{-1}$, $k_{77} = 1.0\ \mu M^{-1}\ s^{-1}$, $k_{78} = 1.0\ \mu M^{-1}\ s^{-1}$, $n = 1.0$. k_{20} starts at $5.0 \cdot 10^2\ \mu M/s$, with a negative increment (K20INCR) of 20.0 and a final lower k_{20} at 20.0 $\mu M/s$, with the equation k_{20}=k_{20}+K20INCR for each time step. Initial conditions (in μM): $Ca^{2+}{}_{cyt} = 7.96397 \cdot 10^{-2}$, PMCA·M* $= 3.13031 \cdot 10^{-3}$, $Ca^{2+}{}_{ext} = 1.0 \cdot 10^3$, $M = 1.05774 \cdot 10^2$, M·Ca4 = 4.21192, $B = 1.0 \cdot 10^5$, B·Ca4 $= 9.95496 \cdot 10^3$, PMCA·M $= 6.27627 \cdot 10^{-3}$, PMCA $= 5.93364 \cdot 10^{-2}$, NCX·M* $= 3.13031 \cdot 10^{-3}$, NCX·M $= 6.27627 \cdot 10^{-3}$, NCX $= 5.93364 \cdot 10^{-4}$, SERCA $= 1.11336 \cdot 10^6$, $Ca^{2+}_{lum} = 1.0 \cdot 10^3$, $L = 1.11112 \cdot 10^3$, L·Ca30 $= 1.38889 \cdot 10^3$, S = 0.0, $R = 1.0 \cdot 10^2$, R·S = 0.0, ARCC = 1.0, IP3R·IP3 $= 6.25566 \cdot 10^2$, IP3R = 2.0, IP3 = 5.0, STIM $= 9.99001 \cdot 10^{-1}$, STIM·Ca $= 9.99001 \cdot 10^2$, SOCC = 1.0. (b) Red data points adapted from Luik et al. identical to (a) [130]. In this calculation the cooperativity n was changed linearly from n = 1.3 at $Ca^{2+}_{lum} = 500\ \mu M$ to n = 0.8 at $Ca^{2+}_{lum} = 200\ \mu M$ (with $\Delta n = 0.0208$).

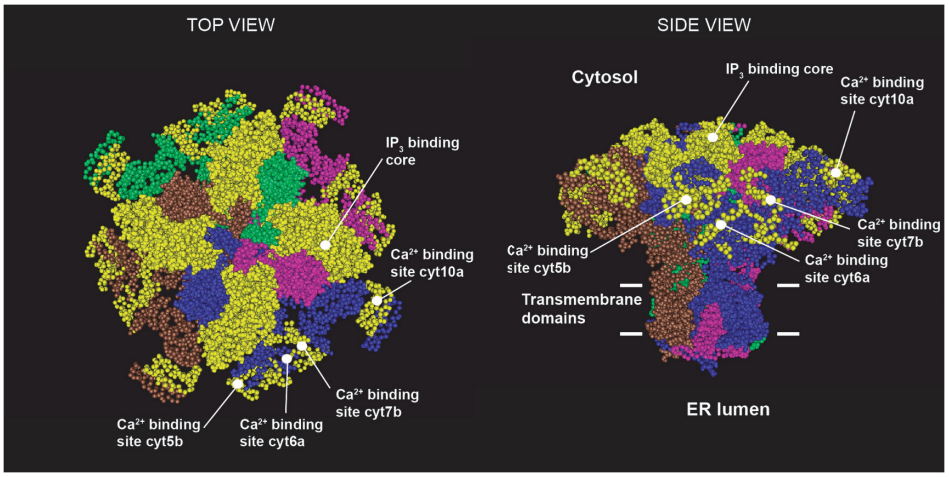

Figure 4.41: Structure of IP_3R with binding sites of IP_3 and Ca^{2+}. IP_3R structure is based on structure 3JAV from rat [147]. The channel consists of four subunits, here shown in blue, brown, purple and green color. The IP_3 binding core (IBC) as well as Ca^{2+} binding sites provided from amino acid sequences from litterature are highlighted in yellow in the structure and pointed out in the figure in white. For simplicity, descriptions in white are given for only one subunit.

The large size of the IP_3R channel as well as being a transmembrane protein has made it difficult to examine its structure[145, 146]. By the use of single particle cryo-EM a 3D structure of IP_3R has been reported by Fan et al. [147]. The IP_3R structure, based on the work by Fan et al., combined with collected data from the research by Sienaert et al. and Ding et al. on binding sites of IP_3 and Ca^{2+} is given in Fig. 4.41 [147, 148, 149].

As to how exactly channel gating works regarding both the activation and inactivation by Ca^{2+}, as well as the precursory binding of IP_3 for activation, is still not fully understood. It is suggested that configuration changes following IP_3 binding to IP_3R makes binding sites for Ca^{2+} available. There are several Ca^{2+} binding sites suggested, but the exact functions are yet to be explored and uncovered [88, 148, 150]. Research indicates that the activation and inhibition by Ca^{2+} on the channel is due to different binding sites with different affinities [88, 151]. A model suggested by Taylor and Tovey describes a mechanism where the binding of IP_3 either makes the activating or inhibitory site for Ca^{2+} available determined by its own presence [88]. CaM has also been suggested to be involved as an accessory protein for Ca^{2+} for its inhibition as opposed to direct Ca^{2+} binding. Mutant studies without the high-affinity Ca^{2+}-CaM binding site

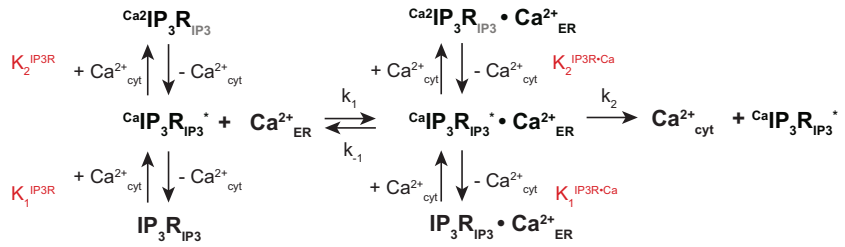

Figure 4.42: Dicalcic model. The middle activated form indicated with the asterix, ${}^{Ca}IP_3R^*_{IP3}$, is able to transport Ca^{2+} through the ER membrane. The forms in the top, ${}^{Ca_2}IP_3R_{IP3}$ and ${}^{Ca}IP_3R^*_{IP3}{\cdot}Ca^{2+}_{ER}$, and bottom, IP_3R_{IP3} and $P_3R^*_{IP3}{\cdot}Ca^{2+}_{ER}$, are inactive forms due to either no cytosolic Ca^{2+} bound in the activating site of the transporter, or that two cytosolic Ca^{2+} have bound to it and inhibiting the channel activity. Dissociation constants are given in red.

does however still give a bell-shaped curve of Ca^{2+} dependency. This finding indicates either direct binding by Ca^{2+} or binding in association with another protein for the inhibition of IP_3R [88, 152]. However, this view is still controversial [153].

In our model, the IP_3R mechanism is based on a IP_3R-IP_3 complex which is either activated or inhibited by Ca^{2+}, see Fig. 4.42. The channel is activated or inhibited based on the concentration of cytosolic Ca^{2+}, with 300 nM being the limit where it switches between being activated or inhibited. We have included a cooperativity of 2 for the inhibitory mechanism which agrees well with the properties in experimental Ca^{2+} biphasic curves by Kaftan et al. [143], see also Fig. 4.44. Analogous to a diprotic model [154], we assume that there is a optimal number of bound Ca^{2+} to IP_3R which leads to maximum channel activity, and term the model as "dicalcic model".

Dicalcic model of IP_3R regulation by cytosolic calcium

The dicalcic model is illustrated in Fig. 4.42.

The model consist of a IP_3R-IP_3 complex where one bound cytosolic Ca^{2+} leads to an active form. Any further binding of cytosolic Ca^{2+} to IP_3R-IP_3 gives an inactive channel. The active IP_3R complex can transport Ca^{2+} from the ER lumen to the cytosol. The kinetics of the IP_3R transporter is described in terms of Michaelis-Menten kinetics. The addition of the dual Ca^{2+} binding model to the model is shown in Fig. 4.43a. An illustration of the different possibilities of Ca^{2+} binding to the IP_3R-IP_3 complex is

given in Fig. 4.43b. At step 7 there is an inhibition with a cooperativity of 2, which means two Ca^{2+} have to bind to the complex at inhibitory sites. In Fig. 4.42 this would be seen as an extra step upwards where you would have $^{Ca3}IP_3R$-IP_3 and $^{Ca3}IP_3R$-$IP_3 \cdot {Ca^{2+}}_{ER}$ with the binding of this extra Ca^{2+}.

The dissociation constants K_1^{IP3R} and K_2^{IP3R} from Fig. 4.42 are given by the following equations

$$K_1^{IP3R} = \frac{(Ca_{cyt}^{2+})(IP_3R_{IP3})}{(^{Ca_{cyt}}IP_3R_{IP3}^*)} \tag{4.61}$$

$$K_2^{IP3R} = \frac{(Ca_{cyt}^{2+})(^{Ca_{cyt}}IP_3R_{IP3}^*)}{(^{Ca_{cyt_2}}IP_3R_{IP3})} \tag{4.62}$$

The transport rate of Ca^{2+} from the ER into the cytosol is described as

$$v = k_2(^{Ca_{cyt}}IP_3R_{IP3}^* \cdot Ca_{ER}^{2+}) \tag{4.63}$$

The two dissociation constants of the two possible processes concerning $^{Ca_{cyt}}IP_3R_{IP3}^* \cdot Ca_{ER}^{2+}$ either releasing the allosterically bound Ca_{cyt}^{2+} or binding another Ca_{cyt}^{2+} to inactivate the channel, are given as

$$K_1^{IP3R \cdot Ca} = \frac{(Ca_{cyt}^{2+})(IP_3R_{IP3} \cdot Ca_{ER}^{2+})}{(^{Ca_{cyt}}IP_3R_{IP3}^* \cdot Ca_{ER}^{2+})} \tag{4.64}$$

$$K_2^{IP3R \cdot Ca} = \frac{(Ca_{cyt}^{2+})(^{Ca_{cyt}}IP_3R_{IP3}^* \cdot Ca_{ER}^{2+})}{(^{Ca_{cyt_2}}IP_3R_{IP3} \cdot Ca_{ER}^{2+})} \tag{4.65}$$

The transport rate, v, is proportional to IP_3R channel open probabilities at different IP_3 concentrations as a function of Ca^{2+} concentration from experimental results by Kaftan et al. [143]. The expression of v is derived based on an assumption of the transporter mass balance where IP_3R_0 is the total amount of transporter (which for simplicity is assumed to be constant):

$$\begin{aligned} IP_3R_0 = IP_3R_{IP3} + {}^{Ca_{cyt}}IP_3R_{IP3}^* + {}^{Ca_{cyt_2}}IP_3R_{IP3} + IP_3R_{IP3} \cdot Ca_{ER}^{2+} \\ + {}^{Ca_{cyt}}IP_3R_{IP3}^* \cdot Ca_{ER}^{2+} + {}^{Ca_{cyt_2}}IP_3R_{IP3} \cdot Ca_{ER}^{2+} \end{aligned} \tag{4.66}$$

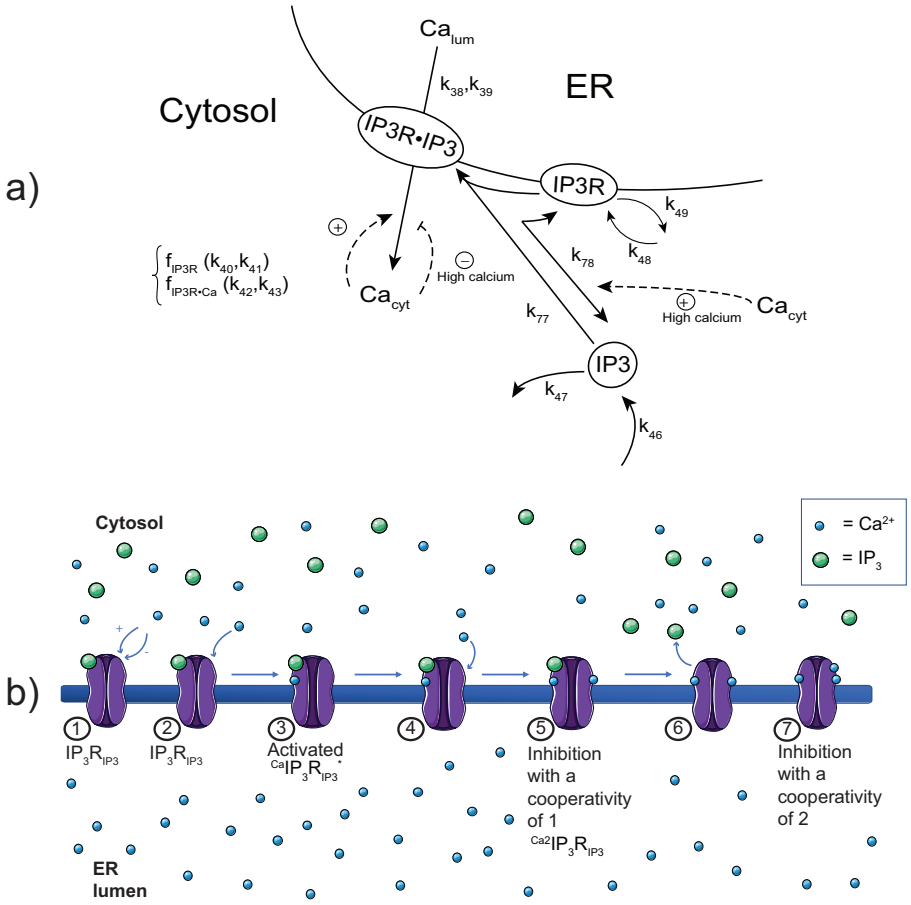

Figure 4.43: The IP_3R channel in the model. (a) A section of the model showing Ca^{2+} transport by IP_3R and how IP_3R is activated and inhibited by cytosolic Ca^{2+}. At low cytosolic Ca^{2+} concentrations $Ca^{2+}{}_{cyt}$ activates the IP_3R-IP_3 complex, while at higher levels (above 300 nM) Ca^{2+} will inhibit it. In addition, high Ca^{2+} will also activate the dissociation of the complex such that IP_3 is released. (b) Similar to Fig. 2.11 in the introduction, this gives a visual illustration of the activating and inhibiting function by cytosolic Ca^{2+} on IP_3R. This illustration however is based on the mechanism included in the model and therefore also includes an additional step with a cooperativity of 2 in the binding of Ca^{2+} to the IP_3R. 1: The IP_3R-IP_3 complex is available for Ca^{2+} interaction, 2: Ca^{2+} binds to the activation site, 3: IP_3R-IP_3 is activated and is able to transport Ca^{2+} from the ER into the cytosol, 4: At higher Ca^{2+} concentrations it will bind to the inhibitory site of IP_3R-IP_3, 5: IP_3R-IP_3 has bound Ca^{2+} to its inhibitory site with a cooperativity of 1, 6: This new state leads to the release of IP_3 from the IP_3R-IP_3 complex, 7: This state shows the IP_3R with a cooperativity of 2 in its inhibition by Ca^{2+} which will be shown in our results to be a better fit to experimental results.

IP_3R_{IP3} and ${}^{Ca_{cyt2}}IP_3R_{IP3}$ from Eqs. 4.61 and 4.62 can be expressed in terms of ${}^{Ca_{cyt}}IP_3R^*_{IP3}$, while $IP_3R_{IP3}{\cdot}Ca^{2+}_{ER}$ and ${}^{Ca_{cyt2}}IP_3R_{IP3}{\cdot}Ca^{2+}_{ER}$ from Eqs. 4.64 and 4.65 can be expressed in terms of ${}^{Ca_{cyt}}IP_3R^*_{IP3}{\cdot}Ca^{2+}_{ER}$. This leads to the expressions of two new constants termed f_{IP3R} and $f_{IP3R{\cdot}Ca}$ given as

$$f_{IP3R} = 1 + \frac{K_1^{IP3R}}{Ca^{2+}_{cyt}} + \frac{Ca^{2+}_{cyt}}{K_2^{IP3R}} \tag{4.67}$$

and

$$f_{IP3R{\cdot}Ca} = 1 + \frac{K_1^{IP3R{\cdot}Ca}}{Ca^{2+}_{cyt}} + \frac{Ca^{2+}_{cyt}}{K_2^{IP3R{\cdot}Ca}} \tag{4.68}$$

Using these, the total transporter concentration, Eq. 4.66, can be rewritten as

$$IP3R_0 = f_{IP3R}({}^{Ca_{cyt}}IP_3R^*_{IP3}) + f_{IP3R{\cdot}Ca}({}^{Ca_{cyt}}IP_3R^*_{IP3}{\cdot}Ca^{2+}_{ER}) \tag{4.69}$$

Note that f_{IP3R} and $f_{IP3R{\cdot}Ca}$ are functions of cytosolic Ca^{2+}, which activate or inhibit IP_3R. In Fig. 4.43a the expressions f_{IP3R} and $f_{IP3R{\cdot}Ca}$ can be seen, where $k_{40} = K_1^{IP3R}$, $k_{41} = K_2^{IP3R}$, $k_{42} = K_1^{IP3R{\cdot}Ca}$, and $k_{43} = K_3^{IP3R{\cdot}Ca}$.

The assumption of steady state of ${}^{Ca_{cyt}}IP_3R^*_{IP3}{\cdot}Ca^{2+}_{ER}$, is also made

$$\frac{\mathrm{d}({}^{Ca_{cyt}}IP_3R^*_{IP3}{\cdot}Ca^{2+}_{ER})}{\mathrm{d}t} = 0 \tag{4.70}$$

leading to a dynamical equilibrium constant relating Ca^{2+}_{ER} and ${}^{Ca_{cyt}}IP_3R^*_{IP3}$ with ${}^{Ca}IP3R^*_{IP3}{\cdot}Ca^{2+}_{ER}$, analogous to Michaelis Menten kinetics and K_M:

$$K_M = \frac{(Ca^{2+}_{ER})({}^{Ca_{cyt}}IP_3R^*_{IP3})}{({}^{Ca_{cyt}}IP3R^*_{IP3}{\cdot}Ca^{2+}_{ER})} = \frac{k_{-1} + k_2}{k_1} \tag{4.71}$$

By rearranging the expression of K_M, ${}^{Ca_{cyt}}IP_3R^*_{IP3}$ can be expressed in terms of ${}^{Ca_{cyt}}IP3R^*_{IP3}{\cdot}Ca^{2+}_{ER}$

$${}^{Ca_{cyt}}IP_3R^*_{IP3} = \frac{K_M}{Ca^{2+}_{ER}}\left({}^{Ca_{cyt}}IP3R^*_{IP3}{\cdot}Ca^{2+}_{ER}\right) \tag{4.72}$$

Inserting this into the rewritten mass balance of IP_3R_0 from Eq. 4.69 gives

$$IP_3R_0 = \left(f_{IP3R} \cdot \frac{K_M}{Ca_{ER}^{2+}} + f_{IP3R \cdot Ca} \right) ({}^{Ca_{cyt}} IP_3R^*_{IP3} \cdot Ca_{ER}^{2+}) \tag{4.73}$$

This can now be inserted into the v expression from Eq. 4.63:

$$v = \frac{V_{max} \cdot (Ca_{ER}^{2+})}{f_{IP3R} \cdot K_M + f_{IP3R \cdot Ca} \cdot (Ca_{ER}^{2+})} \tag{4.74}$$

where V_{max}=$k_2 \cdot (IP_3R_0)$.

Comparing calculated results of biphasic curves given by the binding of cytosolic Ca^{2+} to the IP_3R-IP_3 complex with experimental results by Kaftan et al. [143] a cooperation of 2 for the inhibitory step gives a much better model representation This indicates that a cooperative binding of 2 in the inhibitory step of Ca^{2+} to the complex, as illustrated in Fig. 4.43b, appears present, possibly to enforce a more abrupt shut-down of the transporter in order to avoid too high cytosolic Ca^{2+} levels otherwise building up. A comparison between theoretical calculations and experimental data can be seen in Fig. 4.44.

The calculations of the Ca^{2+} binding to the IP_3R-IP_3 complex is done by determining the theoretical rate by using equation 4.74. Calculations show similar behavior to the experimental results, however the experimental inhibition of the channel opening occurs more rapid than the model predicts. Since cooperativity is known to give more abrupt transitions compared to non-cooperative, a cooperativity of 2 was applied for the inhibitory binding of Ca^{2+}. As can be seen from the green curves in Fig. 4.44 this gives a better fit to the experimental data by Kaftan et al. [143].

The model approach (including the dicalcic model) to IP_3R activity gives a good fit to experimental data as shown from the Fig. 4.44. Some newer approaches addressed for instance in the review by Dupont and Sneyd [155] include modal models of IP_3R. Modal models are a way of describing variations in the channel open probability by IP_3R, that have been observed even at constant levels of both Ca^{2+} and IP_3. The modal description of IP_3R activity shows that channel open probability switches between different modes where the channel is more or less likely to open [155, 156]. One type of model describes a "park" mode, where IP_3R rarely opens, and a "drive

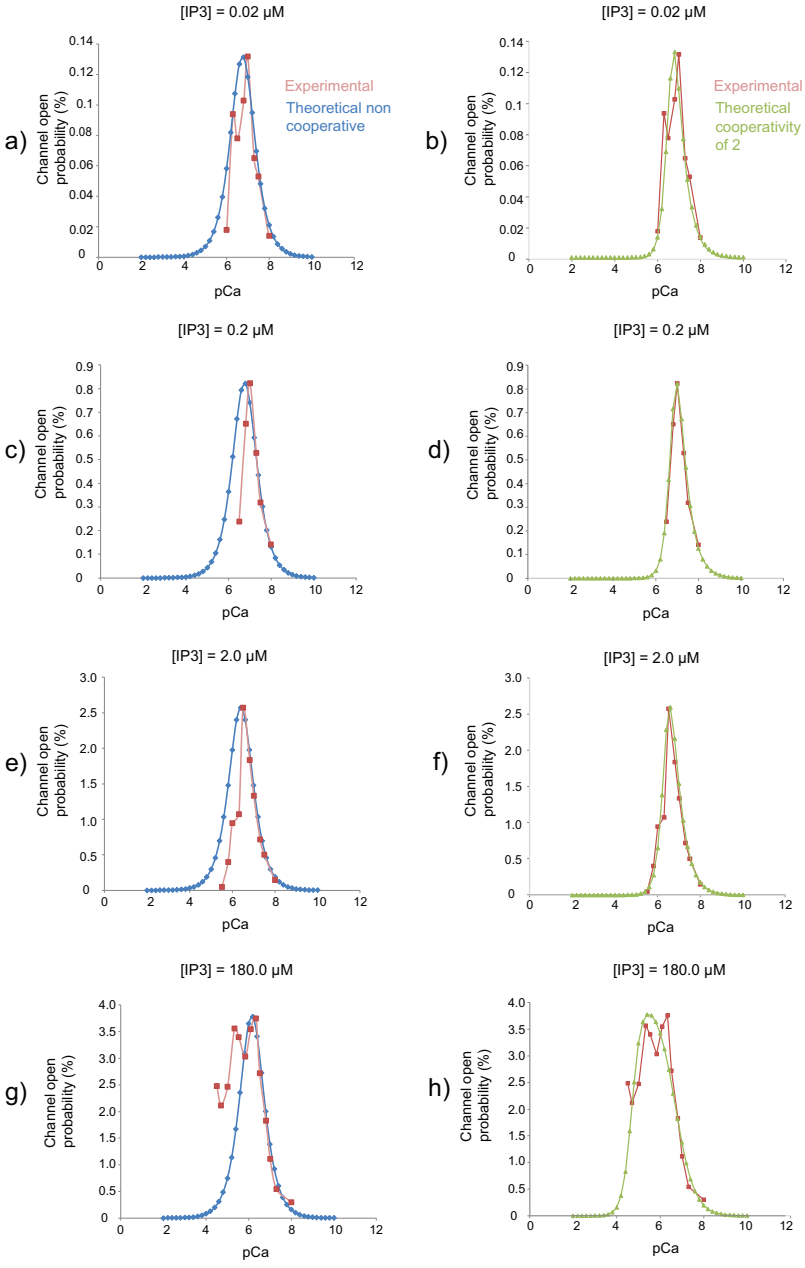

Figure 4.44: (Caption next page.)

Figure 4.44: (Continued from Previous Page.) **Biphasic curves of channel open probability vs. pCa at different IP_3 concentrations.** Graphs show biphasic curves based on experimental data from Kaftan et al. [143] Figure 2 represented by the red lines, and theoretical calculations based on the dual calcium binding model with no cooperativity represented by the blue lines, and a cooperativity of 2 in the inhibitory binding by Ca^{2+} represented by green lines. The different graphs are the result of different IP_3 concentrations where (a) and (b) are the result at $[IP_3]$ = 0.02 μM, (c) and (d) at $[IP_3]$ = 0.2 μM, (e) and (f) at $[IP_3]$ = 2.0 μM, and (g) and (h) at $[IP_3]$ = 180 μM. The pCa peak shifts to the left with an increasing concentration of IP_3. (a), (c), (e) and (g) show the curves with no cooperativity in the binding of Ca^{2+} to the IP_3R-IP_3 complex, whereas the other four (b), (d), (f) and (h) show curves calculated with a cooperativity of 2 in the inhibitory binding of Ca^{2+} to the IP_3R-IP_3 complex. Theoretical calculations are based on channel open probability = $V_{max} \cdot 1/(f_{IP3R} \cdot K_M + f_{IP3R \cdot Ca} \cdot 1)$ for different Ca^{2+} concentrations. For all calculations: pCa = 2 - 10, Ca = 10^{-pCa}, K_M = 0.01 μM, substrate concentration = 1.0 μM, ${K_1}^{IP3R} = {K_1}^{IP3R \cdot Ca} = 10^{-p{K_1}^{IP3R}}$, ${K_2}^{IP3R} = {K_2}^{IP3R \cdot Ca} = 10^{-p{K_2}^{IP3R}}$, ${Ca^{2+}}_{ER}$ = 1 μM. In noncooperative calculations: [IP3]=0.02 μM: V_{max} = 0.4 μM/s, $p{K_1}^{IP3R}$ = 6.75, $p{K_2}^{IP3R}$ = 6.75. [IP3]=0.2 μM: V_{max} = 2.5 μM/s, $p{K_1}^{IP3R}$ = 6.75, $p{K_2}^{IP3R}$ = 6.75. [IP3]=2.0 μM: V_{max} = 7.8 μM/s, $p{K_1}^{IP3R}$ = 6.4, $p{K_2}^{IP3R}$ = 6.4. [IP3]=180.0 μM: V_{max} = 11.5 μM/s, $p{K_1}^{IP3R}$ = 6.15, $p{K_2}^{IP3R}$ = 6.15. In calculations with cooperativity of 2 in inhibitory binding: [IP3]=0.02 μM: V_{max} = 1.07 μM/s, $p{K_1}^{IP3R}$ = 13.9, $p{K_2}^{IP3R}$ = 6.1. [IP3]=0.2 μM: V_{max} = 8.15 μM/s, $p{K_1}^{IP3R}$ = 14.4, $p{K_2}^{IP3R}$ = 6.2. [IP3]=2.0 μM: V_{max} = 14.2 μM/s, $p{K_1}^{IP3R}$ = 13.3, $p{K_2}^{IP3R}$ = 6.1. [IP3]=180.0 μM: V_{max} = 4.15 μM/s, $p{K_1}^{IP3R}$ = 9.4, $p{K_2}^{IP3R}$ = 6.7. Also $f_{IP3} = f_{IP3R}$n where n = 2, and Ca^{2+} to the power of 2 is divided by ${K_2}^{IP3R}$ in the original equation. This applies equally to $f_{IP3R \cdot Ca}$n. pCa = $-\log_{10}{Ca^{2+}}_{cyt}$.

mode" where it opens more frequently. Another model set-up includes three modes with low, intermediate and high open probabilities combined with the number of Ca^{2+} and IP_3 bound to the channel [155, 156]. Difficulties of constructing such models are described as the availability of data on single-channel behavior of IP_3R, and also set-up of the model in terms of identifying and transitioning between modes [155].

Influence of cytosolic Ca^{2+} on the dissociation of IP_3R-IP_3

Implementing these findings into the model, a concentration of IP_3 of 2 μM was used, in addition to a cooperativity of 2 in the inhibitory binding by Ca^{2+}. Different feedback set-ups and kinetics were applied to demonstrate and see the variation in the Ca^{2+} outflow from ER as a function of cytosolic Ca^{2+}. A comparison in the way cytosolic Ca^{2+} influences the IP_3R-IP_3 dissociation can be seen in Fig. 4.45.

The plots in Fig. 4.45b shows a biphasic curve comparable to the familiar shape of Fig. 4.45a, already shown from the experiments by Kaftan et al.

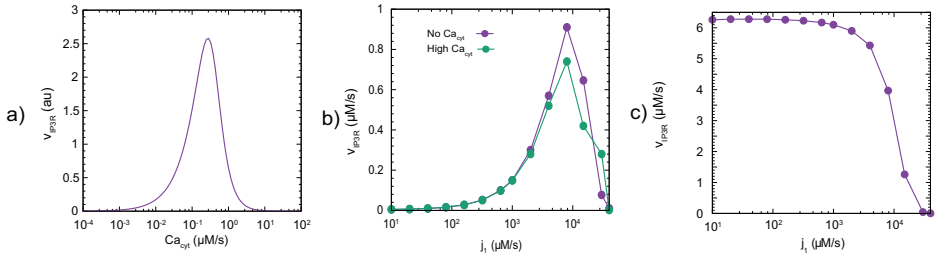

Figure 4.45: Influence of cytosolic Ca^{2+} on the dissociation of $IP_3R{\cdot}IP_3$. (a) Biphasic curve showing the addition of the cooperative binding model of Ca^{2+} to the model with a cooperativity of 2 in the inhibitory binding of Ca^{2+} to the IP_3R channel, and [IP3] = 2 μM. Based on the same calculations as in Fig. 4.44f. (b) Plots show Ca^{2+} outflow through the IP_3R from the ER with no Ca^{2+} influence on the IP_3R-IP_3 dissociation (dissociation kinetics: $k_{78} \cdot (IP_3R\text{-}IP_3)$), and with influence of high Ca^{2+} on the dissociation with the following kinetics: $k_{78} \cdot (IP_3R\text{-}IP_3)$ (1+ Ca^{2+}). The time step in the computations is given as $1.0 \cdot 10^{-2}$ s, phase 1 = $1.0 \cdot 10^{3}$ s, phase 2 = $9.0 \cdot 10^{3}$ s. Rate constants are given as: $k_1 = 1.0 \cdot 10^{-2}$ s^{-1}, $k_2 = 0.0$ s^{-1}, $k_3 = 5.0 \cdot 10^{4}$ s^{-1}, $k_4 = 1.2$ μM, $k_5 = 16.0$ μM^{-1} s^{-1}, $k_6 = 8.0 \cdot 10^{-3}$ μM/s, $k_7 = 1.0 \cdot 10^{-6}$ μM, $k_8 = 2.5$ μM^{-1} s^{-1}, $k_9 = 5.0$ s^{-1}, $k_{10} = 1.0 \cdot 10^{2}$ μM^{-1} s^{-1}, $k_{11} = 80.0$ s^{-1}, $k_{12} = 1.0 \cdot 10^{-2}$ μM^{-1} s^{-1}, $k_{13} = 1.0 \cdot 10^{-1}$ s^{-1}, $k_{14} = 0.0$ μM/s, $k_{15} = 0.0$ s^{-1}, $k_{16} = 0.0$ μM/s, $k_{17} = 0.0$ s^{-1}, $k_{18} = 0.0$ μM/s, $k_{19} = 0.0$ s^{-1}, $k_{20} = 1.0 \cdot 10^{3}$ μM/s, $k_{21} = 1.0$ s^{-1}, $k_{22} = 1.0 \cdot 10^{-4}$ μM, $k_{23} = 1.0 \cdot 10^{-2}$ s^{-1}, $k_{24} = 1.3 \cdot 10^{-5}$ μM, $k_{25} = 1.25 \cdot 10^{3}$ μM^{-1} s^{-1}, $k_{26} = 1.0 \cdot 10^{6}$ s^{-1}, $k_{27} = 1.2 \cdot 10^{-2}$ s^{-1}, $k_{28} = 0.0$ μM/s, $k_{29} = 0.0$ s^{-1}, $k_{30} = 0.0$ μM/s, $k_{31} = 1.0 \cdot 10^{2}$ s^{-1}, $k_{32} = 0.0$ μM/s, $k_{33} = 0.0$ s^{-1}, $k_{34} = 1.0 \cdot 10^{2}$ μM^{-1} s^{-1}, $k_{35} = 1.0 \cdot 10^{2}$ s^{-1}, $k_{36} = 0.0$ μM^{-1} s^{-1}, $k_{37} = 1.0 \cdot 10^{-2}$ μM, $k_{38} = 5.0 \cdot 10^{-1}$ s^{-1}, $k_{39} = 1.0 \cdot 10^{-2}$ μM, $k_{40} = 2.26 \cdot 10^{-1}$, $k_{41} = 7.94 \cdot 10^{-1}$, $k_{42} = 2.26 \cdot 10^{-1}$, $k_{43} = 7.94 \cdot 10^{-1}$, $k_{44} = 1.0$ μM/s, $k_{45} = 1.0$ s^{-1}, $k_{46} = 50.0$ μM^{-1} s^{-1}, $k_{47} = 1.0$ s^{-1}, $k_{48} = 2.0$, $k_{49} = 1.0$ s^{-1}, $k_{50} = 84.0$ μM^{-1} s^{-1}, $k_{51} = 8.4$ s^{-1}, $k_{52} = 10.0$ μM/s, $k_{53} = 1.0$ s^{-1}, $k_{54} = 10.0$ μM^{-1} s^{-1}, $k_{55} = 1.0$, $k_{56} = 1.0 \cdot 10^{-3}$ μM^{-1} s^{-1}, $k_{57} = 10.0$ s^{-1}, $k_{58} = 10.0$ μM/s, $k_{59} = 1.0$ s^{-1}, $k_{60} = 16.0$ μM^{-1} s^{-1}, $k_{61} = 8.0 \cdot 10^{-3}$ μM/s, $k_{62} = 1.0 \cdot 10^{-6}$ μM, $k_{63} = 1.0 \cdot 10^{5}$ s^{-1}, $k_{64} = 1.0 \cdot 10^{2}$ μM, $k_{65} = 0.0$ μM/s, $k_{66} = 0.0$ s^{-1}, $k_{67} = 1.0 \cdot 10^{-2}$ μM^{-1} s^{-1}, $k_{68} = 1.0 \cdot 10^{-1}$ s^{-1}, $k_{69} = 0.0$ μM/s, $k_{70} = 0.0$ s^{-1}, $k_{71} = 1.0$ μM^{-1} s^{-1}, $k_{72} = 1.0$ s^{-1}, $k_{73} = 10.0$ μM^{-1} s^{-1}, $k_{74} = 1.0 \cdot 10^{-7}$ μM, $k_{75} = 1.0$ μM/s, $k_{76} = 1.0$ s^{-1}, $k_{77} = 1.0$ μM^{-1} s^{-1}, $k_{78} = 1.0$ μM^{-1} s^{-1}. Initial conditions (in μM): $Ca^{2+}_{cyt} = 8.10976 \cdot 10^{-4}$, PMCA·M* = $3.25883 \cdot 10^{-1}$, $Ca^{2+}_{ext} = 1.0 \cdot 10^{3}$, M = $1.07015 \cdot 10^{2}$, M·Ca4 = $4.33933 \cdot 10^{-2}$, B = $9.98988 \cdot 10^{2}$, B·Ca4 = 1.01269, PMCA·M = $6.16508 \cdot 10^{-1}$, PMCA = $5.76095 \cdot 10^{-3}$, NCX·M* = $1.50566 \cdot 10^{-8}$, NCX·M = $9.14533 \cdot 10^{-3}$, NCX = $8.54584 \cdot 10^{-4}$, SERCA = $1.22012 \cdot 10^{3}$, $Ca^{2+}_{lum} = 1.0 \cdot 10^{3}$, L = $1.11111 \cdot 10^{3}$, L·Ca30 = $1.38890 \cdot 10^{3}$, S = 0.0, R = $1.0 \cdot 10^{2}$, R·S = 0.0, ARCC = 1.0, IP3R·IP3 = 10.0, IP3R = 2.0, IP3 = 5.0, STIM = $1.00798 \cdot 10^{-1}$, STIM·Ca = $1.00798 \cdot 10^{2}$, SOCC = 1.0.(c) Plot show a first-order influence of $IP_3R{\cdot}IP_3$ dissociation by Ca^{2+}, where low $Ca^{2+}{}_{cyt}$ leads to low $IP_3R{\cdot}IP_3$ dissociation, with the following kinetics: $k_{78} \cdot (IP_3R{\cdot}IP_3) \cdot Ca^{2+}$. Same rate constants as in panel b.

[143]. There is no vast difference in whether Ca^{2+} has no influence on the dissociation of $IP_3R{\cdot}IP_3$ or if only high concentrations of Ca^{2+} influences this dissociation. In Fig. 4.45c the plot shows how an influence of cytosolic Ca^{2+} activating the dissociation of $IP_3R{\cdot}IP_3$ influences the rate of Ca^{2+} transport through the IP_3R channel. In this case lower concentrations of Ca^{2+} in the cytosol (represented by a low j_1) influences the outflow through IP_3R such that the bell-shaped transport rate disappears. This transport profile through IP_3R does not compare well to experiments since there are low transport rates at low cytosolic Ca^{2+} concentrations. Based on the profile of the curves given in Fig. 4.45b either of these could explain the way Ca^{2+} could have an influence on the dissociation of $IP_3R{\cdot}IP_3$.

Plots in Fig. 4.45 is based on a number of calculations with vIP_3R vs. cytosolic Ca^{2+} which are given in Table 4.1.

j_1 (μM/s)	Ca^{2+}_{cyt}	j_{IP3R} (μM/s) (No Ca^{2+} influence)	j_{IP3R} (μM/s) (1+Ca^{2+})	j_{IP3R} (μM/s) (1.order Ca^{2+} influence)
10	$8.0{\cdot}10^{-4}$	$5.1{\cdot}10^{-3}$	$5.1{\cdot}10^{-3}$	6.26
20	$1.1{\cdot}10^{-3}$	$6.6{\cdot}10^{-3}$	$6.6{\cdot}10^{-3}$	6.28
40	$1.5{\cdot}10^{-3}$	$9.6{\cdot}10^{-3}$	$9.6{\cdot}10^{-3}$	6.28
80	$2.5{\cdot}10^{-3}$	$1.6{\cdot}10^{-2}$	$1.6{\cdot}10^{-2}$	6.28
160	$4.4{\cdot}10^{-3}$	$2.7{\cdot}10^{-2}$	$2.7{\cdot}10^{-2}$	6.26
320	$8.3{\cdot}10^{-3}$	$5.2{\cdot}10^{-2}$	$5.1{\cdot}10^{-2}$	6.23
640	$1.6{\cdot}10^{-2}$	$1.0{\cdot}10^{-1}$	$9.8{\cdot}10^{-2}$	6.17
1000	$2.5{\cdot}10^{-2}$	$1.5{\cdot}10^{-1}$	$1.49{\cdot}10^{-1}$	6.1
2000	$5.1{\cdot}10^{-2}$	$3.0{\cdot}10^{-1}$	$2.8{\cdot}10^{-1}$	5.9
4000	$1.05{\cdot}10^{-1}$	$5.7{\cdot}10^{-1}$	$5.2{\cdot}10^{-1}$	5.43
8000	$2.3{\cdot}10^{-1}$	$9.1{\cdot}10^{-1}$	$7.4{\cdot}10^{-1}$	3.97
$1.5{\cdot}10^{4}$	$5.1{\cdot}10^{-1}$	$6.46{\cdot}10^{-1}$	$4.2{\cdot}10^{-1}$	1.26
$3.0{\cdot}10^{4}$	1.8	$7.7{\cdot}10^{-2}$	$2.8{\cdot}10^{-1}$	$4.29{\cdot}10^{-2}$
$4.0{\cdot}10^{4}$	4.8	$1.1{\cdot}10^{-2}$	$1.9{\cdot}10^{-2}$	$2.34{\cdot}10^{-3}$

Table 4.1: j_{IP3R} with different Ca^{2+} influences. j_1 is the inflow of external Ca^{2+} into the cytosol. Rate constants and initial conditions as in Fig. 4.45.

Other than the variation in kinetics describing the Ca^{2+} influence of the IP_3R-IP_3 dissociation, the only parameter that has been changed is k_1, which represent the rate of inflow of external Ca^{2+} into the cell. In table 4.1 j_1 can be seen as this change as $j_1 = k_1 \cdot Ca^{2+}_{ext}$.

The Arachidonic Acid Regulated Ca^{2+} Channels (ARCC)

ARC channels have also been added to the model, however not implemented. This is represented in the overview figure Fig. 4.32 in grey color. In this model they are added as a simple agonist-induced channel for Ca^{2+} entry in addition to the simple Ca^{2+} leak through the PM represented by k_1 and the store-dependent capacitative Ca^{2+} entry represented by SOCC. This pathway for Ca^{2+} entry is a relatively new discovery of agonist-induced Ca^{2+} entry. SOCC has been discovered and researched longer, and was thought to be the responsible entry pathway for replenishing Ca^{2+} following agonist induced oscillations following store depletion of the intracellular stores, mainly the ER [157].

ARCCs are activated by arachidonic acid in an intracellular site. Exogenous administration of low concentrations of arachidonic acid is found to induce Ca^{2+} entry to the cytosol without detectable depletion of intracellular stores. ARCCs have been found to be biophysically similar to SOCC as they both consist of Orai-proteins and are both activated by STIM1. However, the STIM which activate ARCC is found in the PM, and it has been found that a small portion of the cellular STIM concentration reside there. A more inclusive role of ARCC could also be investigated further with the model, as it has been suggestions that at low-agonist induced oscillations, the ER is not depleted in such a manner that it would induce SOCE [157]. SOCE as the main Ca^{2+} entry pathway during sustained Ca^{2+} oscillations is well supported [46, 158, 159]. There have however been proposed a valid question as to whether ARCC could be involved in this in a store-independent manner with agonist induced oscillatory conditions [157]. As depletion of more than $\sim$ 35-40 % is needed in order for STIM1 oligomerization and translocation in order for activation of SOCC, this seems to be contradicted with findings from pancreatic acinar cells where only 2-3 % of Ca^{2+} is depleted at the peak of each oscillation [157]. However, a good argument to this could be that STIM2 is in contrast to STIM1 activated at resting and only low depletion conditions of the ER [46, 78]. STIM2 knockdown is not found to affect oscillations however, but STIM1 was shown to be involved in Ca^{2+} entry following knockdown [158]. This was suggested to be explained by STIM1 being activated by a transient depletion of the ER by these agonist-induced oscillations, which would lead to its activation of SOCC [158]. Shuttleworth [157] points out that as it has been discovered that ARCC also consist of Orai1 proteins like in SOCC as well as being activated by STIM1 in the PM, as opposed to in the

ER membrane, a knockdown experiment of these would not be conclusive of a store-operated Ca^{2+} entry being responsible. As this suggests, there are still much to be discovered and researched regarding Ca^{2+} entry and regulation both during signalling events and otherwise.

4.3.6 Model oscillations

As mentioned initially, cytosolic Ca^{2+} oscillations were observed using the model. Sustained oscillations were obtained from the interaction between cytosolic Ca^{2+}, PMCA/NCX, capacitiative Ca^{2+} entry and CICR through IP_3R. We found that the parameters affecting the period length of the oscillations are mostly the Ca^{2+} inflow rate through the plasma membrane (k_1 or others), the set-point for luminal Ca^{2+} (in the ER: k_{20} and k_{21}) and the turnover numbers of SERCA (k_{23}) and IP_3R (k_{38}). This is under an IP_3 independent oscillatory condition. Models are generally classified either as either being IP_3 independent or IP_3 dependent [46, 92]. With a IP_3 dependent oscillatory condition (with $IP_3R{\cdot}IP_3$ dissociation and formation), also different levels of IP_3 can influence the period length. It is also expected that kinetics and mechanisms of other control species in the model can also affect the oscillations. The oscillations have been observed in both the ultradian (2 s) and circadian range (up to 30 h). Examples of oscillations with different period lengths are given in Fig. 4.46.

In this model the oscillations that are generated are not local but rather global events in the sense that the cytosolic Ca^{2+} oscillations represent the whole cytosolic concentration. We know that there are oscillations in certain locations of the cell and that this has a function for signaling purposes. The plots in Fig. 4.46 also show that different fluxes and concentrations oscillate together with the oscillating Ca^{2+} concentration. The oscillations in our deterministic model are regular, and we assume that they have a limit cycle. Calcium oscillations are often modeled using stochastic models, and even if different cells with different densities of IP_3R respond different to stimulus, they way they respond to a change in stimulus seems to result in a similar relative change. Since different cells respond similarly to this change in stimuli, the physiological response is also the same [155]. Further work needs to be done in order to investigate other factors that could contribute to Ca^{2+} oscillations in the cell. It is nevertheless interesting that the model can demonstrate oscillations with such variable period lengths.

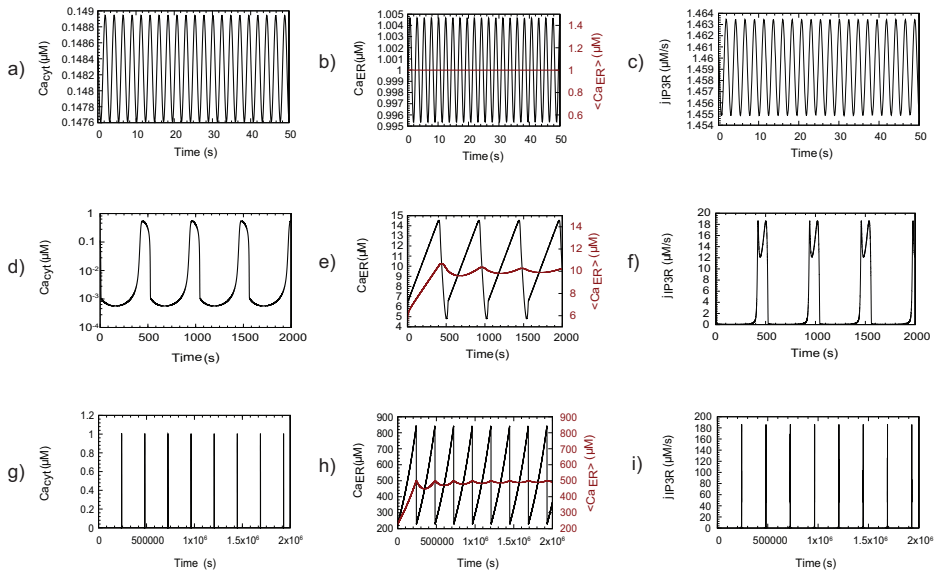

Figure 4.46: Oscillations with different period lengths. Plots a-i show examples of oscillations observed in the model displaying different period lengths. a-c, d-f and g-i shows oscillations of cytosolic Ca^{2+}, luminal Ca^{2+} and j_{IP3R} with a period of 2.35 seconds, 8.6 minutes, and 30.5 hours respectively. The split peak observed in panel f occurs because of the bell-shaped curve of the channel activity dependency of Ca^{2+}. Rate constants are the same as Fig. 4.45, except for the following: (a)-(c): $k_1 = 1.0 \cdot 10^{-3}$ s^{-1}, $k_3 = 5.0 \cdot 10^3$ s^{-1}, $k_{20} = 10.0$ μM/s, $k_{21} = 10.0$ s^{-1}, $k_{22} = 1.0 \cdot 10^{-7}$ μM, $k_{23} = 80.0$ s^{-1}, $k_{24} = 1.0 \cdot 10^{-2}$ μM, $k_{27} = 1.0 \cdot 10^{-1}$ s^{-1}, $k_{31} = 1.0$ s^{-1}, $k_{38} = 10.0$ s^{-1}, $k_{40} = 2.24 \cdot 10^{-1}$, $k_{48} = 1.0$, $k_{52} = 0.0$ μM/s, $k_{53} = 0.0$ s^{-1}, $k_{56} = 0.0$ μM^{-1} s^{-1}, $k_{58} = 0.0$ μM/s, $k_{59} = 0.0$ s^{-1}, $k_{69} = 1.0 \cdot 10^3$ μM/s, $k_{70} = 1.0$ s^{-1}, $k_{71} = 10.0$ μM^{-1} s^{-1}, $k_{72} = 9.6 \cdot 10^2$ s^{-1}, $k_{73} = 1.0 \cdot 10^{-4}$ μM^{-1} s^{-1}, $k_{77} = 0.0$ μM^{-1} s^{-1}, $k_{78} = 0.0$ μM^{-1} s^{-1}. (d)-(f): same as a-c except increase in $k_{20} = 1.0 \cdot 10^2$ μM/s, decreased $k_{23} = 1.0 \cdot 10^{-2}$ s^{-1}, and increase in $k_{38} = 1.0 \cdot 10^2$ s^{-1}. (g)-(i): same as a-c except increase in $k_{20} = 5.0$ μM/s, decreased $k_{23} = 1.0 \cdot 10^{-2}$ s^{-1}, and increase in $k_{38} = 1.0 \cdot 10^3$ s^{-1}. Less increase in k_{20} compared to (a)-(c) than in the condition with 8.6 min oscillations, however k_{38} is one order of magnitude larger.

4.3.7 Calcium in disease

As previously addressed, Ca^{2+} is an ubiquitous and important signaling ion and its regulation is of extreme importance in order to maintain normal cellular conditions. So, what happens when there is a dysregulation of cytosolic Ca^{2+}? There are many diseases and conditions that are associated with abnormalities in the homeostatic machinery of cytosolic Ca^{2+} ranging from cancers, neurodegenerative diseases and other diseases related to the heart, skin and more [160, 161, 162, 163]. Notably, Ca^{2+} signals are found in several studies to promote progression of different types of cancer, in processes like proliferation and migration, such as in breast cancer, ovarian cancer, prostate cancer, colorectal cancer and gliomal cancer [74, 160].

Several channels, pumps and transporters involved in Ca^{2+} regulation have been associated with different types of cancer. In different types of diseases, these pumps and channels are either overexpressed or downregulated which could lead to either evasion of apoptosis, or enhancement of cell proliferation [161]. Other changes could be the localization in the cell, or even expression of other isoforms than the non-cancerous cell equivalents [74]. In fact, targeting these channels or pumps have been used in clinical practice in clinical trials for many different types of cancers as potential targets for new anticancer drugs [160, 161]. Some of these behaviors is the activation of the transcription factor STAT3 which is related to activation of immunosupression related genes. In this case, blocking Ca^{2+} signals could possibly be a strategy in increasing the antitumor immune response [160]. For instance, breast cancer cell line mRNAs (and in some cases also protein) of Orai1, Orai3 and PMCA2 have been found to be upregulated [74]. Ca^{2+} channels such as SOCCs, VOCCs and TRPs have also been associated with the regulation of epithelial-mesenchymal transition (EMT) in, for instance, breast cancer, where the use of channel blockers have been researched as therapeutic strategies [160]. Inhibition of SOCE was also shown to have positive effects with respect to antitumor effects in colorectal cancer [160].

Neurodegenerative diseases like Alzheimers disease, Amyotrophic Lateral Sclerosis (ALS), Huntingtons disease and Parkinsons disease have also been associated with abnormal Ca^{2+} signaling and dysregulation of cytosolic Ca^{2+} homeostasis [162, 164]. In normal aging a change in neuronal Ca^{2+} signaling also occur, for instance by reduction in the number of Ca^{2+} binding proteins and also by the impairment of mitochondria. Compared to neurodegenerative diseases, these changes are less critical, but could also be

making the neurons more vulnerable to these diseases [164]. A large portion of people suffering from dementia are diagnosed with having Alzheimers disease, characterized by the progressive loss of neurons. Magi et al. [162] suggests that manipulating NCX could have a potentially important effect in preventing neuronal degeneration and cell death. As there are so many indicators pointing to Ca^{2+} regulation having a role in diseases, potential drug targets could be found among these Ca^{2+} blockers. The possibility of using computational models as a guide and a helpful tool could also aid in the work on understanding more about these functions.

Chapter 5

Conclusion and Future Perspectives

This thesis presents studies of homeostatic mechanisms and regulatory aspects of biological systems. The controller motifs applied in the work can be arranged according to biological feedback with different kinetic requirements. Mathematical models were developed and used in order to perform calculations which could be compared to/or utilized to investigate physiologically relevant data. In the first study presented, iron homeostasis in non-graminaceous plants was investigated using the set-up of an inflow controller and implementing auxiliary feedback which resulted in improvement in response time of the system. The model is in compliance with experimental data, and we have suggested that the transcription factor FIT is involved in the degradation of the iron transporter IRT1. As iron is an essential nutrient not only for plants, but also for humans, a biofortification strategy in conditions of low environmental iron was also discussed. The next two parts of the study are tied together in highlighting and investigating the homeostasis and regulatory mechanisms of cytosolic Ca^{2+}. First, the concept of homeostasis was suggested to be expanded to include oscillatory conditions as biological oscillators were studied applying controller motif set-ups. The study show that even during oscillatory conditions the set-point can be achieved as an average, which is done by applying compensatory mechanisms as frequency and amplitude modulation. Since cytosolic Ca^{2+} is such an ubiquitous and important signaling ion and is regulated at a very low resting level, it was used as an example for this type of model. Calcium will also oscillate in cells during signaling events, and both frequency and amplitude modulation has been described as means in this signaling process. A simple model was made in order to describe cytosolic Ca^{2+} oscillations based on an outflow controller. The model is based on a very simplistic view of Ca^{2+} regulation and shows that robust

homeostasis can be achieved with frequency modulation. However, as cytosolic Ca^{2+} regulation and homeostasis is such a complex system, we wanted to further investigate and study this in order to learn more about the regulatory aspects involved. We based the model on cytosolic Ca^{2+} in non-excitable cells, and even though the focus was not on oscillations we have included a brief example that certain interactions of components can lead to sustained oscillations with a surprising variability in the period. From a simple two-component model of cytosolic Ca^{2+} and PMCA, an integrative model was built up step by step including several inflow and outflow mechanisms, the ER, capacitative Ca^{2+} entry and Ca^{2+} induced Ca^{2+} release. The model has been developed using biologically relevant kinetic values (as they were available), and has been compared to and used to analyze regulatory mechanisms in the Ca^{2+} homeostasis machinery. We can describe that during pertubations and signaling events the set-point of Ca^{2+} is shifted, which fits with experimental data. Hysteretic behavior in the PMCA has been studied and seem to fit well with experimental data. A dicalcic model, similar to the diprotic model, is presented with regards to the IP_3R regulation. Also a cooperativity in the Ca^{2+} dependency of the Ca^{2+} induced Ca^{2+} release is also suggested. As with all models there are certain limitations. Modeling is a great tool in trying to describe regulatory systems and mechanisms in biology. The model of cytosolic Ca^{2+} for instance describes the cell as a whole, with no spatial variation. Many mechanisms are added, but there are also some organelles and mechanisms that are simplified or not included as such is needed in order to simplify a model. Many aspects of Ca^{2+} signaling occur in local cell areas and changes in concentration may not be globally within the cell. Even though there are limitations, a model is useful in that is can highlight and make suggestions to the physiological mechanisms that can be difficult to study in a cell by experiments. It can also be used as a tool in order to predict outcomes and investigate how systems behave in addition to the experimental investigations.

5.1 Future perspectives

Mathematical modelling has already been widely used. Certainly the application of mathematical modeling would be suggested to have an increasingly important role in the future. The whole world is developing into a more digital and computer based global society and it is only natural that

also the area of biology will continue to follow. Maintaining homeostasis is so important in order for normal functionality that it will still need further investigations in order to build our understanding of it. Evolving our knowledge on adaptation and regulation of different systems will aid in order to help answer questions involving diseases and other issues. Using models in order to describe, suggest, test and predict outcomes of experimental work is of great value as it can often be done more rapidly. With the work on iron, different biofortification approaches would be of interest as there is a vast part of people in not only developing countries, but also industrial countries, that suffer from iron deficiency anaemia. However, there are still many ethical questions, for instance concerning GMO that several countries are sceptical of in terms of environmental and longterm consequences. There are biofortification strategies that are more conventional and does not involve genetic engineering, however genetic modification hold several opportunities that could assist in this important global concern. With regard to the model of cytosolic Ca^{2+} homeostasis and cytosolic Ca^{2+} regulation, the model could be developed even further. Oscillations have only briefly been addressed here and observed in some conditions. This will need to be studied and investigated in more detail, as further development of the model. As we have only included the ER as a storage organelle for Ca^{2+}, there are other organelles like the mitochondria that was not included. It would be very interesting to use the model to describe certain disease conditions as dysregulation in cytosolic Ca^{2+} has been found to be involved in everything from cancers to neurodegenerative diseases. As some of these involve excitable cells, the model could be expanded to include voltage operated Ca^{2+} channels (VOCCs) and other regulatory mechanisms involved in these types of cells or of a specific cell type. Perhaps model calculations could be performed in order to see if other regulatory species could be utilized in the absence of others, which is sometimes the case in these diseases. The presented model could be used as a starting point for improving and adding more parameters, or with a specific research question in mind in order to narrow and specialize for that objective.

Bibliography

[1] Cannon, W. B. (1929) Organization for Physiological Homeostasis. *Physiological Reviews* **9**, 399–431.

[2] Langley, L. L. (1973) *Homeostasis: Origins of the Concept.* (Dowden Hutchinson and Ross) Vol. 1.

[3] Cooper, S. J. (2008) From Claude Bernard to Walter Cannon. Emergence of the concept of homeostasis. *Appetite* **51**, 419–427.

[4] Guthrie, W. K. C. (1969) *A History of Greek Philosophy: Volume 2, The Presocratic Tradition from Parmenides to Democritus.* (Cambridge University Press) Vol. 2.

[5] Boylan, M. (2009) Hippocrates (`http://www.iep.utm.edu/hippocra/`). ISSN 2161-0002. First accessed: 2017-05-08. Last checked: 2022-01-29.

[6] Hunter, J. (1837) The Works of John Hunter, F.R.S.; with Notes. *Br Foreign Med Rev.* **4**, 75–87.

[7] Schulkin, J. (2003) Rethinking homeostasis. *Allostatic Regulation in Physiology and Pathology, MIT Press, Cambridge, MA.*

[8] Mrosovsky, N. (1990) *Rheostasis: The Physiology of Change.* (Oxford University Press).

[9] Schmidt-Nielsen, K. (1991) Regulated change. *Nature* **349**, 750–751.

[10] Sterling, P & Eyer, J. (1988) Allostasis: A New Paradigm to Explain Arousal Pathology. *Handbook of Life stress, Cognition and Health.*

[11] Lloyd, D, Aon, M. A, & Cortassa, S. (2001) Why homeodynamics, not homeostasis? *The Scientific World Journal* **1**, 133–145.

[12] Woods, S. C & Ramsay, D. S. (2007) Homeostasis: Beyond Curt Richter. *Appetite* **49**, 388–398.

[13] Trewavas, A. (2006) A Brief History of Systems Biology. *The Plant Cell* **18**, 2420–2430.

[14] von Bertalanffy, L. (1950) An Outline of General System Theory. *British Journal for the Philosophy of Science* **1**, 134–165.

[15] Wiener, N. (1961) *Cybernetics or Control and Communication in the Animal and the Machine.* (MIT press) Vol. 25.

[16] Wiener, N. (1988) *The Human Use of Human Beings: Cybernetics and Society.* (Perseus Books Group) No. 320.

[17] Kotas, M. E & Medzhitov, R. (2015) Homeostasis, Inflammation, and Disease Susceptibility. *Cell* **160**, 816–827.

[18] Ingalls, B. P. (2013) *Mathematical Modeling in Systems Biology: An Introduction*. (MIT press).

[19] Goodwin, B. C. (1963) *Temporal Organization in Cells*. (Academic Press).

[20] Åström, K. J & Murray, R. M. (2010) *Feedback Systems: An Introduction for Scientists and Engineers*. (Princeton University Press), pp. 1–26.

[21] Hoagland, M. B & Dodson, B. (1995) *The Way Life Works*. (Times Books).

[22] Thomas, R, Thieffry, D, & Kaufman, M. (1995) Dynamical behaviour of biological regulatory networks. i. biological role of feedback loops and practical use of the concept of the loop-characteristic state. *Bulletin of Mathematical Biology* **57**, 247–276.

[23] Franck, U. (1980) Feedback kinetics in physicochemical oscillators. *Berichte der Bunsengesellschaft für physikalische Chemie* **84**, 334–341.

[24] Drengstig, T, Ni, X, Thorsen, K, Jolma, I, & Ruoff, P. (2012) Robust Adaptation and Homeostasis by Autocatalysis. *The Journal of Physical Chemistry B* **116**, 5355–5363.

[25] Thorsen, K, Agafonov, O, Selstø, C. H, Jolma, I. W, Ni, X. Y, Drengstig, T, & Ruoff, P. (2014) Robust Concentration and Frequency Control in Oscillatory Homeostats. *PLoS ONE* **9**, e107766.

[26] Briat, C, Zechner, C, & Khammash, M. (2016) Design of a Synthetic Integral Feedback Circuit: Dynamic Analysis and DNA Implementation. *ACS Synthetic Biology* **5**, 1108–1116.

[27] Drengstig, T, Jolma, I. W, Ni, X. Y, Thorsen, K, Xu, X. M, & Ruoff, P. (2012) A Basic Set of Homeostatic Controller Motifs. *Biophysical Journal* **103**, 2000–2010.

[28] Drengstig, T, Ueda, H. R, & Ruoff, P. (2008) Predicting Perfect Adaptation Motifs in Reaction Kinetic Networks. *The Journal of Physical Chemistry B* **112**, 16752–16758.

[29] Ni, X. Y, Drengstig, T, & Ruoff, P. (2009) The Control of the Controller: Molecular Mechanisms for Robust Perfect Adaptation and tTmperature Compensation. *Biophysical Journal* **97**, 1244–1253.

[30] Jolma, I. W, Ni, X. Y, Rensing, L, & Ruoff, P. (2010) Harmonic Oscillations in Homeostatic Controllers: Dynamics of the p53 Regulatory System. *Biophysical Journal* **98**, 743–752.

[31] Haugen, F. (2012) *Reguleringsteknikk*. (Trondheim: Akademika Forlag), pp. 25–28.

[32] Alon, U, Surette, M. G, Barkai, N, & Leibler, S. (1999) Robustness in bacterial chemotaxis. *Nature* **397**, 168.

[33] Yi, T.-M, Huang, Y, Simon, M. I, & Doyle, J. (2000) Robust perfect adaptation in bacterial chemotaxis through integral feedback control. *Proceedings of the National Academy of Sciences* **97**, 4649–4653.

[34] Briat, C, Gupta, A, & Khammash, M. (2016) Antithetic Integral Feedback Ensures Robust Perfect Adaptation in Noisy Biomolecular Networks. *Cell Systems* **2**, 15–26.

[35] Saunders, P. T, Koeslag, J. H, & Wessels, J. A. (1998) Integral Rein Control in Physiology. *Journal of Theoretical Biology* **194**, 163–173.

[36] El-Samad, H, Goff, J, & Khammash, M. (2002) Calcium Homeostasis and Parturient Hypocalcemia: An Integral Feedback Perspective. *Journal of Theoretical Biology* **214**, 17–29.

[37] Ang, J & McMillen, D. R. (2013) Physical Constraints on Biological Integral Control Design for Homeostasis and Sensory Adaptation. *Biophysical Journal* **104**, 505–515.

[38] Marks, F, Klingmüller, U, & Müller-Decker, K. (2017) *Cellular Signal Processing: An Introduction to the Molecular Mechanisms of Signal tTansduction.* (Garland Science).

[39] Bunning, E. (1967) *The Physiological Clock.* (Springer).

[40] Dunlap, J. C. (1999) Molecular Bases for Circadian Clocks. *Cell* **96**, 271–290.

[41] Kruse, K & Jülicher, F. (2005) Oscillations in cell biology. *Current Opinion in Cell Biology* **17**, 20–26.

[42] Geva-Zatorsky, N, Rosenfeld, N, Itzkovitz, S, Milo, R, Sigal, A, Dekel, E, Yarnitzky, T, Liron, Y, Polak, P, Lahav, G, et al. (2006) Oscillations and variability in the p53 system. *Molecular Systems Biology* **2**.

[43] Lahav, G. (2008) in *Cellular Oscillatory Mechanisms.* (Springer), pp. 28–38.

[44] Berridge, M. J & Galione, A. (1988) Cytosolic calcium oscillators. *The FASEB Journal* **2**, 3074–3082.

[45] Uhlén, P & Fritz, N. (2010) Biochemistry of calcium oscillations. *Biochemical and Biophysical Research Communications* **396**, 28–32.

[46] Dupont, G, Combettes, L, Bird, G. S, & Putney, J. W. (2011) Calcium oscillations. *Cold Spring Harbor Perspectives in Biology* **3**, 1–18.

[47] Boulware, M. J & Marchant, J. S. (2008) Timing in Cellular Ca^{2+} signaling. *Current Biology* **18**, R769–R776.

[48] Gordo, A. C, Rodrigues, P, Kurokawa, M, Jellerette, T, Exley, G. E, Warner, C, & Fissore, R. (2002) Intracellular Calcium Oscillations Signal Apoptosis Rather than Activation in In Vitro Aged Mouse Eggs. *Biology of Reproduction* **66**, 1828–1837.

[49] Gonze, D & Ruoff, P. (2020) The Goodwin Oscillator and its Legacy. *Acta Biotheoretica* pp. 1–18.

[50] Goldbeter, A. (1997) *Biochemical Oscillations and Cellular Rhythms: The Molecular Bases of Periodic and Chaotic Behaviour.* (Cambridge University Press).

[51] Gonze, D & Abou-Jaoudé, W. (2013) The Goodwin Model: Behind the Hill Function. *PLoS ONE* **8**, e69573.

[52] Goodwin, B. C. (1965) Oscillatory Behavior in Enzymatic Control Processes. *Advances in Enzyme Regulation* **3**, 425–437.

[53] Ruoff, P, Vinsjevik, M, Monnerjahn, C, & Rensing, L. (1999) The Goodwin Oscillator: On the Importance of Degradation Reactions in the Circadian Clock. *Journal of Biological Rhythms* **14**, 469–479.

[54] Jeong, J, Cohu, C, Kerkeb, L, Pilon, M, Connolly, E. L, & Guerinot, M. L. (2008) Chloroplast Fe (III) chelate reductase activity is essential for seedling viability under iron limiting conditions. *Proceedings of the National Academy of Sciences* **105**, 10619–10624.

[55] Bienfait, H. (1988) Mechanisms in Fe-efficiency reactions of higher plants. *Journal of Plant Nutrition* **11**, 605–629.

[56] Vert, G, Grotz, N, Dédaldéchamp, F, Gaymard, F, Guerinot, M. L, Briat, J.-F, & Curie, C. (2002) IRT1, an Arabidopsis Transporter Essential for Iron Uptake from the Soil and for Plant Growth. *The Plant Cell* **14**, 1223–1233.

[57] Kobayashi, T & Nishizawa, N. K. (2012) Iron Uptake, Translocation, and Regulation in Higher Plants. *Annual Review of Plant Biology* **63**, 131–152.

[58] Colangelo, E. P & Guerinot, M. L. (2004) The Essential Basic Helix-Loop-Helix Protein FIT1 Is Required for the Iron Deficiency Response. *The Plant Cell* **16**, 3400–3412.

[59] Römheld, V & Marschner, H. (1986) Evidence for a Specific Uptake System for Iron Phytosiderophores in Roots of Grasses. *Plant Physiology* **80**, 175–180.

[60] Marschner, H & Römheld, V. (1994) Strategies of plants for acquisition of iron. *Plant and Soil* **165**, 261–274.

[61] Connorton, J. M, Balk, J, & Rodríguez-Celma, J. (2017) Iron homeostasis in plants–a brief overview. *Metallomics* **9**, 813–823.

[62] Connolly, E. L, Fett, J. P, & Guerinot, M. L. (2002) Expression of the IRT1 Metal Transporter Is Controlled by Metals at the Levels of Transcript and Protein Accumulation. *The Plant Cell* **14**, 1347–1357.

[63] Varotto, C, Maiwald, D, Pesaresi, P, Jahns, P, Salamini, F, & Leister, D. (2002) The metal ion transporter IRT1 is necessary for iron homeostasis and efficient photosynthesis in Arabidopsis thaliana. *The Plant Journal* **31**, 589–599.

[64] Yuan, Y, Wu, H, Wang, N, Li, J, Zhao, W, Du, J, Wang, D, & Ling, H.-Q. (2008) FIT interacts with AtbHLH38 and AtbHLH39 in regulating iron uptake gene expression for iron homeostasis in Arabidopsis. *Cell Research* **18**, 385.

[65] Sivitz, A. B, Hermand, V, Curie, C, & Vert, G. (2012) Arabidopsis bHLH100 and bHLH101 Control Iron Homeostasis via a FIT-Independent Pathway. *PLoS ONE* **7**, e44843.

[66] Lanquar, V, Lelièvre, F, Bolte, S, Hamès, C, Alcon, C, Neumann, D, Vansuyt, G, Curie, C, Schröder, A, Krämer, U, et al. (2005) Mobilization of vacuolar iron by AtNRAMP3 and AtNRAMP4 is essential for seed germination on low iron. *The EMBO Journal* **24**, 4041–4051.

[67] Agafonov, O, Selstø, C. H, Thorsen, K, Xu, X. M, Drengstig, T, & Ruoff, P. (2016) The Organization of Controller Motifs Leading to Robust Plant Iron Homeostasis. *PLoS ONE* **11**, e0147120.

[68] Campbell, A. K. (1983) *Intracellular Calcium, its Universal Role as Regulator.* (Wiley).

[69] Campbell, A. K. (2015) *Intracellular Calcium.* (Wiley).

[70] Carafoli, E. (2002) Calcium signaling: A tale for all seasons. *Proceedings of the National Academy of Sciences* **99**, 1115–1122.

[71] Ringer, S. (1883) A further Contribution regarding the influence of the different Constituents of the Blood on the Contraction of the heart. *The Journal of Physiology* **4**, 29–42.

[72] Shuttleworth, T. J, Thompson, J. L, & Mignen, O. (2004) ARC Channels: A Novel Pathway for Receptor-Activated Calcium Entry. *Physiology* **19**, 355–361.

[73] Dong, Z, Saikumar, P, Weinberg, J. M, & Venkatachalam, M. A. (2006) Calcium in cell injury and death. *Annu. Rev. Pathol. Mech. Dis.* **1**, 405–434.

[74] Monteith, G. R, Davis, F. M, & Roberts-Thomson, S. J. (2012) Calcium Channels and Pumps in Cancer: Changes and Consequences. *Journal of Biological Chemistry* **287**, 31666–31673.

[75] Brini, M & Carafoli, E. (2011) The Plasma Membrane Ca^{2+} ATPase and the Plasma Membrane Sodium Calcium Exchanger Cooperate in the Regulation of Cell Calcium. *Cold Spring Harbor Perspectives in Biology* **3**, 1–15.

[76] Thompson, J. L, Mignen, O, & Shuttleworth, T. J. (2013) The ARC channel – An Endogenous Store-Independent Orai Channel. *Current Topics in Membranes* **71**, 125–148.

[77] Liou, J, Kim, M. L, Do Heo, W, Jones, J. T, Myers, J. W, Ferrell Jr, J. E, & Meyer, T. (2005) STIM Is a Ca^{2+} Sensor Essential for Ca^{2+}-Store-Depletion-Triggered Ca^{2+} Influx. *Current Biology* **15**, 1235–1241.

[78] Brandman, O, Liou, J, Park, W. S, & Meyer, T. (2007) STIM2 Is a Feedback Regulator that Stabilizes Basal Cytosolic and Endoplasmic Reticulum Ca^{2+} Levels. *Cell* **131**, 1327–1339.

[79] Goto, Y, Miura, M, & Iijima, T. (1996) Extrusion mechanisms of intracellular Ca^{2+} in human aortic endothelial cells. *European Journal of Pharmacology* **314**, 185–192.

[80] Di Leva, F, Domi, T, Fedrizzi, L, Lim, D, & Carafoli, E. (2008) The plasma membrane Ca^{2+} ATPase of animal cells: Structure, function and regulation. *Archives of Biochemistry and Biophysics* **476**, 65–74.

[81] Carafoli, E. (2016) The Plasma Membrane Calcium ATPase: Historical Appraisal and Some New Concepts. *Regulation of Ca^{2+}-ATPases, V-ATPases and F-ATPases* pp. 3–11.

[82] Mandal, A, Liyanage, M. R, Zaidi, A, & Johnson, C. K. (2008) Interchange of autoinhibitory domain conformations in plasma-membrane Ca^{2+}-ATPase–calmodulin complexes. *Protein Science* **17**, 555–562.

[83] Niggli, V, Adunyah, E, & Carafoli, E. (1981) Acidic Phospholipids, Unsaturated Fatty Acids, and Limited Proteolysis Mimic the Effect of Calmodulin on the Purified Erythrocyte Ca^{2+}-ATPase. *Journal of Biological Chemistry* **256**, 8588–8592.

[84] Schwaller, B. (2010) Cytosolic Ca^{2+} Buffers. *Cold Spring Harbor Perspectives in Biology* **2**, a004051.

[85] Wang, C.-L. A. (1985) A note on Ca^{2+} binding to calmodulin. *Biochemical and Biophysical Research Communications* **130**, 426–430.

[86] Persechini, A & Stemmer, P. M. (2002) Calmodulin Is a Limiting Factor in the Cell. *Trends in Cardiovascular Medicine* **12**, 32–37.

[87] Yu, R & Hinkle, P. M. (2000) Rapid turnover of calcium in the endoplasmic reticulum during signaling: Studies with cameleon calcium indicators. *Journal of Biological Chemistry* **275**, 23648–23653.

[88] Taylor, C. W & Tovey, S. C. (2010) IP3 Receptors: Toward Understanding Their Activation. *Cold Spring Harbor Perspectives in Biology* **2**, 1–22.

[89] Bezprozvanny, I, Watras, J, & Ehrlich, B. E. (1991) Bell-shaped calcium-response curves of Ins(1,4,5)P3- and calcium-gated channels from endoplasmic reticulum of cerebellum. *Nature* **351**, 751.

[90] Woods, N. M, Cuthbertson, K. R, & Cobbold, P. H. (1986) Repetitive transient rises in cytoplasmic free calcium in hormone-stimulated hepatocytes. *Nature* **319**, 600.

[91] Berridge, M. J. (1993) Inositol trisphosphate and calcium signalling. *Nature* **361**, 315.

[92] Sneyd, J, Tsaneva-Atanasova, K, Reznikov, V, Bai, Y, Sanderson, M, & Yule, D. (2006) A method for determining the dependence of calcium oscillations on inositol trisphosphate oscillations. *Proceedings of the National Academy of Sciences* **103**, 1675–1680.

[93] Radhakrishnan, K & Hindmarsh, A. (1993) Description and Use of LSODE, the Livermore Solver for Ordinary Differential Equations. Lawrence Livermore National Laboratory Report UCRL-ID-113855. *NASA Reference Publication* **1327**.

[94] Christian, P. (2021) Anemia in women – an intractable problem that requires innovative solutions. *Nature Medicine* **27**, 1675–1677.

[95] Ancuceanu, R, Dinu, M, Hovaneţ, M. V, Anghel, A. I, Popescu, C. V, & Negreş, S. (2015) A Survey of Plant Iron Content – A Semi-Systematic Review. *Nutrients* **7**, 10320–10351.

[96] Vasconcelos, M & Grusak, M. A. (2007) Status and future developments involving plant iron in animal and human nutrition. *Iron Nutrition in Plants and Rhizospheric Microorganisms* **1**, 1–22.

[97] WHO. (2022) Anaemia in women and children (`http://www.who.int/medical_devices/initiatives/anaemia_control/en/`). First accessed: 2022-18-2.

[98] Chaparro, C. M & Suchdev, P. S. (2019) Anemia epidemiology, pathophysiology, and etiology in low- and middle-income countries. *Annals of the New York Academy of Sciences* **1450**, 15–31.

[99] Barberon, M, Zelazny, E, Robert, S, Conéjéro, G, Curie, C, Friml, J, & Vert, G. (2011) Monoubiquitin-dependent endocytosis of the IRON-REGULATED TRANSPORTER 1 (IRT1) transporter controls iron uptake in plants. *Proceedings of the National Academy of Sciences* **108**, E450–E458.

[100] Shin, L.-J, Lo, J.-C, Chen, G.-H, Callis, J, Fu, H, & Yeh, K.-C. (2013) IRT1 DEGRADATION FACTOR1, a RING E3 Ubiquitin Ligase, Regulates the Degradation of IRON-REGULATED TRANSPORTER1 in Arabidopsis. *The Plant Cell* pp. 3039–3051.

[101] Sivitz, A, Grinvalds, C, Barberon, M, Curie, C, & Vert, G. (2011) Proteasome-mediated turnover of the transcriptional activator FIT is required for plant iron-deficiency responses. *The Plant Journal* **66**, 1044–1052.

[102] Meiser, J, Lingam, S, & Bauer, P. (2011) Posttranslational Regulation of the Iron Deficiency Basic Helix-Loop-Helix Transcription Factor FIT Is Affected by Iron and Nitric Oxide. *Plant Physiology* **157**, 2154–2166.

[103] Pich, A, Manteuffel, R, Hillmer, S, Scholz, G, & Schmidt, W. (2001) Fe homeostasis in plant cells: Does nicotianamine play multiple roles in the regulation of cytoplasmic Fe concentration? *Planta* **213**, 967–976.

[104] Briat, J.-F, Duc, C, Ravet, K, & Gaymard, F. (2010) Ferritins and iron storage in plants. *Biochimica et Biophysica Acta (BBA)-General Subjects* **1800**, 806–814.

[105] Kok, A. D.-X, Yoon, L. L, Sekeli, R, Yeong, W. C, Yusof, Z. N. B, & Song, L. K. (2018) Iron Biofortification of Rice: Progress and Prospects. *Rice Crop - Current Developments* **3**, 25–44.

[106] Jeong, J & Guerinot, M. L. (2009) Homing in on iron homeostasis in plants. *Trends in Plant Science* **14**, 280–285.

[107] Rensing, L & Ruoff, P. (2002) Temperature effect on entrainment, phase shifting, and amplitude of circadian clocks and its molecular bases. *Chronobiology International* **19**, 807–864.

[108] Bar-Or, R. L, Maya, R, Segel, L. A, Alon, U, Levine, A. J, & Oren, M. (2000) Generation of oscillations by the p53-Mdm2 feedback loop: A theoretical and experimental study. *Proceedings of the National Academy of Sciences* **97**, 11250–11255.

[109] Parekh, A. B. (2011) Decoding cytosolic Ca^{2+} oscillations. *Trends in Biochemical Sciences* **36**, 78–87.

[110] Niggli, V, Adunyah, E, Penniston, J, & Carafoli, E. (1981) Purified (Ca^{2+}-Mg2+)-ATPase of the Erythrocyte Membrane. Reconstitution and Effect of Calmodulin and Phospholipids. *Journal of Biological Chemistry* **256**, 395–401.

[111] Carafoli, E, Guerini, D, & Pan, B. (2003) Expression, Purification, and Characterization of Isoform 1 of the Plasma Membrane Ca^{2+} pump: Focus on Calpain Sensitivity. *Journal of Biological Chemistry* **278**, 38141–38148.

[112] Russell, J, Zhao, W, Christ, G, Ashok, S, & Angeletti, R. H. (1999) Ca^{2+}-induced increases in steady-state concentrations of intracellular calcium are not required for inhibition of parathyroid hormone secretion. *Molecular Cell Biology Research Communications* **1**, 221–226.

[113] Carafoli, E, Fedrizzi, L, Domi, T, Di Leva, F, & Brini, M. (2009) Calcium pumps. *Handbook of Cell Signaling* **118**, 943–947.

[114] Placzek, S, Schomburg, I, Chang, A, Jeske, L, Ulbrich, M, Tillack, J, & Schomburg, D. (2016) BRENDA in 2017: new perspectives and new tools in BRENDA. *Nucleic Acids Research* **45**, D380–D388.

[115] Chen, Q, Mahendrasingam, S, Tickle, J. A, Hackney, C. M, Furness, D. N, & Fettiplace, R. (2012) The development, distribution and density of the PMCA2 calcium pump in rat cochlear hair cells. *European Journal of Neuroscience* **36**, 2302–2310.

[116] Scharff, O & Foder, B. (1982) Rate constants for calmodulin binding to Ca^{2+}-ATPase in erythrocyte membranes. *Biochimica et Biophysica Acta (BBA)-Biomembranes* **691**, 133–143.

[117] Vanagas, L, Rossi, R. C, Caride, A. J, Filoteo, A. G, Strehler, E. E, & Rossi, J. P. F. (2007) Plasma membrane calcium pump activity is affected by the membrane protein concentration: Evidence for the involvement of the actin cytoskeleton. *Biochimica et Biophysica Acta (BBA)-Biomembranes* **1768**, 1641–1649.

[118] Dagher, G & Lew, V. L. (1988) Maximal calcium extrusion capacity and stoichiometry of the human red cell calcium pump. *The Journal of Physiology* **407**, 569–586.

[119] Sedova, M & Blatter, L. (1999) Dynamic regulation of [Ca^{2+}] by plasma membrane Ca^{2+}-ATPase and Na+/Ca^{2+} exchange during capacitative Ca^{2+} entry in bovine vascular endothelial cells. *Cell Calcium* **25**, 333–343.

[120] Choi, H. S & Eisner, D. (1999) The effects of inhibition of the sarcolemmal ca-atpase on systolic calcium fluxes and intracellular calcium concentration in rat ventricular myocytes. *Pflügers Archiv* **437**, 966–971.

[121] Scharff, O, Foder, B, & Skibsted, U. (1983) Hysteretic activation of the Ca^{2+} pump revealed by calcium transients in human red cells. *Biochimica et Biophysica Acta (BBA)-Biomembranes* **730**, 295–305.

[122] Frieden, C. (1979) Slow Transitions and Hysteretic Behavior in Enzymes. *Annual Review of Biochemistry* **48**, 471–489.

[123] Caride, A. J, Elwess, N. L, Verma, A. K, Filoteo, A. G, Enyedi, Á, Bajzer, Ž, & Penniston, J. T. (1999) The Rate of Activation by Calmodulin of Isoform 4 of the Plasma Membrane Ca^{2+} Pump Is Slow and Is Changed by Alternative Splicing. *Journal of Biological Chemistry* **274**, 35227–35232.

[124] Caride, A. J, Filoteo, A. G, Penniston, J. T, & Strehler, E. E. (2007) The Plasma Membrane Ca^{2+} Pump Isoform 4a Differs from Isoform 4b in the Mechanism of Calmodulin Binding and Activation Kinetics: Implications for Ca^{2+} Signaling. *Journal of Biological Chemistry* **282**, 25640–25648.

[125] Foder, B & Scharff, O. (1992) Solitary calcium spike dependent on calmodulin and plasma membrane Ca^{2+} pump. *Cell Calcium* **13**, 581–591.

[126] Wu, X & Bers, D. M. (2007) Free and Bound Intracellular Calmodulin Measurements in Cardiac Myocytes. *Cell Calcium* **41**, 353–364.

[127] Persechini, A & Cronk, B. (1999) The Relationship Between the Free Concentrations of Ca^{2+} and Ca^{2+}-calmodulin in Intact Cells. *Journal of Biological Chemistry* **274**, 6827–6830.

[128] Bayley, P, Ahlstrőm, P, Martin, S. R, & Forsen, S. (1984) The kinetics of calcium binding to calmodulin: Quin 2 and ANS stopped-flow fluorescence studies. *Biochemical and Biophysical Research Communications* **120**, 185–191.

[129] Chou, A.-C, Ju, Y.-T, & Pan, C.-Y. (2015) Calmodulin Interacts with the Sodium/Calcium Exchanger NCX1 to Regulate Activity. *PLoS ONE* **10**, 1–19.

[130] Luik, R. M, Wang, B, Prakriya, M, Wu, M. M, & Lewis, R. S. (2008) Oligomerization of STIM1 couples ER calcium depletion to CRAC channel activation. *Nature* **454**, 538–542.

[131] Camello, C, Lomax, R, Petersen, O. H, & Tepikin, A. (2002) Calcium leak from intracellular stores–the enigma of calcium signalling. *Cell Calcium* **32**, 355–361.

[132] Hogan, P. G & Rao, A. (2015) Store-operated calcium entry: mechanisms and modulation. *Biochemical and Biophysical Research Communications* **460**, 40–49.

[133] Putney Jr, J. W. (2007) New molecular players in capacitative Ca^{2+} entry. *Journal of Cell Science* **120**, 1959–1965.

[134] Zheng, L, Stathopulos, P. B, Li, G.-Y, & Ikura, M. (2008) Biophysical characterization of the EF-hand and SAM domain containing Ca^{2+} sensory region of STIM1 and STIM2. *Biochemical and Biophysical Research Communications* **369**, 240–246.

[135] Stathopulos, P. B, Li, G.-Y, Plevin, M. J, Ames, J. B, & Ikura, M. (2006) Stored Ca^{2+} Depletion-induced Oligomerization of Stromal Interaction Molecule 1 (STIM1) via the EF-SAM Region. *Journal of Biological Chemistry* **281**, 35855–35862.

[136] Gudlur, A, Zeraik, A. E, Hirve, N, Rajanikanth, V, Bobkov, A. A, Ma, G, Zheng, S, Wang, Y, Zhou, Y, Komives, E. A, et al. (2018) Calcium sensing by the STIM1 ER-luminal domain. *Nature Communications* **9**, 1–15.

[137] Fahrner, M, Grabmayr, H, & Romanin, C. (2020) Mechanism of STIM activation. *Current Opinion in Physiology* **17**, 74–79.

[138] Thiel, M, Lis, A, & Penner, R. (2013) STIM2 drives Ca^{2+} oscillations through store-operated Ca^{2+} entry caused by mild store depletion. *The Journal of Physiology* **591**, 1433–1445.

[139] Lanner, J. T, Georgiou, D. K, Joshi, A. D, & Hamilton, S. L. (2010) Ryanodine Receptors: Structure, Expression, Molecular Details, and Function in Calcium Release. *Cold Spring Harbor Perspectives in Biology* **2**, 1–21.

[140] Sanders, K. M. (2001) Invited Review: Mechanisms of calcium handling in smooth muscles. *Journal of Applied Physiology* **91**, 1438–1449.

[141] McCarron, J, Bradley, K, MacMillan, D, & Muir, T. C. (2003) Sarcolemma agonist-induced interactions between InsP3 and ryanodine receptors in Ca^{2+} oscillations and waves in smooth muscle. *Biochemical Society Transactions* **31**, 920–924.

[142] Iino, M. (1990) Biphasic Ca^{2+} Dependence of Inositol 1,4,5-Trisphosphate-induced Ca Release in Smooth Muscle Cells of the Guinea Pig Taenia Caeci. *The Journal of General Physiology* **95**, 1103–1122.

[143] Kaftan, E. J, Ehrlich, B. E, & Watras, J. (1997) Inositol 1,4,5-Trisphosphate (InsP3) and Calcium Interact to Increase the Dynamic Range of InsP3 Receptor-Dependent Calcium Signaling. *The Journal of General Physiology* **110**, 529–538.

[144] Mikoshiba, K. (2007) IP3 receptor/Ca^{2+} channel: from discovery to new signaling concepts. *Journal of Neurochemistry* **102**, 1426–1446.

[145] Baker, M. R, Fan, G, & Serysheva, I. I. (2017) Structure of IP3R channel: High-resolution insights from cryo-EM. *Current Opinion in Structural Biology* **46**, 38–47.

[146] Serysheva, I. I. (2014) Toward a High-Resolution Structure of IP3R Channel. *Cell Calcium* **56**, 125–132.

[147] Fan, G, Baker, M. L, Wang, Z, Baker, M. R, Sinyagovskiy, P. A, Chiu, W, Ludtke, S. J, & Serysheva, I. I. (2015) Gating machinery of InsP3R channels revealed by electron cryomicroscopy. *Nature* **527**, 336–341.

[148] Sienaert, I, Missiaen, L, De Smedt, H, Parys, J. B, Sipma, H, & Casteels, R. (1997) Molecular and Functional Evidence for Multiple Ca^{2+}-binding Domains in the Type 1 Inositol 1,4,5-Trisphosphate Receptor. *Journal of Biological Chemistry* **272**, 25899–25906.

[149] Ding, Z, Rossi, A. M, Riley, A. M, Rahman, T, Potter, B. V, & Taylor, C. W. (2010) Binding of Inositol 1,4,5-trisphosphate (IP3) and Adenophostin A to the N-Terminal Region of the IP3 Receptor: Thermodynamic Analysis Using Fluorescence Polarization with a Novel IP3 Receptor Ligand. *Molecular Pharmacology* **77**, 995–1004.

[150] Prole, D. L & Taylor, C. W. (2019) Structure and Function of IP3 Receptors. *Cold Spring Harbor Perspectives in Biology* **11**, 1–17.

[151] Shinohara, T, Michikawa, T, Enomoto, M, Goto, J.-I, Iwai, M, Matsuura, T, Yamazaki, H, Miyamoto, A, Suzuki, A, & Mikoshiba, K. (2011) Mechanistic basis of bell-shaped dependence of inositol 1,4,5-trisphosphate receptor gating on cytosolic calcium. *Proceedings of the National Academy of Sciences* **108**, 15486–15491.

[152] Nosyreva, E, Miyakawa, T, Wang, Z, Glouchankova, L, Mizushima, A, Iino, M, & Bezprozvanny, I. (2002) The high-affinity calcium–calmodulin-binding site does not play a role in the modulation of type 1 inositol 1,4,5-trisphosphate receptor function by calcium and calmodulin. *Biochemical Journal* **365**, 659–667.

[153] Parys, J. B & Vervliet, T. (2020) New insights in the IP3 receptor and its regulation. *Calcium Signaling* pp. 243–270.

[154] Tipton, K. F & Dixon, H. B. (1979) in *Methods in Enzymology.* (Elsevier) Vol. 63, pp. 183–234.

[155] Dupont, G & Sneyd, J. (2017) Recent developments in models of calcium signalling. *Current Opinion in Systems Biology* **3**, 15–22.

[156] Ullah, G, Daniel Mak, D.-O, & Pearson, J. E. (2012) A data-driven model of a modal gated ion channel: The inositol 1,4,5-trisphosphate receptor in insect Sf9 cells. *Journal of General Physiology* **140**, 159–173.

[157] Shuttleworth, T. J. (2012) STIM and Orai proteins and the non-capacitative ARC channels. *Frontiers in Bioscience* **17**, 847–860.

[158] Bird, G. S, Hwang, S.-Y, Smyth, J. T, Fukushima, M, Boyles, R. R, & Putney Jr, J. W. (2009) STIM1 Is a Calcium Sensor Specialized for Digital Signaling. *Current Biology* **19**, 1724–1729.

[159] Wedel, B, Boyles, R. R, Putney Jr, J. W, & Bird, G. S. (2007) Role of the store-operated calcium entry proteins Stim1 and Orai1 in muscarinic cholinergic receptor-stimulated calcium oscillations in human embryonic kidney cells. *The Journal of Physiology* **579**, 679–689.

[160] Wu, L, Lian, W, & Zhao, L. (2021) Calcium signaling in cancer progression and therapy. *The FEBS Journal* **288**, 6187–6205.

[161] Cui, C, Merritt, R, Fu, L, & Pan, Z. (2017) Targeting calcium signaling in cancer therapy. *Acta Pharmaceutica Sinica B* **7**, 3–17.

[162] Magi, S, Castaldo, P, Macrì, M. L, Maiolino, M, Matteucci, A, Bastioli, G, Gratteri, S, Amoroso, S, & Lariccia, V. (2016) Intracellular Calcium Dysregulation: Implications for Alzheimers Disease. *BioMed Research International* **2016**, 1–14.

[163] Missiaen, L, Robberecht, W, Van Den Bosch, L, Callewaert, G, Parys, J, Wuytack, F, Raeymaekers, L, Nilius, B, Eggermont, J, & De Smedt, H. (2000) Abnormal intracellular Ca^{2+} homeostasis and disease. *Cell Calcium* **28**, 1–21.

[164] Bezprozvanny, I. (2009) Calcium signaling and neurodegenerative diseases. *Trends in Molecular Medicine* **15**, 89–100.

Appendix A

Appendix: Rate equations for Calcium model

The complete model of cytosolic Ca^{2+} in non-excitable cell is shown in Fig. A.1.

Rate equations for the model is as follows:

$$\begin{aligned}\frac{dCa^{2+}_{cyt}}{dt} &= k_1 \cdot Ca^{2+}_{ext} - k_2 \cdot Ca^{2+}_{cyt} - k_3 \cdot \frac{(PMCA \cdot M^*) \cdot Ca^{2+}_{cyt}}{k_4 + Ca^{2+}_{cyt}} \\ &- 4 \cdot k_8 \cdot (M) \cdot (Ca^{2+}_{cyt}) + 4 \cdot k_9 \cdot (M \cdot Ca_4) - 4 \cdot k_{10} \cdot (B) \cdot (Ca^{2+}_{cyt}) \\ &+ 4 \cdot k_{11} \cdot (B \cdot Ca_4) - \frac{k_{23} \cdot (SERCA) \cdot (Ca^{2+}_{cyt})}{k_{24} + Ca^{2+}_{cyt}} + k_{27} \cdot Ca^{2+}_{lum} \\ &+ \frac{k_{36} \cdot (R \cdot S) \cdot (ARCC) \cdot (Ca^{2+}_{ext})}{k_{37} + Ca^{2+}_{ext}} + \frac{k_{38} \cdot (IP_3R \cdot IP_3) \cdot (Ca^{2+}_{lum})}{k_{39} \cdot f_{IP3R} + f_{IP3R.Ca_{ER}} \cdot Ca^{2+}_{lum}} \\ &- \frac{k_{63} \cdot (Ca^{2+}_{cyt}) \cdot (NCX \cdot M^*)}{k_{64} + Ca^{2+}_{cyt}} + \frac{k_{73} \cdot (Ca^{2+}_{ext}) \cdot (SOCC) \cdot (STIM)}{k_{74} + Ca^{2+}_{ext}} \\ &+ k_{51}(Ind \cdot Ca) - k_{50} \cdot (Ca_{cyt}) \cdot (Ind) \end{aligned} \tag{A.1}$$

$$\frac{d(PMCA \cdot M^*)}{dt} = k_5 \cdot Ca^{2+}_{cyt} \cdot (PMCA \cdot M) - \frac{k_6 \cdot (PMCA \cdot M^*)}{k_7 + (PMCA \cdot M^*)} \tag{A.2}$$

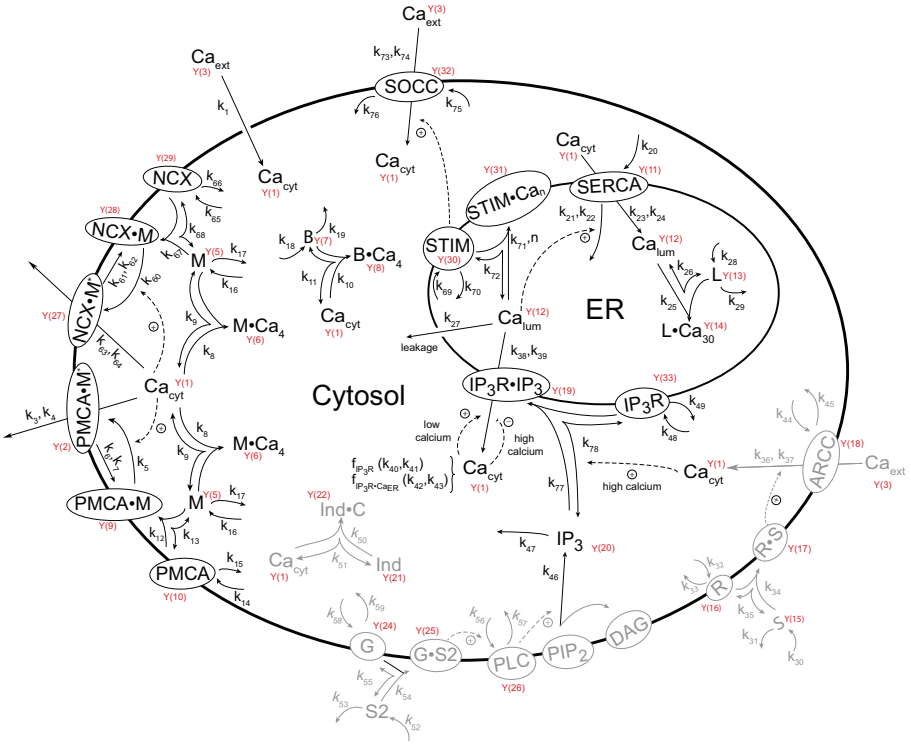

Figure A.1: Complete illustration of the calcium model in a non-excitable cell. Figure shows an illustration of the model in this work with all inflow and outflow paths and other regulatory mechanisms.

$$\frac{d(Ca_{ext})}{dt} = 0 \;\; (\text{extracellular Ca is kept constant at 1 or 2 mM}) \tag{A.3}$$

$$\begin{aligned}\frac{dM}{dt} &= k_{16} - k_{17}{\cdot}M - k_{12}{\cdot}(M){\cdot}(PMCA) + k_{13}{\cdot}(PMCA{\cdot}M) \\ &+ k_9{\cdot}(M{\cdot}Ca_4) - k_8{\cdot}(Ca^{2+}_{cyt}){\cdot}(M) + k_{68}{\cdot}(NCX{\cdot}M) \\ &- k_{67}{\cdot}(M){\cdot}(NCX)\end{aligned} \tag{A.4}$$

$$\frac{d(M{\cdot}Ca_4)}{dt} = k_8{\cdot}(Ca^{2+}_{cyt}){\cdot}(M) - k_9{\cdot}(M{\cdot}Ca_4) \tag{A.5}$$

$$\frac{dB}{dt} = k_{18} - k_{19}{\cdot}B - k_{10}{\cdot}(B){\cdot}(Ca^{2+}_{cyt}) + k_{11}{\cdot}(B{\cdot}Ca_4) \tag{A.6}$$

$$\frac{d(B{\cdot}Ca_4)}{dt} = k_{10}{\cdot}(B){\cdot}(Ca^{2+}_{cyt}) - k_{11}{\cdot}(B{\cdot}Ca_4) \tag{A.7}$$

$$\begin{aligned}\frac{d(PMCA{\cdot}M)}{dt} &= k_{12}{\cdot}(PMCA){\cdot}(M) - k_{13}{\cdot}(PMCA{\cdot}M) \\ &\quad + \frac{k_6{\cdot}(PMCA{\cdot}M^*)}{k_7 + (PMCA{\cdot}M^*)} - k_5{\cdot}(Ca^{2+}_{cyt}){\cdot}(PMCA{\cdot}M)\end{aligned} \tag{A.8}$$

$$\frac{d(PMCA)}{dt} = k_{14} - k_{15}{\cdot}(PMCA) - k_{12}{\cdot}(PMCA){\cdot}(M) + k_{13}{\cdot}(PMCA{\cdot}M) \tag{A.9}$$

$$\frac{d(SERCA)}{dt} = k_{20} - \frac{k_{21}{\cdot}(SERCA){\cdot}(Ca^{2+}_{lum})}{k_{22} + (SERCA)} \tag{A.10}$$

$$\frac{dCa^{2+}_{lum}}{dt} = \frac{k_{23}\cdot(SERCA)\cdot(Ca^{2+}_{cyt})}{k_{24}+Ca^{2+}_{cyt}} - k_{27}\cdot Ca^{2+}_{lum} - 30\cdot k_{25}\cdot(Ca^{2+}_{lum})\cdot(L) + 30\cdot k_{26}\cdot(L\cdot Ca_{30}) - n\cdot k_{71}\cdot(STIM)\cdot(Ca^{2+}_{lum})^n + k_{72}\cdot n\cdot(STIM\cdot Ca_n) - \frac{k_{38}\cdot(IP_3R\cdot IP_3)\cdot(Ca^{2+}_{lum})}{k_{39}\cdot f_{IP3R} + f_{IP3R.Ca_{ER}}\cdot(Ca^{2+}_{lum})} \tag{A.11}$$

$$\frac{dL}{dt} = k_{28} - k_{29}\cdot L - k_{25}\cdot(Ca^{2+}_{lum})\cdot(L) + k_{26}\cdot(L\cdot Ca_{30}) \tag{A.12}$$

$$\frac{d(L\cdot Ca_{30})}{dt} = k_{25}\cdot(Ca^{2+}_{lum})\cdot(L) - k_{26}\cdot(L\cdot Ca_{30}) \tag{A.13}$$

$$\frac{dS}{dt} = k_{30} - k_{31}\cdot S - k_{34}\cdot(S)\cdot(R) + k_{35}\cdot(R\cdot S) \tag{A.14}$$

$$\frac{dR}{dt} = k_{32} - k_{33}\cdot R - k_{34}\cdot(S)\cdot(R) + k_{35}\cdot(R\cdot S) \tag{A.15}$$

$$\frac{d(R\cdot S)}{dt} = k_{34}\cdot(S)\cdot(R) - k_{35}\cdot(R\cdot S) \tag{A.16}$$

$$\frac{dARCC}{dt} = k_{44} - k_{45}{\cdot}ARCC \tag{A.17}$$

$$\frac{d(IP_3R{\cdot}IP_3)}{dt} = k_{77}{\cdot}(IP_3){\cdot}(IP_3R) - k_{78}{\cdot}(IP_3R{\cdot}IP_3){\cdot}(Ca^{2+}_{cyt}), \text{ condition (i)} \tag{A.18}$$

$$\frac{d(IP_3R{\cdot}IP_3)}{dt} = k_{77}{\cdot}(IP_3){\cdot}(IP_3R) - k_{78}{\cdot}(IP_3R{\cdot}IP_3){\cdot}(1 + Ca^{2+}_{cyt}), \text{ condition (ii)} \tag{A.19}$$

$$\frac{d(IP_3R{\cdot}IP_3)}{dt} = k_{77}(IP_3)(IP_3R) - k_{78}{\cdot}(IP_3R{\cdot}IP_3), \text{ condition (iii)} \tag{A.20}$$

$$\begin{aligned}\frac{d(IP_3)}{dt} &= k_{46}{\cdot}(PLC)(PIP_2) - k_{47}{\cdot}(IP_3) - k_{77}{\cdot}(IP_3){\cdot}(IP_3R) \\ &\quad + k_{78}{\cdot}(IP_3R{\cdot}IP_3){\cdot}(Ca^{2+}_{cyt}), \text{ condition (i)}\end{aligned} \tag{A.21}$$

$$\frac{d(IP_3)}{dt} = k_{46}\cdot(PLC)(PIP_2) - k_{47}\cdot(IP_3) - k_{77}\cdot(IP_3)\cdot(IP_3R) + k_{78}\cdot(IP_3R\cdot IP_3)\cdot(1 + Ca^{2+}_{cyt}), \text{ condition (ii)} \tag{A.22}$$

$$\frac{d(IP_3)}{dt} = k_{46}\cdot(PLC)(PIP_2) - k_{47}\cdot(IP_3) - k_{77}\cdot(IP_3)\cdot(IP_3R) + k_{78}\cdot(IP_3R\cdot IP_3), \text{ condition (iii)} \tag{A.23}$$

$$\frac{d(PIP_2)}{dt} = 0, \text{ constant } \mathrm{PIP_2} \text{ at } 1\mu\mathrm{M} \tag{A.24}$$

$$\frac{d(S2)}{dt} = k_{52} - k_{53}\cdot S2 - k_{54}\cdot(S2)\cdot(G) + k_{55}\cdot(G\cdot S2) \tag{A.25}$$

$$\begin{aligned}\frac{d(Ind\cdot Ca)}{dt} &= -k_{51}(Ind\cdot Ca) + k_{50}\cdot(Ca_{cyt})\cdot(Ind) \\ &= -\frac{d(Ind)}{dt}\end{aligned} \tag{A.26}$$

$$\frac{dG}{dt} = -k_{54}\cdot(S2)\cdot(G) + k_{55}\cdot(G\cdot S2) + k_{58} - k_{59}\cdot G \tag{A.27}$$

$$\frac{d(G\cdot S2)}{dt} = k_{54}\cdot(S2)\cdot(G) - k_{55}\cdot(G\cdot S2) \tag{A.28}$$

$$\frac{d(PLC)}{dt} = k_{56}\cdot(G)\cdot(S2) - k_{57}\cdot(PLC) \tag{A.29}$$

$$\frac{d(NCX\cdot M^*)}{dt} = k_{60}\cdot(NCX\cdot M)\cdot(Ca^{2+}_{cyt}) - \frac{k_{61}\cdot(NCX\cdot M^*)}{k_{62} + (NCX\cdot M^*)} \tag{A.30}$$

$$\begin{aligned}\frac{d(NCX\cdot M)}{dt} &= k_{67}\cdot(M)\cdot(NCX) - k_{68}\cdot(NCX\cdot M) \\ &\quad - k_{60}\cdot(NCX\cdot M)\cdot(Ca^{2+}_{cyt}) + \frac{k_{61}\cdot(NCX\cdot M^*)}{k_{62} + (NCX\cdot M^*)}\end{aligned} \tag{A.31}$$

$$\frac{d(NCX)}{dt} = k_{65} - k_{66}\cdot(NCX) - k_{67}\cdot(M)\cdot(NCX) + k_{68}\cdot(NCX\cdot M) \tag{A.32}$$

$$\frac{d(STIM)}{dt} = k_{69} - k_{70}\cdot(STIM) - k_{71}\cdot(STIM)\cdot(Ca_{lum}^{2+})^n + k_{72}(STIM\cdot Ca_n) \tag{A.33}$$

$$\frac{d(STIM\cdot Ca_n)}{dt} = k_{71}\cdot(STIM)\cdot(Ca_{lum}^{2+})^n - k_{72}\cdot(STIM\cdot Ca_n) \tag{A.34}$$

$$\frac{d(SOCC)}{dt} = k_{75} - k_{76}\cdot(SOCC) \tag{A.35}$$

$$\begin{aligned}\frac{d(IP_3R)}{dt} &= k_{48} - k_{49}\cdot(IP_3R) - k_{77}\cdot(IP_3R)\cdot(IP_3) \\ &\quad + k_{78}\cdot(IP_3R\cdot IP_3)\cdot(Ca_{cyt}^{2+}),\ \text{condition (i)}\end{aligned} \tag{A.36}$$

$$\begin{aligned}\frac{d(IP_3R)}{dt} &= k_{48} - k_{49}\cdot(IP_3R) - k_{77}\cdot(IP_3R)\cdot(IP_3) \\ &\quad + k_{78}\cdot(IP_3R\cdot IP_3)\cdot(1 + Ca_{cyt}^{2+}),\ \text{condition (ii)}\end{aligned} \tag{A.37}$$

$$\frac{d(IP_3R)}{dt} = k_{48} - k_{49}\cdot(IP_3R) - k_{77}\cdot(IP_3R)\cdot(IP_3) + k_{78}\cdot(IP_3R{\cdot}IP_3), \text{ condition (iii)} \tag{A.38}$$

$$\frac{d(IP_3R)}{dt} = k_{48} - k_{49}\cdot(IP_3R) - k_{77}\cdot(IP_3R)\cdot(IP_3) + k_{78}\cdot(IP_3R{\cdot}IP_3)\cdot(Ca^{2+}_{cyt}), \text{ condition (i)} \tag{A.39}$$

$$\frac{d(IP_3R)}{dt} = k_{48} - k_{49}\cdot(IP_3R) - k_{77}\cdot(IP_3R)\cdot(IP_3) + k_{78}\cdot(IP_3R{\cdot}IP_3)\cdot(1 + Ca^{2+}_{cyt}), \text{ condition (ii)} \tag{A.40}$$

$$\frac{d(IP_3R)}{dt} = k_{48} - k_{49}\cdot(IP_3R) - k_{77}\cdot(IP_3R)\cdot(IP_3) + k_{78}\cdot(IP_3R{\cdot}IP_3), \text{ condition (iii)} \tag{A.41}$$

Different approaches were applied in some of the calculations, which has been labeled condition i, ii and iii. These conditions were used in the section where the effect of $Ca^{2+}{}_{cyt}$ on the dissociation of $IP_3R{\cdot}IP_3$ was studied.
In addition to the equations in the results section of the thesis, there is also an indicator (Ind) shown in grey in the overview of the complete model as this was added in order to add the effect of an indicator to the model calculations as an indicator would be present in experiments.

Paper 1:
Robust Concentration and Frequency Control in Oscillatory Homeostats

OPEN ACCESS Freely available online

PLOS ONE

Robust Concentration and Frequency Control in Oscillatory Homeostats

Kristian Thorsen[1], Oleg Agafonov[2], Christina H. Selstø[2], Ingunn W. Jolma[2], Xiao Y. Ni[2], Tormod Drengstig[1], Peter Ruoff[2]*

1 Department of Electrical Engineering and Computer Science, University of Stavanger, Stavanger, Norway, **2** Centre for Organelle Research, University of Stavanger, Stavanger, Norway

Abstract

Homeostatic and adaptive control mechanisms are essential for keeping organisms structurally and functionally stable. Integral feedback is a control theoretic concept which has long been known to keep a controlled variable A robustly (i.e. perturbation-independent) at a given set-point A_{set} by feeding the integrated error back into the process that generates A. The classical concept of homeostasis as robust regulation within narrow limits is often considered as unsatisfactory and even incompatible with many biological systems which show sustained oscillations, such as circadian rhythms and oscillatory calcium signaling. Nevertheless, there are many similarities between the biological processes which participate in oscillatory mechanisms and classical homeostatic (non-oscillatory) mechanisms. We have investigated whether biological oscillators can show robust homeostatic and adaptive behaviors, and this paper is an attempt to extend the homeostatic concept to include oscillatory conditions. Based on our previously published kinetic conditions on how to generate biochemical models with robust homeostasis we found two properties, which appear to be of general interest concerning oscillatory and homeostatic controlled biological systems. The first one is the ability of these oscillators ("oscillatory homeostats") to keep the average level of a controlled variable at a defined set-point by involving compensatory changes in frequency and/or amplitude. The second property is the ability to keep the period/frequency of the oscillator tuned within a certain well-defined range. In this paper we highlight mechanisms that lead to these two properties. The biological applications of these findings are discussed using three examples, the homeostatic aspects during oscillatory calcium and p53 signaling, and the involvement of circadian rhythms in homeostatic regulation.

Citation: Thorsen K, Agafonov O, Selstø CH, Jolma IW, Ni XY, et al. (2014) Robust Concentration and Frequency Control in Oscillatory Homeostats. PLoS ONE 9(9): e107766. doi:10.1371/journal.pone.0107766

Editor: Gianluca Tosini, Morehouse School of Medicine, United States of America

Received July 31, 2014; **Accepted** August 11, 2014; **Published** September 19, 2014

Data Availability: The authors confirm that all data underlying the findings are fully available without restriction. All relevant data are within the paper and its Supporting Information files.

Funding: Funding provided by Grant no. 167087/V40 by Norwegian Research Council (http://www.forskningsradet.no) for IWJ and Grant no. 183085/S10 by Norwegian Research Council (http://www.forskningsradet.no) for XYN. This research was also funded by Program Area Fund "Organelle Biology" and the Program Area Fund "Biomedical data analysis group" from the Faculty of Science and Technology, University of Stavanger (https://www.uis.no/fakulteter-institutter-og-sentre/). The funders had no role in study design, data collection and analysis, decision to publish, or preparation of the manuscript.

Competing Interests: The authors have declared that no competing interests exist.

* Email: peter.ruoff@uis.no

Introduction

The biological motivation of this work can be summarized as follows: How can homeostatic mechanisms possibly work when many or even most of the regulatory processes within a cell are based on oscillations? Versions of this question and how oscillatory processes participate in homeostatic and adaptive mechanisms have been repeatedly asked and discussed [1–5]. Our aim is to identify and build homeostatic/adaptive motifs on a rational basis with possible applications within physiology and synthetic biology. In this paper we apply control-engineering and kinetic methods and show how the classical concept of homeostasis [6,7] is linked to oscillatory behavior. We demonstrate how biological oscillators can have robust (perturbation-independent) homeostatic/adaptive behaviors both with respect to average concentration of a regulated variable and with respect to a robust control of the oscillator's frequency. By taking three examples, we argue that such properties appear closely linked to the controlled period lengths of the p53-Mdm2 oscillatory system and circadian rhythms [1,8] or to the homeostatic regulation of cytosolic calcium during signaling [9].

Organisms have developed defending homeostatic mechanisms in order to survive changing or stressful conditions by maintaining their internal physiologies at an approximately constant level [7,10,11]. In this respect, many compounds are tightly regulated within certain concentration ranges, because they are essential for cellular function, but may lead to dysfunction and diseases when their concentrations are outside of their regulated regimes. The term "homeostasis" was introduced by Cannon [6,7] to indicate that the internal milieu of an organism is regulated within narrow limits. The examples Cannon addresses in 1929 [6] are still actual research topics, such as the regulations of body temperature, blood sugar, blood calcium and blood pH levels [12–15]. Today many more homeostatic controlled compounds have been identified, including hormones [16], transcription factors and transcription factor related compounds [17], cellular ions such as plant nitrate

levels [18,19], iron [20], and calcium [21]. The Supplementary Material of Ref. [22] contains further examples.

Because many biochemical processes are oscillatory [1,8,23–27], Cannon's definition of homeostasis has been perceived as unsatisfactory and various alternative homeostasis concepts have been suggested. The term *predictive homeostasis* [1] has been introduced in order to stress the anticipatory homeostatic behavior of circadian regulation. Other concepts include *allostasis* [2,5] to focus on the concerted and interwoven nature of the defending mechanisms, *rheostasis* [3] to put emphasis on set-point changes, and *homeodynamics* [4] to stress the nonlinear kinetic behaviors of the defending mechanisms as part of an open system.

The appearance of cybernetics together with system theory [28–31] caused an interest to understand homeostasis and biological control from the angle of system analysis and control theory [32–39] by introducing control-engineering concepts such as *integral control* [22,40–45]. Integral control allows to keep a controlled variable (say A) precisely and robustly at a given set-point A_{set} by feeding the integrated error back into the process by which A is generated [46]. To gain insights how integral control and homeostasis may appear in biochemical and physiological processes, we started [43] to study two-component negative feedback controllers, where one component is the (homeostatic) controlled variable A, while the other is the manipulated or controller variable E. Each controller consists of the two species A and E and three fluxes, the inflow and outflow to and from E and an E -controlled compensatory flux (either inflow or outflow) of A, denoted j_{comp}. The compensatory flux compensates for disturbances in the level of A caused by perturbations in other uncontrolled inflows/outflows of A. By considering activating or inhibitory signaling events from A to E and vice versa, eight basic negative feedback configurations (controller motifs, Fig. 1a) can be created [22,47]. Two kinetic requirements leading to integral control have so far been identified, one based on a zero-order kinetic removal of the manipulated variable E [22,43,48], the other on an autocatalytic formation of E in association with a first-order degradation [45]. Fig. 1b gives a brief summary of these two kinetic approaches by using motif 5 as an example. For details, the reader is referred to [22,45]. We feel that this approach provides a rational basis to build networks which allow to view the behaviors of the individual controllers and to understand emergent properties of the overall network. By combining individual controller motifs with integral control we previously showed that an integrative and dynamic approach to cellular homeostasis is possible, which includes storage, excretion and remobilization of the controlled variables [19,22,49].

In the present study we extend the concept of homeostasis to include sustained oscillatory or pulsatile conditions. We show that oscillatory homeostats based on the controller motifs in Fig. 1a can maintain robust homeostasis in A. For controllers where E is inhibiting the compensatory flux (motifs 2, 4, 6, and 8, Fig. 1a), the frequency can be shown to depend on the level of E and therefore on the applied perturbation strength. In this class of controllers the frequency generally increases upon increased perturbation strengths; here we use motif 2 as a representative example. For the remaining controller motifs the frequency has been found to be less dependent upon perturbations. As a representative example for this behavior we use motif 5. We further show that robust frequency control can be achieved by either using additional controllers, which keep the average levels of A and E homeostatic regulated, or by using the intrinsic harmonic/quasi-harmonic properties of motifs 1 or 5. The biological significance of these findings is discussed with respect to the oscillatory signaling of cytosolic calcium and p53, as well as the regulating properties of circadian rhythms with respect to homeostasis and temperature compensation.

Results

Kinetic Approach to Implement Integral Control

We consider the negative feedback motifs in Fig. 1. A general condition for integral control can be formulated if the rate equation of the manipulated variable E allows for a rearrangement in form of two functions $g(E)$ and $h(A)$, and where the integral of $1/g(E)$ with respect to E exists and can be written as $G(E)$. Then, the set-point in A is determined by the solution of $h(A)=0$, i.e.

$$\dot{E} = h(A)\cdot g(E) \tag{1}$$

Rearranging Eq. 1 and requiring steady state conditions gives:

$$\frac{\dot{E}}{g(E)} = \dot{G}(E) = h(A) = 0 \tag{2}$$

Eq. 2 has been applied for nonoscillatory steady states with $g(E)=1$ by using zero-order kinetic degradation/inhibition of E [22,43] or with $g(E)=E$ by using first-order autocatalytic formation and degradation in E [45]. Other functions of $g(E)$ may be possible but plausible reaction kinetic mechanisms need to be identified. For the sake of simplicity, we consider here that integral control is achieved by a zero-order removal of E using $g(E)=1$.

To extend the condition of Eq. 2 to sustained stable and marginally stable oscillations, we observe that the integral of the periodic reaction rates $\dot{A}$ and $\dot{E}$ along a closed orbit c in the system's phase space is zero. For $\dot{E}$ this can be written as:

$$<\dot{E}>_c = \oint_c \dot{E}\,dt = \oint_c h(A)\,dt = 0 \tag{3}$$

Dependent on whether A is activating or inhibiting the production or removal of E, two expressions for the set-point of the oscillatory controller can be derived from Eq. 3. In case A is activating (motifs 1, 2, 5, 6) and by assuming first-order kinetics with respect to A in the rate equation for E, the set-point of A is given by (see Eq. S1 in (File S1))

$$<A>_c = \oint_c A(t)\,dt = <A>_{set} \tag{4}$$

where the integral is taken along one (or multiple) closed and stable orbit(s) in the system's phase space. With increasing time t, the average concentration of A, $<A>_t$, will approach its set-point $<A>_{set}$, i.e.,

$$<A>_t = \frac{1}{t}\cdot\int_0^t A(\tau)\,d\tau \rightarrow <A>_{set} \qquad \text{when} \qquad t\rightarrow\infty \tag{5}$$

When A is inhibiting the production or removal of E (motifs 3, 4, 7, 8) and assuming (for the sake of simplicity) that the inhibiting term has a first-order cooperativity with respect to A with an inhibition constant K_I^A, the following expression is conserved and perturbation-independent (see derivation in File S1, Eq. S8):

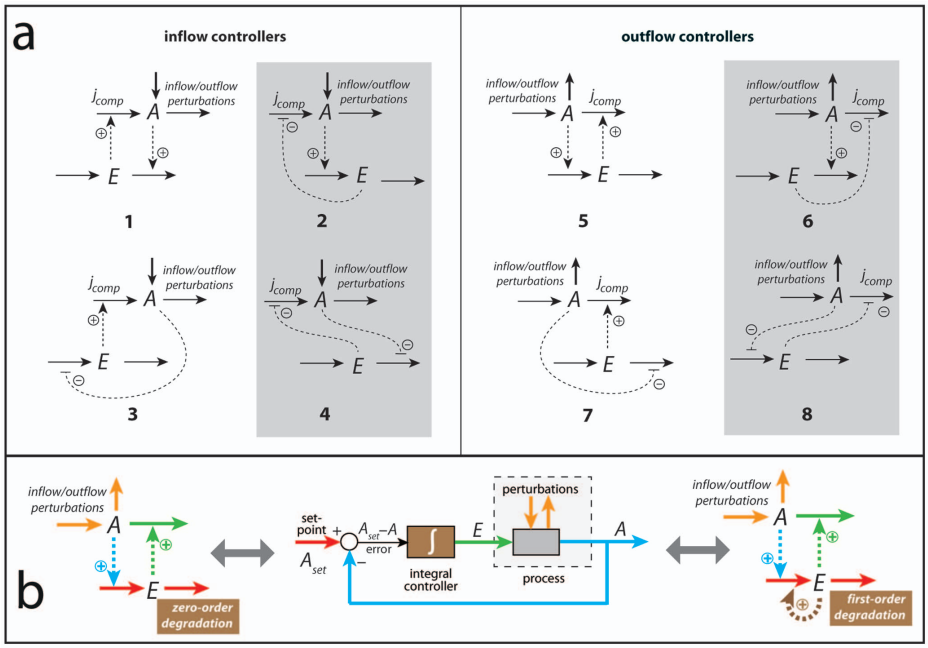

Figure 1. A basic set of two-component homeostatic controller motifs with two implementations of integral control. (a) Compound A is the homeostatic controlled variable and E is the controller or manipulated variable [22]. The motifs fall into two classes termed as inflow and outflow controllers, dependent whether their compensatory fluxes j_{comp} add or remove A from the system. In motifs outlined in gray the controller compound E inhibits the compensatory flux, while in the other motifs E activates the compensatory flux. (b) middle figure shows a standard control engineering flow chart of a negative feedback loop, where the negative feedback results in the subtraction of the concentration of A (blue line) from A's set-point (red line) leading to the error ($A_{set}-A$). The error feeds into the integral controller (brown box). The controller output (the integrated error) is the concentration of E (green line) which regulates the process that creates A. The perturbations which affect the level of A are indicated in orange color. (b) left panel shows the structure of negative feedback (outflow) controller 5. The colors correspond to those of the control engineering flow chart. For example, the set-point (red) is given by the ratio between removing and synthesis rates of E, while the integral controller (brown) is related to the processing kinetics of E, in this case E is removed by zero-order [22,43]. (b) right panel shows the same outflow controller (motif 5). The only difference is that the integral controller is now represented by a first-order autocatalytic formation (indicated by brown dashed arrow) and a first-order removal with respect to E [45].
doi:10.1371/journal.pone.0107766.g001

$$< \frac{1}{K_I^A + A} >_c = \oint_c \frac{dt}{K_I^A + A(t)} = \text{constant} \qquad (6)$$

Homeostasis by Oscillatory Controllers

To illustrate the homeostatic response of the oscillatory controllers, we use, as mentioned above, conservative and limit-cycle versions of inflow controller motif 2 and outflow controller motif 5 as representative examples. These motifs have been chosen, because they represent different ways to achieve negative feedback and homeostasis of the controlled variable A. In motif 2 (as in motifs 4, 6, and 8) E inhibits the compensatory flux, while in motif 5 (as in motifs 1, 3, and 7) the compensatory flux is activated by E. A limit-cycle version of motif 6 will be used to discuss cytosolic Ca^{2+} oscillations in terms of a homeostatic mechanism.

Conservative Oscillatory Controllers. A conservative system is a system for which an energy or Hamiltonian function (H-function) can be found and for which the values of H remain constant in time. Conservative oscillators show periodic motions characterized by that they in phase space do not occur in isolation (i.e. they are not limit cycles). For a given H-level h a periodic motion (a closed path in phase space) is surrounded by a continuum of near-by paths, obtained for neighboring values of h [50]. The dynamics of a two-component conservative oscillator can be derived from the H-function using the following equations:

$$\frac{\partial H}{\partial E} = -\dot{A}\,; \quad \frac{\partial H}{\partial A} = \dot{E} \qquad (7)$$

which are analogous to the Hamilton-Jacobi equations from classical mechanics. In general, solutions of these equations are not necessarily oscillatory, but here we focus only on the conservative

oscillators, which can be derived from the eight controller motifs (Fig. 1a). Dependent on how integral control is implemented, some of the conservative oscillators are well-known; they are: the *harmonic oscillator* [51] based on either motifs 1 or 5 (using zero-order implementation of integral control; see left panel in Fig. 1b), the *Lotka-Volterra oscillator* [45,52,53] also here based on motifs 1 or 5 (but using the autocatalytic implementation of integral control; see right panel in Fig. 1b), and Goodwin's oscillator from 1963 [54] based on motif 2. In the literature the Goodwin oscillator comes in two versions, which are both based on motif 2. There is a conservative oscillator version from 1963 [54] with two components. There is also another version from 1965 with three components [55]. The difference between the two versions lies in the kinetics of the degradation rates of the oscillators' components. In the 1965 three-component version the degradation rates are first-order with respect to the degrading species, while in the conservative case (1963 version) the degradation rates have zero-order kinetics. These kinetic differences change the oscillatory behavior of the two systems significantly. To get limit-cycle oscillations, it is well-known from the literature [56] that the three-dimensional system where the components are degraded by first-order kinetics requires a cooperativity of the inhibiting species of about 9 or higher. Our results presented here using motif 2 confirms Goodwin's 1963 results that when components are degraded by zero-order kinetics the system can oscillate with a cooperativity of 1 with respect to the inhibiting species E. Here we also extend Goodwin's results by showing that *limit-cycle oscillations* can be created based on motif 2, but still using a cooperativity of 1 with respect to the inhibiting species E (see below).

The following two requirements are needed to get conservative oscillations for any motif from Fig. 1a: (i) integral control has to be implemented in the rate equation for E, and (ii) all removal of A should either occur by zero-order kinetics with respect to A, or, when the removal of A is first (or nth)-order with respect to A, the formation of A needs to be a first (or nth)-order autocatalytic reaction [45]. When conditions (i) and (ii) are fulfilled, a function $H(A,E)$ can be constructed, which describes the dynamics of the system analogous to the Hamilton-Jacobi equations from classical mechanics, where the form of H depends on the system's kinetics. Details on how H is constructed for the various situations is given in File S1.

Fig. 2a shows a reaction kinetic representation of motif 2, which is closely related to Goodwin's 1963 oscillator [54]. It was Goodwin who first drew attention to the analogy between the dynamics of a set of two-component cellular negative feedback oscillators and classical mechanics [54]. In this inflow-type of controller, increased outflow perturbations (i.e., increased k_2 values) are compensated by a decreased average amount of E (i.e., $<E>$, Fig. 2b), thereby neutralizing the increased removal of A by use of an increased compensating flux

$$j_{comp} = k_3 \cdot K_I^E/(K_I^E + E) \tag{8}$$

In this way the average level of A, $<A>$, is kept at its set-point $V_{max}^{E_{set}}/k_4$ (see Eq. S5 in the File S1). During the adaptation in $<A>$ (when k_2 is changed) the controller's frequency as well as the $<E>$-level are affected. The frequency ω for each of the eight conservative oscillators can roughly be estimated by a harmonic approximation (see File S1), which in case of motif 2 (Fig. 2a) is given by (assuming $k_1 = 0$)

$$\omega = \frac{\sqrt{k_3 \cdot k_4 \cdot K_I^E}}{K_I^E + E_{ss}} \tag{9}$$

E_{ss} $(= k_3 K_I^E/k_2 - K_I^E)$ is the steady state of E, which is obtained when $\dot{A} = 0$ (Fig. 2a). Because the level of $<E>$ is decreasing with increasing k_2 values, Eq. 9 indicates, and as shown by the computations in Figs. 2b and 2c, that the frequency of the oscillator increases with increasing perturbation strengths (k_2 values) while keeping $<A>$ at its set-point. In fact, the increase in frequency upon increased perturbation strengths appears to be a general property of oscillatory homeostats, where the manipulated variable E inhibits the compensatory flux (for limit-cycle examples, see below).

At high k_2 values, i.e., when the E level becomes lower than K_I^E, the compensatory flux j_{comp} approaches its maximum value k_3. At this stage the homeostatic capacity of the controller is reached. Any further increase of k_2 cannot be met by an increased compensatory flux and will therefore lead to a breakdown of the controller. For discussions about controller breakdowns and controller accuracies, see Refs. [22,48].

The scheme in Fig. 2d shows outflow controller motif 5, which will compensate any inflow perturbations of A (due to changes in k_1) by increasing the compensatory flux

$$j_{comp} = k_3 \cdot E \tag{10}$$

When $K_M^A \ll A$ and $K_M^{E_{set}} \ll E$ the oscillator is harmonic and is described by a single sine function which oscillates around the set-point $<A>_{set} = V_{max}^{E_{set}}/k_4$ with frequency $\omega = \sqrt{k_3 \cdot k_4}$ and a period of $2\pi/\sqrt{k_3 \cdot k_4}$. Increased levels in k_1 (Figs. 2e and 2f) are compensated by increased $<E>$ levels which keep $<A>$ at its set-point. Harmonic oscillations can also be obtained for the counterpart inflow motif 1 (see Fig. S9 and Eqs. S44–S50 in File S1).

For the harmonic oscillators (motifs 1 or 5) $<A>$-homeostasis is kept by an increase in $<E>$, which matches precisely the increase in the (average) compensatory flux without any need to change the frequency. For the other motifs either an increase or a decrease in frequency is observed with increasing perturbation strengths dependent whether E inhibits or activates the compensatory flux, respectively.

Limit-Cycle Controllers. The conservative oscillatory controllers described above can be transformed into limit-cycle oscillators by including an additional intermediate, and, as long as integral control is present, homeostasis in A is maintained by means of Eq. 4 or 6. Fig. 3a gives an example of a limit-cycle homeostat using motif 2. Dependent on the rate constants the oscillations can show pulsatile/excitable behavior (Fig. 3b). In these pulsatile and highly nonlinear oscillations $<A>$ homeostasis is maintained at the set-point $<A>_{set} = V_{max}^{E_{set}}/k_4$, although the peak value in A exceeds the set-point by over one order of magnitude (Fig. 3b). As already observed for the conservative case, an increase in the perturbation strength (i.e., by increasing k_2) leads to an increase in frequency while homeostasis in $<A>$ is preserved (Fig. 3c).

Similarly, a limit-cycle homeostat of motif 5 can be created (Fig. 4a) by including intermediate e and maintaining integral control with respect to A. With increasing perturbation strengths (k_1 values, Fig. 4b), homeostasis in $<A>$ is maintained by increasing $<E>$. Compared to the conservative situation

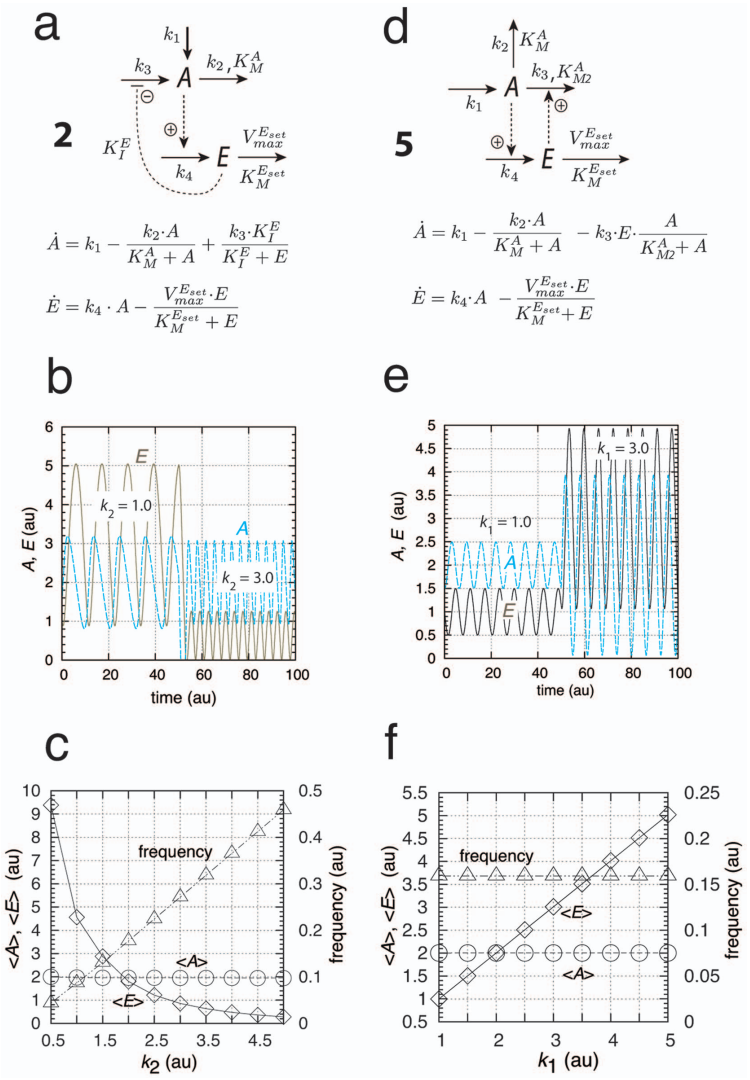

Figure 2. Representation and kinetics of conservative oscillators based on motif 2 and motif 5. (a)–(c) "Goodwin's oscillator" (motif 2). Conservative oscillations occur when $K_M^A \ll A$ and $E \ll K_M^{E_{set}}$; the latter condition introduces integral feedback and thereby robust homeostasis [22,43]. (b) Conservative oscillations in A and E, with $k_1 = 0.0$, $k_2 = 1.0$, $K_M^A = 1 \times 10^{-6}$, $k_3 = 6.0$, $K_I^E = 0.5$, $k_4 = 1.0$, $V_{max}^{E_{set}} = 2.0$, $K_M^{E_{set}} = 1 \times 10^{-6}$. Initial concentrations: $A_0 = 1.5$, $E_0 = 1.0$. At time t = 50.0 k_2 is changed from 1.0 to 3.0. (c) $<A>$, $<E>$, and frequency as a function of the perturbation k_2. While the frequency increases and $<E>$ decreases with increasing k_2, $<A>$ is kept at its set-point $V_{max}^{E_{set}}/k_4 = 2.0$. (d)–(f) Harmonic oscillator representation of motif 5. Conservative (harmonic) oscillations occur when $K_M^A \ll A$ (or $k_2 = 0$) and $E \ll K_M^{E_{set}}$. (e) Harmonic oscillations in A and E, with $k_1 = 1.0$ (the perturbation), $k_2 = 0.0$, $k_3 = 1.0$, $K_{M2}^A = 1 \times 10^{-6}$, $k_4 = 1.0$, $V_{max}^{E_{set}} = 2.0$, and $K_M^{E_{set}} = 1 \times 10^{-6}$. At time t = 50.0 k_1 is changed from 1.0 to 3.0. Initial concentrations: $A_0 = 1.5$, $E_0 = 1.0$. (f) $<A>$, $<E>$, and frequency as a function of the perturbation k_1. Typical for the harmonic oscillator is the constancy of the frequency upon changing k_1 values. $<E>$ increases with increasing k_1, while $<A>$ is kept at its set-point $V_{max}^{E_{set}}/k_4 = 2.0$.
doi:10.1371/journal.pone.0107766.g002

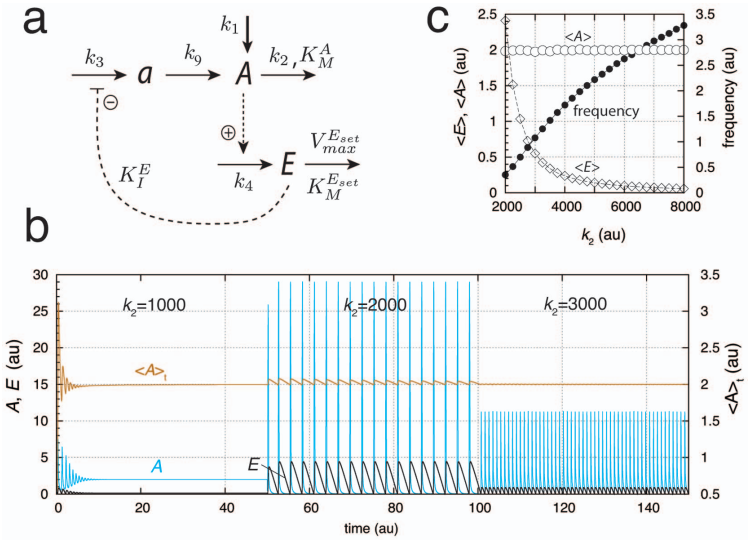

Figure 3. A limit-cycle model of controller motif 2. (a) Reaction scheme. Rate equations: $\dot{A}=k_1 - k_2 \cdot A/(K_M^A+A)+k_9 \cdot a$; $\dot{E}=k_4 \cdot A - V_{max}^{E_{set}} \cdot E/(K_M^{E_{set}}+E)$; $\dot{a}=k_3 \cdot K_I^E/(K_I^E+E) - k_9 \cdot a$. (b) Homeostatic response of the model for three different perturbations (k_2 values). For time t between 0 and 50 units, $k_2=1.0\times10^3$, for t between 50 and 100 units, $k_2=2.0\times10^3$, and for t between 100 and 150 units, $k_2=3.0\times10^3$. In the oscillatory case $<A>$ at time t is given as $<A>_t=(1/t)\times\int_0^t A(t')dt'$ (ordinate to the right) showing that $<A>$ is under homeostatic control despite the fact that A peak values may be over one order of magnitude larger than the set-point. (c) $<A>$, $<E>$, and frequency values as a function of k_2. Simulation time for each data point is 100.0 time units. Note that $<A>$ is kept at $<A>_{set}$ independent of k_2. Rate constant values (in au): $k_1=1.0$, $k_3=1.0\times10^5$, $k_4=1.0$, $K_I^E=1.0\times10^{-3}$, $K_M^A=1.0$, $V_{max}^{E_{set}}=2.0$, $K_M^{E_{set}}=1.0\times10^{-6}$, and $k_9=2.0$. It may further be noted that the degradation kinetics with respect to A are no longer zero-order as required in the conservative case (Figs. 2a–c). Initial concentrations in (b): $A_0=1.5$, $E_0=0.3$, and $a_0=166.17$. Initial concentrations in (c) for each data point: $A_0=1.725\times10^{-6}$, $E_0=1.585$, and $a_0=0.861$.
doi:10.1371/journal.pone.0107766.g003

(Fig. 2f), the frequency now shows both slight decreasing and increasing values. However, the overall frequency changes are not as large as for motif 2, indicating that similar to the harmonic case, the frequency of the motif 5 based oscillator has a certain intrinsic frequency compensation on k_1-induced perturbations (Fig. 4c).

Robust Frequency Control and Quenching of Oscillations

In this section we present for the first time biochemical models that can show robust (perturbation-independent) frequency control. There are several biological oscillators where the frequency/period is under homeostatic regulation. Probably the best known example is the temperature compensation of the circadian period, i.e. these rhythms show an approximately constant period length of about 24 h at different but constant temperatures [57]. Temperature compensation is also observed in certain ultradian rhythms [58,59]. Another biological oscillator with a fairly constant period is the p53-Mdm2 system [60], where the number of oscillations may indicate the strength of the DNA damage in the cell [61].

We show two ways how robust frequency control can be achieved. One is due to the presence of quasi-harmonic kinetics, i.e. the system, although still being a limit-cycle oscillator, behaves more like a harmonic oscillator. On basis of experimental results, we believe that the p53-Mdm2 system falls into this category (see discussion below). In the other approach, frequency homeostasis is obtained by regulating E itself by additional inflow/outflow controllers I_1,I_2. This approach leads to many possible ways how I_1,I_2 can interact with the central negative feedback A-E loop/oscillator and several ways are illustrated using motif 2 and motif 5. Such an approach may apply to the period homeostasis of circadian rhythms (see discussion below).

Robust Frequency Control by Quasi-Harmonic Kinetics. We consider now the case when the intermediate that has been implemented to obtain limit-cycle behavior (compounds a or e in Figs. 3a or 4a) obeys *approximately* the steady-state assumption, i.e., $\dot{a}\approx0$ or $\dot{e}\approx0$. We term the oscillators' resulting behavior as *quasi-conservative*, because these systems still have a limit-cycle, but behave also as a conservative system. An interesting case occurs when the system is quasi-harmonic, i.e. when motifs 1 or 5 are used. In this case the limit-cycle oscillations and the frequency can approximately be described by a harmonic oscillator, i.e., a single sine function. This is illustrated in Fig. 5 where an increased k_5 value is applied to the scheme of Fig. 4a (which leads to $\dot{e}\approx0$). Fig. 5a shows the oscillations for three different perturbations (k_1 values). The oscillations in A show a practically perfect overlay with a single sine function, outlined in black for $k_1=1.0$. When k_1 is increased the oscillations (outlined in blue) undergo a phase shift and an increase in amplitude, but the frequency stays constant at the value of the (quasi) harmonic oscillator. For high k_1 values the

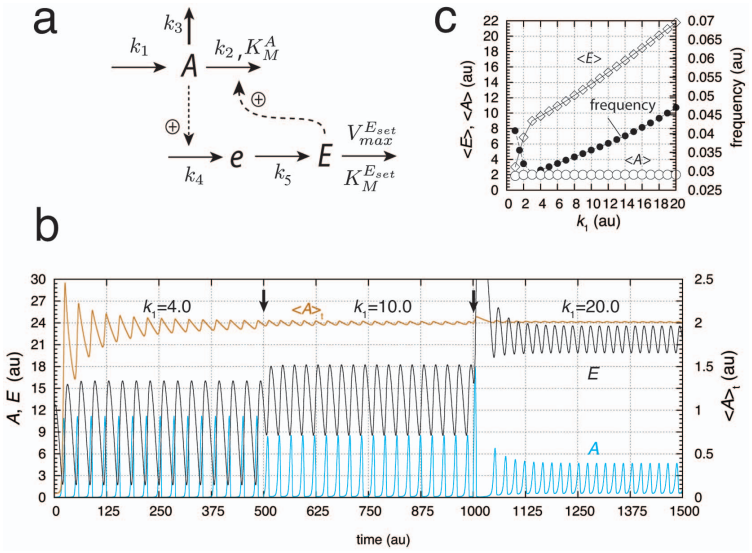

Figure 4. A limit-cycle model of controller motif 5. (a). Rate equations: $\dot{A}=k_1-k_2\cdot E\cdot A/(K_M^A+A)-k_3\cdot A$; $\dot{e}=k_4\cdot A-k_5\cdot e$; $\dot{E}=k_5\cdot e-V_{max}^{E_{set}}\cdot E/(K_M^{E_{set}}+E)$. (b) Homeostatic behavior in $<A>$ illustrated by three different perturbations (k_1 values). At time $t=500.0$ k_1 is changed from 4.0 to 10.0, and at $t=1000.0$ k_1 is changed from 10.0 to 20.0 (indicated by solid arrows). The set-point of $<A>$ is given as $V_{max}^{E_{set}}/k_4=2.0$. Rate constant values: k_1 is variable, $k_2=1.0$, $K_M^A=0.1$, $k_3=0.0$, $k_4=0.5$, $k_5=0.2$, $V_{max}^{E_{set}}=1.0$, and $K_M^{E_{set}}=1.0\times10^{-6}$. Initial concentrations: $A_0=1.9964\times10^{-2}$, $e_0=8.0983$, and $E_0=12.0258$. (c) $<A>$, $<E>$, and frequency values as a function of k_1 showing that $<A>$ is kept at the set-point independent of k_1. Rate constants as in (b). Initial concentrations for each data point: $A_0=7.6383\times10^{-1}$, $e_0=1.6887$, and $E_0=18.8155$. Simulation time for each data point is 10000.0 time units.
doi:10.1371/journal.pone.0107766.g004

A-amplitude of the oscillator becomes saturated, which is a secondary effect of the oscillator's homeostatic property. Due to symmetry reasons and because the oscillator is locked on to the harmonic frequency, the value of A cannot exceed beyond twice the level of its set-point, which in this case has been set to 12.5 (Figs. 5a and 5b). As in the harmonic case (Fig. 2f), $<E>$ increases with increasing k_1 (Fig. 5b). Fig. 5c shows the approach to the limit-cycle (outlined in black). When k_5 increases further and the steady state approximation for e becomes better and better, the limit-cycle disappears and the system becomes purely harmonic.

Quenching of Oscillations in Quasi-Conservative Systems. A requirement to obtain conservative oscillations and an oscillatory promoting condition for limit cycle oscillations is the presence of zero-order degradation in A. Changing the zero-order degradation in A may lead to the loss of oscillations. For example, in quasi-conservative systems the oscillations can be effectively quenched by either adding a first-order removal term with respect to A (with rate constant k_3, Fig. 4a) or by replacing the zero-order kinetics degradation in A (using k_2, K_M^A) by first-order kinetics with respect to A, or by increasing K_M^A. Fig. 5d illustrates the suppression of the quasi-harmonic oscillations by adding a first-order removal with respect to A. In contrast, when an oscillatory system does not show quasi-conservative kinetics, addition of a first-order removal with respect to A does not necessarily abolish the oscillations. A detailed parameter analysis showing how the value of k_5 affects the period of the oscillations and how first-order degradation in A affects the size of the parameter space in which sustained oscillations are found is given in (Figs. S10 and S11 in File S1).

Robust Frequency Homeostasis by Control of $<E>$. When considering the relationship between $<E>$ and the frequency, as for example shown in Fig. 3c, we wondered whether it would be possible to design an oscillator with a robust frequency homeostasis by using an additional control of $<E>$. For this purpose, two extra controllers I_1 and I_2 with their own set-points for $<E>$ are introduced. Note, that the integral control for $<A>$ by E is still operative and has its own defined set-point. In the following we show three examples of robust frequency control using motifs 2 and 5. Two of the examples illustrate different feedback arrangements of I_1 and I_2 using motif 2. An example using still another arrangement using motif 2 is described in File S1 (Figs. S12–S14).

In Fig. 6a a set-up for robust frequency homeostasis is shown by using a limit-cycle oscillator based on controller motif 5. The set-points for $<E>$, given by the rate equations for I_1 and I_2, are $<E>_{set}^{I_1}=k_6/V_{max}^{I_1}$ and $<E>_{set}^{I_2}=V_{max}^{I_2}/k_7$. Fig. 6b shows the results for a set of calculations when k_1 varies from 1 to 20 au. In these calculations it was assumed that the I_1 and I_2 controllers have the same set-point of 20.0 au. In the absence of controllers I_1 and I_2, the frequency varies as indicated in Fig. 4c, which in Fig. 6b is shown as gray dots. When I_1 and I_2 controllers are both

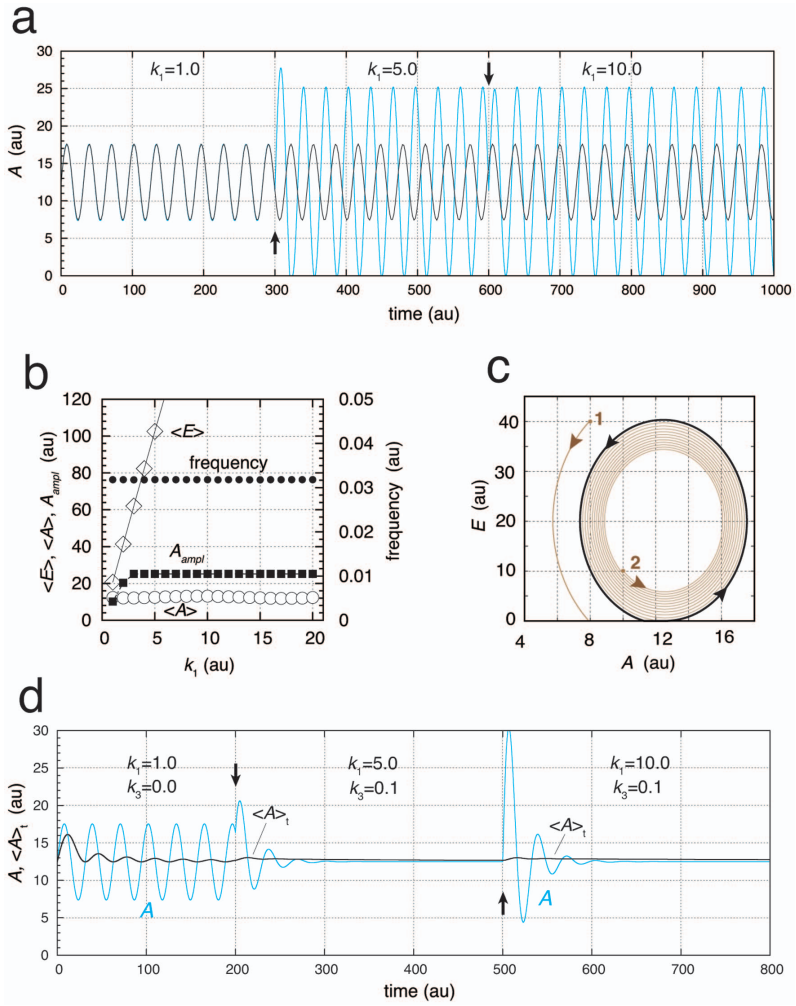

Figure 5. Quasi-harmonic behavior of motif 5 oscillator (Fig. 4a). For time $t<300$, a perfect overlay between the numerical calculation of $A(t)$ (blue color) and the single harmonic $A(t)=A_{ampl}\cdot\sin(2\pi/P+\phi)\ +<A>_{set}$ (black color) is found, where $k_1=1.0$, $A_{ampl}=5.0791$, $P=31.44$, $\phi=-0.05$, and $<A>_{set}=V_{max}^{E_{set}}/k_4\ =12.5$. A_{ampl} and P represent the numerically calculated amplitude and period length, respectively. ϕ was adjusted to give a closely matching overlay. Other rate constant values (numerical calculations): $k_2=5.0\times10^{-2}$, $k_3=0.0$, $K_M^A=1.0\times10^{-6}$, $k_4=0.8$, $k_5=20.0$, $V_{max}^{E_{set}}=10.0$, and $K_M^{E_{set}}=1.0\times10^{-6}$. Initial concentrations: $A_0=12.4290$, $e_0=0.4952$, and $E_0=1.0139\times10^{-4}$. At times $t=300$ and $t=600$ (solid arrows) k_1 is changed to respectively 5.0 and 10.0. For these k_1 values the amplitude of A has reached its maximum, which is twice the value of the set-point. (b) $<A>$, A_{ampl}, $<E>$, and frequency as a function of k_1. Simulation time for each data point is 1000.0 time units. (c) Demonstration of limit-cycle behavior of the quasi-harmonic oscillations. Same initial conditions as in (a) with $k_1=1.0$, and $e_0=0.4952$. (d) Same system as in (a), but at times $t=200$ and $t=500$ (solid arrows) k_3 is changed and kept to 0.1. The oscillations are efficiently quenched, but A remains under homeostatic control.

doi:10.1371/journal.pone.0107766.g005

active, $<E>$ shows robust homeostasis at 20.0 (Fig. 6b) and the frequency is practically constant (black dots). Fig. 6c shows the response when controller I_1 has been "knocked out". While in this case the $<A>$ values are still under homeostatic control, $<E>$ approaches its set-point (defined by $<E>^{I_2}_{set}$) only at high k_1 values, but without a control of the frequency. When controller I_2 is knocked-out (Fig. 6d), control of $<E>$ and frequency homeostasis is observed. Due to the absence of controller I_2, homeostasis in $<E>$ and in the frequency is lost for higher k_1 values. The role of I_2 in this type of regulator is to diminish/suppress the inflow to A by k_1, such that controller I_1 can supply the necessary amount of A in order to keep $<E>$ and the frequency under homeostatic control. This mechanism is illustrated in Fig. 6e by a "static" work mode of I_2, where the concentration of I_2 is kept constant. In this case the k_1-region of frequency homeostasis increases with increasing but constant concentrations of I_2 (Fig. 6f).

A corresponding approach to achieve robust frequency homeostasis by using motif 2 is shown in Fig. 7a. The set-up differs from that used for motif 5 (Fig. 6a) by allowing that I_1 and I_2 act upon a and upstreams of A. For the sake of simplicity, both controllers are assumed to have set-points at 20.0 au. Note that in this version of the motif 2 oscillator, the removal of A is now purely first-order with respect to A (using only k_2). Because motif 2 has been the core for many circadian rhythm models, we will below discuss implications of robust frequency control with respect to properties of circadian rhythms. In this context we note that the region outlined in gray in Fig. 7a shows the part of the oscillator where rate constants have no influence on the frequency, i.e. the sensitivity coefficients $\partial(\textit{frequency})/\partial k_i$ are zero.

Fig. 7b shows the homeostatic behavior in frequency (black dots) in comparison with the uncontrolled oscillator (gray dots). In the controlled case, both $<A>$ and $<E>$ are under homeostatic regulation with set-points of 2.0 au and 20.0 au, respectively. To elucidate the effect of the added controllers I_1 and I_2, we removed them one by one (knocking them out). In Figs. 7c and 7d controllers I_1 and I_2 have been removed, respectively. When outflow controller I_1 is not operative, the system is not able to remove sufficient a at low k_2 values. In this case $<E>$ levels are high and unregulated at low k_2's and showing an increase in frequency. Only at sufficiently high k_2 values controller I_2 is able to compensate for the decreased levels in $<E>$. The situation is reversed in Fig. 7d, when controller I_2 is not operative. At low k_2 values controller I_1 can remove excess of E by diminishing the level of a and keeping $<E>$ at its set-point. However, the $<E>$ regulation breaks down at high values of k_2, because no additional supply for E via a can now be provided. In this way controllers I_1/I_2 act as an antagonistic pair of outflow/inflow controllers, respectively. Note that the by E controlled level of $<A>$ (with set-point of 2.0 au) is kept at its set-point independently whether $<E>$ is regulated by I_1/I_2 or not. Fig. 7e shows the oscillations when both I_1 and I_2 are operative (Fig. 7b, black dots) and k_2 being changed from 3.0 to 8.0 at t = 250.0 units (indicated by arrow). The level of $<E>$ is controlled to its set-point (20.0), while the amplitude of A has increased with the increase of k_2. For each spike (after steady state has been established) the average amount of A is the same and independent of the value of k_2, leading to the same frequency and homeostasis in $<A>$.

Oscillator with Two Homeostatic Frequency Domains

In the I_1 and I_2-controlled oscillators described above the set-point of $<E>$ will determine the frequency. Fig. 8a shows an example of a motif-2-based homeostat, where I_1 and I_2 feed back to A and a, respectively. For an example where I_1 and I_2 feed back to A only, see Fig. S12 in File S1. In the calculations of Fig. 8, different set-points for $<E>$ by controllers I_1 and I_2 have been chosen. As a result, dependent whether the perturbation strength (value of k_2) is high or low, the oscillator shifts between two different homeostatic controlled frequency regimes separated by a transition zone (Fig. 8b). Fig. 8c shows the oscillations, $<A>$ and $<E>$ values and the frequency switch when k_2 is changed from 3.0 to 8.0.

Discussion

Classifications of Biochemical Oscillators and Influence of Positive Feedback

There has been several approaches how chemical and biochemical oscillators can be understood and classified [62–66]. The controller motifs shown in Fig. 1a can be considered as a basic set of negative feedback oscillators. For example, the Lotka-Volterra oscillator can be viewed as a negative feedback oscillator based on motifs 1 or 5, but where integral control is implemented in terms of autocatalysis [45] and where the controlled variable A is formed by autocatalysis and degraded by a first-order process with respect to A. The same motif can show harmonic oscillations, when integral control and removal of the controlled variable is incorporated by means of zero-order kinetics. Two additional oscillator types based on the same motif can be created by implementing mixed autocatalytic/zero-order kinetics for integral control and for the generation/degradation of the controlled variable ('Text S1'). The other motifs can be extended in a similar way, giving rise to 32 basic (mostly unexplored) oscillator types. This type of classification supplements the one given earlier by Franck, where the eight negative feedback loops where combined with their positive counterparts to create what Franck termed *antagonistic feedback* [63] An often discussed question is the role positive feedback, or autocatalysis, may play in biological oscillators. Using a Monte-Carlo approach Tsai et al. [26] studied the robustness and frequency responses of oscillators with only negative feedback loops and oscillators with a combined positive-plus-negative feedback design. The authors concluded that the combination of a negative and a positive feedback is the best option for having robust and tunable oscillations. In particular, the positive loop appears necessary to make the oscillator tunable at a constant amplitude. We here have shown how homeostasis and tunable oscillators may be achieved without any positive feedback (but generally associated with a changing amplitude). To put our results in relation to those from Tsai et al. [26], we wondered, triggered by the comments from a reviewer, how an oscillator with an autocatalytic-based integral controller might behave in comparison. For this purpose we used controller motif 2 (Fig. 9a), analogous to the scheme shown in Fig. 3a. Interestingly, and in agreement with the findings by Tsai et al. [26], the autocatalytic step resulted now in relaxation-type of oscillations. As expected, the frequency of the oscillator increases with increasing perturbation strengths k_2, and $<A>$ is under homeostatic control (Fig. 9b). However, as indicated by the results of Tsai et al. the oscillator's amplitude has now become independent of k_2! These results show that Franck's original concept of antagonistic feedback, i.e. combining positive and negative feedback loops in various ways [63] appear to be of relevance for many biological oscillators [26].

Homeostatic Regulation under Oscillatory Conditions

In his definition of homeostasis Cannon introduced the term *homeo* instead of *homo* to indicate that certain variations in the concentrations of the homeostatic controlled species are still

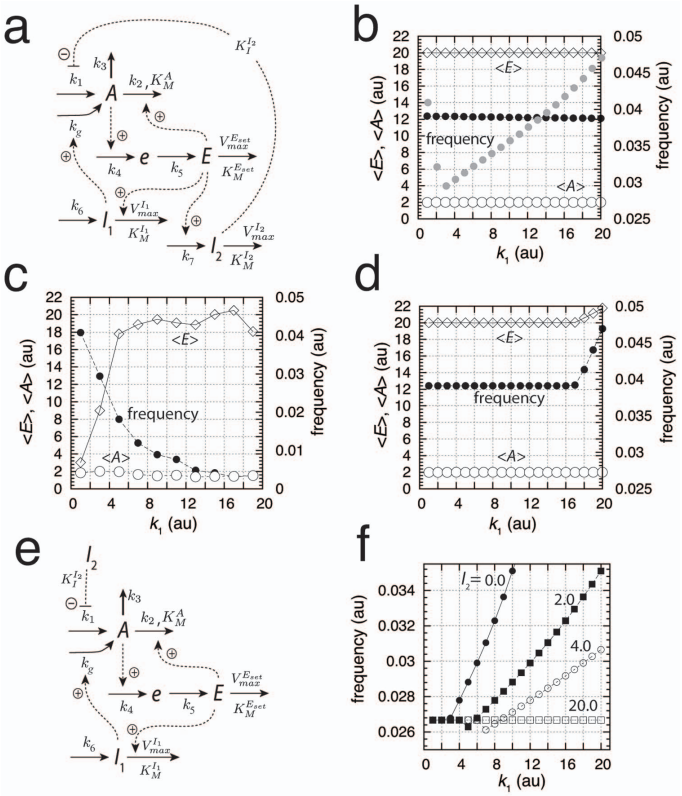

Figure 6. Oscillator based on motif 5 with robust frequency control. (a) Reaction scheme. Rate equations: $\dot{A}=k_1\cdot K_I^{I_2}/(K_I^{I_2}+I_2)+k_g\cdot I_1-k_2\cdot E\cdot A/(K_M^A+A)-k_3\cdot A$; $\dot{e}=k_4\cdot A-k_5\cdot e$; $\dot{E}=k_5\cdot e-V_{max}^{E_{set}}\cdot E/(K_M^{E_{set}}+E)$; $\dot{I}_1=k_6-E\cdot V_{max}^{I_1}\cdot I_1/(K_M^{I_1}+I_1)$; $\dot{I}_2=k_7\cdot E-V_{max}^{I_2}\cdot I_2/(K_M^{I_2}+I_2)$. (b) Demonstration of robust frequency control. $<A>$, $<E>$, and frequency are shown as functions of k_1. Rate constants: $k_1=1.0$, $k_2=1.0$, $K_M^A=0.1$, $k_3=0.0$, $k_4=0.5$, $k_5=0.2$, $V_{max}^{E_{set}}=1.0$, $K_M^{E_{set}}=1.0\times10^{-6}$, $k_6=20.0$, $V_{max}^{I_1}=1.0$, $K_M^{I_1}=1.0\times10^{-6}$, $k_7=1.0$, $V_{max}^{I_2}=20.0$, and $K_M^{I_2}=1.0\times10^{-6}$. Set-points for E by controllers I_1 and I_2 are given as $<E>_{set}^{I_1}=k_6/V_{max}^{I_1}=20.0$ and $<E>_{set}^{I_2}=V_{max}^{I_2}/k_7=20.0$, respectively. Initial concentrations for each data point (black dots): $A_0=0.7638$, $E_0=18.8155$, $e_0=1.6887$, $I_{1,0}=1.6695\times10^3$, and $I_{2,0}=2.7657\times10^2$. Gray dots show the frequency as a function of k_1 without control by I_1 and I_2. (c) System as in (b), but controller I_1 not present. (d) System as in (b), but controller I_2 not present. (e) Reaction scheme of oscillator, but with a constant I_2 concentration. Rate constants otherwise as in (b). (f) Frequency as a function of k_1 for the system described in (e) using different constant I_2 concentrations (indicated within the graph). The homeostatic region of the frequency increases with increasing I_2 concentrations.
doi:10.1371/journal.pone.0107766.g006

allowed, but within certain limits [6]. As typical examples, Cannon mentions the variations of body temperature, variations in blood sugar, blood calcium, and blood pH levels [6]. We have shown that the concept of homeostasis can be extended to oscillatory conditions and that the term *set-point* still can be given a precise meaning, even when peak values of the controlled variable may exceed the set-point by over one order of magnitude (Figs. 3 and 7). In these cases the set-point relates to the mean value of the oscillatory species, $<A>$. Many compounds are known to be under a tight homeostatic regulation to avoid cellular dysfunction, such as is the case for cytosolic calcium. There is no particular reason to assume that protective homeostatic mechanisms should cease to exist once a compound becomes oscillatory and functions, as in case of calcium, as a signaling device. Allowing a species (such as cytosolic calcium) to oscillate while defending the mean value of these oscillations makes it possible to relay signaling without exposing the cell to long term overload. In the following we discuss three examples where oscillatory homeostats appear to be involved: in the homeostatic regulation of calcium and p53 during oscillations/signaling, and in the homeostatic function and period regulation of circadian rhythms.

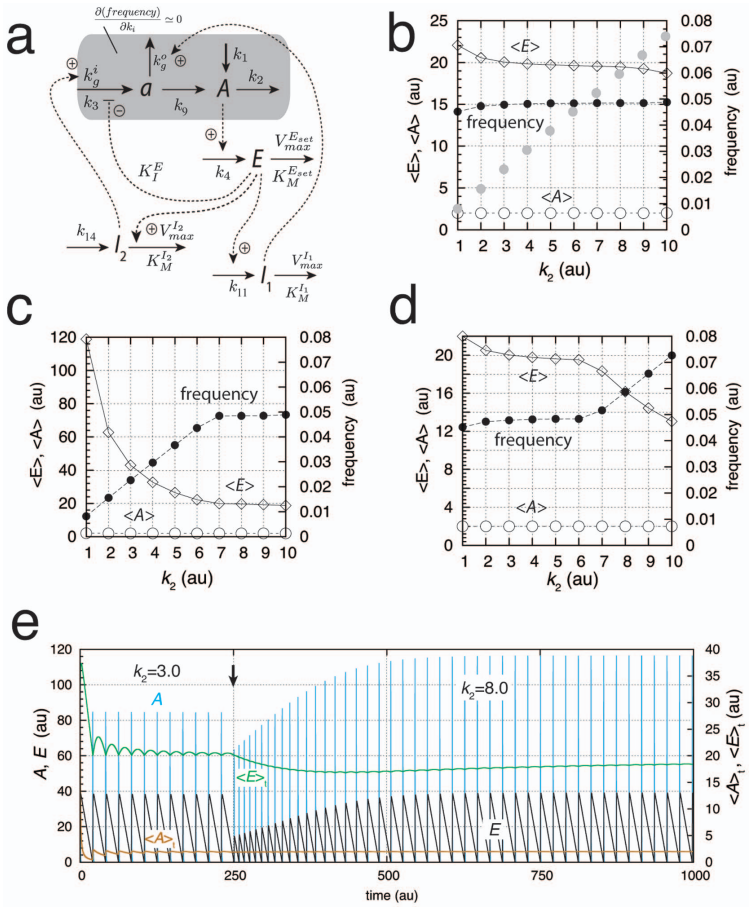

Figure 7. Oscillator based on motif 2 with robust frequency control. (a) Reaction scheme. Rate equations: $\dot{A}=k_1-k_2\cdot A+k_9\cdot a$; $\dot{E}=k_4\cdot A-V^{E_{set}}_{max}\cdot E/(K^{E_{set}}_M+E)$; $\dot{a}=(k_3+k^i_g\cdot I_2)\cdot K^E_I/(K^E_I+E)-(k_9+k^o_g\cdot I_1)\cdot a$; $\dot{I}_1=k_{11}\cdot E-V^{I_1}_{max}\cdot I_1/(K^{I_1}_M+I_1)$; $\dot{I}_2=k_{14}-E\cdot V^{I_2}_{max}\cdot I_2/(K^{I_2}_M+I_2)$. Shaded area indicates part of the model for which the control coefficents of the frequency/period with respect to the parameters within this area become zero when frequency homeostasis is enforced by controllers I_1 and I_2. (b) Demonstration of frequency homeostasis by varying k_2. Black dots show the frequency when controllers I_1 and I_2 are active. Rate constants: $k_1=0.0$, $k_2=1.0$, $k_3=1.0\times10^6$, $k_4=1.0$, $K^E_I=1.0\times10^{-6}$, $V^{E_{set}}_{max}=2.0$, $K^{E_{set}}_M=1.0\times10^{-6}$, $k_9=2.0$, $k^i_g=1.0\times10^2$, $k^o_g=1.0\times10^{-3}$, $k_{11}=5.0$, $V^{I_1}_{max}=1.0\times10^2$, $K^{I_1}_M=1.0\times10^{-6}$, $k_{14}=99.99$, $V^{I_2}_{max}=5.0$, and $K^{I_2}_M=1.0\times10^{-6}$. Set-points for E by controllers I_1 and I_2 are given as $<E>^{I_1}_{set}=V^{I_1}_{max}/k_{11}=20.0$ and $<E>^{I_2}_{set}=k_{14}/V^{I_2}_{max}=19.998$, respectively. The set-point $<E>^{I_1}_{set}$ of the *outflow* controller I_1 has been set slightly higher than $<E>^{I_2}_{set}$ for the *inflow* controller I_2 to avoid integral windup and that the controllers work "against" each other [22]. Initial concentrations for each data point (black dots): $A_0=50.4903$, $E_0=23.9425$, $a_0=3.2629$, $I_{1,0}=8.2955\times10^3$, and $I_{2,0}=57.8533$. Gray dots show the frequency as a function of k_2 for the uncontrolled case, i.e., in the absence of controllers I_1 and I_2. (c) System as in (b), but controller I_1 is "knocked out" by setting k_{11} and $I_{1,0}$ to zero. Homeostasis occurs only at high k_2 values when controller I_2 is active. (d) System as in (b), but inflow controller I_2 is inactivated by setting k_{14} and $I_{2,0}$ to zero. Frequency homeostasis is observed for low k_2 when controller I_1 is active. At high k_2 values the frequency homeostasis breaks down, because controller I_2 is not present to compensate the increased outflow of A, which leads to low $<E>$ values. (e) Oscillations of system in (b) illustrating frequency homeostasis. At time $t=250$ (solid arrow) k_2 is changed from 3.0 to 8.0. Initial concentrations: $A_0=27.3167$, $E_0=31.7283$, $a_0=0.1237$, $I_{1,0}=1.3473\times10^4$, and $I_{2,0}=5.0919\times10^2$.
doi:10.1371/journal.pone.0107766.g007

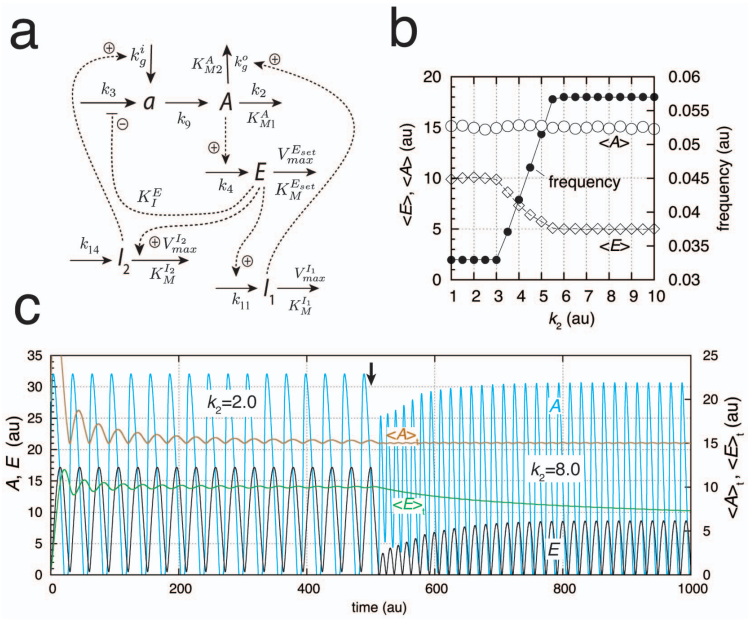

Figure 8. Oscillator based on motif 2 with robust frequency control but alternative feedback regulation by I_1 and I_2. (a) Reaction scheme. Rate equations: $\dot{A}=k_9\cdot a-k_2\cdot A/(K_{M1}^A+A)-k_g^o\cdot A\cdot I_1/(K_{M2}^A+A)$, $\dot{E}=k_4\cdot A-V_{max}^{E_{set}}\cdot E/(K_M^{E_{set}}+E)$; $\dot{a}=k_3\cdot K_I^E/(K_I^E+E)-k_9\cdot a+k_g^i\cdot I_2$; $\dot{I}_1=k_{11}\cdot E-V_{max}^{I_1}\cdot I_1/(K_M^{I_1}+I_1)$; $\dot{I}_2=k_{14}-E\cdot V_{max}^{I_2}\cdot I_2/(K_M^{I_2}+I_2)$. (b) Using different set-points $<E>_{set}^{I_1}=V_{max}^{I_1}/k_{11}=10.0$ and $<E>_{set}^{I_2}=k_{14}/V_{max}^{I_2}=5.0$, the frequency (solid dots) can switch between two homeostatic frequency regimes, dependent whether k_2 is low or high. The two regimes are separated by a transition zone. Rate constants: $k_2=1.0$, $k_3=20.0$, $k_4=0.1$, $V_{max}^{E_{set}}=1.5$, $K_M^{E_{set}}=1.0\times10^{-6}$, $k_{11}=1.0$, $V_{max}^{I_1}=10.0$, $K_M^{I_1}=1.0\times10^{-6}$, $k_{14}=5.0$, $V_{max}^{I_2}=1.0$, $K_M^{I_2}=1.0\times10^{-6}$, $K_I^E=1.0$, $k_g^i=k_g^o=1.0\times10^{-2}$, $K_{M1}^A=K_{M2}^A=1.0\times10^{-6}$. Initial concentrations: $A_0=0.6677$, $E_0=1.0536$, $a_0=2.5828\times10^{-2}$, $I_{1,0}=1.1614\times10^3$, and $I_{2,0}=7.5008\times10^2$. (c) Oscillations of system in (b) illustrating frequency switch. At time $t=500$ (solid arrow) k_2 is changed from 2.0 to 8.0. Initial concentrations: $A_0=19.7178$, $E_0=0.6272$, $a_0=0.4178$, $I_{1,0}=1.3696\times10^2$, and $I_{2,0}=12.9828$.
doi:10.1371/journal.pone.0107766.g008

Calcium Signaling. Cytosolic calcium (Ca^{2+}) levels are under homeostatic control to concentrations at about 100 nM while extracellular levels are in the order of 1 mM. High Ca^{2+} concentrations are also found in the endoplasmatic reticulum (ER) and in mitochondria (between 0.1–10 mM), which act as calcium stores. To keep cytosolic Ca^{2+} concentrations at such a low level Ca^{2+} is actively pumped out from the cytoplasm into the extracellular space and into organelles by means of various Ca^{2+} ATPases located in the plasma membrane (PMCA pumps) and in organelle membranes [21,67]. Dysfunction of these pumps leads to a variety of diseases including cancer, hypertension, cardiac problems, and neurodegeneration [68–70]. During Ca^{2+} signaling [71,72] cytosolic Ca^{2+} levels show oscillations [73–75] but signaling can also occur as individual sparks or spikes [76]. Ca^{2+} oscillations have been found to occur in many cell types and differ considerably in their shapes and time scales with peak levels up to one order of magnitude higher than resting levels. Similar to the behavior of stimulated (perturbed) oscillatory homeostats as for example shown in Fig. 3b, Ca^{2+} oscillations have been found to increase their frequency upon increased stimulation of cells [73–75]. The frequency modulation of Ca^{2+} oscillations [77] is considered to be an important property for controlling biological processes [75]. The tight homeostatic regulation of cytosolic calcium combined with its oscillatory signaling suggests that oscillatory homeostats appear to be operative also under signaling conditions.

Although a variety of mathematical models have been suggested to describe Ca^{2+} oscillations [78–84], none of them have so far included an explicit homeostatic regulation of cytosolic Ca^{2+}. Fig. 10a shows how Ca^{2+} oscillations can be obtained based on an outflow homeostatic controller, which removes excess and toxic amounts of cytosolic Ca^{2+}. The model considers a stationary situation of an activated cell, where a Ca^{2+} channel is activated by an external signal leading to the inflow of Ca^{2+} into the cytosol. The increased Ca^{2+} levels in the cytosol induce an additional inflow of Ca^{2+} from the internal Ca^{2+} store, a mechanism termed "Calcium-Induced Calcium Release" (CICR) [85]. Both inflows are lumped together and described by rate constant k_1. The CICR flux is maintained by pumping cytosolic Ca^{2+} into the ER and keeping the Ca^{2+} load in the ER high. It should be mentioned that

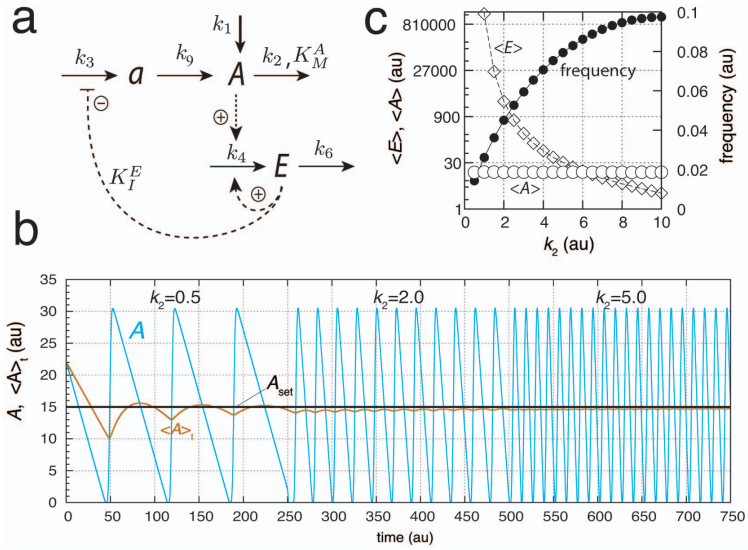

Figure 9. A limit-cycle model of controller motif 2 using autocatalysis as an integral controller. (a) Reaction scheme. Rate equations: $\dot{A} = k_1 - k_2 \cdot A/(K_M^A + A) + k_9 \cdot a$; $\dot{E} = k_4 \cdot A \cdot E - k_6 \cdot E$; $\dot{a} = k_3 \cdot K_I^E/(K_I^E + E) - k_9 \cdot a$. (b) Homeostatic response of the model for three different perturbations (k_2 values). For time t between 0 and 250 units, $k_2 = 0.5$, for t between 250 and 500 units, $k_2 = 2.0$, and for t between 500 and 750 units, $k_2 = 5.0$. $<A>$ at time t is defined as in Fig. 3. (c) $<A>$, $<E>$, and frequency values as a function of k_2. Simulation time for each data point is 2000.0 time units. Note that $<A>$ is kept at $A_{set} = 15.0$ (solid black line) independent of k_2. Rate constant values (in au): $k_1 = 0.0$, $k_3 = 20.0$, $k_4 = 0.1$, $K_I^E = 1.0$, $K_M^A = 1.0 \times 10^{-3}$, $k_6 = 1.5$, and $k_9 = 30.0$. Initial concentrations in (b): $A_0 = 22.09$, $E_0 = 1.71 \times 10^{10}$, and $a_0 = 4.0 \times 10^{-11}$. Initial concentrations in (c) for each data point are the same as in (b).
doi:10.1371/journal.pone.0107766.g009

the cause of the Ca^{2+} entry across the plasma membrane into the cytosol is not fully understood and different views have been expressed how this can occur [86,87].

For the sake of simplicity, the Ca^{2+} concentration in the ER is considered to be constant and only the pumping of Ca^{2+} from the cytosol into the extracellular space is taken into account without an increased cooperativity (Hill-function) with respect to the Ca^{2+} concentration. Fig. 10b shows the oscillations of cytosolic Ca^{2+} and the homeostat's performance at different inflow rates $k_1 \cdot Ca_{ext}^{2+}$ into the cytosol, which can reflect different external Ca^{2+} concentrations and/or different activation levels of the cell. As observed experimentally [74] the period of the oscillations decreases with increased external Ca^{2+} concentration or with an increased stimulation of the cell. As shown by $< Ca_{cyt}^{2+} >_t$ in Fig. 10b and by total $< Ca_{cyt}^{2+} >$ in Fig. 10c, on average, robust Ca^{2+} homeostasis is preserved at varying Ca^{2+} inflow rates. In the absence of oscillations the Ca^{2+} concentration is still kept at its homeostatic set-point (Fig. 10b).

Why Ca^{2+} oscillations? A non-oscillatory signaling mechanism by cytosolic Ca^{2+} would clearly be limited, because a homeostatic regulation of cytosolic Ca^{2+} would not allow varying Ca^{2+} levels as a function of external stimulation strengths. On the other hand, a frequency-based signaling due to an oscillatory Ca^{2+}-homeostat would overcome these limitations, because homeostasis is still maintained. This has been a brief outline on how Ca^{2+} oscillations may be understood on basis of oscillatory homeostasis. More detailed studies will be needed, for example by including the homeostatic aspect in existing models in order to investigate in more detail the implications oscillatory homeostats have on the regulatory role of Ca^{2+}.

p53 Signaling. p53 is a transcription factor with tumor suppressor properties. In more than half of all human tumors p53 is mutated and in almost all tumors p53 regulation is not functional [88]. In the presence of DNA damage and other abnormalities p53 initiates the removal of damaged cells by apoptosis. A central negative feedback component in p53 regulation is Mdm2, an ubiquitin E3 ligase, which leads to the proteasomal degradation of p53 and other tumor suppressors [89]. In the presence of DNA damage, p53 is upregulated by several mechanisms [90–92], and both p53 and Mdm2 have been found to oscillate [60]. An interesting feature of these oscillations is that their amplitude is highly variable, while their frequency is fairly constant [60]. The mean height of the oscillations was found to be constant [61]. It was also found that with an increased strength of DNA damaging radiation the number of cells with increased p53 cycles increased statistically [61]. Jolma *et al*. [51] used the basic negative feedback motif 5 (where A is p53 and E is Mdm2) and found that the influence of noise on the harmonic properties of the oscillations was able to describe the variable amplitudes and the approximately constancy of the period. Fourier analysis of the experimental data indeed showed that the p53-Mdm2 oscillations have a major harmonic component [93] supporting a quasi-harmonic character of the p53-Mdm2 oscillations. For such

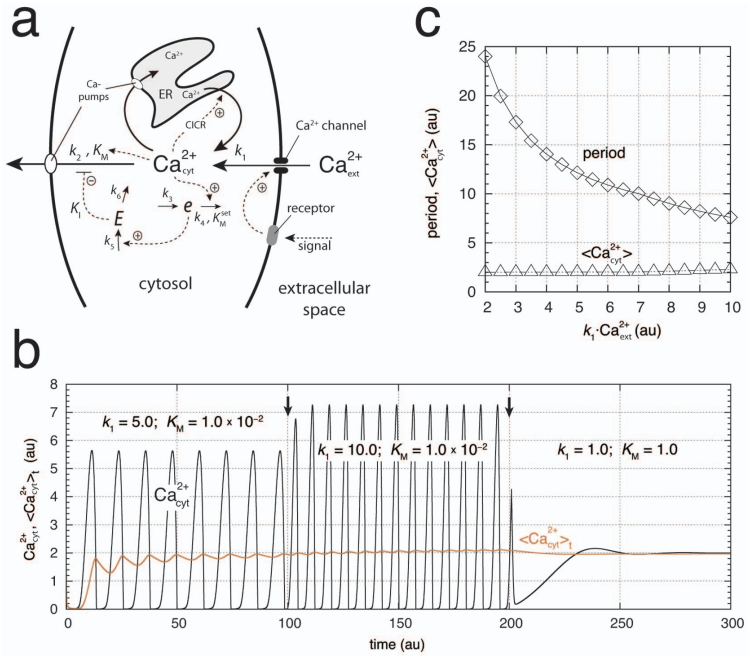

Figure 10. A homeostatic model of cytosolic Ca^{2+} oscillations. The model considers a stimulated non-excitable cell under stationary conditions using an extended version of outflow controller motif 6, where E is the controller molecule. Intermediate e has been included to get limit-cycle oscillations. Rate constant k_1 describes the total inflow of Ca^{2+} from the ER and from the extracellular space into the cytosol and reflects the strength of the stimulation. For the sake of simplicity the external Ca^{2+} concentration (Ca^{2+}_{ext}) is considered to be constant ($Ca^{2+}_{ext}=1.0$). Ca^{2+}_{cyt} denotes cytosolic Ca^{2+} and its concentration. (a) Reaction scheme. Rate equations: $Ca^{2+}_{cyt}=k_1-k_2\cdot K_I\cdot Ca^{2+}_{cyt}/((K_M+Ca^{2+}_{cyt})\cdot(K_I+E))$; $\dot{e}=k_3-k_4\cdot e\cdot Ca^{2+}_{cyt}/(K^{set}_M+e)$; $\dot{E}=k_5\cdot e-k_6\cdot E$. Rate constants: k_1, variable; $k_2=500$; $k_3=2.0$; $k_4=1.0$; $K^{set}_M=1.0\times10^{-6}$; $k_5=k_5=1.0$; $K_I=0.1$. The homeostat's set-point for Ca^{2+}_{cyt} is given by $k_3/k_4=2.0$. (b) Ca^{2+}_{cyt} oscillations and average cytosolic Ca^{2+} concentration, $<Ca^{2+}_{cyt}>_t$, at different stimulations and as a function of time t. Initial concentrations: $Ca^{2+}_{cyt,0}=1.772$, $e_0=2.908\times10^{-3}$; $E_0=1.643$. The quenching of oscillations at low k_1 is due to an increased K_M value. (c) Period length and average cytosolic Ca^{2+} concentration ($<Ca^{2+}_{cyt}>$) calculated after 2000 time units for different stimulation strengths (k_1 values). Same rate constants as in (b) with $K_M=0.01$. Initial concentrations for each calculated data point: $Ca^{2+}_{cyt,0}=6.126\times10^{-2}$, $e_0=30.693$; $E_0=28.806$.

doi:10.1371/journal.pone.0107766.g010

harmonic or quasi-harmonic oscillations our results (Figs. 2f and 5b) indicate that p53 is homeostatic regulated both in average concentration and in period length to allow to expose the system probably to an optimum amount of p53 during each cycle. Because the number of p53 cycles appear positively correlated with an increased exposure of damaging radiation, the total amount of released p53 may be related to a repair mechanism. A support along these lines comes from a recent study, which indicates that p53 oscillations lead to the recovery of DNA-damaged cells, while p53 levels kept at their peak value lead to senescence and to a permanent cell cycle arrest [94]. Thus, like for cytosolic Ca^{2+}, elevated and oscillatory p53 levels seem to remain under homeostatic control in order to mediate signaling events and information which appear to be encoded in the oscillations.

Homeostasis of the Circadian Period. Circadian rhythms play an important role in the daily and seasonal adaptation of organisms to their environment and act as physiological clocks [8,95,96]. Functioning as clocks, their period is under homeostatic regulation towards a variety of environmental influences, such as changing temperature (''temperature compensation'') or food supply (''nutritional compensation''). Circadian rhythms participate in the homeostatic control of a variety of physiological variables, such as body temperature, potassium content, hormone levels, as well as sleep [1,8,95,96]. As an example, potassium homeostasis in our bodies is under a circadian control, where potassium ion is daily excreted with peak values at the middle of the day [1].

One of the questions still under discussion is how the circadian period P is kept under homeostatic control as for example seen in temperature compensation. In the antagonistic balance approach [97] the variation of the period P with respect to temperature T, expressed as $\mathrm{d}\ln P/\mathrm{d}\ln T$, is given as the sum of the control

coefficients [36] $C_{k_i}^P = \partial \ln P / \partial \ln k_1$ multiplied with the RT-scaled activation energies E_i (R is the gas constant):

$$C_T^P = \frac{\mathrm{d}\ln P}{\mathrm{d}\ln T} = \sum_i \left(\frac{\partial \ln P}{\partial \ln k_i}\right) \cdot \left(\frac{\partial \ln k_i}{\partial \ln T}\right) = \sum_i C_{k_i}^P \cdot \left(\frac{E_i}{RT}\right) \qquad (11)$$

The sum runs over all temperature-dependent processes i with rate constants k_i, where the temperature dependence of the rate constants is expressed in terms of the Arrhenius equation $k_i = A_i \cdot \exp(-E_i/RT)$ [98]. A_i is the so-called pre-exponential factor and can, to a first approximation, be treated as temperature-independent. Eq. 11 applies to any kinetic model as long as the temperature dependence of the individual reactions are formulated in terms of the Arrhenius law.

The condition for temperature compensation is obtained by setting Eq. 11 to zero. Because in oscillatory systems the $C_{k_i}^P$'s have generally positive and negative values, there is a large set of balancing E_i combinations which can lead to temperature compensation. The various combinations can be considered to arise by evolutionary selective processes acting on the activation energies [99]. Because the temperature homeostasis of circadian rhythms involves a compensatory mechanism [100], which needs to be distinguished from temperature-independence where all $C_{k_i}^P$'s are zero, temperature compensation implies that there is a certain set of non-zero control coefficients with associated activation energies which (under ideal conditions) will satisfy the balancing condition $C_T^P = 0$ within a certain temperature range.

The argument has been made that the balancing condition $C_T^P = 0$ should be non-robust and should therefore not match the many examples where mutations have no influence on the circadian period [101]. However, it should be noted that Eq. 11 is *model-independent* and provides a general description how the period of an oscillator will depend on temperature in terms of the individual reactions defined by the k_i's. Robustness, on the other hand, is a property of the actual oscillator model, where the number of zero $C_{k_i}^P$'s can be taken as a measure for robustness. For the frequency controlled oscillators described earlier, there are certain regions in parameter space such as the shaded region in Fig. 7a, for which the oscillator's period is independent towards variations of those k_i's which lie within this region. As a result, frequency controlled oscillators will show an increased robustness against environmental factors that affect rate constants, such as pH, salinity, or temperature [43,98] and therefore appear to be candidates for modeling temperature compensation.

We feel that the here shown possibilities how robust concentration and period homeostasis can be achieved provide a new handle how the negative (and positive) feedback regulations in circadian pacemakers [102] can be approached. The incorporation of these principles into models of circadian rhythms may provide further insights how temperature compensation is achieved and how circadian rhythms participate in the homeostatic regulation of organisms [1,103].

Materials and Methods

Computations were performed by using Matlab/Simulink (mathwork.com) and the Fortran subroutine LSODE [104]. Plots were generated with gnuplot (www.gnuplot.info)/Matlab. To make notations simpler, concentrations of compounds are denoted by compound names without square brackets. All concentrations, time units, and rate constants are given in arbitrary units (au).

Supporting Information

File S1 (with Figs. S1–S14 and Eqs. S1–S57), contains derivation of the set-point under oscillatory conditions, construction of the *H*-function in conservative systems, the harmonic approximation of the frequency in conservative controllers, quenching of quasi-harmonic oscillations, and an alternative example of I_1/I_2 feedback leading to robust frequency control in a motif 2 based limit-cycle oscillator.
(PDF)

Author Contributions

Conceived and designed the experiments: KT TD PR. Performed the experiments: KT OA CHS IWJ XYN TD PR. Analyzed the data: KT OA CHS TD PR. Contributed reagents/materials/analysis tools: KT OA CHS IWJ XYN TD PR. Wrote the paper: KT TD PR.

References

1. Moore-Ede M (1986) Physiology of the circadian timing system: Predictive versus reactive homeostasis. Am J Physiol 250: R737–52.
2. Sterling P, Eyer J (1988) Allostasis: A new paradigm to explain arousal pathology. In: Fisher, S and Reason, J, editor, Handbook of Life Stress, Cognition and Health, New York: John Wiley & Sons. pp. 629–49.
3. Mrosovsky N (1990) Rheostasis. The Physiology of Change. New York: Oxford University Press.
4. Lloyd D, Aon M, Cortassa S (2001) Why Homeodynamics, Not Homeostasis? The Scientific World 1: 133–145.
5. Schulkin J (2004) Allostasis, Homeostasis and the Costs of Physiological Adaptation. Cambridge, Massachusetts: Cambridge University Press.
6. Cannon W (1929) Organization for Physiological Homeostatics. Physiol Rev 9: 399–431.
7. Cannon W (1939) The Wisdom of the Body. Revised and Enlarged Edition. New York: Norton.
8. Dunlap J, Loros J, DeCoursey P (2004) Chronobiology. Biological Timekeeping. Sunderland, MA: Sinauer.
9. Berridge M, Bootman M, Roderick H (2003) Calcium signalling: dynamics, homeostasis and remodelling. Nat Rev Mol Cell Biol 4: 517–529.
10. Bernard C (1957) An Introduction to the Study of Experimental Medicine. English translation of the 1865 French edition by Henry Copley Greene. Dover: Macmillan & Co., Ltd.
11. Langley LL, editor (1973) Homeostasis. Origins of the Concept. Stroudsbourg, Pennsylvania: Dowden, Hutchinson & Ross, Inc.
12. Hers H (1990) Mechanisms of blood glucose homeostasis. J Inherit Metab Dis 13: 395–410.
13. Osundiji M, Evans M (2013) Brain control of insulin and glucagon secretion. Endocrinol Metab Clin North Am 42: 1–14.
14. Powell T, Valentinuzzi M (1974) Calcium homeostasis: responses of a possible mathematical model. Med Biol Eng 12: 287–294.
15. El-Samad H, Goff J, Khammash M (2002) Calcium homeostasis and parturient hypocalcemia: an integral feedback perspective. J Theor Biol 214: 17–29.
16. Galton V, Wood E, St Germain E, Withrow C, Aldrich G, et al. (2007) Thyroid Hormone Homeostasis and Action in the Type 2 Deiodinase-Deficient Rodent Brain during Development. Endocrinology 148: 3080–3088.
17. O'Dea E, Barken D, Peralta R, Tran K, Werner S, et al. (2007) A homeostatic model of IκB metabolism to control constitutive NF-κB activity. Mol Syst Biol 3: 111.
18. Miller A, Smith S (2008) Cytosolic nitrate ion homeostasis: Could it have a role in sensing nitrogen status? Annals of Botany 101: 485–489.
19. Huang Y, Drengstig T, Ruoff P (2011) Integrating fluctuating nitrate uptake and assimilation to robust homeostasis. Plant, Cell and Environment 35: 917–928.
20. Jeong J, Guerinot M (2009) Homing in on iron homeostasis in plants. Trends in Plant Science 14: 280–285.
21. Hancock J (2010) Cell Signalling. New York: Oxford University Press.
22. Drengstig T, Jolma I, Ni X, Thorsen K, Xu X, et al. (2012) A Basic Set of Homeostatic Controller Motifs. Biophys J 103: 2000–2010.
23. Goldbeter A (1996) Biochemical Oscillations and Cellular Rhythms. Cambridge: Cambridge University Press.
24. Goldbeter A (2002) Computational approaches to cellular rhythms. Nature 420: 238–245.

25. Tyson J, Chen K, Novak B (2003) Sniffers, buzzers, toggles and blinkers: dynamics of regulatory and signaling pathways in the cell. Curr Opin Cell Biol 15: 221–231.
26. Tsai T, Choi Y, Ma W, Pomerening J, Tang C, et al. (2008) Robust, tunable biological oscillations from interlinked positive and negative feedback loops. Science 321: 126–9.
27. Maroto M, Monk N (2008) Cellular oscillatory mechanisms. New York: Springer.
28. Wiener N (1961) Cybernetics: or Control and Communication in the Animal and the Machine. Second Edition. Cambridge, Massachusetts: The MIT Press.
29. von Bertalanffy L (1975) Perspectives on General System Theory. New York: George Braziller.
30. Savageau M (1976) Biochemical Systems Analysis. A Study of Function and Design in Molecular Biology. Reading: Addison-Wesley.
31. Voit E (2013) Biochemical Systems Theory: A Review. ISRN Biomathematics 2013: 1–53.
32. Wiener N (1954) The Human Use of Human Beings. Boston: Houghton Mifflin and Da Capo Press.
33. Curtis H, Koshland M, Nims L, Quastler H (1957) Homeostatic Mechanisms. Brookhaven Symposia in Biology, Number 10. Upton, New York: Brookhaven National Laboratory.
34. Hughes G (1964) Homeostasis and Feedback Mechanisms. New York: Academic Press.
35. Milsum J (1966) Biological Control Systems Analysis. New York: McGraw-Hill.
36. Heinrich R, Schuster S (1996) The Regulation of Cellular Systems. New York: Chapman and Hall.
37. Sontag E (2004) Some new directions in control theory inspired by systems biology. Syst Biol 1: 9–18.
38. Alon U (2006) An Introduction to Systems Biology: Design Principles of Biological Circuits. New York: Chapman & Hall.
39. Ingalls B, Yi TM, Iglesias P (2006) Using Control Theory to Study Biology. In: Szallasi, Z and Stelling, J and Periwal, V, editor, System Modeling in Cellular Biology, Cambridge, Massachusetts: MIT Press. pp. 243–267.
40. Yi T, Huang Y, Simon M, Doyle J (2000) Robust perfect adaptation in bacterial chemotaxis through integral feedback control. PNAS 97: 4649–53.
41. El-Samad H, Goff J, Khammash M (2002) Calcium homeostasis and parturient hypocalcemia: an integral feedback perspective. J Theor Biol 214: 17–29.
42. Drengstig T, Ueda H, Ruoff P (2008) Predicting Perfect Adaptation Motifs in Reaction Kinetic Networks. J Phys Chem B 112: 16752–16758.
43. Ni X, Drengstig T, Ruoff P (2009) The control of the controller: Molecular mechanisms for robust perfect adaptation and temperature compensation. Biophys J 97: 1244–53.
44. Ang J, Bagh S, Ingalls B, McMillen D (2010) Considerations for using integral feedback control to construct a perfectly adapting synthetic gene network. J Theor Biol 266: 723–738.
45. Drengstig T, Ni X, Thorsen K, Jolma I, Ruoff P (2012) Robust Adaptation and Homeostasis by Autocatalysis. J Phys Chem B 116: 5355–5363.
46. Wilkie J, Johnson M, Reza K (2002) Control Engineering. An Introductory Course. New York: Palgrave.
47. Thorsen K, Drengstig T, Ruoff P (2013) Control Theoretic Properties of Physiological Controller Motifs. In: ICSSE 2013, IEEE International Conference on System Science and Engineering. Budapest, pp. 165–170.
48. Ang J, McMillen D (2013) Physical constraints on biological integral control design for homeostasis and sensory adaptation. Biophys J 104: 505–15.
49. Thorsen K, Drengstig T, Ruoff P (2014) Transepithelial glucose transport and Na^+/K^+ homeostasis in enterocytes: an integrative model. Am J Physiol - Cell Physiol: in press.
50. Andronov A, Vitt A, Khaikin S (1966) Theory of Oscillators. New York: Dover.
51. Jolma I, Ni X, Rensing L, Ruoff P (2010) Harmonic oscillations in homeostatic controllers: Dynamics of the p53 regulatory system. Biophys J 98: 743–52.
52. Lotka A (1910) Contribution to the Theory of Periodic Reaction. J Phys Chem 14: 271–74.
53. Lotka A (1920) Undamped Oscillations Derived from the Law of Mass Action. J Am Chem Soc 42: 1595–99.
54. Goodwin B (1963) Temporal Organization in Cells. London: Academic Press.
55. Goodwin B (1965) Oscillatory behavior in enzymatic control processes. In: Weber, G, editor, Advances in Enzyme Regulation, Vol. 3, Oxford, UK: Pergamon Press. pp. 425–438.
56. Griffith J (1968) Mathematics of cellular control processes I. Negative feedback to one gene. J Theor Biol 20: 202–208.
57. Rensing L, Ruoff P (2002) Temperature effect on entrainment, phase shifting, and amplitude of circadian clocks and its molecular bases. Chronobiology International 19: 807–864.
58. Iwasaki K, Liu D, Thomas J (1995) Genes that control a temperature-compensated ultradian clock in *Caenorhabditis elegans*. PNAS 92: 10317–10321.
59. Dowse H, Ringo J (1987) Further evidence that the circadian clock in Drosophila is a population of coupled ultradian oscillators. J Biol Rhythms 2: 65–76.
60. Geva-Zatorsky N, Rosenfeld N, Itzkovitz S, Milo R, Sigal A, et al. (2006) Oscillations and variability in the p53 system. Mol Syst Biol 2: 2006 0033.
61. Lahav G (2008) Oscillations by the p53-Mdm2 Feedback Loop. In: Maroto, M and Monk, NAM, editor, Cellular Oscillatory Mechanisms, New York: Landes Bioscience and Springer Science+Business Media. pp. 28–38.
62. Higgins J (1967) Oscillating reactions. Industrial & Engineering Chemistry 59: 18–62.
63. Franck U (1980) Feedback Kinetics in Physicochemical Oscillators. Berichte der Bunsengesellschaft für Physikalische Chemie 84: 334–41.
64. Eiswirth M, Freund A, Ross J (1991) Mechanistic classification of chemical oscillators and the role of species. Adv Chem Phys 80: 127–199.
65. Goldbeter A (2002) Computational approaches to cellular rhythms. Nature 420: 238–245.
66. Novák B, Tyson J (2008) Design principles of biochemical oscillators. Nat Rev Mol Cell Biol 9: 981–991.
67. Marks F, Klingmüller U, Müller-Decker K (2009) Cellular Signal Processing. An Introduction to the Molecular Mechanisms of Signal Transduction. New York: Garland Science.
68. Bodalia A, Li H, Jackson M (2013) Loss of endoplasmic reticulum Ca^{2+} homeostasis: contribution to neuronal cell death during cerebral ischemia. Acta Pharm Sinica 34: 49–59.
69. Giacomello M, De Mario A, Scarlatti C, Primerano S, Carafoli E (2013) Plasma membrane calcium ATPases and related disorders. Int J Biochem & Cell Biol 45: 753–762.
70. Schapira A (2013) Calcium dysregulation in Parkinson's disease. Brain 136: 2015–2016.
71. Carafoli E (2002) Calcium signaling: A tale for all seasons. PNAS 99: 1115–1122.
72. Berridge M, Bootman M, Roderick H (2003) Calcium signalling: dynamics, homeostasis and remodelling. Nat Rev Mol Cell Biol 4: 517–529.
73. Woods H, Cuthbertson K, Cobbold P (1986) Repetitive transient rises in cytoplasmic free calcium in hormone-stimulated hepatocytes. Nature 319: 600–602.
74. Berridge M, Galione A (1988) Cytosolic calcium oscillators. The FASEB Journal 2: 3074–3082.
75. Parekh A (2011) Decoding cytosolic Ca^{2+} oscillations. Trends Biochemical Sciences 36: 78–87.
76. Cheng H, Lederer W (2008) Calcium Sparks. Physiol Rev 88: 1491–1545.
77. De Koninck P, Schulman H (1998) Sensitivity of CaM Kinase II to the Frequency of Ca^{2+} oscillations. Science 279: 227–230.
78. Goldbeter A, Dupont G, Berridge M (1990) Minimal model for signal-induced Ca2+ oscillations and for their frequency encoding through protein phosphorylation. PNAS 87: 1461–1465.
79. Dupont G, Berridge M, Goldbeter A (1991) Signal-induced Ca^{2+} oscillations: Properties of a model based on Ca^{2+}-induced Ca^{2+} release. Cell Calcium 12: 73–85.
80. Schuster S, Marhl M, Höfer T (2002) Modelling of simple and complex calcium oscillations. From single-cell responses to intercellular signalling. Eur J Biochem 269: 1333–1355.
81. Sneyd J, Tsaneva-Atanasova K, Yule D, Thompson J, Shuttleworth T (2004) Control of calcium oscillations by membrane fluxes. PNAS 101: 1392–6.
82. Politi A, Gaspers L, Thomas A, Höfer T (2006) Models of IP3 and Ca2+ oscillations: frequency encoding and identification of underlying feedbacks. Biophys J 90: 3120–33.
83. Putney J, Bird G (2008) Cytoplasmic calcium oscillations and store-operated calcium influx. J Physiol 586: 3055–9.
84. Knoke B, Bodenstein C, Marhl M, Perc M, Schuster S (2010) Jensen's inequality as a tool for explaining the effect of oscillations on the average cytosolic calcium concentration. Theory Biosci 129: 25–38.
85. Berridge M (2005) Unlocking the secrets of cell signaling. Annu Rev Physiol 67: 1–21.
86. Shuttleworth T (1999) What drives calcium entry during Ca_i^{2+} oscillations?–challenging the capacitative model. Cell calcium 25: 237–246.
87. Bird G, Putney J (2005) Capacitative calcium entry supports calcium oscillations in human embryonic kidney cells. J Physiol 562: 697–706.
88. Levine A (1997) p53, the cellular gatekeeper for growth and division. Cell 88: 323–31.
89. Fu W, Ma Q, Chen L, Li P, Zhang M, et al. (2009) MDM2 acts downstream of p53 as an E3 ligase to promote FOXO ubiquitination and degradation. J Biol Chem 284: 13987–4000.
90. Michael D, Oren M (2003) The p53-Mdm2 module and the ubiquitin system. Semin Cancer Biol 13: 49–58.
91. Stommel J, Wahl G (2004) Accelerated MDM2 auto-degradation induced by DNA-damage kinases is required for p53 activation. EMBO J 23: 1547–56.
92. Asher G, Lotem J, Kama R, Sachs L, Shaul Y (2002) NQO1 stabilizes p53 through a distinct pathway. PNAS 99: 3099–104.
93. Geva-Zatorsky N, Dekel E, Batchelor E, Lahav G, Alon U (2010) Fourier analysis and systems identification of the p53 feedback loop. PNAS 107: 13550–13555.
94. Purvis J, Karhohs K, Mock C, Batchelor E, Loewer A, et al. (2012) p53 dynamics control cell fate. Science 336: 1440–1444.
95. Bünning E (1963) The Physiological Clock. Berlin: Springer-Verlag.
96. Edmunds L (1988) Cellular and Molecular Bases of Biological Clocks. New York: Springer-Verlag.
97. Ruoff P (1992) Introducing temperature-compensation in any reaction kinetic oscillator model. J Interdiscipl Cycle Res 23: 92–99.
98. Noggle J (1996) Physical Chemistry. Third Edition. New York: Harper Collins.

99. Ruoff P (1994) General homeostasis in period-and temperature-compensated chemical clock mutants formed by random selection conditions. Naturwissenschaften 81: 456–459.
100. Zimmerman W, Pittendrigh C, Pavlidis T (1968) Temperature compensation of the circadian oscillation in *Drosophila pseudoobscura* and its entrainment by temperature cycles. J Insect Physiol 14: 669–684.
101. Hong C, Conrad E, Tyson J (2007) A proposal for robust temperature compensation of circadian rhythms. PNAS 104: 1195–1200.
102. Dunlap J (1999) Molecular bases for circadian clocks. Cell 96: 271–290.
103. Bonny O, Firsov D (2009) Circadian clock and the concept of homeostasis. Cell Cycle 8: 4015–14.
104. Radhakrishnan K, Hindmarsh A (1993) Description and Use of LSODE, the Livermore Solver for Ordinary Differential Equations. NASA Reference Publication 1327, Lawrence Livermore National Laboratory Report UCRL-ID-113855. Cleveland, OH 44135-3191: National Aeronautics and Space Administration, Lewis Research Center.

Paper 2:
The Organization of Controller Motifs Leading to Robust Plant Iron Homeostasis

PLOS ONE

RESEARCH ARTICLE

The Organization of Controller Motifs Leading to Robust Plant Iron Homeostasis

Oleg Agafonov[1], Christina Helen Selstø[1], Kristian Thorsen[2], Xiang Ming Xu[1], Tormod Drengstig[2], Peter Ruoff[1]*

1 Centre for Organelle Research, University of Stavanger, Stavanger, Norway, **2** Department of Electrical Engineering and Computer Science, University of Stavanger, Stavanger, Norway

* peter.ruoff@uis.no

OPEN ACCESS

Citation: Agafonov O, Selstø CH, Thorsen K, Xu XM, Drengstig T, Ruoff P (2016) The Organization of Controller Motifs Leading to Robust Plant Iron Homeostasis. PLoS ONE 11(1): e0147120. doi:10.1371/journal.pone.0147120

Editor: Stephan Neil Witt, Louisiana State University Health Sciences Center, UNITED STATES

Received: April 15, 2015

Accepted: December 29, 2015

Published: January 22, 2016

Data Availability Statement: All relevant data are within the paper and its Supporting Information files.

Funding: This research was funded by Program Area Fund "Organelle Biology" and the Program Area Fund "Biomedical data analysis group" from the Faculty of Science and Technology, University of Stavanger (https://www.uis.no/fakulteter-institutter-og-sentre/). The funders had no role in study design, data collection and analysis, decision to publish, or preparation of the manuscript.

Competing Interests: The authors have declared that no competing interests exist.

Abstract

Iron is an essential element needed by all organisms for growth and development. Because iron becomes toxic at higher concentrations iron is under homeostatic control. Plants face also the problem that iron in the soil is tightly bound to oxygen and difficult to access. Plants have therefore developed special mechanisms for iron uptake and regulation. During the last years key components of plant iron regulation have been identified. How these components integrate and maintain robust iron homeostasis is presently not well understood. Here we use a computational approach to identify mechanisms for robust iron homeostasis in non-graminaceous plants. In comparison with experimental results certain control arrangements can be eliminated, among them that iron homeostasis is solely based on an iron-dependent degradation of the transporter IRT1. Recent IRT1 overexpression experiments suggested that IRT1-degradation is iron-independent. This suggestion appears to be misleading. We show that iron signaling pathways under IRT1 overexpression conditions become saturated, leading to a breakdown in iron regulation and to the observed iron-independent degradation of IRT1. A model, which complies with experimental data places the regulation of cytosolic iron at the transcript level of the transcription factor *FIT*. Including the experimental observation that FIT induces inhibition of IRT1 turnover we found a significant improvement in the system's response time, suggesting a functional role for the FIT-mediated inhibition of IRT1 degradation. By combining iron uptake with storage and remobilization mechanisms a model is obtained which in a concerted manner integrates iron uptake, storage and remobilization. In agreement with experiments the model does not store iron during its high-affinity uptake. As an iron biofortification approach we discuss the possibility how iron can be accumulated even during high-affinity uptake.

Introduction

Iron is an essential element required by all organisms, but becomes toxic at higher levels. Iron is needed as a cofactor for many enzymes and proteins. To provide a sufficient level of available iron in the cytosol without leading to toxicity, iron is under homeostatic control. Plants have

also the problem that iron in the soil under aerobic conditions is generally present as low-soluble iron(III)-oxide forms which require a high-affinity transport system for its uptake. To cope with these difficulties plants have developed two main strategies for iron-uptake, one termed strategy I for non-graminaceous plants (plants not belonging to the grass family) and the other termed strategy II for graminaceous plants [1]. During recent years considerable advances have been made to identify molecular components of the iron uptake and storage mechanisms [2–7]. In this work we focus on iron regulation of strategy I plants which includes the model plant *Arabidopsis thaliana*. Fig 1 gives an overview of the iron flow, storage, and regulatory components in these plants. IRT1 has been identified as the major transporter responsible for the high-affinity uptake of iron from the soil [8–10].

Prior to the uptake of iron(II) by IRT1, iron(III)'s solubility in the soil is increased by secreting H^+ using H^+-ATPases followed by the reduction of iron(III) to iron(II) by a membrane-bound ferric reductase oxidase (FRO2). The helix-loop-helix (bHLH) transcription factor FIT [11] has been found to be required for the iron deficiency response in Arabidopsis, where several iron regulated genes appear under the control of FIT [12]. FIT interacts with two other bHLH proteins, AtbHLH38 and AtbHLH39, where the transcription of *FRO2* and *IRT1* are regulated by FIT/AtbHLH38 and FIT/AtbHLH39 [13]. Once inside the cell, iron(II) is complexed and buffered by several organic compounds, among them Nicotianamine (NA), which is considered to stabilize predominantly Fe(II) but also Fe(III) [14] and appears to be an important transport form of iron in all plants [15–19].

By using *IRT1* knockout plants Vert et al. [10] observed that IRT1 is necessary for plant survival in the presence of low external iron levels, but that the absence of IRT1 plants can be counteracted by adding iron into the watering solution.

In accordance with results from metal-ion homeostasis in yeast [20], Connolly et al. [21] suggested a homeostasis-mediating mechanism based on the iron-dependent degradation of IRT1, where the amino acids K164 or K171 in IRT1 have been found to be necessary for IRT1 turnover [22]. This suggestion is supported by experiments [21] showing that the level of IRT1 (and its transcript) is high at low external iron concentrations, but declines once plants are transferred to sufficient iron conditions. In further agreement with an iron-dependent IRT1--degradation mechanism, 35S-*IRT1* plants which overexpress IRT1 in an Arabidopsis wild-type background have higher *IRT1* transcript levels, while protein levels were low and comparable to wild-type plants [22].

Barberon et al. [23] observed that overexpression of IRT1 in an *IRT1*-knockout background leads to elevated iron levels and toxicity. Furthermore, the IRT1 degradation rate under such conditions was found to be independent of the actual iron supply, in contrast to the earlier suggestion by Connolly et al. [21] of an iron-dependent degradation of IRT1. Despite the discrepancy whether IRT1 is subject to an iron-dependent degradation or not, there is a consensus that in roots mRNA and protein levels of *IRT1* and *FIT* are inversely correlated to the amount of external iron [10, 12, 21–23]. In other words, a sufficient supply of iron leads to low levels of *IRT1* and *FIT* transcripts and low levels of the corresponding proteins. Decreased supply levels of iron result in the up-regulation of both the *IRT1/FIT* transcripts and the corresponding proteins.

Chloroplasts require large amounts of iron due to photosynthesis, heme biosynthesis and Fe-S cluster synthesis. Besides chloroplasts, also mitochondria have a large demand for iron due to iron-containing respiratory enzymes. It is therefore expected that also these iron-requiring organelles have mechanisms to maintain iron homeostasis. Comparative studies of determined iron levels in roots and leaves performed with different wild-type and mutant plants show that roots have generally an iron content which is approximately one order of magnitude higher than in leaves (S1 Table). This indicates that in roots protective and homeostatic

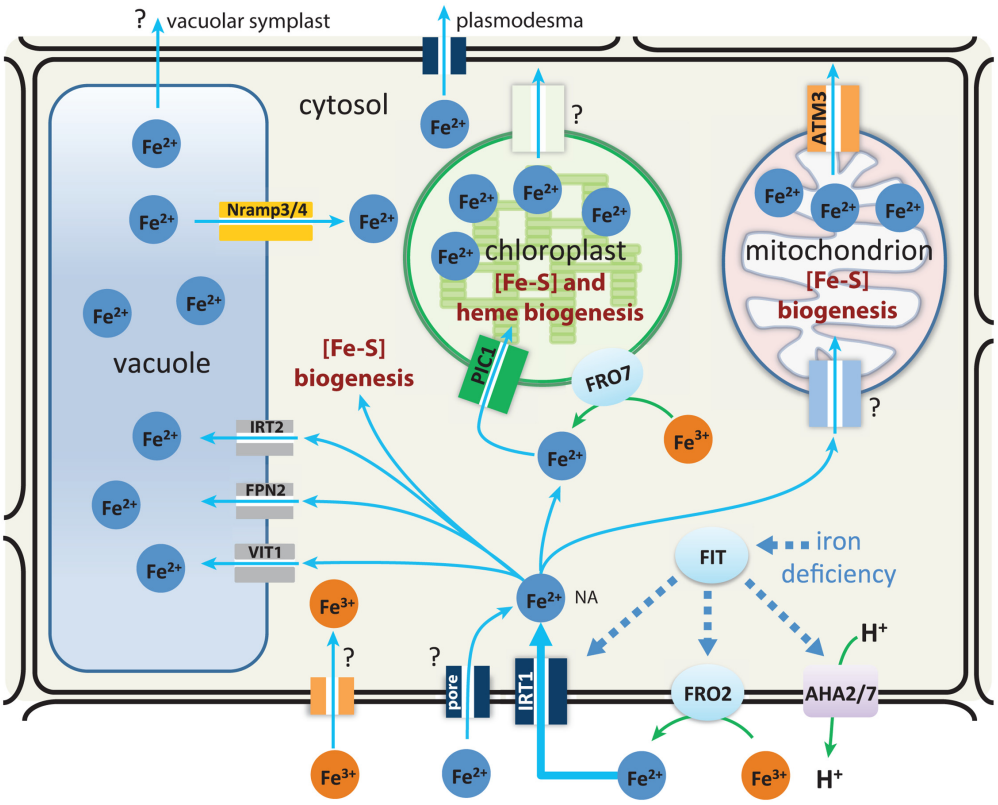

Fig 1. Regulatory components of iron homeostasis in non-graminaceous plant cells. In the presence of iron deficiency the transcription factor FIT activates the excretion of H^+ by ATPases AHA2/7, which leads to an increased solubility of Fe(III). FIT also induces the reduction of solubilized Fe(III) to Fe(II) by the membrane-bound enzyme FRO2 and activates the high-affinity transporter IRT1 and the uptake of Fe(II). Iron is stored in different organelles with the vacuole as a major store. Several transporters which move iron into organelles and the vacuole have been identified (see main text). Iron transport to other parts of the plant occurs in complexed form with the water flow, i.e. via the cytosolic symplast connected by plasmodesmata and perhaps also by a transport route using a vacuolar symplast. Transporter candidates for iron remobilization from the store are Nramp3/4.

doi:10.1371/journal.pone.0147120.g001

mechanisms need to be present in order to avoid iron toxicity while delivering iron to other parts of the plant.

The aim of this work is to rationalize, in agreement with experimental results, the organization of controller motifs, which lead to robust iron homeostasis in root cells during iron uptake, its assimilation and transport to other parts of the plant, as well as iron storage and its remobilization from the store. Before dealing with the aspects of iron regulation we give an overview of the concept of integral control, its importance for robust homeostasis and the kinetic implementations which lead to integral control in biochemical systems.

Kinetic Requirements for Robust Homeostasis

The term *homeostasis* was introduced by Cannon in 1929 [24]. According to Cannon's definition homeostasis maintains the steady states of compounds in an organism/cell at approximately constant and stable levels, where variations of these compounds may occur within certain but narrow limits [24–26]. Homeostasis is a concept which is closely related to the internal stability of organisms and cells [27]. Langley [26] provided an interesting compilation of key contributions which led to the development of the concept.

In control engineering it is well established that *integral control* (see e.g. [28]), as part of a negative feedback loop, will keep the level of a certain variable precisely at a given set-point even in the presence of environmental perturbations. Although the concept of integral control has extensively been used in industrial control processes since the last century its relevance with respect to the regulation of biochemical processes in organisms and cells was only relative recently pointed out [29] and studied in relation to several homeostatic processes [30–39].

We have been studying the kinetic requirements which lead to integral control in biochemical systems containing a negative feedback [33, 37, 38] including an extension of the homeostasis concept to oscillatory conditions [40]. To illustrate the effect of negative feedback regulation on a compound A consider the process:

$$\xrightarrow{k_1} A \xrightarrow{k_2} \tag{1}$$

where k_1 and k_2 are rate constants describing the inflow and outflow of A according to the rate equation:

$$\dot{A} = k_1 - k_2 \cdot A \tag{2}$$

Because the steady state level of A depends both on k_1 and k_2, i.e., $A_{ss} = k_1/k_2$, it is obvious that A_{ss} is not under homeostatic control.

To keep the level of A at a certain set-point A_{set}, integral control is invoked as part of a negative feedback controller loop. In integral control (Fig 2a) the difference (error e) between the actual value of A and its set-point A_{set}, is calculated and integrated over time. The integrated error E is then used to compensate for perturbations in the concentration of A (for example when k_1 or k_2 are changed by environmental influences), which would drive the level of A away from its set-point. The controller loops can be divided into two classes, which we have termed *inflow* and *outflow* controllers [37]. An inflow controller provides a compensatory flux, which *adds A* from some other source to the system when uncontrolled perturbations decrease the level of A. In an outflow controller the situation is reversed, i.e., the compensatory flux *removes A* from the system by excreting A or moving it to a store [37]. Although a negative feedback loop is necessary to obtain robust homeostasis, negative feedback alone is not sufficient unless integral control is invoked. A justification of this statement is given in S1 Text. To illustrate the kinetic condition that leads to integral control and robust homeostasis, Fig 2b shows an inflow controller (motif 1, Ref. [37]), where integral control is implemented by an enzyme termed E_{set}, which removes E under close to saturation conditions (low $K_M^{E_{set}}$ value). The name E_{set} reflects the enzyme's importance for determining the set-point of A. The dashed arrows in Fig 2b with positive signs going from A to E indicate signaling events where A activates enzyme E_{set}. In cybernetic terms the signaling from A to E is termed *measurement* and is part of the A-sensing mechanism of the controller. The dashed arrows from E to A indicate the signaling event where E activates the synthesis of A. In cybernetic terms this represents the *control input*, which is part of the compensatory mechanism and maintains homeostasis in A. For the sake of simplicity we assume here that the signaling events originating from A and E are proportional

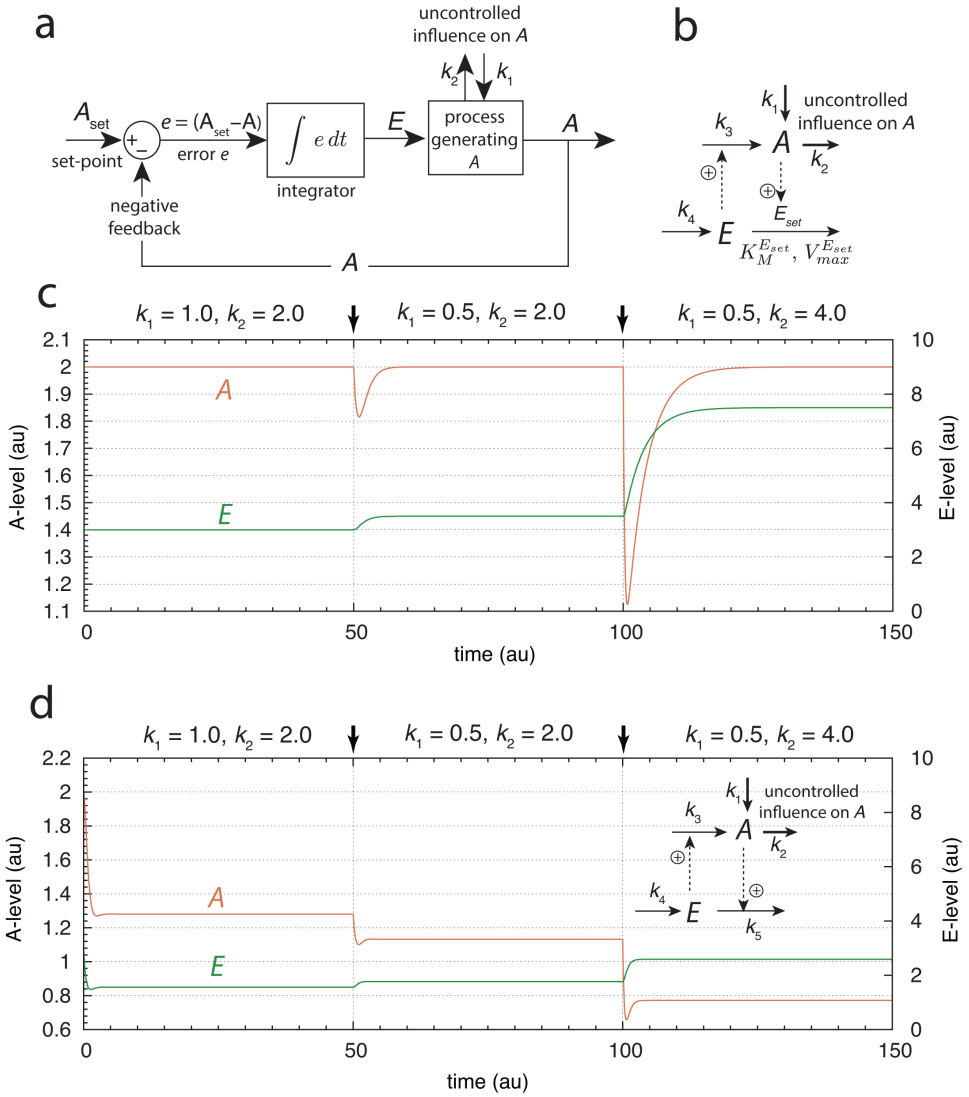

Fig 2. Negative Feedback Loops with and without Integral Control. (a) Flow diagram illustrating the concept of integral control. The regulated value of *A* is compared with its set-point A_{set} and the integral *E* of the error *e* between *A* and its set-point is calculated. *E* is fed into the process to compensate uncontrolled inflow or outflow to and from *A*. (b) Scheme of an inflow controller, where integral control is represented by removing *E* with enzyme E_{set}, which is

saturated with substrate E and reflected by a low $K_M^{E_{set}}$ value. (c) Illustration of robust homeostasis in A for different k_1, k_2 combinations with set-point $k_1/V_{max}^{E_{set}}$ Eq (6). The change in k_1 and k_2 occurs at t = 50.0 and t = 100.0 time units indicated by the arrows. Rate constants: k_3 = 1.0, k_4 = 2.0, $V_{max}^{E_{set}} = 1.0$, and $K_M^{E_{set}} = 1 \times 10^{-4}$. Initial concentrations: A_0 = 2.0, and E_0 = 3.0. (d) Same negative feedback loop as in (b), but without integral control. The saturating kinetics of the E-removal is now replaced by a first-order process with respect to E with k_5 = 1.0. The system is now not able to maintain robust homeostasis in A. Initial concentrations and the other rate constants are as in (c).

doi:10.1371/journal.pone.0147120.g002

to the concentrations of A and E, respectively. The rate equations for A and E are written as:

$$\dot{A} = k_1 + k_3 \cdot E - k_2 \cdot A \tag{3}$$

$$\dot{E} = k_4 - A \cdot \frac{V_{max}^{E_{set}} \cdot E}{K_M^{E_{set}} + E} \tag{4}$$

Eq (4) determines the set-point for A. For $K_M^{E_{set}} \ll E$, the removal of E becomes zero-order with respect to E and Eq (4) simplifies to

$$\dot{E} \approx k_4 - V_{max}^{E_{set}} \cdot A = V_{max}^{E_{set}} \left(\frac{k_4}{V_{max}^{E_{set}}} - A \right) = V_{max}^{E_{set}} (A_{set} - A) \tag{5}$$

We see that $\dot{E}$ is proportional to the error $e = (A_{set} - A)$, and as required by integral control, the concentration of E is proportional to the integrated error (Fig 2a).

Under these conditions, the steady state concentration in A is given as

$$A_{ss} = A_{set} = k_4 / V_{max}^{E_{set}} \tag{6}$$

and is independent of k_1 and k_2. Fig 2c illustrates the homeostatic behavior of the system when k_1 and k_2 values are varied.

The inset in Fig 2d shows the same negative feedback structure as in Fig 2b, but without the implementation of an integral controller. The zero-order removal of E in Fig 2b is now replaced by first-order kinetics:

$$\dot{E} = k_4 - k_5 \cdot A \cdot E \tag{7}$$

Because integral control with a defined set-point is lacking the steady state concentration of A (A_{ss}) depends now on all four rate constants:

$$A_{ss} = \frac{k_1 + \sqrt{\frac{k_1^2 \cdot k_5 + 4 k_2 \cdot k_3 \cdot k_4}{k_5}}}{2 \cdot k_2} \tag{8}$$

Fig 2d shows the numerical results when the same changes in k_1 and k_2 are applied as in Fig 2c, but without integral control. In this case robust homeostasis cannot be maintained, although the steady state value of A for the negative feedback loop alone (Fig 2d) is higher than it would be without any negative feedback. Without a negative feedback the steady state would be $A_{ss} = k_1/k_2$, i.e., 0.5, 0.25 and 0.125 for the three different combinations of k_1 and k_2 in Fig 2d.

As we will show below, a negative feedback without integral control can still significantly affect another integral controller's behavior by improving (decreasing) its response time while keeping the set-point unchanged.

Materials and Methods

The experimental results on mRNA and protein levels we here will refer to have been reported in form of relative grayness levels of gel- and/or Western blots. Because experimentally determined cellular concentrations and associated rate parameters of compounds are still unknown, concentrations, rate constant and parameter values used in the models are kept in arbitrary units (au). However, to make the correspondence between modeling and experimental results as close as possible modeling results are reported, as experiments, in a blot-wise manner where gray levels reflect uncalibrated concentrations. According to the agreed convention in plant molecular biology, mRNAs are referred to in capitalized italic letters, while protein names are written capitalized and non-italic. Plants that had their *IRT1-gene* knocked-out are referred to with small italic letters, i.e. *irt1*. Computations were performed by using the Fortran subroutine LSODE [41] and compared with corresponding Matlab/Simulink calculations. Plots were generated with gnuplot (www.gnuplot.info) and Adobe Illustrator (adobe.com). To make notations simpler, concentrations of compounds are denoted by compound names without square brackets. To make the computational results available, Matlab files are provided as Supporting Information.

Results and Discussion

Negative Feedback with an Iron-dependent IRT1 degradation

We first investigated the suggestion by Connolly et al. [21] that IRT1 is degraded in an iron-dependent manner in comparison with the observation by Barberon et al. [23] that overexpression of IRT1 leads to an iron-independent degradation of IRT1.

To understand these apparently opposing viewpoints we studied the model shown in Fig 3a, where iron homeostasis during iron uptake is based on an iron-dependent removal of the transporter protein IRT1. The inflow control structure of the model (the rate equations are given in S2 Text) is able to maintain homeostasis when the cellular demand for iron is relatively high.

For simplicity, the (high-affinity) uptake rate of iron by IRT1 is described as

$$j_{\mathrm{IRT1}}^{\mathrm{Fe-uptake}} = k_1 \cdot \mathrm{IRT1} \cdot \mathrm{Fe_{ext}} \tag{9}$$

where $j_{\mathrm{IRT1}}^{\mathrm{Fe-uptake}}$ is proportional to the concentration of the transporter IRT1 and to the concentration of external iron, $\mathrm{Fe_{ext}}$. Because the IRT1-based uptake of iron in general will show saturation kinetics, Eq (9) implies that iron uptake by IRT1 is far from saturation. By using isothermal titration calorimetry Grossoehme et al. [42] found that Fe^{2+} and other IRT1-transported metal-ions show a relative weak binding to IRT1 and that the description by Eq (9) appears approximately valid. To further simplify the model, the flux which maintains the cell's need for iron and the transport flux of iron from the root to other parts of the plant are lumped together and described by the term $j_{\mathrm{Fe\text{-}assim}}$

$$j_{\mathrm{Fe-assim}} = k_2 \cdot \mathrm{Fe_{cyt}} \tag{10}$$

The *IRT1*-mRNA (variable *IRT1*) is considered to be synthesized at a constant rate (k_3) and degraded by a first-order process with respect to *IRT1*. The IRT1-transporter (variable IRT1) synthesis rate is proportional to the amount of *IRT1* transcript (variable *IRT1*). IRT1-protein is considered to be removed in an iron-dependent manner, where iron binds and thereby activates the IRT1-degrading enzyme E_{set}. The fraction of activated enzyme removing IRT1 is given as f_a^{Fe}:

$$f_a^{\mathrm{Fe}} = \frac{\mathrm{Fe_{cyt}}}{K_a^{\mathrm{Fe}} + \mathrm{Fe_{cyt}}} \tag{11}$$

where K_a^{Fe} is the dissociation constant between $\mathrm{Fe_{cyt}}$ and the nonactive form of the

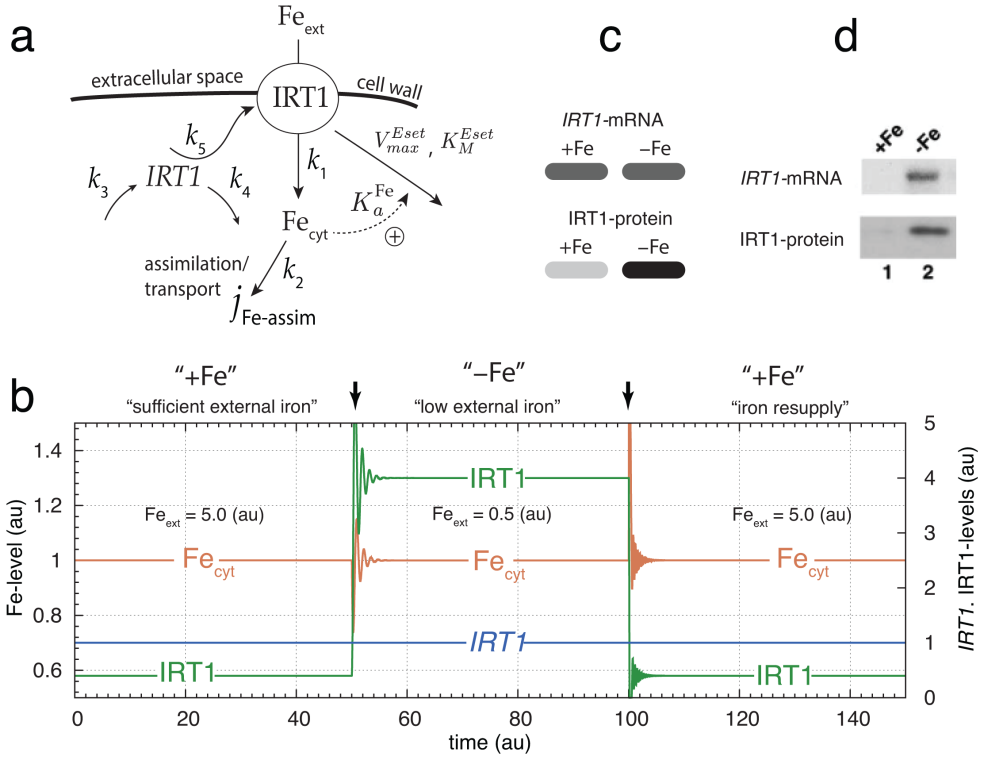

Fig 3. Regulatory loop of high affinity iron uptake and cytosolic iron homeostasis based on an iron-dependent IRT1 degradation. (a) Scheme of the control loop. Fe_{ext} and Fe_{cyt} denote external and cytosolic iron, respectively. *IRT1* and IRT1 denote mRNA and its protein, respectively. The extracellular iron concentration, Fe_{ext}, is allowed to change to different but constant levels. (b) Homeostasis in cytosolic iron levels (Fe_{cyt}) with respect to sufficient and low external iron conditions. The set-point for the level of cytosolic iron is given by Eq (12) and is arbitrarily set to $Fe_{cyt}^{set} = 1.0$. In the first phase (time $t = 0$ to $t = 50$) $Fe_{ext} = 5.0$ and relative high. To keep iron at its homeostatic set-point during this phase the required concentration of IRT1 is relative low. In the second phase starting at $t = 50$ (arrow) Fe_{ext} is reduced to 0.5. Due to this reduction the IRT1 level is increased to keep the cytosolic iron concentration close at its set-point. In the third phase ($t = 100$ to $t = 150$) iron is resupplied and IRT1 levels decrease again. Other rate parameters remain unchanged during the three phases, i.e. $k_1 = 1.0$, $k_2 = 2.0$, $k_3 = 1.0 \times 10^2$, $k_4 = 1.0 \times 10^2$, $k_5 = 1.0 \times 10^2$, $V_{max}^{Eset} = 2.0 \times 10^2$, $K_M^{Eset} = 1.0 \times 10^{-4}$, and $K_a^{Fe} = 1.0$. Initial concentrations are $Fe_{cyt,0} = 1.0$, $IRT1_{0=1.0}$, and $IRT1_{0=0.4}$. (c) Representation of results in a 'blot-like' manner. +Fe and –Fe denote sufficient and low external ion conditions, respectively. For each component (*IRT1*, IRT1) the gray levels (0–100%) reflect the relative *IRT1*/IRT1 concentrations at +Fe and –Fe conditions. (d) Experimental data, slightly rearranged from Fig 6A in Ref. [21].

doi:10.1371/journal.pone.0147120.g003

IRT1-degrading enzyme not having bound IRT1. The binding event between iron and the IRT1-removing enzyme can be seen as part of an iron sensing mechanism, where the amount of IRT1 reflects the concentration of cytosolic iron and may mediate this information to the regulation of other substances. Such a mechanism appears to be present to nitrate uptake in Arabidopsis where the nitrate transporters influences other uptake mechanisms [43, 44]. Due to the binding of iron to E_{set}, f_a^{Fe} has saturation properties. IRT1-degradation by the activated enzyme is described by a Michaelis-Menten type of reaction with a relative strong binding to its substrate, i.e. with a relative low $K_M^{E_{set}}$ value. Experiments indicate that IRT1 is degraded by the proteasome after ubiquinitation [23, 45]. The kinetics of the iron-induced IRT1 removal defines the set-point for cytosolic iron homeostasis. Setting both $\dot{\mathrm{IRT1}} = 0$ and $\dot{IRT}1 = 0$ together with $K_M^{E_{set}} \ll$ IRT1, gives the following expression for the set-point (see S2 Text):

$$\mathrm{Fe}_{\mathrm{cyt},set} = \frac{k_3 \cdot k_5 \cdot K_a^{\mathrm{Fe}}}{k_4 \cdot V_{max}^{E_{set}} - k_3 \cdot k_5} \tag{12}$$

The condition $K_M^{E_{set}} \ll$ IRT1 represents an idealization used here for illustration, such that the controlled variable (here cytosolic iron) is kept at its set-point with high precision. However, it is presently not known at what degree of precision biochemical controllers usually operate. For controllers where $K_M^{E_{set}}$ values do not meet the condition $K_M^{E_{set}} \ll$ IRT1 it has been shown that the value of $K_M^{E_{set}}$ is a direct measure of the controller's accuracy [37].

Fig 3b shows the levels of $\mathrm{Fe}_{\mathrm{cyt}}$, *IRT1*-mRNA and the IRT1 transporter for sufficient ("+Fe") and low ("−Fe") external iron conditions. The term 'sufficent' here means that the level of external iron is such that no significant up-regulation of IRT1 is necessary to meet the iron need of the cell/plant as expressed by the assimilation flux $j_{\text{Fe-assim}} = k_2 \cdot \mathrm{Fe}_{\mathrm{cyt}}$. In the case when the external iron concentration is low IRT1 needs up-regulation in order to meet the plant's requirement for iron while keeping $\mathrm{Fe}_{\mathrm{cyt}}$ close to its set-point.

Fig 3c shows the *IRT1* transcript and IRT1 protein levels in terms of a blot/gel-like view as would be obtained by Northern and Western blots, respectively. The relative concentrations in IRT1 at +Fe and −Fe conditions are expressed in terms of the gray percentage value, where the high IRT1 value of 4.0 (at "−Fe" condition) has been assigned a gray-level of 100% (black), while at the +Fe condition the gray-level has been reduced to 10% in accordance with the reduction of the IRT1-level to 0.4.

Ignoring for the moment the *IRT1* transcript data, the IRT1 protein dynamics of the controller are in good qualitative agreement with experimental results [10, 21, 23, 45], showing that at sufficient iron conditions, IRT1 levels are kept low but increase when iron becomes less available (Fig 3b and 3c). Fig 3d shows corresponding experimental data by Connolly et al. [21]. The up-regulation of *IRT1*-mRNA and IRT1-protein at iron-deficient conditions is clearly seen. When iron is resupplied, experiments and calculations show that IRT1-levels decrease again (see Fig 2 in [21] and Fig 3b).

IRT1 Overexpression Leads to Saturation in Iron Signaling

When *IRT1* is over-expressed in plants with an *IRT1*-knockout background Barberon et al. [23] observed accumulation of IRT1, metal/iron overload, and oxidative stress. Under these conditions IRT1 degradation rates were found to be independent of the amount of supplied external iron, in contrast to the suggestion of an iron-dependent degradation of IRT1 considered in earlier work [21, 22]. We here show that under *IRT1* overexpression conditions the observation of iron overload and an iron-independent degradation of IRT1 can be rationalized by the homeostasis model in Fig 3a. In the model overexpression of *IRT1* is achieved by

increasing k_3. As k_3 increases the set-point of cytosolic iron also increases see Eq (12) and leads to elevated levels of cytosolic iron, which can explain the observation [23] of iron overload. Fig 4a shows the model's behavior when k_3 is increased from 1.0×10^2 to 1.9×10^2 at $t = 50$. This increase in k_3 leads to an increased set-point from 1.0 to 19.0. In addition, IRT1 levels are also increased in order to maintain homeostasis at the higher set-point. Although the homeostatic performance of the system is still functional at the new k_3 value, the signaling pathway from iron to IRT1 degradation is reaching its capacity limit with a change of f_a^{Fe} from 0.50 to 0.95. Accordingly, the rate of IRT1 degradation, $j_{\mathrm{IRT1\text{-}degr}}$, described by Eq (13) has moved close to its maximum level of $V_{max}^{E_{set}}$ (Fig 4a).

$$j_{\mathrm{IRT1-degr}} = \frac{\mathrm{Fe_{cyt}}}{K_a^{\mathrm{Fe}} + \mathrm{Fe_{cyt}}} \cdot \frac{V_{max}^{E_{set}} \cdot \mathrm{IRT1}}{K_M^{E_{set}} + \mathrm{IRT1}} \tag{13}$$

Once the synthesis rate of IRT1 ($j_{\mathrm{IRT1-synth}} = k_5 \cdot IRT1$) exceeds the capacity $V_{max}^{E_{set}}$ of the IRT1-degrading enzyme, IRT1-protein and cytosolic iron levels increase dramatically. This is shown in the third phase of Fig 4a when $k_3 = 1 \times 10^3$. As a result of the large $j_{\mathrm{IRT1\text{-}synth}}$ flux, the signaling pathway from iron to IRT1 degradation becomes saturated, i.e., $f_a^{\mathrm{Fe}} \rightarrow 1$, the negative feedback is no longer operational, and IRT1 levels rise. At this stage the IRT1 degradation rate becomes saturated and independent of the external iron concentration, as illustrated in Fig 4b. In Fig 4c the calculated overexpression results are replotted in form of dot blots. Fig 4d shows corresponding experimental results taken from Fig 1D by Barberon et al. [23]. In agreement with the modeling results for IRT1-protein (Fig 3c), the experimental results by Barberon et al. show the same wild-type (WT) regulation as previously observed by Connolly et al. [21] (Fig 3d) and others. However, for 35S-IRT1 overexpression conditions, the results by Barberon et al. [23] indicate a loss of IRT1-regulation by external iron (Fig 4d), while Fig 6B (lanes 1 and 2) by Connolly et al. [21] still shows such a regulation. This apparent disagreement between the 35S-IRT1 overexpression results can be rationalized by assuming that the IRT1 synthesis rate in the experiments by Connolly et al. rate is still below the capacity of the cell's IRT1 degradation capacity, while for the IRT1 overexpression conditions by Barberon et al. the IRT1 synthesis rate has exceeded that capacity. The signaling event from cytosolic iron to the degradation machinery for IRT1 in Fig 3a can be interpreted to be part of the system's iron sensing mechanism which breaks down. The breakdown/saturation of a still undiscovered iron sensing mechanism would be another alternative to interpret the iron-insensitivity of IRT1 degradation/inactivation at strong IRT1 overexpressing conditions. Thus, overexpression studies alone do not provide sufficient evidence to rule out an iron-dependent degradation/inactivation of IRT1 at normal operating conditions.

Model including *IRT1*-mRNA and regulation by *FIT*

The model in Fig 3a did not include the regulation of *IRT1* transcript levels as indicated by the experiments shown in Fig 3d. In addition, the *FIT* gene was found to be essential for the high-affinity uptake of iron [10, 12, 21, 23, 46, 47]. The complex between AtbHLH38/AtbHLH39 and FIT has been found to activate *IRT1* and *FRO2* expression [13]. In addition, FIT was found to take part in the inhibiting of IRT1-protein degradation [12]. Model calculations shown below predict that the FIT-induced inhibition of IRT1 degradation has a role in improving (decreasing) the response time of the plant's iron homeostatic system.

Fig 5a shows an extended model for the high-affinity uptake of iron and cytosolic iron homeostasis including *IRT1* and *FIT* transcript and protein levels. The rate equations of this model are given in S3 Text. The variable TF (Fig 5a) lumps together the transcription factors

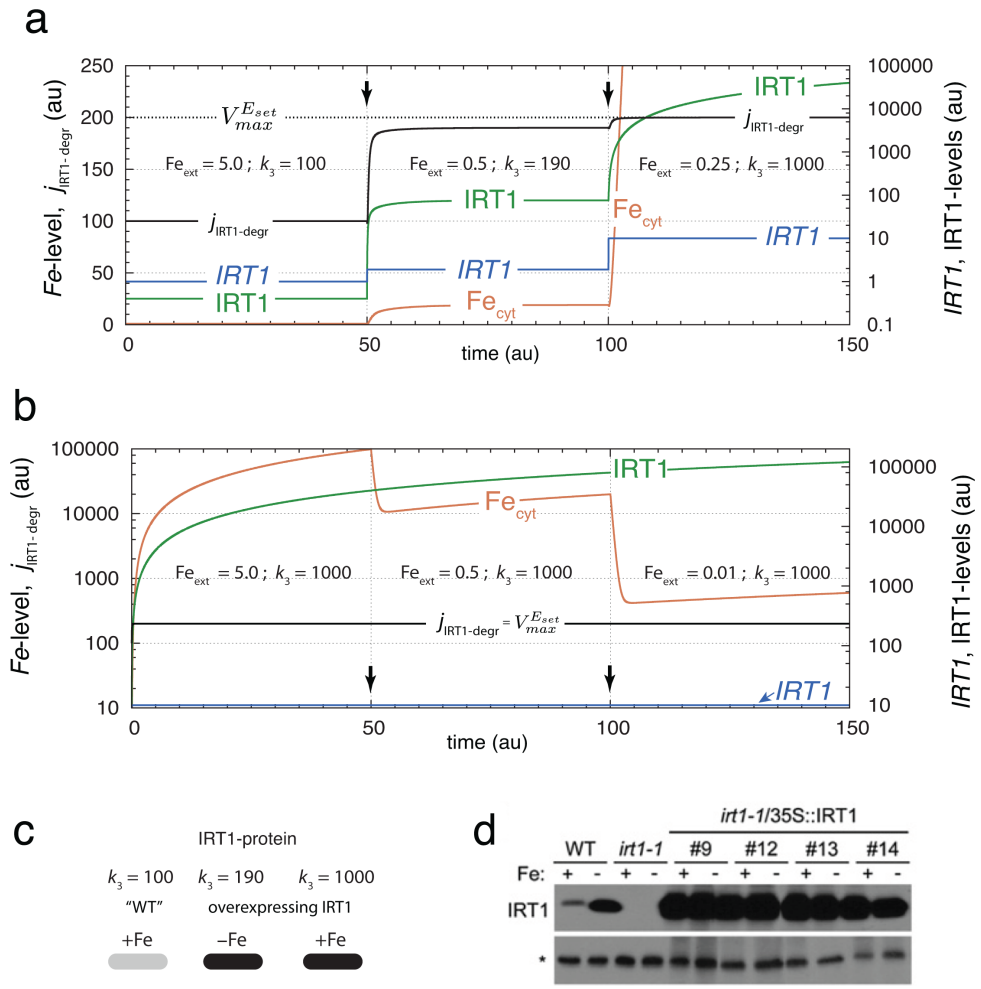

Fig 4. *IRT1* overexpression leads to an increased iron set-point, iron overload and to saturation in the iron-dependent degradation of IRT1. (a) Increase of *IRT1* synthesis rate k_3 at different external iron levels. At times $t = 50$ and $t = 100$ (indicated by arrows) the values of Fe_{ext} and k_3 are changed as indicated in the figure. As long as the IRT1 syntesis rate $j_{IRT1\text{-}synth}$ is lower than its degradation rate ($t = 0$ to $t = 100$), the cytosolic iron concentration is under homeostatic control at its new set-point Eq (12). When $j_{IRT1\text{-}synth}$ becomes larger than $j_{IRT1\text{-}degr}$ iron levels rise and the IRT1 degradation rate $j_{IRT1\text{-}degr}$ goes into saturation ($t = 100$ to $t = 150$). The negative feedback loop is broken and iron homeostasis lost. (b) Demonstration of iron-independent degradation of IRT1 when $j_{IRT1\text{-}synth} > j_{IRT1\text{-}degr}$. The overexpression rate (k_3) is kept constant at 1×10^3 while external iron concentrations Fe_{ext} are changing. For each Fe_{ext} value (5.0, 0.5, and 0.01) the IRT1 degradation rate is at its maximum value $V_{max}^{E_{set}}$ and independent of the cytosolic iron concentration. Rate constants, except k_3, are as in Fig 3c. (c) Calculated IRT1 expression levels shown as "dot-blots". (d) Corresponding experimental results by Barberon et al. (Fig 1D in [23]).

doi:10.1371/journal.pone.0147120.g004

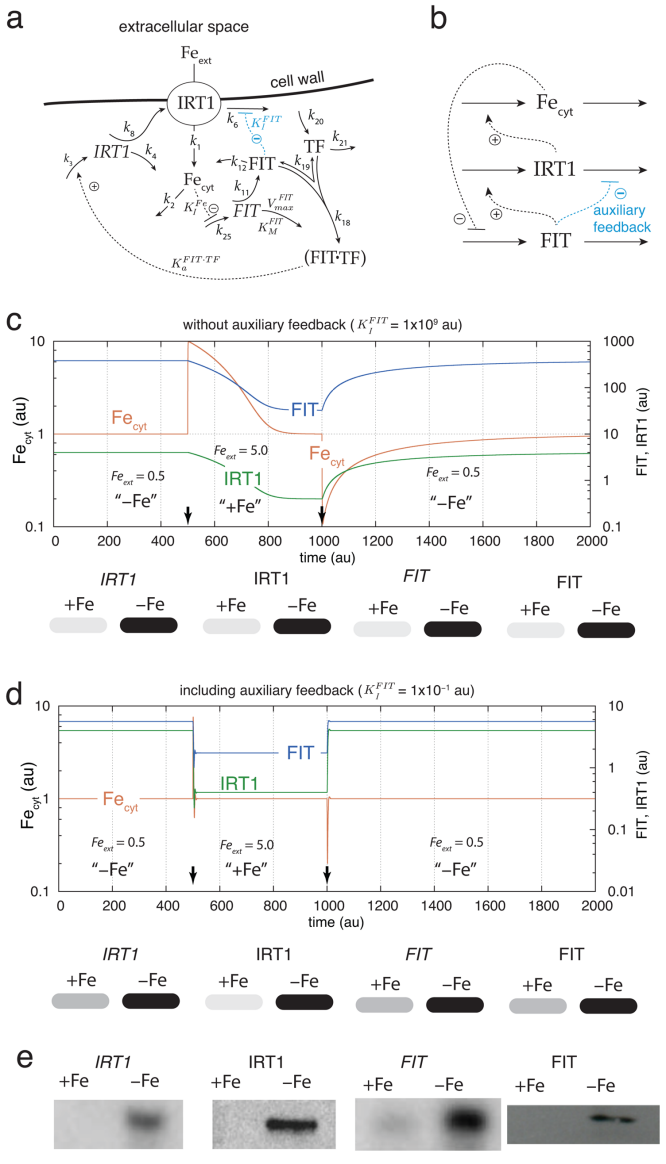
a
extracellular space
Fe ext
cell wall
IRT1
k6
K I FIT
k20
TF
k21
k8
k1
IRT1
k4
k3
k12
FIT
k19
Fe cyt
k11
k2
K I Fe
FIT
V max FIT
K M FIT
k25
k18
K d FIT·TF
(FIT·TF)
b
Fe cyt
IRT1
auxiliary feedback
FIT
c
without auxiliary feedback (K I FIT = 1x10⁹ au)
Fe cyt (au)
FIT, IRT1 (au)
FIT
Fe cyt
Fe ext = 5.0
IRT1
Fe ext = 0.5
"+Fe"
Fe cyt
Fe ext = 0.5
"−Fe"
"−Fe"
time (au)
IRT1
FIT
+Fe
−Fe
d
including auxiliary feedback (K I FIT = 1x10⁻¹ au)
Fe cyt (au)
FIT, IRT1 (au)
FIT
IRT1
Fe cyt
Fe ext = 0.5
"−Fe"
Fe ext = 5.0
"+Fe"
Fe ext = 0.5
"−Fe"
time (au)
IRT1
FIT
+Fe
−Fe
e
IRT1
FIT
+Fe
−Fe

Fig 5. Model for iron uptake including *IRT1* and *FIT*. (a) Reaction scheme of the model. See S3 Text for rate equations. (b) Overview over the feedback structure of the model at the protein and cytosolic iron levels. The inhibition outlined in blue defines an additional auxiliary negative feedback which does not influence the set-point of cytosolic iron, but accelerates the adaptation kinetics of the controller (see (d)). (c) Regulation of *IRT1*- and *FIT*-mRNA and protein levels and response kinetics of the iron uptake system at low (-Fe) and high (+Fe) external iron concentrations and in the absence of the auxiliary feedback ($K_I^{\mathrm{FIT}} = 1 \times 10^9$). The lower part of the panel shows the *IRT1*- and *FIT*-mRNA and protein levels in a blot-like representation, where high levels under -Fe conditions have a gray scale of 100%, while +Fe levels have a reduced gray scale in relation to their reduced numerical values. (d) Same as in (c), but now in the presence of the auxiliary feedback ($K_I^{\mathrm{FIT}} = 1 \times 10^{-1}$). Note the improvement in the adaptation kinetics of the system. Rate constants for (c) and (d): $k_1 = 1.0$, $k_2 = 2.0$, $k_3 = 1 \times 10^2$, $k_4 = 1.0$, $k_6 = 4 \times 10^2$, $k_8 = 1 \times 10^2$, $K_I^{\mathrm{FIT}} = 1 \times 10^9$, $k_{11} = 1 \times 10^3$, $k_{12} = 1 \times 10^3$, $K_a^{\mathrm{FIT{\cdot}TF}} = 1 \times 10^4$, $k_{18} = 1 \times 10^2$, $k_{19} = 1 \times 10^1$, $k_{20} = 1 \times 10^4$, $k_{21} = 2 \times 10^4$, $K_I^{\mathrm{Fe}} = 1.0$, $k_{25} = 4.0$, $V_{max}^{FIT} = 2.0$, $K_M^{FIT} = 1 \times 10^{-4}$. Initial concentrations for (c): $\mathrm{Fe_{cyt0}} = 1.0$, $\mathrm{IRT1_0} = 4.0$, $IRT1_0 = 16.0$, $\mathrm{FIT_0} = 381.0$, $\mathrm{TF_0} = 0.5$, $\mathrm{FIT{\cdot}TF_{0\,=\,1905.0}}$, $FIT_0 = 381.0$. Initial concentrations for (d): $\mathrm{Fe_{cyt0}} = 1.0$, $\mathrm{IRT1_0} = 4.0$, $IRT1_0 = 0.3$, $\mathrm{FIT_0} = 5.6$, $\mathrm{TF_0} = 0.5$, $\mathrm{FIT{\cdot}TF_{0\,=\,28.0}}$, $FIT_0 = 5.6$. (e) Experimental results of IRT1 and FIT mRNA and protein levels in wild-type Arabidopsis roots under iron sufficient ("+Fe") and iron deficient ("-Fe") conditions. The IRT1-protein and mRNA results as well as the *FIT*-mRNA blot are reproduced with permission from Fig 1 of Ref. [12]. The FIT-protein Western blot is reproduced with permission from Fig 4A of Ref. [47].

doi:10.1371/journal.pone.0147120.g005

AtbHLH38 and AtbHLH39 which bind to FIT (FIT·TF) and activate the transcription of *IRT1* [13]. The activations of *FRO2* and AHA2/7 by FIT is not considered in the model. Many experiments confirm that the levels of *IRT1*- and *FIT*-mRNAs as well as IRT1 and FIT proteins are up- or down-regulated when external iron levels are decreased or increased, respectively. [10, 21, 23, 45–47]. The simplest way to rationalize the behaviors of these components is to place the homeostatic regulation point of cytosolic iron at the level of *FIT*-mRNA. An increase of *FIT*-mRNA levels when external and cytosolic iron are low (iron limiting conditions) will induce an increase in FIT-protein, and as a follow-up reaction, an increase in both *IRT1*-mRNA and IRT1 protein levels. Thus, separate regulatory loops for *IRT1*-mRNAs as well as FIT and IRT1-protein levels are in principle not necessary, although additional regulations are possible such as the identified FIT-induced inhibition of IRT1-degradation [12], which increase the performance of the homeostatic system. In the model, the regulation of *FIT*-mRNA is included in form of an iron-induced inhibition of *FIT*-mRNA synthesis. Alternatively, an iron-induced activation of *FIT*-mRNA degradation is possible, which shows practically the same up- and down-regulation characteristics of the components (data not shown). These are the only two possibilities of inflow controller motifs which match with the up- and down-regulation of the "E"-component [37] in the regulatory loop (here the "E"-component is the *FIT*-mRNA). There are presently no experimental indications favoring the inhibition of *FIT*-mRNA synthesis over an activation of its degradation or *vice versa*. For this model (Fig 5a) the set-point for cytosolic iron is determined by the rate equation for *FIT*:

$$\dot{FIT} = \frac{k_{25} \cdot K_I^{\mathrm{Fe}}}{K_I^{\mathrm{Fe}} + \mathrm{Fe_{cyt}}} - \frac{V_{max}^{FIT} \cdot FIT}{K_M^{FIT} + FIT} \tag{14}$$

Setting $\dot{FIT} = 0$ and using the condition/assumption that $K_M^{FIT} \ll FIT$ the following expression for the set-point of $\mathrm{Fe_{cyt}}$ is obtained

$$\mathrm{Fe}_{\mathrm{cyt,set}}^{FIT} = K_I^{\mathrm{Fe}} \left(\frac{k_{25}}{V_{max}^{FIT}} - 1 \right) \tag{15}$$

Fig 5b shows the outline of the feedback structures for the model in panel a. The inhibition of IRT1 degradation induced by FIT, outlined in blue, defines an additional experimentally

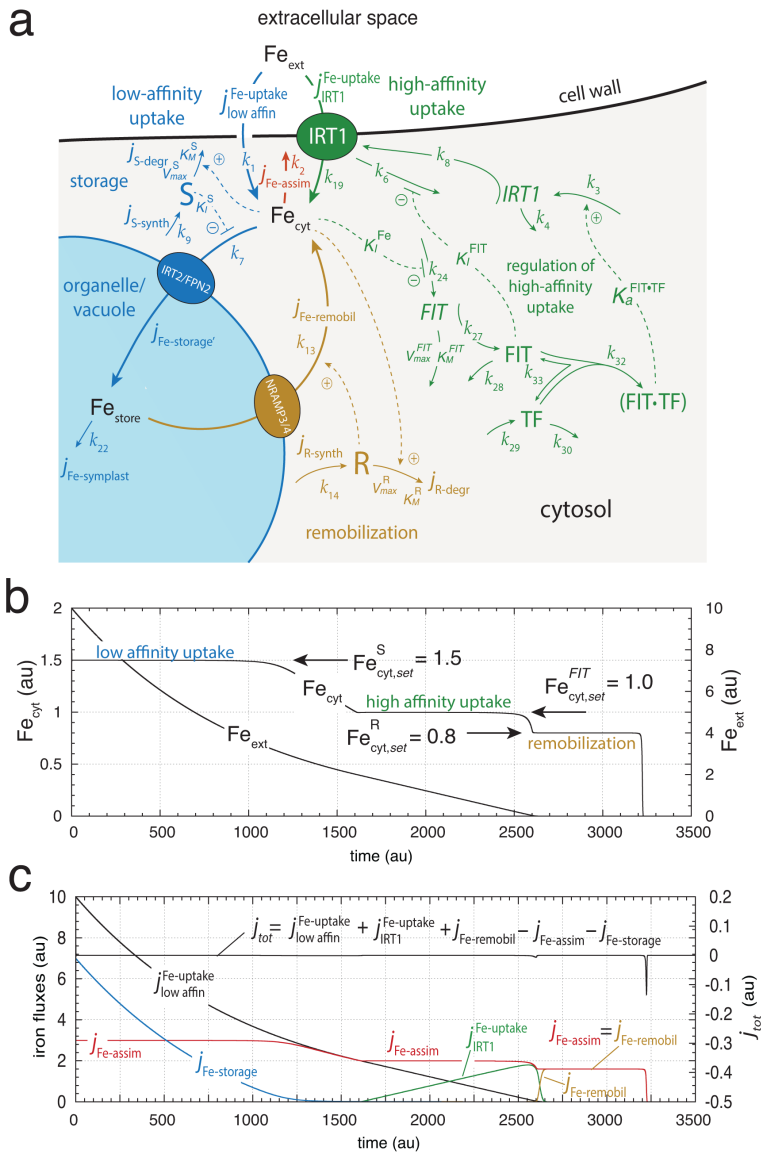
a
extracellular space
Fe ext
low-affinity uptake
j Fe-uptake low affin
j Fe-uptake IRT1
high-affinity uptake
cell wall
IRT1
storage
S
Fe cyt
IRT1
organelle/ vacuole
IRT2/FPN2
j Fe-storage'
Fe store
NRAMP3/4
j Fe-remobil
FIT
regulation of high-affinity uptake
FIT
(FIT•TF)
TF
j R-synth
R
j R-degr
j Fe-symplast
remobilization
cytosol
b
low affinity uptake
Fe S cyt,set = 1.5
Fe cyt
high affinity uptake
Fe FIT cyt,set = 1.0
Fe ext
Fe R cyt,set = 0.8
remobilization
Fe cyt (au)
Fe ext (au)
time (au)
c
j tot = j Fe-uptake low affin + j Fe-uptake IRT1 + j Fe-remobil − j Fe-assim − j Fe-storage
j Fe-uptake low affin
j Fe-assim
j Fe-storage
j Fe-assim
j Fe-uptake IRT1
j Fe-assim = j Fe-remobil
j Fe-remobil
iron fluxes (au)
j tot (au)
time (au)

Fig 6. Model of plant iron homeostasis integrating uptake, storage, assimilation/transport and remobilization from the store. (a) The model combines a low-affinity iron uptake based on an iron-dependent derepression mechanism of inhibitor S [53], which leads to iron storage (outlined in blue), an R-based iron remobilization mechanism from the store (outlined in ochre), the FIT-based high-affinity iron uptake mechanism from Fig 5a (outlined in green) and a lumped expression for the iron assimilation and transport flux to other parts of the plant (outlined in red). Note the renumbering for some of the rate constants in comparison with Fig 5a. See S4 Text for rate equations. (b) Calculation showing cytosolic and external iron concentrations during the low- and high-affinity uptake of iron and iron remobilization from the vacuole. (c) Same calculation as in (b), but showing the different iron fluxes. Rate constants and initial concentrations for (b) and (c): $k_1 = 1.0$, $k_2 = 2.0$, $k_3 = 1 \times 10^2$, $k_4 = 1.0$, $k_6 = 4 \times 10^2$, $k_7 = 1 \times 10^2$, $k_8 = 1 \times 10^2$, $k_9 = 15.0$, $V^S_{max} = 10.0$, $K^S_M = 1 \times 10^{-4}$, $K^S_I = 0.1$, $k_{13} = 0.5$, $k_{14} = 0.8$, $V^R_{max} = 1.0$, $K^R_M = 1 \times 10^{-6}$, $k_{19} = 0.5$, $k_{22} = 5 \times 10^{-4}$, $K^{Fe}_I = 1.0$, $k_{24} = 4.0$, $V^{FIT}_{max} = 2.0$, $K^{FIT}_M = 1 \times 10^{-4}$, $k_{27} = 1 \times 10^3$, $k_{28} = 1 \times 10^3$, $k_{29} = 1 \times 10^4$; $k_{30} = 2 \times 10^4$, $k_{32} = 1 \times 10^2$, $k_{33} = 10.0$, $K^{FIT.TF}_s = 1 \times 10^4$, $K^{FIT}_I = 0.01$. $Fe_{ext,0} = 10.0$, all other initial concentrations are zero.

doi:10.1371/journal.pone.0147120.g006

identified negative feedback [12]. We incorporated this feedback, like that in Fig 2d, without an integral controller and with no influence upon the set-point value of Fe_{cyt} Eq (15).

Although having no influence on Fe_{cyt}'s set-point, the feedback generated by the FIT-induced inhibition of IRT1 degradation, significantly improves the controller's adaptation kinetics to the set-point (Fig 5c and 5d) and indicates a biological role for the FIT-induced inhibition of IRT1 degradation. We suggest to call this type of negative feedback loop for an 'auxiliary feedback'.

Besides the inhibition of IRT1 degradation by FIT [12] several other additional negative feedback arrangements either in form of auxiliary feedbacks or containing an integral controller appear possible. An additional candidate for a helper feedback may be an iron-dependent degradation of FIT. Experiments have shown that the proteasomal degradation of FIT is necessary for the plant's iron deficiency response [47, 48], but whether cytosolic iron regulates a proteasomal FIT degradation is presently not known. Also an iron-dependent degradation of IRT1 as previously suggested [21] can act as an additional auxiliary feedback.

The model results described in Fig 5c and 5d are in good agreement with corresponding experimental findings shown in Fig 5e where the results from different laboratories are shown, i.e., the respective up- and down-regulations of IRT1 and FIT transcript and protein levels at high and low external iron conditions.

Iron Homeostasis Including Storage and Remobilization

At high external iron concentrations iron is taken up by an IRT1-independent mechanism [10], possibly due to a low-affinity uptake of iron by other metal-ion transporters [49–51].

Under high cytosolic iron concentrations the inflow controller in Fig 5a will automatically shut-down [37], while iron can still enter the cell and lead to high and potentially toxic iron levels [52]. To avoid the buildup of excess iron in the cytosol plants store and bind inflowing iron. One of the components is ferritin, a protein which is able to bind a large number of iron atoms. Ferritin is found in leaf chloroplasts [53] but also in mitochondria [54] probably reflecting the high abundance of iron in these organelles. Although ferritins are essential to protect the cell and its organelles from oxidative stress, ferritin is not considered to be a major iron pool for either seedling development or for the photosynthetic apparatus [52, 55]. Another molecule, Nicotianamine (NA), which is synthesized from three S-adenosylmethionine molecules, binds both Fe(II) and Fe(III). Although the binding constants are high for both oxidation states, Fe (II) is kinetically stabilized under aerobic conditions [14]. The NA-Fe(II) complex appears to be an important intracellular iron transport form for all plants and is a relative poor Fenton reagent [14, 16–18]. In the tomato mutant plant *chloronerva* where NA is nonfunctional due to a single base change [15], retarded growth of shoots and roots was observed, despite the fact

that sufficient external iron was made available. In these plants precipitation of Fe(III)-phosphate occurred [56], providing an explanation why iron in *chloronerva* appeared less available.

Localization studies of NA, used as an indicator for the NA-Fe(II) complex and thereby for iron, revealed for different wild type plants that at low external iron concentrations most of the NA label appeared in the cytosol. For high iron loading conditions NA was found to be located in the vacuole [16]. This suggests that the vacuole acts as an iron store at sufficient high external iron concentrations, but that no vacuolar storage of iron occurs under iron-limiting conditions. In yeast, iron is stored as Fe(III), which during its remobilization from the vacuole is reduced by Fre6p to Fe(III) [57]. For plants, no corresponding metalloreductase has so far been found [58] indicating that the main storage form of iron in the vacuole appears to be complexed Fe(II).

A candidate for transporting iron into the vacuole is IRT2, a homolog to IRT1 which is co-regulated with FRO2 and IRT1 [59]. IRT2 is expressed in intracellular membranes. It has been suggested that IRT2 is part of an overflow mechanism [18], which sequesters iron into the vacuole or other non-characterized intracellular vesicles [60]. Other candidate transporters for moving cytosolic iron into the vacuole are VIT1 (during seed development) [61], FPN2 [62], a homolog of mammalian ferroportin and VTL [63]. In Arabidopsis, NRAMP3 and NRAMP4 take part in the iron remobilization from the vacuole into the cytosol during iron deficiency [18, 64, 65].

Fig 6a shows a model integrating low- and high-affinity iron uptake with iron storage and iron remobilization. The S4 Text describes the rate equations. The change in cytosolic iron concentration can be expressed by the following fluxes

$$\dot{\mathrm{Fe}}_{\mathrm{cyt}} = j_{\mathrm{low\ affin}}^{\mathrm{Fe-uptake}} + j_{\mathrm{IRT1}}^{\mathrm{Fe-uptake}} - j_{\mathrm{Fe-assim}} - j_{\mathrm{Fe-storage}} + j_{\mathrm{Fe-remobil}} \tag{16}$$

$j_{\mathrm{low\ affin}}^{\mathrm{Fe-uptake}}$ (outlined in blue) is the low affinity uptake rate of iron, which we for the sake of simplicity assumed to be proportional to the concentration of the external iron concentration $\mathrm{Fe}_{\mathrm{ext}}$, i.e., not necessarily only diffusion-driven

$$j_{\mathrm{low\ affin}}^{\mathrm{Fe-uptake}} = k_1 \cdot \mathrm{Fe}_{\mathrm{ext}} \tag{17}$$

$j_{\mathrm{IRT1}}^{\mathrm{Fe-uptake}}$ (outlined in green) is the high affinity uptake rate of iron

$$j_{\mathrm{IRT1}}^{\mathrm{Fe-uptake}} = k_{19} \cdot \mathrm{IRT1} \cdot \mathrm{Fe}_{\mathrm{ext}} \tag{18}$$

where IRT1 is the concentration of IRT1-protein in the membrane.

$j_{\mathrm{Fe\text{-}assim}}$ (outlined in red) is the flux combining the assimilation of iron and its transport to other parts of the plant. This flux is described as Eq (10), i.e.

$$j_{\mathrm{Fe-assim}} = k_2 \cdot \mathrm{Fe}_{\mathrm{cyt}} \tag{19}$$

$j_{\mathrm{Fe\text{-}storage}}$ (outlined in blue) is the flux moving cytosolic iron into the store (the vacuole and other organelles). The activation of this flux is based on a mechanism which was described for the activation of ferritins in the presence of excess iron [53]. Under low iron conditions the transport of iron into the store is blocked by a still unknown inhibitor S. However, when iron inflow into the cytoplasm becomes high S is degraded by the proteosome in an iron-dependent manner and iron can enter the store [53]. The iron flux into the store is described by

$$j_{\mathrm{Fe-storage}} = k_7 \cdot \mathrm{Fe}_{\mathrm{cyt}} \cdot \left(\frac{K_I^{\mathrm{S}}}{K_I^{\mathrm{S}} + \mathrm{S}} \right) \tag{20}$$

where K_I^{S} is a inhibition constant by which S inhibits $j_{\mathrm{Fe\text{-}storage}}$. For the sake of simplicity the

concentration of the transporters (IRT2/FPN2) moving iron into the store are considered to be constant, i.e., $k_7 = k'_7 \cdot (\mathrm{IRT2/FPN2}) = \text{constant}$, such that the flux of iron into the store is proportional to the concentration of $\mathrm{Fe_{cyt}}$. The inhibitor S may act at different levels, i.e. either directly inhibiting the transporter which moves iron into the store, or, like in the case of ferritin, acting at the transcriptional level [53].

The remobilization of iron from the store into the cytosol (ochre-colored) is formulated as

$$j_{\mathrm{Fe-remobil}} = k_{13} \cdot \mathrm{Fe_{store}} \cdot \mathrm{R} \tag{21}$$

where R is the remobilization regulator and an inflow controller with respect to cytosolic iron. The rate equation of R is given as:

$$\dot{\mathrm{R}} = j_{\mathrm{R-synth}} - j_{\mathrm{R-degr}} = k_{14} - \left(\frac{V^{\mathrm{R}}_{max} \cdot \mathrm{R}}{K^{\mathrm{R}}_{M} + \mathrm{R}}\right) \cdot \mathrm{Fe_{cyt}} \tag{22}$$

Also here the concentration of the transporters NRAMP3/4 is considered to be constant, i.e., $k_{13} = k'_{13} \cdot \mathrm{NRAMP3/4} = \text{constant}$. We are not aware of any identified feedback scheme with respect to iron remobilization from the vacuole. In this respect, the here suggested mechanism involving R is hypothetical. The set-point concentration of cytosolic iron with respect to inflow controller R is obtained by setting Eq (22) to zero and assuming that $K^{\mathrm{R}}_{M} \ll \mathrm{R}$. Solving for $\mathrm{Fe_{cyt}}$ gives

$$\mathrm{Fe}^{\mathrm{R}}_{\mathrm{cyt},set} = \frac{k_{14}}{V^{\mathrm{R}}_{max}} \tag{23}$$

The kinetics of the external iron source is described as

$$\dot{\mathrm{Fe}}_{\mathrm{ext}} = -j^{\mathrm{Fe-uptake}}_{\mathrm{low\ affin}} - j^{\mathrm{Fe-uptake}}_{\mathrm{IRT1}} \tag{24}$$

The rate equation for iron within the store is given by

$$\dot{\mathrm{Fe}}_{\mathrm{store}} = j_{\mathrm{Fe-storage}} - j_{\mathrm{Fe-remobil}} - j_{\mathrm{Fe-symplast}} \tag{25}$$

Finally, we have the rate equation of the regulator S for iron storage:

$$\dot{\mathrm{S}} = j_{\mathrm{S-synth}} - j_{\mathrm{S-degr}} \tag{26}$$

where $j_{\mathrm{S\text{-}synth}}$ is a constant (k_9), while $j_{\mathrm{S\text{-}degr}}$ is activated by cytosolic iron and described by Michaelis-Menten kinetics

$$j_{\mathrm{S-degr}} = \mathrm{Fe_{cyt}}\left(\frac{V^{\mathrm{S}}_{max} \cdot \mathrm{S}}{K^{\mathrm{S}}_{M} + \mathrm{S}}\right) \tag{27}$$

The set-point during storage is determined by setting $\dot{\mathrm{S}} = 0$ Eq (26), which leads to

$$\mathrm{Fe}^{\mathrm{S}}_{\mathrm{cyt},set} = \frac{j_{\mathrm{S-synth}}}{V^{\mathrm{S}}_{max}} \tag{28}$$

To ensure that the combined controllers work flawlessly together, their set-points need to be in a certain hierarchical order as wind-up may occur otherwise [36, 37]. We have chosen the rate parameters such that $\mathrm{Fe}^{\mathrm{S}}_{\mathrm{cyt},set} = 1.5$, $\mathrm{Fe}^{FIT}_{\mathrm{cyt},set} = 1.0$, and $\mathrm{Fe}^{\mathrm{R}}_{\mathrm{cyt},set} = 0.8$. The different set-point values also allow that the phases of storage, high-affinity uptake, and remobilization from the store can be easily identified (Fig 6b).

Fig 6b shows the concerted and integrative behavior of the combined controllers. The initial concentration of external iron, $\mathrm{Fe_{ext}}$, is 10.0 and relative high. At this condition the IRT1-based

high-affinity uptake system is down-regulated and a still unknown uptake system moves iron into the cell [10]. To avoid a buildup of toxic iron within the cytosol, the excess of incoming iron (relative to the set-point of the S-controller) is moved by the S-controller into the vacuole/store. The negative feedback control loop for keeping homeostasis during storage (controller motif 6, [37]) is analogous to the motif identified for ferritin regulation ([53], see also above).

The flux into the store, $j_{\text{Fe-storage}}$, decreases gradually with the decrease in the external iron concentration. At approximately 1250 time units (Fig 6b and 6c) there is not sufficient external ion available to maintain the homeostasis by the S-controller and the cytosolic iron concentration decreases (Fig 6b). As $j_{\text{low affin}}^{\text{Fe-uptake}}$ decreases the need for iron is satisfied by an increased IRT1-based uptake flux, $j_{\text{IRT1}}^{\text{Fe-uptake}}$, such that $j_{\text{low affin}}^{\text{Fe-uptake}}$ and $j_{\text{IRT1}}^{\text{Fe-uptake}}$ together compensate the assimilatory flux $j_{\text{Fe-assim}}$ and maintain cytosolic iron homeostasis, i.e.,

$$j_{\text{Fe-assim}} = j_{\text{low affin}}^{\text{Fe-uptake}} + j_{\text{IRT1}}^{\text{Fe-uptake}} \tag{29}$$

The successive up-regulation of $j_{\text{IRT1}}^{\text{Fe-uptake}}$ continues until the external supply of iron is exhausted. In the model calculation this occurs at about 2600 time units (Fig 6b and 6c). In the final phase starting at about 2600 time units, the remobilization flux $j_{\text{Fe-remobil}}$ from the store is activated and solely balances the assimilatory flux $j_{\text{Fe-assim}}$.

The arrangement of controller motifs in Fig 6a leads only to iron storage when a large amount of iron can enter the cell. In case the external iron concentration is low and iron becomes limiting, no significant storage of iron can occur. This is illustrated in Fig 7 showing the system's response when the external iron concentration is kept at 1.0. While the FIT/IRT1--based controller balances the assimilatory flux $j_{\text{Fe-assim}}$ no significant flux into the store occurs, and the store is emptied by the putative symplast iron transport [66, 67] which connects the vacuole to other parts of the plant (described by the flux $j_{\text{Fe-symplast}} = k_{22} \cdot \text{Fe}_{\text{store}}$, Fig 6a). This strategy of vacuolar iron storage when there is only a surplus of external iron available fits well with experimental findings when NA-labelled plants are exposed to low and high external iron concentrations [16].

Increasing Vacuolar Storage of Iron at Low External Iron Concentrations

According to the World Health Organization iron deficiency is the most common and widespread nutritional disorder in the world [68]. As reviewed by Jeong and Guerinot [6] an understanding of iron homeostasis is not only important for getting better plant growth and increasing crop yields but also to improve human nutrition. Different approaches for iron biofortification in plants have been used, among them increasing the amount of ferritin and NA. Based on the properties of the here described controller motifs, we suggest a model-guided approach to increase the amount of stored iron in roots even when iron is taken up by the high-affinity system. The strategy is to place an inflow controller with respect to vacuolar iron within the vacuolar membrane while target the controller molecule into the vacuole (Fig 8a, outlined in gray). An inflow controller motif will try to maintain an iron homeostatic set-point in the vacuole defined by the negative feedback structure of the controller molecule I. Four controller motifs are in principle possible to achieve inflow control [37]. We here illustrate the approach using motif 1 [37] with an iron-induced degradation of controller I, while I is activating the inflow of iron into the vacuole (Fig 8a). The set-point of this controller is given by the ratio between I expression and its maximum degradation rate. An expression for the set-point is obtained by setting the rate equation for I to zero and solving for Fe_{store}, i.e.,

$$\dot{\text{I}} = k_{18} - \text{Fe}_{\text{store}} \cdot \left(\frac{V_{max}^{\text{I}} \cdot \text{I}}{K_M^{\text{I}} + \text{I}} \right) = 0 \tag{30}$$

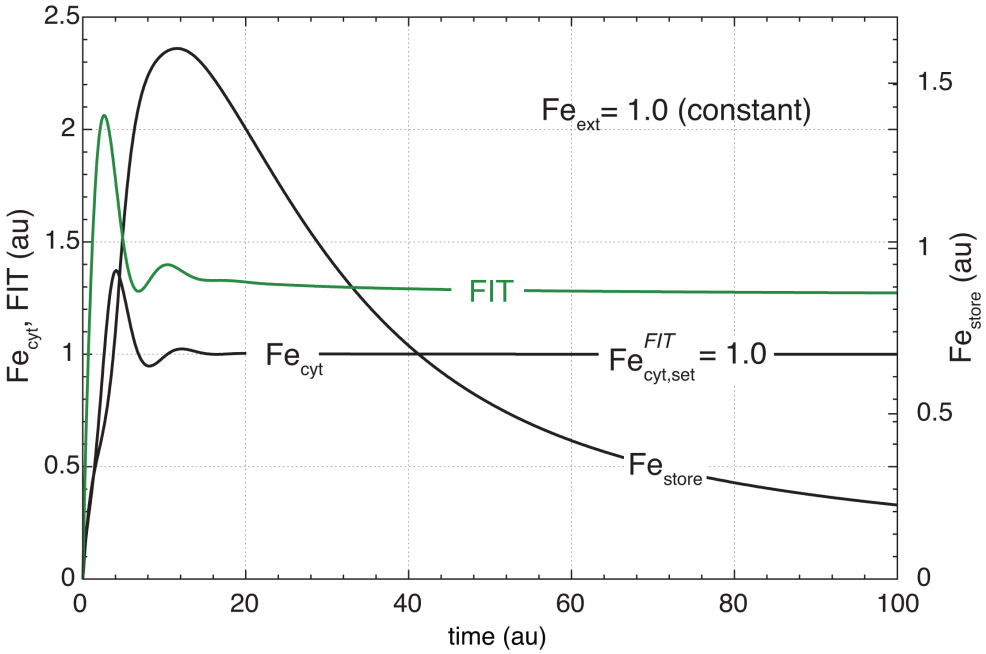

Fig 7. Iron-based derepression mechanism of iron storage is not active at low external iron concentrations. The figure shows that the iron-based derepression mechanism for iron storage (Fig 6a) cannot activate iron storage at low external iron concentrations when the IRT1 high-affinity uptake system is active. In this calculation the external iron concentration Fe_{ext} is kept constant at 1.0. Initial concentrations and rate constants for this calculation are as in Fig 6b and 6c, except for k_{22} (= 0.1) which accounts for a symplastic removal of iron out of the vacuole and leads to a decrease in Fe_{store}. The FIT and IRT1-based high affinity uptake is able to keep the cytosolic iron at its set-point $Fe^{FIT}_{cyt,set} = 1.0$, while the S-based outflow controller (Fig 6a), responsible for iron storage, is inactive.

doi:10.1371/journal.pone.0147120.g007

Assuming that $K^1_M \ll$ I, the vacuolar iron set-point is given by

$$Fe^1_{store,set} = \frac{k_{18}}{V^1_{max}} \tag{31}$$

Fig 8b illustrates the behavior of the system with a $Fe^1_{store,set} = 700$. Even at low iron conditions the system now accumulates iron in the vacuole, where $Fe^1_{store,set}$ is an upper limit for the vacuolar iron concentration. At present this approach is purely theoretical, but transport routes to incorporate newly synthesized/overexpressed transporters such as FRP2 into the vacuolar membrane are known and can be used in a synthetic biology approach to generate iron accumulating plants. The usage of the vacuole to store increased amounts of iron has the advantage that increased iron concentration inside the vacuole are nontoxic to the plant, because FRP2-mediated transport of iron protects the plant from iron shock [69]. Although there has

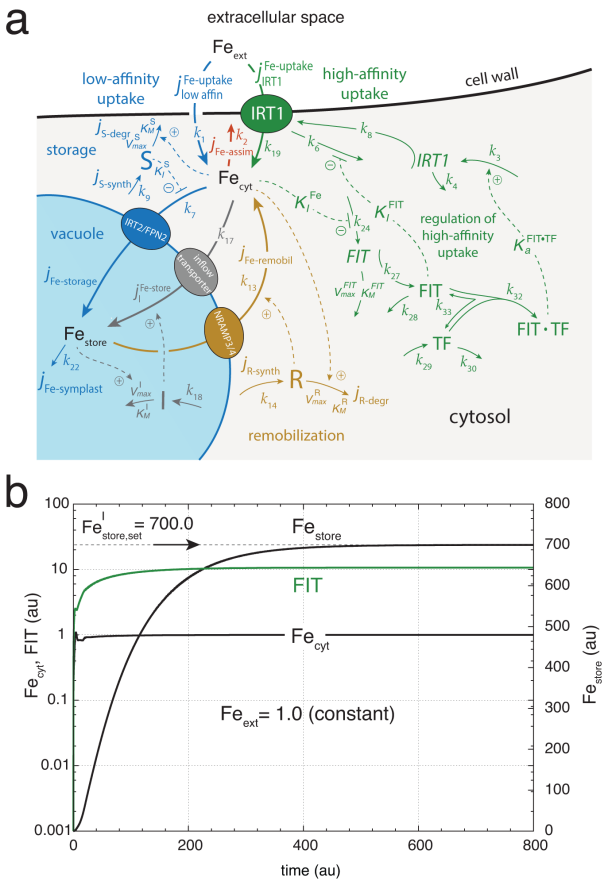

Fig 8. Iron storage during high-affinity uptake. (a) The model is an extension of that in Fig 6a containing in addition inflow controller molecule I inside the vacuole which activates a transporter located in the vacuolar membrane. Controller molecule I is subject to an iron-dependent degradation. The rate equation for I is: $\dot{I} = k_{18} - \mathrm{Fe}_{\mathrm{store}} \cdot V^{I}_{max} \cdot I/(K^{I}_{M} + I)$ (b) Calculation showing the increase of iron in the vacuole, $\mathrm{Fe}_{\mathrm{store}}$, as a function of time. The iron set-point inside the vacuole is given by Eq (31) and set to 700.0. The flux of iron entering the vacuole due to controller I is given as: $j_{I}^{Fe-store} = k_{17} \cdot \mathrm{Fe}_{\mathrm{cyt}} \cdot I$. The additional parameter values are: $k_{17} = 1 \times 10^{-3}$, $k_{18} = 700.0$, $V^{I}_{max} = 1.0$, $K^{I}_{M} = 1 \times 10^{-4}$. Other parameter values and initial concentrations as in Fig 6. The initial concentration of controller I is zero.

doi:10.1371/journal.pone.0147120.g008

been made considerable progress in the understanding of plant iron regulation, our knowledge about the iron regulatory elements, their concentrations and kinetics are still fragmentary. We hope that the here suggested model-guided approach may stimulate further theoretical and experimental work leading to an increased understanding and better modification of iron regulation in higher plants.

Hierarchical Arrangement of Inflow and Outflow Controllers

We have presented a model of plant iron homeostasis in root cells with emphasis on non-graminaceous plants/Arabidopsis, which integrates low- and high-affinity iron uptake, iron storage and remobilization as well iron assimilation and transport of iron to other parts of the plant. The model is based on a hierarchical arrangement of set-points when combining inflow and outflow controllers with respect to cytosolic iron. The outflow control arrangement (controller S) has the highest set-point ($Fe^{S}_{cyt,set}$) and moves iron from the cytoplasm to another part of the cell (store). An inflow controller associated with a high-affinity uptake system provides the next level of control with a set-point ($Fe^{FIT}_{cyt,set}$) below that of the outflow controller. This control level does not allow for storage, but balances the need of the cell for iron to maintain its functions while keeping the cytosolic iron concentration at a high enough level. The final level of control is that of remobilizing iron from the store back into the cytosol to balance the assimilatory flux and the need to maintain cellular function. The set-point of this control level ($Fe^{R}_{cyt,set}$) has the lowest value. This hierarchical arrangement of set-points

$$Fe^{S}_{cyt,set} > Fe^{FIT}_{cyt,set} > Fe^{R}_{cyt,set} \tag{32}$$

allows for a concerted and cooperative manner of how the controllers are activated in response to external and internal iron supplies and requirements. Otherwise, if for example $Fe^{FIT}_{cyt,set} < Fe^{R}_{cyt,set}$ the store of iron would be always emptied *before* external iron is used by the high affinity uptake system. When $Fe^{S}_{cyt,set} < Fe^{FIT}_{cyt,set}$ the iron concentration will settle somewhere between both set-points, while both controllers are actively trying to move the cytosolic iron concentration to the level of their respective set-points. This behavior, when both S- and FIT-controllers are working "against each other" and leading to a constant upregulation of S, *FIT*-mRNA, and FIT-protein is referred to as "integral wind-up" [37]. To avoid windup, we anticipate that in all robustly homeostatic controlled systems a hierarchy of set-points is established as described by Eq (32) in order to maintain a concerted operation of the individual controllers.

Sensor Mechanisms

Organisms need certain mechanisms to adapt to environmental changes. In this respect sensors and sensor mechanisms appear necessary to get information about the environment. The sequence of processes

$$\text{sensing} \rightarrow \text{transduction} \rightarrow \text{reaction} \tag{33}$$

has been considered as a general model how organisms and cells adapt to a changing environment [70]. In the literature [6] the anticipation of a not yet identified iron sensor upstream of *FIT* participating in iron homeostasis has been expressed. The regulatory structure in Fig 5b for the uptake of iron suggests an iron-sensing and signaling mechanism from Fe_{cyt} to *FIT*. As indicated above two possibilities exists for an inflow controller arrangement which matches the FIT and IRT1 dynamics upon external iron changes: either an inhibition of *FIT*-mRNA synthesis or an activation of its degradation. In addition to these sensing mechanisms as part of the regulatory negative feedback, there may be additional sensors that could, for example, be part

of a feedforward control mechanism [71] to further optimize the system's homeostatic response. In feedforward control environmental changes are measured/sensed and integrated into the negative feedback loop. Feedforward behavior is preset and appears to have developed due to an evolutionary process. Feedforward mechanisms are associated with anticipative behaviors of a system [72, 73] as found for example in circadian control [74, 75]. Plant iron has actually been found to be under a circadian regulation [53, 76]. Although not considered here, we have recently found that some of the controller motifs can be extended to work under oscillatory conditions [40], which will be a subject of further investigations.

Supporting Information

S1 Table. Overview of Determined Root and Leaf Iron Concentrations (μg Fe per mg dry weight of tissue).
(PDF)

S1 Text. Robustness of Integral Control.
(PDF)

S2 Text. Dynamic model of Fig 3 and Derivation of Eq (12).
(PDF)

S3 Text. Dynamic model of Fig 5.
(PDF)

S4 Text. Dynamic model of Fig 6.
(PDF)

S5 Text. How to run the matlab files.
(TXT)

S1 File. matlab_fig2c.m file.
(M)

S2 File. ODEs_for_Figure_2c.m file.
(M)

S3 File. matlab_fig2d.m file.
(M)

S4 File. ODEs_for_Figure_2d.m file.
(M)

S5 File. matlab_fig3b.m file.
(M)

S6 File. ODEs_for_Figure_3b.m file.
(M)

S7 File. matlab_fig4a.m file.
(M)

S8 File. matlab_fig4b.m file.
(M)

S9 File. ODEs_for_Figure_4ab.m file.
(M)

S10 File. matlab_fig5c.m file.
(M)

S11 File. matlab_fig5d.m file.
(M)

S12 File. ODEs_for_Figure_5cd.m file.
(M)

S13 File. matlab_fig6.m file.
(M)

S14 File. ODEs_for_Figure_6bc.m file.
(M)

S15 File. matlab_fig7.m file.
(M)

S16 File. ODEs_for_Figure_7.m file.
(M)

S17 File. matlab_fig8b.m file.
(M)

S18 File. ODEs_for_Figure_8b.m file.
(M)

Acknowledgments

This research was financed in part by Program Area Funds from the University of Stavanger to TD and PR.

Author Contributions

Conceived and designed the experiments: XMX TD PR. Performed the experiments: OA CHS KT XMX TD PR. Analyzed the data: OA CHS KT XMX TD PR. Contributed reagents/materials/analysis tools: OA CHS TD PR. Wrote the paper: TD PR.

References

1. Römheld V, Marschner H. Evidence for a specific uptake system for iron phytosiderophores in roots of grasses. Plant Physiology. 1986; 80(1):175–180. doi: 10.1104/pp.80.1.175 PMID: 16664577
2. Curie C, Briat JF. Iron transport and signaling in plants. Annu Rev Plant Biol. 2003; 54:183–206. doi: 10.1146/annurev.arplant.54.031902.135018 PMID: 14509968
3. Briat JF, Curie C, Gaymard F. Iron utilization and metabolism in plants. Current Opinion in Plant Biology. 2007; 10:276–282. doi: 10.1016/j.pbi.2007.04.003 PMID: 17434791
4. Kim SA, Guerinot ML. Mining iron: iron uptake and transport in plants. FEBS Letters. 2007; 581 (12):2273–2280. doi: 10.1016/j.febslet.2007.04.043 PMID: 17485078
5. Walker EL, Connolly EL. Time to pump iron: iron-deficiency-signaling mechanisms of higher plants. Current Opinion in Plant Biology. 2008; 11:530–535. doi: 10.1016/j.pbi.2008.06.013 PMID: 18722804
6. Jeong J, Guerinot ML. Homing in on iron homeostasis in plants. Trends in Plant Science. 2009; 14 (5):280–285. doi: 10.1016/j.tplants.2009.02.006 PMID: 19375375
7. Kobayashi T, Nishizawa NK. Iron uptake, translocation, and regulation in higher plants. Annual review of plant biology. 2012; 63:131–52. doi: 10.1146/annurev-arplant-042811-105522 PMID: 22404471
8. Eide D, Broderius M, Fett J, Guerinot ML. A novel iron-regulated metal transporter from plants identified by functional expression in yeast. PNAS. 1996; 93(11):5624–5628. doi: 10.1073/pnas.93.11.5624 PMID: 8643627

9. Korshunova YO, Eide D, Clark WG, Guerinot ML, Pakrasi HB. The IRT1 protein from Arabidopsis thaliana is a metal transporter with a broad substrate range. Plant Molecular Biology. 1999; 40(1):37–44. doi: 10.1023/A:1026438615520 PMID: 10394943
10. Vert G, Grotz N, Dédaldéchamp F, Gaymard F, Guerinot ML, Briat JF, et al. IRT1, an Arabidopsis transporter essential for iron uptake from the soil and for plant growth. The Plant Cell. 2002; 14(6):1223–1233. doi: 10.1105/tpc.001388 PMID: 12084823
11. Bauer P, Ling HQ, Guerinot ML. *FIT*, the *FER-LIKE IRON DEFICIENCY INDUCED TRANSCRIPTION FACTOR* in *Arabidopsis*. Plant Physiology and Biochemistry. 2007; 45(5):260–261. doi: 10.1016/j.plaphy.2007.03.006 PMID: 17466530
12. Colangelo EP, Guerinot ML. The essential basic helix-loop-helix protein FIT1 is required for the iron deficiency response. The Plant Cell. 2004; 16(12):3400–3412. doi: 10.1105/tpc.104.024315 PMID: 15539473
13. Yuan Y, Wu H, Wang N, Li J, Zhao W, Du J, et al. FIT interacts with AtbHLH38 and AtbHLH39 in regulating iron uptake gene expression for iron homeostasis in Arabidopsis. Cell Research. 2008; 18 (3):385–397. doi: 10.1038/cr.2008.26 PMID: 18268542
14. von Wirén N, Klair S, Bansal S, Briat JF, Khodr H, Shioiri T, et al. Nicotianamine chelates both FeIII and FeII. Implications for metal transport in plants. Plant Physiology. 1999; 119(3):1107–1114. doi: 10.1104/pp.119.3.1107 PMID: 10069850
15. Ling HQ, Koch G, Bäumlein H, Ganal MW. Map-based cloning of chloronerva, a gene involved in iron uptake of higher plants encoding nicotianamine synthase. PNAS. 1999; 96(12):7098–7103. doi: 10.1073/pnas.96.12.7098 PMID: 10359845
16. Pich A, Manteuffel R, Hillmer S, Scholz G, Schmidt W. Fe homeostasis in plant cells: does nicotianamine play multiple roles in the regulation of cytoplasmic Fe concentration? Planta. 2001; 213(6):967–976. doi: 10.1007/s004250100573 PMID: 11722133
17. Hell R, Stephan UW. Iron uptake, trafficking and homeostasis in plants. Planta. 2003; 216(4):541–551. PMID: 12569395
18. Schmidt W. Iron stress responses in roots of strategy I plants. In: Barton LL, Abadia J, editors. Iron Nutrition in Plants and Rhizospheric Microorganisms. Dordrecht: Springer; 2006. pp. 229–250.
19. Rellán-Álvarez R, Abadía J, Álvarez-Fernández A. Formation of metal-nicotianamine complexes as affected by pH, ligand exchange with citrate and metal exchange. A study by electrospray ionization time-of-flight mass spectrometry. Rapid Communications in Mass Spectrometry. 2008; 22(10):1553–1562. doi: 10.1002/rcm.3523 PMID: 18421700
20. Gitan RS, Eide DJ. Zinc-regulated ubiquitin conjugation signals endocytosis of the yeast ZRT1 zinc transporter. Biochem J. 2000; 346:329–336. doi: 10.1042/bj3460329 PMID: 10677350
21. Connolly EL, Fett JP, Guerinot ML. Expression of the IRT1 metal transporter is controlled by metals at the levels of transcript and protein accumulation. The Plant Cell. 2002; 14(6):1347–1357. doi: 10.1105/tpc.001263 PMID: 12084831
22. Kerkeb L, Mukherjee I, Chatterjee I, Lahner B, Salt DE, Connolly EL. Iron-induced turnover of the Arabidopsis IRON-REGULATED TRANSPORTER1 metal transporter requires lysine residues. Plant Physiology. 2008; 146(4):1964–1973. doi: 10.1104/pp.107.113282 PMID: 18305211
23. Barberon M, Zelazny E, Robert S, Conéjéro G, Curie C, Friml J, et al. Monoubiquitin-dependent endocytosis of the iron-regulated transporter 1 (IRT1) transporter controls iron uptake in plants. PNAS. 2011; 108(32):E450–E458. doi: 10.1073/pnas.1100659108 PMID: 21628566
24. Cannon W. Organization for Physiological Homeostasis. Physiol Rev. 1929; 9:399–431.
25. Hughes GM. Homeostasis and Feedback Mechanisms. New York: Academic Press; 1964.
26. Langley, LL, editor. Homeostasis. Origins of the Concept. Stroudsbourg, Pennsylvania: Dowden, Hutchinson & Ross, Inc.; 1973.
27. Schulkin J. Allostasis, Homeostasis and the Costs of Physiological Adaptation. Cambridge, Massachusetts: Cambridge University Press; 2004.
28. Wilkie J, Johnson M, Reza K. Control Engineering. An Introductory Course. New York: Palgrave; 2002.
29. Yi TM, Huang Y, Simon MI, Doyle J. Robust perfect adaptation in bacterial chemotaxis through integral feedback control. PNAS. 2000; 97(9):4649–53. doi: 10.1073/pnas.97.9.4649 PMID: 10781070
30. El-Samad H, Goff JP, Khammash M. Calcium homeostasis and parturient hypocalcemia: an integral feedback perspective. J Theor Biol. 2002; 214:17–29. doi: 10.1006/jtbi.2001.2422 PMID: 11786029
31. Ingalls BP, Yi TM, Iglesias PA. Using Control Theory to Study Biology. In: Szallasi Z and Stelling J and Periwal V, editor. System Modeling in Cellular Biology. Cambridge, Massachusetts: MIT Press; 2006. p. 243–267.

32. Cloutier M, Wellstead P. The control systems structures of energy metabolism. Journal of The Royal Society Interface. 2009;
33. Ni XY, Drengstig T, Ruoff P. The control of the controller: Molecular mechanisms for robust perfect adaptation and temperature compensation. Biophys J. 2009; 97:1244–1253. doi: 10.1016/j.bpj.2009.06.030 PMID: 19720012
34. Ang J, Bagh S, Ingalls BP, McMillen DR. Considerations for using integral feedback control to construct a perfectly adapting synthetic gene network. J Theor Biol. 2010 Oct; 266(4):723–738. doi: 10.1016/j.jtbi.2010.07.034 PMID: 20688080
35. Jolma IW, Ni XY, Rensing L, Ruoff P. Harmonic oscillations in homeostatic controllers: Dynamics of the p53 regulatory system. Biophys J. 2010; 98(5):743–52. doi: 10.1016/j.bpj.2009.11.013 PMID: 20197027
36. Huang Y, Drengstig T, Ruoff P. Integrating fluctuating nitrate uptake and assimilation to robust homeostasis. Plant, Cell and Environment. 2011; 35:917–928. doi: 10.1111/j.1365-3040.2011.02462.x PMID: 22070777
37. Drengstig T, Jolma I, Ni X, Thorsen K, Xu X, Ruoff P. A basic set of homeostatic controller motifs. Biophys J. 2012; 103(9):2000–2010. doi: 10.1016/j.bpj.2012.09.033 PMID: 23199928
38. Drengstig T, Ni X, Thorsen K, Jolma I, Ruoff P. Robust adaptation and homeostasis by autocatalysis. The Journal of Physical Chemistry B. 2012; 116(18):5355–5363. doi: 10.1021/jp3004568 PMID: 22506960
39. Ang J, McMillen DR. Physical Constraints on Biological Integral Control Design for Homeostasis and Sensory Adaptation. Biophys J. 2013 Jan; 104(2):505–515. doi: 10.1016/j.bpj.2012.12.015 PMID: 23442873
40. Thorsen K, Agafonov O, Selstø CH, Jolma IW, Ni XY, Drengstig T, et al. Robust Concentration and Frequency Control in Oscillatory Homeostats. PLOS ONE. 2014; 9(9):e107766. doi: 10.1371/journal.pone.0107766 PMID: 25238410
41. Radhakrishnan K, Hindmarsh AC. Description and Use of LSODE, the Livermore Solver for Ordinary Differential Equations. NASA Reference Publication 1327, Lawrence Livermore National Laboratory Report UCRL-ID-113855. Cleveland, OH 44135-3191: National Aeronautics and Space Administration, Lewis Research Center; 1993.
42. Grossoehme NE, Akilesh S, Guerinot ML, Wilcox DE. Metal-Binding Thermodynamics of the Histidine-Rich Sequence from the Metal-Transport Protein IRT1 of *Arabidopsis thaliana*. Inorganic Chemistry. 2006; 45(21):8500–8508. doi: 10.1021/ic0606431 PMID: 17029360
43. Krouk G, Lacombe B, Bielach A, Perrine-Walker F, Malinska K, Mounier E, et al. Nitrate-regulated auxin transport by NRT1. 1 defines a mechanism for nutrient sensing in plants. Developmental Cell. 2010; 18(6):927–937. doi: 10.1016/j.devcel.2010.05.008 PMID: 20627075
44. Wang YY, Hsu PK, Tsay YF. Uptake, allocation and signaling of nitrate. Trends in Plant Science. 2012; 17(8):458–467. doi: 10.1016/j.tplants.2012.04.006 PMID: 22658680
45. Shin LJ, Lo JC, Chen GH, Callis J, Fu H, Yeh KC. IRT1 DEGRADATION FACTOR1, a RING E3 ubiquitin ligase, regulates the degradation of IRON-REGULATED TRANSPORTER1 in Arabidopsis. The Plant Cell. 2013; 25(8):3039–3051. doi: 10.1105/tpc.113.115212 PMID: 23995086
46. Lingam S, Mohrbacher J, Brumbarova T, Potuschak T, Fink-Straube C, Blondet E, et al. Interaction between the bHLH transcription factor FIT and ETHYLENE INSENSITIVE3/ETHYLENE INSENSITIVE3-LIKE1 reveals molecular linkage between the regulation of iron acquisition and ethylene signaling in Arabidopsis. The Plant Cell. 2011; 23(5):1815–1829. doi: 10.1105/tpc.111.084715 PMID: 21586684
47. Meiser J, Lingam S, Bauer P. Posttranslational regulation of the iron deficiency basic helix-loop-helix transcription factor FIT is affected by iron and nitric oxide. Plant Physiology. 2011; 157(4):2154–2166. doi: 10.1104/pp.111.183285 PMID: 21972265
48. Sivitz A, Grinvalds C, Barberon M, Curie C, Vert G. Proteasome-mediated turnover of the transcriptional activator FIT is required for plant iron-deficiency responses. The Plant Journal. 2011; 66 (6):1044–1052. doi: 10.1111/j.1365-313X.2011.04565.x PMID: 21426424
49. Eide DJ. The molecular biology of metal ion transport in Saccharomyces cerevisiae. Annual Review of Nutrition. 1998; 18(1):441–469. doi: 10.1146/annurev.nutr.18.1.441 PMID: 9706232
50. Guerinot ML. The ZIP family of metal transporters. Biochimica et Biophysica Acta (BBA)-Biomembranes. 2000; 1465(1):190–198. doi: 10.1016/S0005-2736(00)00138-3
51. Wintz H, Fox T, Wu YY, Feng V, Chen W, Chang HS, et al. Expression profiles of Arabidopsis thaliana in mineral deficiencies reveal novel transporters involved in metal homeostasis. Journal of Biological Chemistry. 2003; 278(48):47644–47653. doi: 10.1074/jbc.M309338200 PMID: 13129917
52. Ravet K, Touraine B, Boucherez J, Briat JF, Gaymard F, Cellier F. Ferritins control interaction between iron homeostasis and oxidative stress in Arabidopsis. The Plant Journal. 2009; 57(3):400–412. doi: 10.1111/j.1365-313X.2008.03698.x PMID: 18826427

53. Briat JF, Duc C, Ravet K, Gaymard F. Ferritins and iron storage in plants. Biochimica et Biophysica Acta (BBA)-General Subjects. 2010; 1800(8):806–814. doi: 10.1016/j.bbagen.2009.12.003

54. Vigani G, Tarantino D, Murgia I. Mitochondrial ferritin is a functional iron-storage protein in cucumber (Cucumis sativus) roots. Frontiers in Plant Science. 2013; 4:316. doi: 10.3389/fpls.2013.00316 PMID: 23967005

55. Taiz L, Zeiger E. Plant Physiology. Sunderland, MA: Sinauer Associates; 2010.

56. Becker R, Fritz E, Manteuffel R. Subcellular localization and characterization of excessive iron in the nicotianamine-less tomato mutant chloronerva. Plant Physiology. 1995; 108(1):269–275. PMID: 12228472

57. Singh A, Kaur N, Kosman DJ. The metalloreductase Fre6p in Fe-efflux from the yeast vacuole. Journal of Biological Chemistry. 2007; 282(39):28619–28626. doi: 10.1074/jbc.M703398200 PMID: 17681937

58. Jain A, Wilson GT, Connolly EL. The diverse roles of FRO family metalloreductases in iron and copper homeostasis. Frontiers in Plant Science. 2014; 5:100. doi: 10.3389/fpls.2014.00100 PMID: 24711810

59. Vert G, Barberon M, Zelazny E, Séguéla M, Briat JF, Curie C. Arabidopsis IRT2 cooperates with the high-affinity iron uptake system to maintain iron homeostasis in root epidermal cells. Planta. 2009; 229 (6):1171–1179. doi: 10.1007/s00425-009-0904-8 PMID: 19252923

60. Thomine S, Vert G. Iron transport in plants: better be safe than sorry. Current Opinion in Plant Biology. 2013; 16(3):322–327. doi: 10.1016/j.pbi.2013.01.003 PMID: 23415557

61. Kim SA, Punshon T, Lanzirotti A, Li L, Alonso JM, Ecker JR, et al. Localization of iron in Arabidopsis seed requires the vacuolar membrane transporter VIT1. Science. 2006; 314(5803):1295–1298.

62. Morrissey J, Baxter IR, Lee J, Li L, Lahner B, Grotz N, et al. The ferroportin metal efflux proteins function in iron and cobalt homeostasis in Arabidopsis. The Plant Cell. 2009; 21(10):3326–3338. doi: 10.1105/tpc.109.069401 PMID: 19861554

63. Gollhofer J, Timofeev R, Lan P, Schmidt W, Buckhout TJ. Vacuolar-Iron-Transporter1-Like Proteins Mediate Iron Homeostasis in Arabidopsis. PLOS ONE. 2014; 9(10):e110468. doi: 10.1371/journal.pone.0110468 PMID: 25360591

64. Curie C, Alonso J, Le Jean M, Ecker J, Briat J. Involvement of NRAMP1 from Arabidopsis thaliana in iron transport. Biochem J. 2000; 347:749–755. doi: 10.1042/0264-6021:3470749 PMID: 10769179

65. Jaquinod M, Villiers F, Kieffer-Jaquinod S, Hugouvieux V, Bruley C, Garin J, et al. A proteomics dissection of Arabidopsis thaliana vacuoles isolated from cell culture. Molecular & Cellular Proteomics. 2007; 6(3):394–412. doi: 10.1074/mcp.M600250-MCP200

66. Velikanov GA. Vacuolar symplast and methodological approach to monitoring water self-diffusion between vacuoles of contacting root cells. Russian Journal of Plant Physiology. 2007 Sep; 54(5):683–692. doi: 10.1134/S1021443707050172

67. Andreev IM. The vacuolar symplast: Does it really exist in plants? (Comments on Publications of G.A. Velikanov et al. in Russian Journal of Plant Physiology). Russian Journal of Plant Physiology. 2008 Oct;55(6):843–845.

68. De-Regil L, Jefferds M, Sylvetsky A, Dowswell T. Intermittent iron supplementation for improving nutrition and development in children under 12 years of age (Review). The Cochrane Library. 2011; Issue 12: .

69. Blaby-Haas CE, Merchant SS. Lysosome-related organelles as mediators of metal homeostasis. Journal of Biological Chemistry. 2014; 289(41):28129–28136. doi: 10.1074/jbc.R114.592618 PMID: 25160625

70. Claus J, Chavarría-Krauser A. Modeling regulation of zinc uptake via ZIP transporters in yeast and plant roots. PLOS ONE. 2012; 7(6):e37193. doi: 10.1371/journal.pone.0037193 PMID: 22715365

71. Alon U. An Introduction to Systems Biology. Design Principles of Biological Circuits. London: CRC press; 2006.

72. Louie AH. Robert Rosen's anticipatory systems. Foresight. 2010; 12(3):18–29. doi: 10.1108/14636681011049848

73. Rosen R. Anticipatory systems. New York: Springer; 2012.

74. Moore-Ede MC, Sulzman FM, Fuller CA. The clocks that time us. Cambridge, Massachusetts: Harvard University Press; 1982.

75. Moore-Ede M. Physiology of the circadian timing system: Predictive versus reactive homeostasis. Am J Physiol. 1986; 250:R737–52. PMID: 3706563

76. Duc C, Cellier F, Lobréaux S, Briat JF, Gaymard F. Regulation of iron homeostasis in Arabidopsis thaliana by the clock regulator time for coffee. Journal of Biological Chemistry. 2009; 284(52):36271–36281. doi: 10.1074/jbc.M109.059873 PMID: 19828447

Paper 3:
A basic model of calcium homeostasis in non-excitable cells

A basic model of calcium homeostasis in non-excitable cells

Christina H. Selstø, Peter Ruoff*

Department of Chemistry, Bioscience, and Environmental Engineering, University of Stavanger, Stavanger, Norway

* peter.ruoff@uis.no

Abstract

The level of cytosolic calcium (Ca^{2+}) in cells is tightly regulated to about 100 nM (pCa $\approx$ 7). Due to external stimuli, the basal cytosolic Ca^{2+} level can temporarily be raised to much higher values. The resulting Ca^{2+} transients take part in cell-intrinsic signals, which result in cellular responses. Because of its signaling importance and that high levels of Ca^{2+} can lead to apoptosis, regulation and homeostatic control of cytosolic Ca^{2+} is essential. Based on experimentally known molecular interactions and kinetic data together with control theoretic concepts (integral feedback) we developed a basic computational model describing robust cytosolic Ca^{2+} homeostasis. The aim of the model is to describe the integrative mechanisms involved in cytosolic Ca^{2+} homeostasis in non-excitable cells. From a model perspective, the cytosolic steady state value (set point) of 100 nM is determined by negative feedback loops (outflow controllers), one of these represented by the plasma membrane Ca^{2+} ATPase (PMCA) - calmodulin (CaM) pump and its activation by cytosolic Ca^{2+}. Hysteretic behaviors of the Ca pumps and transporters have been added leading to improved kinetic behaviors indicating that hysteretic properties of the Ca^{2+} pumps appear important how cytosolic Ca^{2+} transients are formed. Supported by experimental data the model contains new findings that the activation of the inositol 1,4,5,-tris-phosphate receptor by cytosolic Ca^{2+} has a cooperativity of 1, while increased Ca^{2+} leads to a pronounced inhibition with a cooperativity of 2. The model further suggests that the capacitative inflow of Ca^{2+} into the cytosol at low Ca^{2+} storage levels in the ER undergoes a successive change in the cooperativity of the Store Operated calcium Channel (SOCC) as Ca^{2+} levels in the ER change. Integrating these aspects the model can show sustained oscillations with period lengths between 2 seconds and 30 hours.

Author Summary

Cytosolic calcium is subject to a general homeostatic regulation to about 100 nM against a ten thousand times larger extracellular calcium concentration. We investigated the conditions for robust cytosolic and luminal (endoplasmatic reticulum, ER) calcium homeostasis in non-excitable blood and epithelial cells and how external and internal calcium perturbations affect these homeostatic mechanisms. We found that gradual time-dependent (hysteretic) changes of calcium pumps and transporters and their associated cooperativities play an essential role in observed kinetics of the calcium flow in and out of the ER. Using a two-site calcium binding model we quantitatively describe the cytosolic calcium-induced calcium transport out of the ER with a cooperativity of 1, and its inhibition at higher cytosolic calcium concentrations with a cooperativity of 2. For the capacitative Ca entry by Store Operated Calcium Channels (SOCCs) when ER calcium

needs to be refilled we find excellent agreement between experimental kinetic data and the model when the cooperativity of luminal calcium changes from 1.3 at 500 μM to 0.8 at 20 μM. Integrating these different aspects of cytosolic and store calcium regulation leads to a basic model for cellular calcium homeostasis, which can show oscillations with period lenths from a few seconds up to 30 hours!

Introduction

Calcium is one of the most abundant and versatile cations in organisms and the human body. Not only important for the maintenance of the skeleton, calcium is also important for the overall health and signaling processes [1]. As a second messenger calcium plays a role in nearly all physiological processes ranging from fertilization, photoreceptor regulation to cell death [1–6].

The concentration of free cytosolic Ca^{2+} in a resting cell is kept at around 100 nM while in the extracellular environment the Ca^{2+} concentration is about ten thousand times higher, i.e., about 1 mM. To keep the level of cytosolic Ca^{2+} robustly at such low levels any perturbation in cytosolic Ca^{2+} is opposed by compensatory homeostatic mechanisms [7]. These mechanisms consist of negative feedback loops where transporters remove excess of cytosolic Ca^{2+} by excreting it or moving it to cellular stores.

An overview of the components involved in cytosolic Ca^{2+} homeostasis is shown in Fig 1. In non-excitable cells, the Arachidonic Acid Regulated Ca^{2+} Channel (ARCC) and the Store Operated Ca^{2+} Channel (SOCC) constitute the main Ca^{2+} entry pathways into the cell. They are both Orai channels connecting to STIM in either the plasma membrane (PM) or the ER membrane for ARCC and SOCC respectively [8]. Orai proteins are proteins found in the plasma membrane which constitute the pore subunit of the channels [8,9]. The difference between these channels is that while SOCCs are dependent on the Ca^{2+} level in the ER store, the ARCCs are not activated by Ca^{2+} in the ER, but by extracellular signals. This occurs by first activating arachidonic acid, which in turn will then activate the ARCCs. While STIM is assumed to be bound to ARCC, ARCC is not explicitly included in the model. The SOCCs, also known as Calcium Release Activated Channels (CRACs), are responsible for the inflow of Ca^{2+} into the cell to refill the ER with calcium, when depleted by leaks [10] or by signaling events [8, 11, 12].

When Ca^{2+} enters the cytosol through channels in the plasma membrane (PM), the cytosolic concentration of Ca^{2+} is regulated to about 100 nM by binding to buffering proteins, by organelle sequestration of Ca^{2+} and by extruding Ca^{2+} through the PM. There are several Ca^{2+} binding proteins which act either as buffers (buffer proteins) or mediate an effect by Ca^{2+} (effector proteins). Calmodulin (CaM) is an important effector protein which takes part in the Ca^{2+} activation of PMCA and NCX, but plays also an important role in Ca^{2+} dependent signaling [13, 14]. The PMCA appears to be the most important efflux path for Ca^{2+} in non-excitable cells, although some non-excitable cells have in addition the Na^{+}/Ca^{2+} exchanger (NCX). Some controversy exists on how important the role of NCX is in non-excitable cells, whereas in excitable cells NCX appears most important for removing Ca^{2+} from the cytosol through the PM [15, 16]. The PMCA has been thought of having a housekeeping function, because of its high affinity to Ca^{2+} and a relatively low throughput thereby bringing cytosolic Ca^{2+} concentrations down to their resting levels. The PMCA comes in different isoforms with various Ca^{2+} affinities and transport rates, which have been suggested as a fine tuner of signals in localized areas of the cell [15, 17, 18]. NCX, on the other hand, is a low affinity transporter with a high throughput in Ca^{2+} removal, which is needed in excitable cells where rapid increases in cytosolic Ca^{2+} concentrations occur.

In contrast to the cytosol, both the ER and mitochondria contain much higher Ca^{2+}

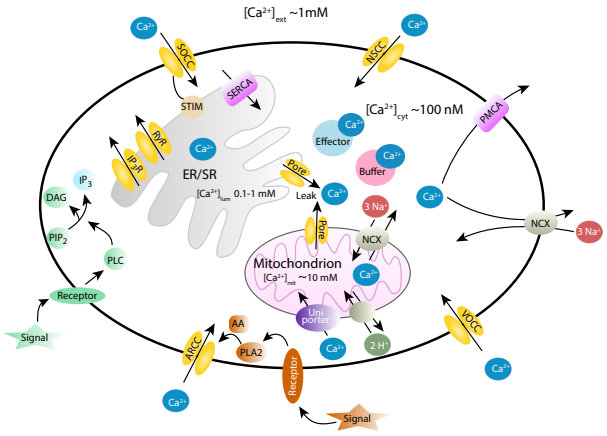

Fig 1. Overview of Ca^{2+}-ion transport in an eukaryotic cell. The illustration shows the channels, pumps, receptors, and organelles involved in the Ca^{2+} transport to and from the cytosol. The channels for Ca^{2+} influx from the extracellular space include the Voltage Operated Calcium Channels (VOCCs) in excitable cells, ligand operated Ca^{2+} channels like the Arachidonic acid Regulated Calcium Channels (ARCCs), Store Operated Calcium Channels (SOCCs) and Non-Specific Cation Channels (NSCC). Ca^{2+} can also enter the cytosol from organelle stores such as the endoplasmic reticulum (ER) and mitochondria. The Inositol 4,5-Trisphosphate Receptor (IP_3R) and Ryanodine Receptors (RYRs) release Ca^{2+} into the cytosol in a Ca^{2+} dependent manner. There is also evidence that there is a Ca^{2+} leakage from the ER or organelle stores into the cytosol. The IP_3R channel is activated by IP_3. IP_3 is the result of a signal transduction chain originating from a signal which activates a G-protein coupled receptor and produces phospholipase C (PLC). PLC catalyzes the hydrolysis of phosphatidylinositol 4,5-bisphosphate (PIP_2) which produces IP_3. Mitochondria can expel Ca^{2+} through pores and ion exchangers (Na^+/Ca^{2+} and H^+/Ca^{2+}). Plasma Membrane Ca^{2+} ATPase (PMCA) and the sodium-calcium exchanger (NCX) transport cytosolic Ca^{2+} into the extracellular space. The Sarco/Endoplasmic Reticulum Calcium ATPase (SERCA) is responsible for the Ca^{2+} transport into the ER, while transport of Ca^{2+} into mitochondria occurs via an uniporter. In addition, proteins both present in the cytosol and organelles can bind Ca^{2+} and act as buffers (buffer proteins), like calsequestrin or calreticulin, while other Ca^{2+} binding proteins, such as calmodulin (CaM), mediate Ca^{2+} effects (effector proteins). For references about these processes see main text.

concentrations, i.e., 0.1 - 1mM in the ER, and around 10mM in mitochondria. In this work, the mitochondria being involved in the storage and buffering of Ca^{2+} are not included in the model. On the other hand, the ER, which holds important roles in both signaling, in forming Ca^{2+} transients, and in Ca^{2+} storage, has been included as part of the cytosolic and organelle Ca^{2+} homeostatic machinery. As mentioned, SOCCs are mainly responsible for refilling the ER with Ca^{2+} by an ATPase called the sarco/endoplasmic reticulum Ca^{2+} ATPase (SERCA), when Ca^{2+} is depleted in the ER by either the inositol 4,5-trisphosphate receptors (IP_3R) or by ryanodine receptors (RyR), both located in the ER membrane. Since the RyR's are mainly responsible for the ER-Ca^{2+} depletion in excitable cells, the IP_3R channel is considered in the model as the only Ca^{2+} outflow path from the ER, in addition to leakage [10]. IP_3R is activated both by IP_3 and by cytosolic Ca^{2+} [19]. The activation and inhibition kinetics of IP_3R are described in more detail below.

Materials and methods

Rate equations were solved by using the Fortran subroutine LSODE [20]. When not mentioned otherwise, concentrations and time units are in μM and seconds (s), respectively. Plots were generated with gnuplot (www.gnuplot.info) and edited with Adobe Illustrator (adobe.com). Experimental data were extracted from graphs by using GraphClick (https://graphclick.en.softonic.com/mac). The analyses of experimental data were done with gnuplot or Excel, and then implemented into the model. The program Cn3D [21] was used for the structural analysis of rat IP_3R [22]. To make annotations simpler, concentrations of compounds are denoted by compound names without square brackets. The Supporting Informations contain source files, compiled binaries, and instructions how to execute the different models.

Illustrating integral control: A PMCA-based minimal model

The role of Ca^{2+} in signaling is complex and so are the Ca^{2+} fluxes and transport paths in the cell. The intention of this work has been to get an understanding of how robustness in cytosolic Ca^{2+} homeostasis can be achieved while allowing the occurrence of experimentally observed Ca^{2+} transients during an inflow perturbation of Ca^{2+} into the cytosol. The model was developed by starting initially with a simple set of regulatory elements where experimentally known pathways and dynamic properties were then successively added. The initial (minimal) model contains the Ca^{2+} pump PMCA as the essential regulatory element together with Ca^{2+}-binding buffer proteins (lumped into variable B) and the Ca^{2+}-binding effector protein Calmodulin (variable M). Perturbation of cytosolic Ca^{2+} occurs by a constant inflow k_1 of external Ca^{2+} into the cytosol.

To achieve cytosolic Ca^{2+} homeostasis the PMCA is considered to be part of a negative feedback loop in maintaining a low and stable cytosolic Ca^{2+} concentration. In addition we include integral control in the loop (Fig 2A), which is a concept from control engineering [23–32]. Integral control (or integral feedback) allows to maintain robust homeostasis, i.e. keeping in our case the cytosolic Ca^{2+} level at a given set-point Ca^{2+}_{set} for different but constant (k_1) inflow perturbations. In general, integral control is achieved to integrate with respect to time the error ϵ, which is the difference between the Ca^{2+} set-point (Ca^{2+}_{set}) and the actual cytosolic Ca^{2+} concentration. The integrated error is then used to compensate for changes in the cytosolic Ca^{2+} concentration (Fig 2A).

There are presently three main kinetic approaches how integral control can be achieved in a chemical system. One approach, which we use here, is based on a zero-order removal of the negative feedback species (controller species) [23, 26, 28]. The second approach (antithetic control) is using two controller species, which react with each other either

directly [30, 31] or via an enzyme [33], while one of the controllers feeds back negatively to the controlled variable. In the third approach the controller variable is produced by first-order autocatalysis, but needs to be removed by a first-order reaction [34–36].
Fig 2B shows a molecular representation of Fig 2A using a zero-order removal of the controller variable PMCA (our initial model). The following PMCA-Ca^{2+}_{cyt} negative feedback loop is considered: cytosolic Ca^{2+} is activating PMCA [37] and thereby transporting Ca^{2+}_{cyt} out of the cell and opposing the effect of an increasing Ca^{2+}_{cyt}. PMCA inactivation is considered to occur by internalization [38] as for other plasma membrane proteins [39]. Activation and deactivation of PMCA are outlined in red, and as we will show below are important for determining the Ca^{2+} set-point in the cytosol. To achieve integral control with a robust set-point we focus here on a zero-order internalization of PMCA as a requirement for integral control.

$$\dot{\mathrm{PMCA}}=\frac{\mathrm{d\,PMCA}}{\mathrm{d}t}= \underbrace{k_5\cdot \mathrm{Ca}^{2+}_{\mathrm{cyt}}}_{\text{PMCA activation}} - \underbrace{\frac{k_6\cdot\mathrm{PMCA}}{k_7+\mathrm{PMCA}}}_{\text{internalization}} \overset{k_7\ll \mathrm{PMCA}}{\approx} -k_5\overbrace{\left[\underbrace{\left(\frac{k_6}{k_5}\right)}_{\mathrm{Ca}^{2+}_{\mathrm{set}}} -\mathrm{Ca}^{2+}_{\mathrm{cyt}}\right]}^{error} \quad (1)$$

Zero-order kinetics for PMCA internalization is obtained when $k_7 \ll$ PMCA, i.e. PMCA binds tightly to the enzymatic internalization machinery where k_7 plays the role of a dissociation/Michaelis constant. Eq. 1 shows the rate equation for PMCA, its activation and internalization terms and the reorganization of the equation into the error term between set-point and the actual Ca^{2+} concentration when zero-order condition applies. Fig 2C shows the robust perfect adaptation of cytosolic calcium to its set-point for different k_1 inflow rates when zero-order internalization kinetics are applied.
On the other hand, when internalization of PMCA becomes first-order with respect to PMCA, i.e., when

$$\dot{\mathrm{PMCA}} = k_5\cdot \mathrm{Ca}^{2+}_{\mathrm{cyt}} - k_6\cdot\mathrm{PMCA} \quad (2)$$

then the robustness of the PMCA negative feedback loop is lost and Ca^{2+}_{cyt} increases proportionally with k_1 (Fig 2D). For a complete set of the rate equations, rate constant values and initial concentrations, see Supporting Information S1 Program.

Results and discussion

Overview of the cellular model

Fig 3 shows the model considered here, including all parts and dynamic behaviors which we deemed necessary for describing cellular Ca^{2+} homeostasis. As a Ca^{2+} store we have focused on the endoplasmatic reticulum (ER), but have not included other organelles such as mitochondria.

While the primary focus of our work was on Ca-homeostasis and not on oscillations, we observed that negative feedback loops have the potential to oscillate, either regular or chaotic, and that even under such conditions the negative feedback mechanisms are able to maintain robust homeostasis [40, 41]. It was therefore not surprising that the model can relatively easy exhibit oscillations and still maintain Ca-homeostasis in both the cytosol and in the ER. At the end of the paper we briefly describe some of these oscillations, which, dependent on parameter values can have period lengths from a few seconds up to 30 hours!

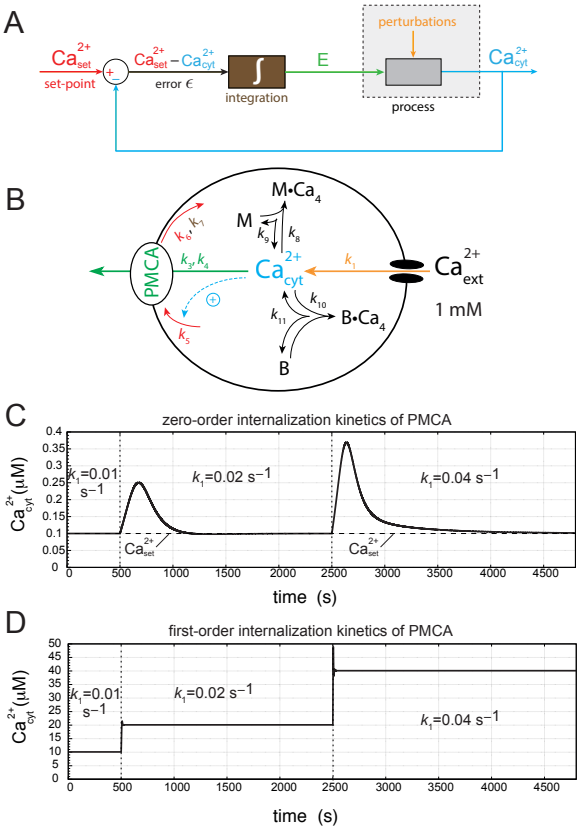

Fig 2. Minimal feedback model of cytosolic Ca^{2+} homeostasis with and without integral control. (A) General flow diagram of negative feedback with integral control. The red color indicates the set-point of the controlled variable (Ca^{2+}_{cyt}) while the blue color refers to its actual value. Integration (brown color) of the error (difference between set-point and actual value) leads to the integrated error E (outlined in green) which for step-wise inflow perturbations k_1 (orange color) will precisely move the controlled variable (blue) to its set-point [24]. (B) Minimal molecular model of PMCA-based cytosolic Ca^{2+} homeostasis with color codes matching the flow diagram in panel (A). M and B denote two Ca^{2+} binding proteins with arbitrary binding properties. The kinetics of PMCA internalization (indicated by rate constants k_6 and k_7) determines whether integral control is invoked or not. (C) Zero-order PMCA internalization kinetics leads to integral control and robust homeostasis. In this case the Ca^{2+}_{cyt} concentration returns to the set-point Ca^{2+}_{set} for the different inflow perturbation rates k_1. (D) Loss of robust Ca^{2+}_{cyt} homeostasis when PMCA internalization kinetics is no longer zero-order but first-order. For details, see main text and Supporting Information S1 Program.

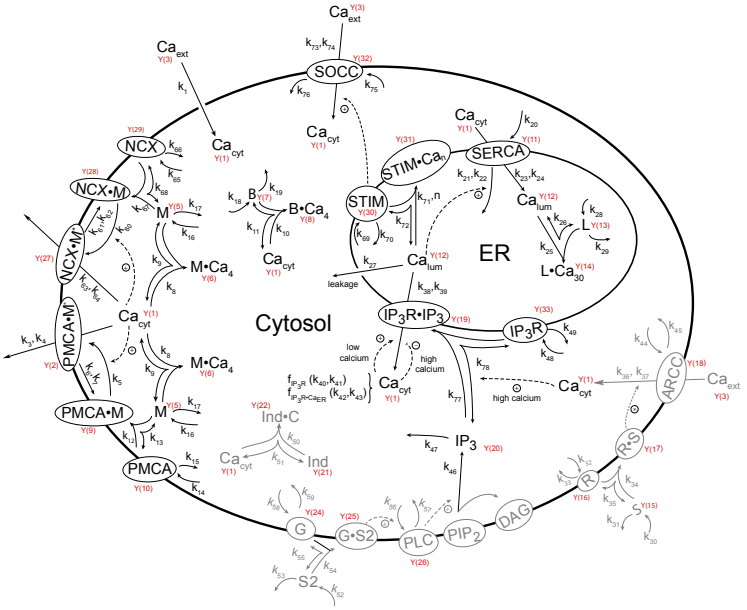

Fig 3. Model of Ca^{2+} homeostasis in the cytosol and endoplasmatic reticulum (ER). Components and rate constants of the model are shown in this overview figure. The Y(i)'s outlined in red are the LSODE Y vector's components [20], which are assigned to each biochemical species in the model. Arrows represent reactions of the involved species while dashed lines indicate signaling pathways, i.e., how components activate or inhibit each other. The grayed-out reactions with rate constants and Y(i)'s are included in the model, but are not explicitly presented. The set of rate equations together with a list of abbreviations and the LSODE Y(i) assignments are described in S1 Text.

In the following we describe in more detail the different aspects of the model in comparison with experimental results.

The plasma membrane Ca^{2+} ATPase

The cell type we consider first are erythrocytes. They lack most organelles including the nucleus, mitochondria, the Golgi apparatus and the endoplasmatic reticulum (ER). Ca^{2+} homeostasis in these cells is maintained by PMCA, which appears to be the most abundant pump in these cells. To transport one Ca^{2+} out of the cell the PMCA requires one ATP and exchanges H^+ ions for Ca^{2+}. The stoichiometry of the Ca^{2+}/H^+ exchange is controversial [15], but neither ATP nor H^+ ions are explicitly included in the model (which have their own homeostasis mechanisms). Maximum activation of the PMCA pump requires the presence of calmodulin (M); its importance in PMCA activation is

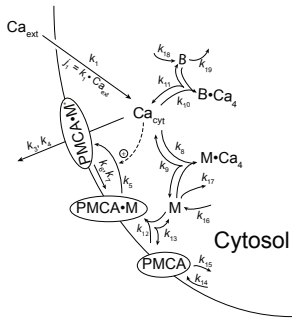

Fig 4. Calmodulin and Ca^{2+} activation of PMCA. The figure shows the activation of PMCA by calmodulin (M) and Ca^{2+}. Although experiments have shown that PMCA can apparently transport Ca^{2+} in the absence of calmodulin, but less effectively [15, 45], we have in the model not included a PMCA based Ca^{2+} transport without calmodulin.

widely agreed upon [37, 42–44]. PMCA can also function and be partially active without calmodulin, probably due to acidic phospholipids, but only to about half of its maximal activity [37, 43].

Fig 4 shows part of the model with calmodulin (M) activating PMCA by forming PMCA•M. The PMCA•M complex is further activated by Ca^{2+} leading to PMCA•M^*, which is the form with the maximum Ca^{2+} pump activity. PMCA is a high affinity pump with a K_d (with respect to Ca^{2+}) of 0.1–1 μM when calmodulin is bound, but a K_d of about 10–20 μM when calmodulin is absent [15, 45].

In our calculations we have taken the set-point for cytosolic Ca^{2+} to be 0.1 μM. To achieve robust homeostasis we consider, as for the minimal model (Fig 2), a first-order activation of PMCA by Ca^{2+} with rate constant k_5 (Fig 4) leading to the active form PMCA•M^*. The inactivation of PMCA•M^* is considered a zero-order process with respect to PMCA•M^*. The set-point for cytosolic Ca^{2+} is given by the steady state condition for PMCA•M^*, i.e.,

$$\frac{\mathrm{d\,PMCA{\bullet}M^*}}{\mathrm{d}\,t} = k_5{\cdot}(\mathrm{PMCA{\bullet}M}){\cdot}(\mathrm{Ca^{2+}}) - \frac{k_6{\cdot}(\mathrm{PMCA{\bullet}M^*})}{k_7{+}(\mathrm{PMCA{\bullet}M^*})} = 0 \qquad (3)$$

where k_7 plays the role of a dissociation (Michaelis) constant. Applying zero-order kinetics with respect to PMCA•M^*, $k_7 \ll PMCA{\bullet}M^*$, the steady state condition of Eq. 3 becomes

$$k_5{\cdot}(\mathrm{PMCA{\bullet}M}){\cdot}(\mathrm{Ca^{2+}}) = k_6 \qquad (4)$$

which determines the steady state value of cytosolic Ca^{2+}

$$\mathrm{Ca^{2+}_{set}} = \mathrm{Ca^{2+}_{ss}} = \frac{\mathrm{k_6}}{\mathrm{k_5{\cdot}(PMCA{\bullet}M)}} \qquad (5)$$

and which is independent of the Ca inflow perturbation $j_1{=}k_1{\cdot}\mathrm{Ca_{ext}}$ (see Fig 4).

Since we applied first-order kinetics with respect to PMCA•M in its Ca^{2+} activation, the set-point of Ca^{2+} depends on the concentration of PMCA•M. This leads to the possibility of a *variable* set-point, as has been argued for by Mrosovsky on general grounds [46]. As will be shown/discussed below such a variable set-point does well describe the experimental results.

PMCA kinetic parameters

In the following we discuss the parameter values used in the model focusing first on red blood cells. To the extent this is possible we try to use or derive rate and bindings constants primarily from *in vivo* studies.
For PMCA's pump rate v_{pump} we are using a simple Michaelis-Menten type expression

$$v_{pump} = \frac{k_3 \cdot (\text{PMCA} \bullet \text{M}^*) \cdot (\text{Ca}^{2+}_{\text{cyt}})}{k_4 + (\text{Ca}^{2+}_{\text{cyt}})} = \frac{V_{max} \cdot (\text{Ca}^{2+}_{\text{cyt}})}{K_M + (\text{Ca}^{2+}_{\text{cyt}})} \quad (6)$$

where PMCA•M^* denotes the active form of the pump, V_{max}=k_3·(PMCA • M^*) with k_3 and k_4 as turnover number (k_{cat}) and dissociation (Michaelis) constant, respectively.

PMCA K_M values. - The enzyme data base BRENDA [47] has 6 K_M entries for human PMCA and SERCA (Ca-ATPases) with values for erythrocytes, liver, and heart ranging from 0.013–20 μM [48–50]. For red blood cells, we have analyzed the *in vitro* data by Niggli et al. [51], which indicate a K_M value for PMCA of about 1 μM (see S2 Text). By using two protocols, Kubitscheck et al. [52] determined the K_M value of PMCA in single red blood cells to 24 μM and 1 μM. The 24 μM value has been interpreted by the authors due to an inactive calmodulin in one of their protocols. A K_M value of about 0.2 μM was indicated by Bruce [53] for non-excitable cells, while Blaustein [54] refers to a K_M value of 0.1 μM, but in both cases no explicit reference to experimental work was provided. However, our calculations indicate no practical differences when K_M values of 0.1 μM or 1 μM are used (see S2 Text).

PMCA Turnover number and V_{max} values. - Entries in BRENDA for the human PMCA turnover number (k_{cat}) vary from 9.5–149 s^{-1}. In Bradshaw and Dennis' "Handbook of Cell Signaling" Blaustein lists a k_{cat} value of 30 s^{-1} [54] (without reference to experiments), while Chen et al. reported a k_{cat} of about 200 s^{-1} in rat cochlear hair cells [55].
Considering red blood cells Schatzmann [56] found a V_{max} for PMCA of 148 μM/min. A similar value of 120 μM/min (average, see S2 Text) was obtained by Dagher and Lew [57]. In the Dagher and Lew experiments, also using erythrocytes, the zero-order kinetic extrusion rate of PMCA was determined by using the ionophore A23187 for massively loading the cells with Ca^{2+} and then inhibiting A23187 by using $CoCl_2$ (Fig 5A). Due to the large amount of cytosolic Ca^{2+} in comparison with the pump's K_M value the pump runs at maximum speed (V_{max}). By using the same method Tiffert et al. [58] measured the PMCA-mediated Ca^{2+} extrusion rate in red cells from freshly drawn blood in relation to the hemoglobin content of the cells. By assuming that one red blood cell contains 270×10^6 hemoglobin molecules and that one red blood cell has a volume of approximately 10^{-13} liter, V_{max} for the pump was estimated to 234 μM/min (S2 Text for details). In addition, Tiffert et al. [58] alternatively measured the pump rate in relation to the number of cells. Using these values we estimate a V_{max} of about 156 μM/min (S2 Text) close to the value originally determined by Schatzmann [56].
Fig 5A shows the above referred experiment by Dagher and Lew [57] when PMCA (with possibly other pumps) balance a large inflow of Ca^{2+} by use of the ionophore

A23187. When the ionophore is blocked the kinetics of the pumps' Ca^{2+} extrusion can be observed. Fig 5B shows a corresponding set of model calculations.

PMCA activation and cytosolic calcium profile

Using bovine endothelial cells Sedova and Blatter [59] investigated PMCA activation by following the inflow of Ca^{2+} into the cytosol when 2mM extracellular calcium is applied. The cellular inflow of Ca^{2+} occurs, because the calcium level in the ER is low and leads to a so-called 'capacitative Ca entry' [60] into the cell to refill the ER with calcium (see also section 'Store operated Ca^{2+} entry' below). The inflow of calcium into the cytosol activates PMCA, which reduces the level of cytosolic Ca^{2+} leading to a biphasic response. Fig 6A (phases 1 and 2) shows the increase and decrease in cytosolic Ca^{2+} concentration when cells are treated with 2 mM extracellular calcium. In phase 3 the extracellular calcium is washed out and cells were treated with the PMCA inhibitor carboxyeosin. Then the inhibitor was washed out and 2mM extracellular calcium was reapplied. Sedova and Blatter now observed a slower increase of cytosolic Ca^{2+} (Fig 6A, phase 4). We used the parameters k_1 (inflow of Ca^{2+} into the cytosol) and k_3 (maximum rate of PMCA) to describe the observed behaviors, but are neglecting here the further transfer of cytosolic calcium into the ER. The slower increase of cytosolic Ca^{2+} in phase 4 is based on two assumptions we made: (i) carboxyeosin partly inhibits the inflow of calcium into the cytosol. This assumption is based on results by Choi and Eisner for rat myocytes [61], who observed that the inflow of Ca^{2+} into the cytoplasm was inhibited by carboxyeosin. The other assumption was that PMCA still remained partly inhibited, as not all carboxyeosin may have been washed out and/or the reactivation of PMCA is slow due to a hysteretic property of the pump. Panels B and C in Fig 6 show the calculated cytosolic Ca^{2+} profiles and the underlaying changes in k_1 and k_3.
Another explanation could be that in absence of PMCA the Na^{+}-Ca^{2+} exchanger NCX brings Ca^{2+} down to low concentrations similar to PMCA [59]. However, since NCX is considered to have a lower affinity for calcium and is generally believed to be active at higher Ca^{2+} concentrations in comparison to PMCA this suggestion remains controversial [15, 16].

PMCA's hysteretic behavior

However, the changes invoked on k_1 and k_3 alone are not sufficient to model the transients observed in the above experiments by Sedova and Blatter. There needs to be present an inherent slowness in PMCA's response kinetics. In other words, PMCA acts as hysteretic enzyme, i.e. shows a slow activation/reactivation kinetics [59, 62, 63]. Frieden [63] studied this slowness of certain enzymes upon activations and termed the phenomena 'hysteretic' behavior. Scharff et al. [62] concluded that PMCA reacts hysteretically to increases in cytosolic Ca^{2+} inflow and that this is a necessary property to enable the occurrence of transients.
In general, transients are important in signaling and differences in the transient's strength in amplitude or frequency (if oscillatory) are interpreted as different signals. For example, the slowness in PMCA activation allows the concentration of Ca^{2+} in the cytosol to increase to a relevant concentration for signaling purposes, while a slowness in its deactivation would give the PMCA time to function as an extrusion mechanism to bring the cytosolic Ca^{2+} level down to its set-point again.
As a way of incorporating hysteresis, we have employed the calmodulin (CaM) binding as the limiting factor, as it is widely agreed upon that CaM binding to PMCA isoforms can vary, and that CaM binding is notoriously slow. Those pump isoforms dominantly found in non-excitable cells are characterized as "slow PMCA pumps", whereas in excitable cells where Ca^{2+} can vary frequently and rapidly, some isoforms of PMCA are

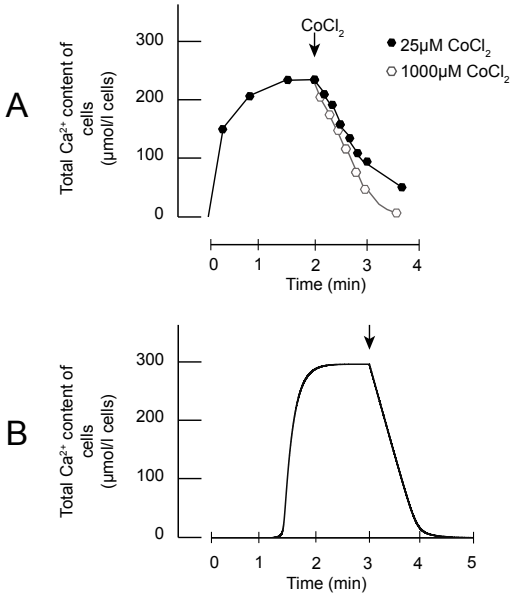

Fig 5. Changes in Ca^{2+} concentration for extrusion rate determination in erythrocytes. Panel A shows experimental plots adapted from Dagher and Lew [57], where the ionophore A23187 is used to let Ca^{2+} enter the cytosol until PMCA (and other pumps) can match the Ca-inflow, which leads to a steady state in cellular Ca^{2+}. Then, $CoCl_2$ was added to block the ionophore (indicated by arrow). With higher $CoCl_2$ concentrations the rate of Ca^{2+} extrusion becomes linear with respect to time and shows close to zero-order kinetics with respect to cellular Ca^{2+}. This indicates that the pump's removal of Ca^{2+} from the cells is at a maximum rate (V_{max}). Panel B shows the results from a corresponding model calculation. Rate equations, parameter values and initial concentrations are given in 'S2 Program' together with the Fortran source code and executables.

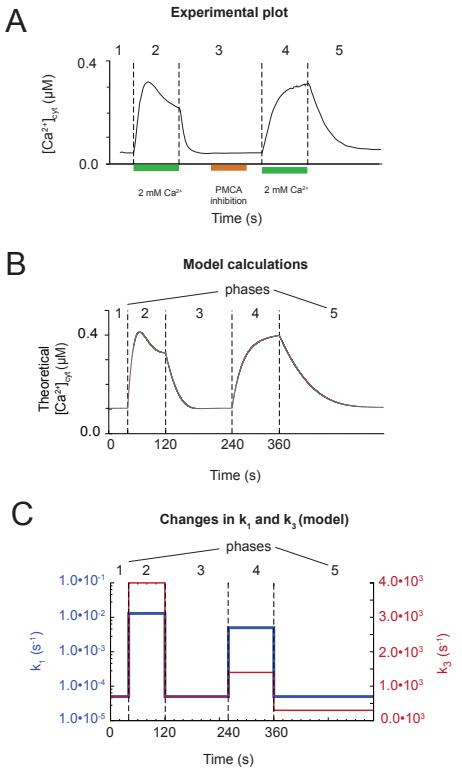

Fig 6. PMCA induced Ca^{2+}_{cyt} dynamics before and after its inhibition. Panel A shows a redrawn figure of Sedova and Blatter's experimental results (Fig 1A in [59]) showing the dynamics of cytosolic Ca^{2+} upon capacitative Ca loading. The figure is divided into 5 phases indicated by dashed vertical lines. Phase 1: steady state of cytosolic Ca^{2+} prior to extracellular Ca treatment; phase 2: cells are treated with 2 mM extracellular Ca^{2+}; phase 3: external Ca^{2+} is washed out and PMCA is inhibited by carboxyeosin; phase 4: 2 mM extracellular Ca^{2+} is re-applied; phase 5: extracellular Ca^{2+} is washed out. Panel B shows our model's response in cytosolic calcium when the inflow of calcium into the cell (k_1) and the activity of PMCA (k_3) undergo step-wise changes. Panel C shows the applied changes in k_1 and k_3 during the five phases to mimic the experimental Ca profiles. Phase 1: k_1=5×10^{-5}s^{-1}, k_3=7.0×10^{2}s^{-1}; phase 2: k_1=1.3×10^{-2}s^{-1}, k_3=4.0×10^{3}s^{-1}; phase 3: k_1=5×10^{-5}s^{-1}, k_3=7.0×10^{2}s^{-1}; phase 4: k_1=5×10^{-5}s^{-1},k_3=1.4×10^{3}s^{-1}; phase 5: 5×10^{-5}s^{-1}, k_3=3.0×10^{2}s^{-1}. Other rate constant values, initial concentrations, and the model's Fortran source file together with executables can be found in the Supporting Information 'S3 Program'.

characterized as "fast pumps" [64–66].
CaM is also described as a limiting factor in the cell for regulation of its targets. Some researchers report that most CaM in the cytosol exist as ApoCaM (unbound to Ca^{2+}) at resting Ca^{2+} levels, and that in most cases ApoCaM does not bind to its targets as long as Ca^{2+} has not bound to it [67,68]. However, Wu and Bers note that some ApoCaM also binds to many proteins like ion channels, membrane proteins and receptors etc. either as part of their structure or for the purpose of local activation by Ca^{2+} binding. This means that upon Ca^{2+} binding, targets already bound to (Apo)CaM can immediately be activated, while the unbound targets need to compete for free Ca^{2+}-CaM in the cytosol. This arrangement fits well with our model where ApoCaM (M in the model) first binds to PMCA (leading to PMCA•M in the model) before activation by Ca^{2+} occurs leading to the active pump form PMCA•M^*. However, there are also arguments that PMCA competes for the free Ca^{2+}-CaM complex [67, 69]. Nevertheless, it appears more likely that CaM binds to PMCA and Ca^{2+} as targets instead of being present as a free Ca^{2+}-CaM complex in the cytosol: it has been estimated that only about 1 % of the total intracellular CaM exist as free Ca^{2+}-CaM complexes [70]. In our model the portion of free Ca^{2+}-CaM complex varies between about 4 – 10 % depending on the rate constants applied in the calculation, where most of them have been taken from literature. The total CaM concentration is set to 10 μM in the model [67]. Rate constant k_9 for the off-rate, i.e. the dissociation of M·Ca_4 into M (CaM) and Ca^{2+}, is 5.0 s^{-1} and k_8 for the on-rate, for the association of Ca^{2+} and M (CaM) to M·Ca_4, is set to 2.5 $\mu M^{-1}\cdot s^{-1}$ in order to keep the K_d at a defined value of 2 μM [70, 71].
In addition to the PMCA-CaM binding, a change in k_3 can also add to the hysteretic behavior of the pump as seen in Fig 6C. The hysteretic properties of the pump regarding k_3 was investigated in more detail when the NCX pump was added to the model (see next section).

Implementing NCX

Next we added the Na^+-Ca^{2+} exchanger (NCX) to the model. NCX moves one Ca^{2+} ion out of the cell with the exchange of 3 Na^+ ions. Using bovine endothelial cells Sedova and Blatter [59] investigated the role of NCX when PMCA was inhibited by La^{3+} ions, and when NCX was inactivated by Na^+ free conditions. They found that under Na^+ free conditions and in the presence of La^{3+}, i.e. when both PMCA and NCX are not active, cytosolic Ca^{2+} cannot reach resting levels. However, when Na^+ was added in presence of La^{3+}, i.e. when only NCX was active, Ca^{2+} concentrations were able to reach resting levels, but more slowly. These results indicate that NCX alone is able to reduce cytosolic Ca^{2+} to resting levels in the absence of PMCA.
Based on the findings by Chou [72], we have included calmodulin (M in model) as a regulator of NCX activation by Ca^{2+}. In this way, the NCX is modeled analogous to PMCA, i.e. NCX is complexed with calmodulin (NCX•M) with the activated form (NCX•M^*). Fig 7A shows, outlined in red, the added NCX part to the model.
Thus, similar to Ca^{2+} regulation by PMCA, a set-point for cytosolic Ca^{2+} can also be formulated for NCX. Setting the rate equation of the calcium-activated calmodulin-associated form ($NCX{\cdot}M^*$) to zero,

$$\dot{(NCX{\cdot}M^*)} = k_{60}{\cdot}(NCX{\bullet}M){\cdot}Ca^{2+} - \frac{k_{61}{\cdot}(NCX{\cdot}M^*)}{k_{62}+(NCX{\cdot}M^*)} \stackrel{!}{=} 0 \qquad (7)$$

assuming that $k_{62} \ll (NCX{\cdot}M^*)$, and then solving from resulting Eq 8 for Ca^{2+}_{ss}=$Ca^{2+}_{set,\,NCX}$

$$k_{60}{\cdot}(NCX{\bullet}M){\cdot}Ca^{2+}_{ss} - k_{61} = 0 \qquad (8)$$

we get for the NCX-based set-point:

$$\mathrm{Ca}^{2+}_{\mathrm{set,\,NCX}} = \frac{k_{61}}{k_{60}(NCX\bullet M)} \tag{9}$$

Model calculations including NCX in comparison with experimental results

In comparison with the experimental results by Sedova and Blatter [59] (Fig 7B) we show here calculations with the inclusion of NCX. Since NCX is assumed to bind calcium less efficiently than PMCA the $\mathrm{K_M}$ of NCX was taken to be 100 μM, which is approximately 2 orders of magnitude larger than the $\mathrm{K_M}$ with respect to calcium for PMCA. On the other hand, the turnover number of NCX (in the model described by k_{63}) is set to $1{\times}10^5$ s^{-1}, which is two orders of magnitude larger than the turnover number (k_3) of PMCA. Fig 7C shows the calculated cytosolic calcium concentration mimicking the experimental results by Sedova and Blatter. In the model we have, in addition, assumed time-dependent hysteretic behaviors both in the capacitative inflow of calcium into the cytosol (described by rate constant k_1) and in the transport of Ca^{2+} by PMCA (described by rate constant k_3). In phases 2 and 4 k_1 is assumed to increase and reaching a maximum value according to the relationships:

$$\text{Phase 2} : k_{1,ph2}(t) = k_{1,ph1} + k^{max}_{1,ph2}{\cdot}(1 - e^{-\alpha(t-t_{ph1})}) \tag{10}$$

and

$$\text{Phase 4} : k_{1,ph4}(t) = k_{1,ph3} + k^{max}_{1,ph4}{\cdot}(1 - e^{-\alpha(t-t_{ph3})}) \tag{11}$$

In Eqs 10 and 11 $k_{1,ph1}$ and $k_{1,ph3}$ are constants both having a value of $1{\times}10^{-4}\mathrm{s}^{-1}$. $k^{max}_{1,ph2}$ and $k^{max}_{1,ph4}$ are the maximum values of k_1 for respective phases 2 and 4 with a value of $1.4{\times}10^{-2}\mathrm{s}^{-1}$ each. The parameter α is $4.5{\times}10^{-2}\mathrm{s}^{-1}$. t_{ph1} and t_{ph3} denote the times when phases 1 and 3 end, respectively. When these k_1-time dependencies are implemented into the model we get the k_1 profile as shown in Fig 7D (outlined in blue). The hysteretic changes of k_3 in phases 2 and 4 is described by the linear relationships

$$\text{Phase 2} : k_{3,ph2}(t) = k_{3,ph1} + \beta(t - t_{p1}) \tag{12}$$

and

$$\text{Phase 4} : k_{3,ph4}(t) = k_{3,ph3} + \beta(t - t_{p3}) \tag{13}$$

with β=200s^{-2} and $k_{3,ph1}$=$k_{3,ph3}$=$5{\times}10^3\mathrm{s}^{-1}$. In phase 5 k_1 and k_3 are zero, except k_{63} (turnover number of NCX), which for all five phases is $1{\times}10^5\mathrm{s}^{-1}$. For a description of the other rate constants, initial concentrations, and how to run the program see Supporting Information 'S4 Program'.

Comparing Figs 7B and C shows that the model calculations represent a good fit to the experiment. The model also shows that NCX can drive cytosolic Ca^{2+} concentrations down to resting values without PMCA present, but at a slower rate, just as observed in the experiments. This is mainly because of the difference between the K_M values of PMCA and the NCX making PMCA a high affinity pump with low K_M (=k_4). The relative high K_M (=k_{64}) of NCX makes NCX a low affinity pump. In order to get the peak shape of the cytosolic Ca^{2+} concentration during phases 2 and 4, the above hysteretic changes of Ca^{2+} inflow (via SOCC, represented here by k_1) and Ca^{2+} outflow

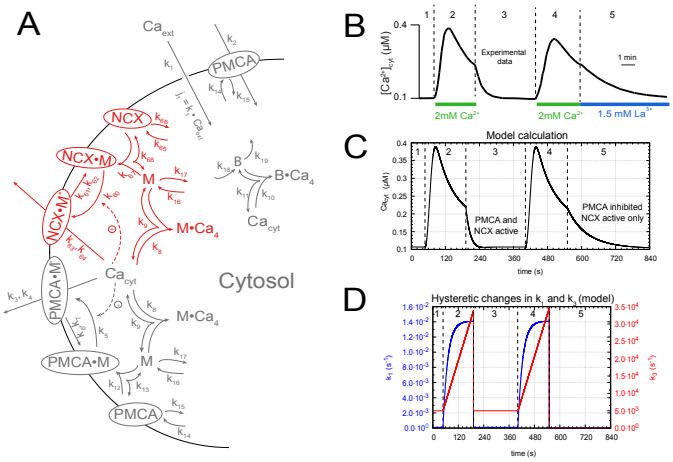

Fig 7. Cytosolic calcium concentration changes during PMCA-NCX based and NCX-only based calcium efflux. Panel A shows the model with NCX incorporated (outlined in red). The rest of the model is seen in grey representing the reactions that were already introduced. Panel B shows the experimental results redrawn from Sedova and Blatter (see Figure 6A in [59]). Panel C shows the corresponding model calculations. Phases 1 and 3: The cell is at resting state with both PMCA and NCX active. Phases 2 and 4: Cells are treated with 2 mM extracellular Ca^{2+} - in the model this change is represented by an increase of k_1 (see text). Phase 5: Only NCX is active, PMCA is inhibited by La^{3+} - in the model this is done by setting k_3 to zero. Panel D shows the (hysteretic) changes in the parameters k_1 and k_3 during phases 2 and 4 described by Eqs 10, 11, 12, and 13. Other rate constants, initial concentrations, and instructions how to run the model are found in Supporting Information 'S4 Program'.

(via PMCA k_3) appear necessary. Possibly, also NCX may exhibit hysteretic behavior, but this was not included.

In an additional set of experiments (Fig 8A) Sedova and Blatter investigated the sequential and simultaneous inhibition of PMCA and NCX. While NCX was inhibited using Na^+-free conditions cells were treated with 2mM extracellular Ca^{2+}. The increase and decrease of cytosolic calcium indicate an active PMCA pump (phase 2, Fig 8A). Then, in phase 3 extracellular Ca^{2+} was washed out and cells were treated with La^{3+} to inhibit PMCA while still having Na^+-free conditions (Fig 8A). Since both PMCA and NCX were now inactive cytosolic calcium levels did not change much (phase 3, Fig 8A). Finally, in phase 4 cells were treated with sodium ions, which activated NCX and drives cytosolic calcium levels down to resting values close to 0.1μM. This clearly indicates that NCX was responsible for the decrease of cytosolic calcium in phase 4.

Fig 8B shows a corresponding calculation of the model mimicking the results by Sedova and Blatter. The experiments show that the La^{3+}-treated cells in phase 3 still show a slight decrease in cytosolic calcium, indicating that the the PMCA inhibition was not 100% perfect or that there may be a still unknown constitutive calcium outflow from the cytosol.

Role of ER in calcium regulation

Overview

The inflow and outflow of Ca^{2+} between the endoplasmatic reticulum (ER) and the cytosol plays a major role in the calcium homeostasis in the ER as well as in the cytosol. The ER functions as a calcium store with concentrations comparable to extracellular calcium. Furthermore, the ER is heavily involved in calcium-mediated signaling (Ca^{2+} inflow into the cytosol) through the inositol 1,4,5-triphosphate receptor IP_3R and ryanodine receptor RyR located in the ER membrane (Fig 1). The activity of the IP_3-bound IP_3R channel ($IP_3R{\bullet}IP_3$, Fig 3) shows a bell-shaped activity profile with a maximum at around pCa 7 [73]. The $IP_3R{\bullet}IP_3$ channel is activated by low cytosolic Ca^{2+} concentrations, i.e. when pCa > 7, while inhibition occurs at higher cytosolic concentrations, i.e. when pCa < 7. An analysis of the experimental data by Kaftan et al. [73] (shown below) indicates an asymmetric channel activity profile with a stronger Ca^{2+}-inhibition cooperativity around 2, while the activation cooperativity is found to be approximately 1.

When the calcium content in the ER is low stromal interaction molecules 1 and 2 (STIM1 and STIM2, represented as STIM in the model, Fig 3) activate store operated Ca^{2+} channels (SOCCs), which lead to an inflow of Ca^{2+} into the cytosol. Subsequently, the ER is refilled through the sarco-endoplasmatic reticulum Ca^{2+} ATPase (SERCA), an ATPase similar to PMCA.

There is evidence that ER-luminal Ca^{2+} leaks into the cytosol. Analyzing the data by Luik et al. [74] shows a good agreement with a first-order kinetic Ca depletion of the ER with a rate constant of 0.012 s^{-1} and an initial leakage velocity of 0.36 μM/s (S6 Program). The leak data recorded by Camello et al. [10] shows almost zero-order Michaelis-Menten kinetics with a slight hysteretic increase of V_{max} and an average leakage rate of 0.22 μM/s (S6 Program).

The ER also contains several high-capacity Ca^{2+}-binding proteins, such a calreticulin [75, 76], which represent ER's (and other organelle's) overall Ca^{2+} storage capacity. According to Michalak et al. (see [75], and references therein) one calreticulin molecule can bind between 20-50 Ca^{2+} ions. In the model (Fig 3) we have represented these high-capacity storage proteins inside the ER with the letter L and enabled them to bind 30 Ca^{2+} ions.

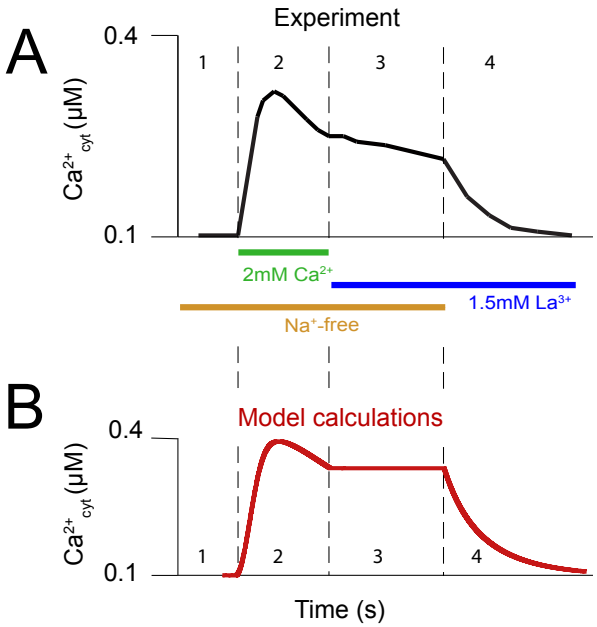

Fig 8. Ca^{2+} efflux following La^{3+} inhibition of PMCA. Panel A is redrawn from Sedova and Blatter's experimental record (Fig 6B in [59]). Panel B derives from a model calculation (S5 Program) simulating the experimental results in A. Phase 1: Cells are at resting conditions, no Ca^{2+} enters the cytosol. Only PMCA is active, NCX is inactive due to Na^{+}-free conditions. In the model inactive NCX is achieved by setting k_{63} to zero. Phase 2: Cells are treated with 2mM extracellular calcium and the capacitative inflow of calcium into the cytosol starts. In the model k_1 and k_3 increase hysteretically (Eqs 10 and 12, S5 Program). Only PMCA is considered to be responsible for pumping calcium out of the cytosol. Phase 3: Extracellular calcium is removed and cells are treated with La^{3+} inhibiting PMCA. Since the medium is still sodium-free NCX is inactive. In the model both k_3 and k_{63} are set to zero. Phase 4: NCX is activated by adding a sodium salt solution to the medium, while PMCA is still inactive due to the presence of La^{3+}. In the model NCX activation is achieved by setting $k_{63}=1\times10^{5}s^{-1}$. Initial concentrations, other rate constant values, and how to run the model are described in Supporting Information 'S5 Program'.

Store operated (capacitative) Ca^{2+} entry

Fig 9 shows, outlined in red, the reaction scheme of the capacitative Ca^{2+} entry in the model determined by the Ca^{2+} concentration in the ER (Ca_{lum}). For simplicity, only one STIM form has been considered in the model. Biologically, there have been found two STIM forms (STIM1 and STIM2), and even though STIM1 and STIM2 have a similar binding affinity towards Ca^{2+} (STIM1: K_d 0.2-0.6 mM, STIM2: K_d 0.5 mM) they display differences in the regulation of SOCC possibly due to structural reasons [77, 78]. STIM2 responds to small changes of Ca^{2+} [77]. The results from Zheng et al. [77] indicate that STIM1 is the only Ca^{2+} sensor responsible for SOCC activation, while STIM2 seems only to play a minor role. On the other hand, Brandman et al. [12] investigated the effects of smaller decreases in luminal Ca^{2+} concentration and suggested that also STIM2 takes part in the feedback regulation of calcium in the cytosol and ER. These findings are supported by the work of Thiel et al. [79]. In the model, when STIM dissociates at low Ca_{lum} concentrations from the STIM•Ca complex (Fig 9), STIM concentration increases and activates the Ca^{2+} inflow through nearby SOCC channels [74, 80].

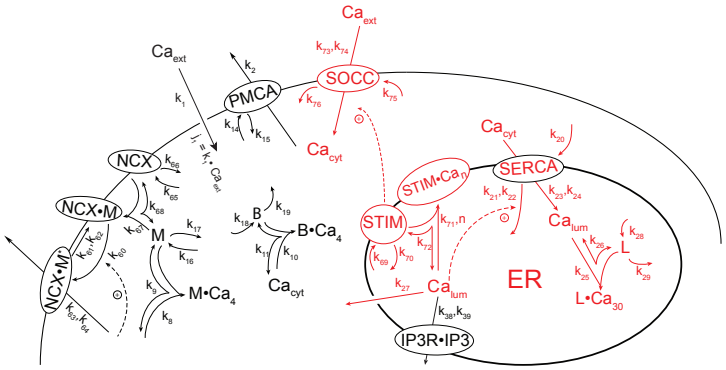

Fig 9. Capacitative Ca^{2+} entry. Outlined in red is the scheme used in the model. Decreasing Ca concentrations in the ER (Ca_{lum}) lead to a dissociation of the STIM•Ca complex and to increased STIM levels activating nearby SOCC channels. The parameter n describes the Ca_{lum}-cooperativity when binding to STIM. To see the relationship between j_{SOCC} at different Ca_{lum} concentrations by STIM activation, the SERCA channel has been formulated as an inflow controller [28] for Ca_{lum}, which allows to keep Ca_{lum} constant at different levels by changing k_{20}. For details, see text and S7 Program.

Luik et al. [74] studied the inflow rate of calcium into the cytosol by the SOCC channel (rate: j_{SOCC}) as a function of the calcium concentration in the ER (Ca_{lum}). We have analyzed the Luik et al. data (Fig 10) in terms of a Ca_{lum} derepression relationship, which activates j_{SOCC} via STIM (Fig 9), i.e., using the relationship

$$j_{SOCC} = \frac{K_I^n \cdot STIM_{tot}}{K_I^n + Ca_{lum}^n} = \frac{\alpha}{\beta + Ca_{lum}^n} \tag{14}$$

where K_I is an inhibition constant, $STIM_{tot}$ is the total (constant) STIM concentration and n is the cooperativity (Hill-coefficient) of the j_{SOCC} inhibition by Ca_{lum}. α, β, and n in Eq 14 were fitted to the experimental data by Luik et al. (S7 Program). Although

Eq 14 is slightly different from the Hill-equation used by Luik et al. the obtained fit and Hill-coefficient n are comparable. While Luik et al. interpreted their Hill-coefficient of 4.2 as a sign of STIM1 oligomerization, we feel that in our case a Hill-coefficient of 3.59 appear misleading, although representing a "best-fit". Our high Hill-coefficient may be misleading by two reasons: firstly, Eq 14 implies a derepression mechanism, where Ca_{lum} apparently inhibits j_{SOCC}, but this is mechanistically only done indirectly via binding to STIM. Secondly, the fit in Fig 10A (green line) indicates that the slope $dj_{SOCC}/d(Ca_{lum})$ should be reaching a plateau at low Ca_{lum} concentrations, which is not strongly supported by the data. We have therefore analyzed the Luik et al. data in terms of a cooperative reversible Ca_{lum} binding to STIM with Hill-coefficient n, described by the process (see S1 Text for the rate equations):

$$n\,Ca_{lum} + STIM \underset{k_{72}}{\overset{k_{71}}{\rightleftharpoons}} STIM{\bullet}Ca_n \tag{15}$$

By successively changing Ca_{lum} from 20μM to 500μM (by steps of 20μM) we found that an eye-balled "best fit" to the Luik et al. data can be obtained (Fig 10B) when n is changed linearly from 0.8 at Ca_{lum}=20μM to n=1.3 at high Ca_{lum}=500μM. We interpret the changing Hill-coefficent as a hysteretic/conformational effect. In other words, at low Ca_{lum} concentrations not all Ca-binding sites are available for binding to Ca, while at higher Ca_{lum} concentrations conformational changes may expose more Ca-binding sites such that more than one Ca^{2+} ion can bind to STIM. Such a view is in agreement with the review by Grabmayr et al. [81], which indicates that some STIM isoforms can bind more than one Ca^{2+} ion.

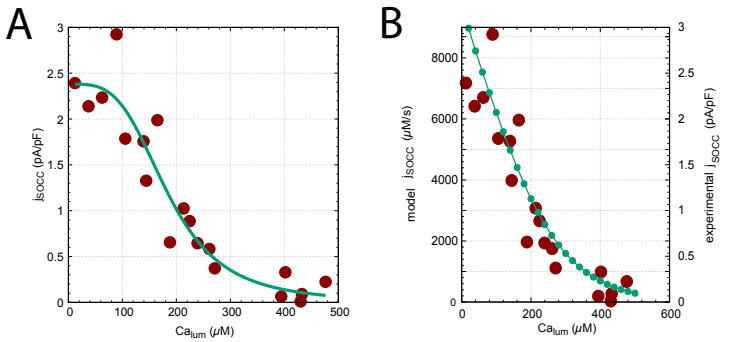

Fig 10. Capacitative Ca^{2+} inflow rate j_{SOCC} as a function of calcium concentration in the ER (Ca_{lum}). Panel A: experimental results (red solid dots) redrawn after Fig 1c from Luik et al. [74]. Green line shows a nonlinear fit for a constant Hill-coefficient with n=3.59±0.9 (Eq 14). For details, see S7 Program. Panel B: model calculation using Eq 14 with a variable Ca_{lum} cooperativty n changing linearly from n=0.8 at Ca_{lum}=20 μM to n=1.3 at Ca_{lum}=500μM. For details, see S7 Program.

In the model the steady state of Ca_{lum} is determined by the SERCA channel, which has been 'wired' in form of a negative feedback [28] inflow controller. The amount of SERCA is increased by k_{20}, while Ca_{lum} signals a zero-order decrease of SERCA, i.e.

$$\frac{dSERCA}{dt} = k_{20} - Ca_{lum} \cdot \frac{k_{21} \cdot SERCA}{k_{22} + SERCA} \tag{16}$$

At steady-state (i.e., $S\dot{E}RCA$=0) and zero-order condition with respect to SERCA, ($k_{22} \ll (SERCA)$), the Ca_{lum} set-point is determined by Eq 16:

$$Ca_{lum,set} = Ca_{lum,ss} = \frac{k_{20}}{k_{21}} \tag{17}$$

Fig 11 illustrates the robustness of the Ca_{lum} set-point by calculating $Ca_{lum,ss}$ at five different phases (1-5) in which k_{20} is changed from k_{20}=1000μM/s (phase 1) to 200μM/s (phase 5) by steps of 200μM/s. Panel A shows the decrease in Ca_{lum} concentration when k_{20} is successively decreased, while panel B shows the corresponding increase of j_{SOCC}. See S7 Program for details.

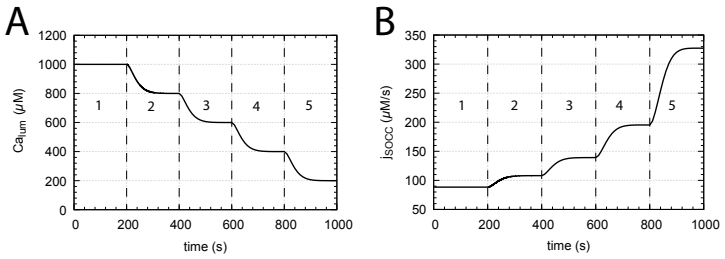

Fig 11. SERCA inflow control determines Ca_{lum} concentration. The figure illustrates the decrease in Ca_{lum} concentration as its set-point (Eq 17) decreases with changing k_{20} together with the corresponding up-regulation of j_{SOCC} as Ca_{lum} gets lower. Panel A: Five phases 1-5 show the changed Ca_{lum} concentrations when k_{20} values are successively decreased. Phase 1: k_{20}=1000μM/s, phase 2: k_{20}=800μM/s, phase 3: k_{20}=600μM/s, phase 4: k_{20}=400μM/s, and phase 5: k_{20}=200μM/s. k_{21}=1s^{-1} in all five phases. Panel B: corresponding increase of j_{SOCC} in response to the Ca_{lum} concentration changes in panel A. For details, see Supporting Information S7 Program.

We have revisited the experiments by Sedova and Blatter (Ref [59] and Fig 7) and calculated Ca_{cyt} concentrations by using the capacitative Ca inflow mechanism from Fig 9. Fig 12 shows the obtained Ca_{cyt} concentrations (panel A, phases 2 and 4) when cells are exposed to 2mM external Ca at zero Ca_{lum} levels. During phase 5 PMCA is inhibited and only NCX is active.

To achieve the Ca_{cyt} profiles as in Fig 7 we assumed that SOCC and PMCA show hysteretic behaviors, i.e., for both channels it takes some time until their maximum activities are established. No hysteretic effects are imposed on NCX. Here, the channel turnover number is kept high and constant at k_{63}=1×10^{5}s^{-1} throughout all five phases.

Ca_{cyt}-induced calcium release through IP_3R and its inhibition at high Ca_{cyt}

We have chosen to include IP_3R as the only Ca^{2+} release channel in the ER membrane. This is because the RyRs are located in the sarcoplasmic reticulum of excitable cells and are involved in events like the excitation-contraction coupling in both cardiac and skeletal muscle [82]. Also of relevance is the fact that IP_3R alone has been found to produce agonist-induced Ca^{2+} oscillations. A bit contradictory, Sanders showed in 2001 that both IP_3R and RyR were needed for sufficient oscillatory behavior in vascular smooth muscle cells (VSMCs) [83]. However, two years later, in 2003, McCarron found that even if RyRs are blocked IP_3R alone can sufficiently produce agonist-induced Ca^{2+}

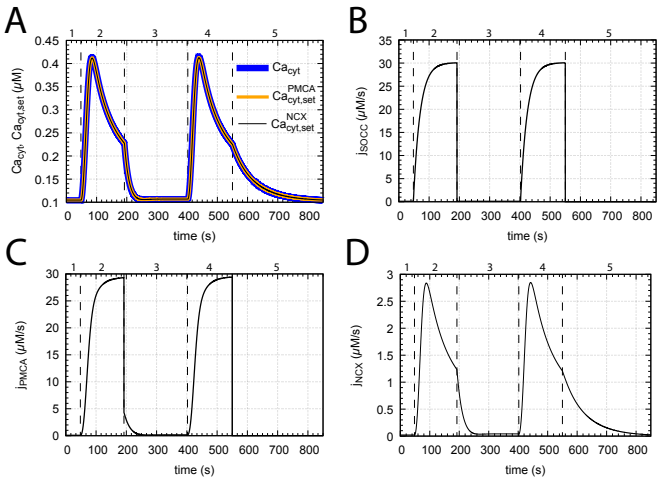

Fig 12. Cytosolic Ca^{2+} changes due to capacitative Ca inflow. Computations were performed with the mechanism outlined in Fig 9. In phases 2 and 4 extracellular Ca was set to 2 mM along with no Ca in the ER (Ca_{lum}=0μM) and a fully-inhibited SERCA (k_{23}=0s^{-1}). Panel A: calculated Ca_{cyt} and set-points for PMCA and NCX as a function of time. Panels B and C: SOCC and PMCA are imposed to undergo hysteretic changes in phases 2 and 4, such that it takes some time until maximum channel activities are established. Panel D: the channel turnover number of NCX k_{63} is kept high ($1\times10^5 s^{-1}$) but constant for all five phases. For details, see Supporting Information S7 Program.

oscillations [84]. These results were from excitable cells, which could also justify the usage of only the IP_3R channel to move Ca from a store (here ER) into the cytosol. In this work we have not primarily been focussed on oscillations, but at the end of the paper we show that the concerted action of the SOCC-SERCA-IP_3R axis together with PMCA/NCX can result in sustained oscillations.

IP_3R is regulated by both IP_3 and Ca_{cyt}, where the regulation of IP_3R by Ca_{cyt} is biphasic and results in a bell-shaped IP_3R activity profile with a maximum at about 100-300 nM Ca_{cyt} (pCa_{cyt}≈6.5-7) [73,85–88]. The Ca^{2+} release from the store (ER) due to Ca_{cyt} activation is termed Calcium-Induced Calcium-Release (CICR) [5,89,90]. IP_3 originates from an extracellular signal (e.g. hormones, growth factors, light, odorants, neurotransmitters) stimulating a G protein-coupled receptor in the cell membrane, which activates phospholipase C (PLC), and hydrolyzes phosphatidylinositol 4,5-bisphosphate (PIP2) into IP_3 and diacylglycerol (DAG) [89–92]. The IP_3R channel has three isoforms, but in this model we have chosen to have only one type of IP_3R. Physiologically, IP_3R1 is the most common and widespread form throughout cell types. All IP_3R's have a high affinity binding to IP_3 with a K_d varying from about 14 to 163 nM. Some variations are found, but type 1 has been found to have a K_d between 50 - 89 nM [93–96]. All IP_3R isoform activities display a bell-shaped Ca_{cyt} dependency. It is type 1 which has its peak at around 300 nM Ca_{cyt}. We use this peak value in our model in agreement

with experimental studies [73, 85–88, 94, 97].
IP_3R's large size made it difficult to study its structure, but advances in this direction have been made [22, 92, 98]. The structure based on the work by Fan et al. [22] is presented in Fig 13 together with the locations of the binding sites for IP_3 and Ca^{2+} as suggested by Sienaert et al. and Ding et al. [99, 100].
IP_3R gating, i.e. its activation by IP_3 and Ca^{2+} as well as its inhibition by Ca^{2+} has been vastly investigated. Nevertheless, the mechanisms behind Ca-induced pore opening and closure are still not well understood and are somewhat controversial [89, 92, 101]. IP_3R activation and inhibition by Ca^{2+} appear to be the result of conformational changes once Ca^{2+} and IP_3 bind. There are currently 8 suggested Ca^{2+} binding sites on IP_3R which are distributed over different structural domains. Their roles with respect to activating or inhibiting IP_3R is not known [88, 89, 92, 101]. A calcium sensor region (Cas) has been suggested to be responsible for channel modulation by Ca^{2+} [98]. Concerning the inhibition of IP_3R by Ca^{2+} there has also been the question whether the inhibition is due to a direct Ca^{2+} binding to an inhibitory site or if inhibition happens in association with a protein like calmodulin. On the other hand, studies have shown that calmodulin is not needed for Ca^{2+} inhibition, even though the Ca^{2+}-calmodulin complex can inhibit the channel. Mutant studies lacking the high affinity Ca^{2+}-calmodulin binding site displays a bell shaped Ca^{2+} dependence similar to the wild type. This indicates that Ca^{2+} itself or by the help of a different protein than calmodulin can inhibit IP_3R [102, 103]. In a proposed model how Ca^{2+} influences IP_3R Taylor and Tovey [89] and Taylor and Prole [104] suggest that IP_3 makes the activating or inhibiting binding site accessible for Ca^{2+} dependent where IP_3 binds on IP_3R. Fig 13C gives an overview of the presumed activation and inhibition steps of IP_3. It was also proposed that luminal Ca^{2+} might be tuning the channel in a way that it is less sensitive to IP_3 when ER is depleted for calcium [89, 105, 106].

Based on the scheme in Fig 13C we have constructed a simple model ("dicalcic model", Fig 14) which can describe the bell-shaped form of IP_3R activity in response to the cytosolic calcium concentration Ca_{cyt}.

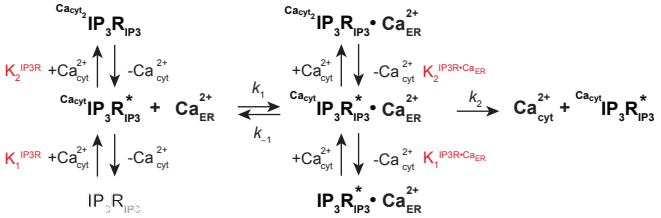

Fig 14. Dicalcic model. In this model the IP_3R•IP_3 channel has two cytosolic Ca binding sites, one that activates IP_3R•IP_3 at low cytosolic Ca^{2+} concentrations, while a binding at high cytosolic Ca^{2+} concentrations to the second site inhibits IP_3R•IP_3. The active form of the channel which transports Ca out of the ER into the cytosol is indicated by an asterisk. The four dissociation constants are outlined in red.

The model is analogous to the so-called diprotic model, which describes bell-shaped activity profiles of enzymes in dependence to pH [107]. In the dicalcic model we assume that IP_3 is always bound to IP_3R. We further assume that we have three IP_3R forms: At low Ca_{cyt} concentrations ($pCa_{cyt} \gg 7$) no Ca_{cyt} is bound to IP_3R•IP_3 and the channel is inactive (closed). At intermediate Ca_{cyt} concentrations ($pCa_{cyt} \approx 7$) Ca_{cyt} binds and

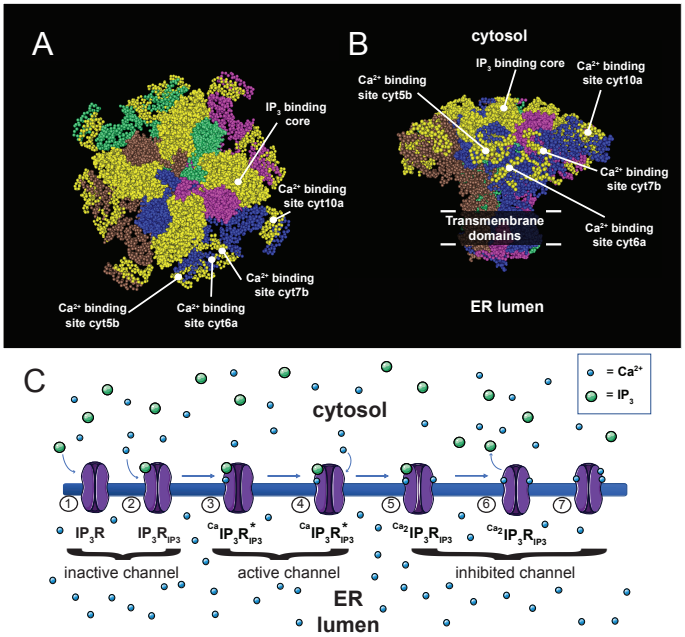

Fig 13. IP_3R structure and mechanism of its activation and inhibition. Panels A and B show the IP_3R channel structure based on the Protein Data Bank entry 3JAV (www.rcsb.org) from rat [22]. The four isomers are shown in blue, brown, purple and green color. Amino acid (aa) sequences of the Ca^{2+} binding sites and the IP_3 binding core (IBC) were taken from Sienaert et al. and Ding et al., respectively, and are highlighted in yellow [99,100]. Panel A shows the top view, while panel B gives a side view of the channel. Panel C shows an illustration of how IP_3R channel may be activated and inhibited in a Ca^{2+} and IP_3 dependent manner. Numbers 1-4 indicate the transition from an inactive to an active channel when Ca^{2+} and IP_3 bind. Numbers 5-7 indicate the mechanisms of channel inhibition by the additional binding of Ca^{2+} and/or the dissociation of IP_3 from $IP_3R{\bullet}IP_3$.

activates $IP_3R{\bullet}IP_3$. This form is now able to transport calcium out of the ER and into the cytosol. At high Ca_{cyt} concentrations ($pCa_{cyt} \ll 7$) there is further binding of Ca_{cyt} to $IP_3R{\bullet}IP_3$ which leads to its inhibition.

We further assume that the binding between Ca_{cyt} and the IP_3R channel can be formulated by four rapid equilibria

$$^{Ca_{cyt}}IP_3R_{IP3}{}^{*} \overset{K_1^{IP3}}{\rightleftharpoons} IP_3R_{IP3} + {Ca_{cyt}}^{2+} \tag{18}$$

$$^{Ca_{cyt_2}}IP_3R_{IP3} \overset{K_2^{IP3}}{\rightleftharpoons} {}^{Ca_{cyt}}IP_3R_{IP3}{}^{*} + {Ca_{cyt}}^{2+} \tag{19}$$

$$^{Ca_{cyt}}IP_3R_{IP3}{}^{*}{\bullet}{Ca_{ER}}^{2+} \overset{K_1^{IP3\cdot Ca_{ER}}}{\rightleftharpoons} IP_3R_{IP3}{\bullet}{Ca_{ER}}^{2+} + {Ca_{cyt}}^{2+} \tag{20}$$

$$^{Ca_{cyt_2}}IP_3R_{IP3}{\bullet}{Ca_{ER}}^{2+} \overset{K_2^{IP3\cdot Ca_{ER}}}{\rightleftharpoons} {}^{Ca_{cyt}}IP_3R_{IP3}{}^{*}{\bullet}{Ca_{ER}}^{2+} + {Ca_{cyt}}^{2+} \tag{21}$$

with dissociation constants K_1^{IP3}, K_2^{IP3}, $K_1^{IP3\cdot Ca_{ER}}$, and $K_2^{IP3\cdot Ca_{ER}}$. The asterisk in $^{Ca_{cyt}}IP_3R^{*}_{IP3}$ denotes the active form of the transporter, where one Ca_{cyt} has bound to IP_3R (indicated by the left superscript 'Ca_{cyt}'). The right subscript 'IP3' in $^{Ca_{cyt}}IP_3R^{*}_{IP3}$ indicates the bound IP_3. The active form $^{Ca_{cyt}}IP_3R^{*}_{IP3}$ can bind Ca_{ER} and transport it into the cytosol (with channel turnover number k_2, Fig 14). Although $^{Ca_{cyt_2}}IP_3R_{IP3}$ can bind Ca_{ER} and lead to $^{Ca_{cyt_2}}IP_3R_{IP3}{\bullet}Ca^{2+}_{ER}$, $^{Ca_{cyt_2}}IP_3R_{IP3}{\bullet}Ca^{2+}_{ER}$ is not an active transport form (see Fig 14). The transport rate v_{IP3R} of the $IP_3R{\bullet}IP_3$ channel is expressed as:

$$v_{IP3R} = k_2 \cdot ({}^{Ca_{cyt}}IP_3R^{*}_{IP3}{\bullet}Ca^{2+}_{ER}) = \frac{k_2{\cdot}(IP_3R_{IP3})_0{\cdot}(Ca^{2+}_{ER})}{f_{IP3R}{\cdot}K_M + f_{IP3R.Ca_{ER}}(Ca^{2+}_{ER})} \tag{22}$$

$(IP_3R_{IP3})_0$ is the total concentration of the $IP_3R{\bullet}IP_3$ channel, which, for the sake of simplicity is considered to be constant. The factors f_{IP3R} and $f_{IP3R.Ca_{ER}}$ are analogous to the Michaelis acidity functions [107] and defined as:

$$f_{IP3R} = 1 + \frac{Ca^{2+}_{cyt}}{K_1^{IP3}} + \frac{K_2^{IP3}}{Ca^{2+}_{cyt}} \tag{23}$$

$$f_{IP3R.Ca_{ER}} = 1 + \frac{Ca^{2+}_{cyt}}{K_1^{IP3\cdot Ca_{ER}}} + \frac{K_2^{IP3\cdot Ca_{ER}}}{Ca^{2+}_{cyt}} \tag{24}$$

The K_M in Eq 22 is given as:

$$K_M = \frac{(Ca^{2+}_{ER})({}^{Ca_{cyt}}IP_3R^{*}_{IP3})}{({}^{Ca_{cyt}}IP_3R^{*}_{IP3}{\bullet}Ca^{2+}_{ER})} \tag{25}$$

As anticipated, in Eq 22 cytosolic calcium acts both as an inhibitor and activator. The inhibition and activation terms are given by, respectively, $(Ca^{2+}_{cyt}/K_1^{IP3})$ and $(K_2^{IP3}/Ca^{2+}_{cyt})$ in Eq 23, while they are in Eq 24 $(Ca^{2+}_{cyt}/K_1^{IP3\cdot Ca_{ER}})$ and $(K_2^{IP3\cdot Ca_{ER}}/Ca^{2+}_{cyt})$. Thus, the K_1's take the form of inhibition constants, while the K_2's are activation constants.

We have used the experimental data by Kaftan et al. [73] to estimate the parameters in Eq 22. Kaftan et al. studied the Channel Open Probability of $IP_3R{\bullet}IP_3$ as a function of Ca concentration at four different IP_3 levels. We extracted the data (Fig 2 in [73]; see also S3 Text) and recalculated the experimental data as a function of Channel Open Probability versus pCa. Fig 15 shows the experimental data together with two fits at

2 μM IP_3. Panel A shows a fit of Eq 22 to the Kaftan et al. data when f_{IP3R} and $f_{IP3R.Ca_{ER}}$ are taken from Eqs 23 and 24, respectively. We see that the experimental data (outlined in red) decrease much more abrupt with increasing Ca_{cyt} concentrations (decreasing pCa_{cyt}) than the model (outlined in blue). A significantly better fit is obtained in panel B (outlined in green) when the cooperativity (Hill-coefficient) n for the increasing Ca^{2+}_{cyt} concentration in f_{IP3R} and $f_{IP3R.Ca_{ER}}$ is increased to 2. In this case f_{IP3R} and $f_{IP3R.Ca_{ER}}$ take the form:

$$f_{IP3R} = 1 + \frac{(Ca^{2+}_{cyt})^n}{K_1^{IP3}} + \frac{K_2^{IP3}}{Ca^{2+}_{cyt}} \tag{26}$$

$$f_{IP3R.Ca_{ER}} = 1 + \frac{(Ca^{2+}_{cyt})^n}{K_1^{IP3\cdot Ca_{ER}}} + \frac{K_2^{IP3\cdot Ca_{ER}}}{Ca^{2+}_{cyt}} \tag{27}$$

with n=2. Supporting Information 'S3 Text' shows the details of fitting the dicalcic model to all four IP_3 concentrations used by Kaftan et al. [73].
A possible explanation of the more abrupt IP_3R inhibition at high Ca_{cyt} concentrations may be due to the binding of further Ca ions to the channel which then results in a conformational change inhibiting IP_3R.

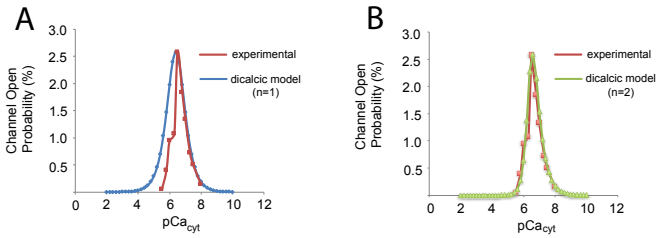

Fig 15. Channel Open Probability of IP_3R in the presence of 2 μM IP_3 as a function of pCa_{cyt}. The redrawn experimental data by Kaftan et al. [73] are outlined in red. Panel A shows the fit of the dicalcic model with a inhibiting cooperativity of 1. The discrepancy between model and experiment is clearly seen for high cytosolic Ca concentrations (low pCa_{cyt}). In panel B the inhibiting cooperativity is 2, which results in a much better overall fit. The fits to all four experimental data sets by Kaftan et al. are presented in the Supporting Information S3 Text.

Fig 16 indicates the implementation of the dicalcic model into the overall cell model of calcium homeostasis. The parameters k_{40} and k_{41} play the respective roles of K_1^{IP3} and K_2^{IP3}; k_{42} and k_{43} represent $K_1^{IP3\cdot Ca_{ER}}$ and $K_2^{IP3\cdot Ca_{ER}}$, respectively. Parameters k_{38} and k_{39} are, respectively, the channel turnover number (k_2 in Fig 14) and the K_M defined by Eq 25.

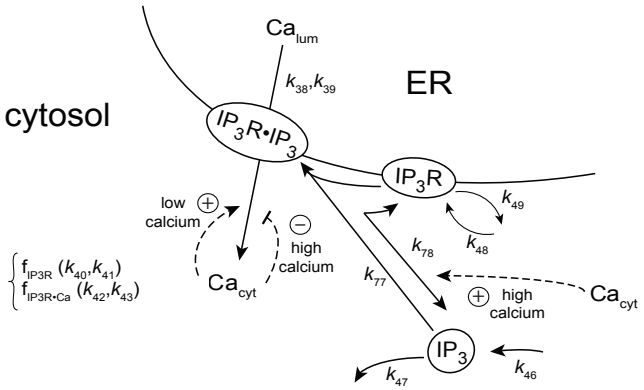

Fig 16. Incorporation of the dicalcic IP_3R•IP_3 channel activity (Fig 14) into the overall model. For a description of rate constant assignments, see text.

Effect of cytosolic calcium on the dissociation of IP_3R•IP_3

We also investigated the possible outcomes when cytosolic calcium has an influence on the dissociation of IP_3R•IP_3, as outlined in Fig 16. We have modelled three scenarios how cytosolic calcium could influence the stability of IP_3R•IP_3:

(i) considering a first-order kinetic influence of Ca^{2+}_{cyt} on the IP_3R•IP_3 dissociation by using the term $k_{78}\cdot(IP_3R\bullet IP_3)\cdot(Ca^{2+}_{cyt})$

(ii) considering the term $k_{78}\cdot(IP_3R\bullet IP_3)\cdot[1+(Ca^{2+}_{cyt})]$, when only Ca^{2+}_{cyt} levels $\gg 1$ μM have a significant influence on IP_3R•IP_3 dissociation, or finally

(iii) when Ca^{2+}_{cyt} levels have no influence on IP_3R•IP_3 dissociation, i.e. using the dissociation term $k_{78}\cdot(IP_3R\bullet IP_3)$.

In order to test the three above conditions on the IP_3R•IP_3 transport rate v_{IP3R} we used a calcium inflow term j_1=$k_1(Ca_{ext})$ into the cytosol which changed between 10 μM/s and 4×10^4 μM/s. This caused a cytosolic calcium increase from 8.1×10^{-4} μM to 4.8 μM for all the three cases (i)-(iii) (Fig 17A). Interestingly, when Ca^{2+}_{cyt} influences IP_3R•IP_3 dissociation by first-order kinetics (case (i)) the bell-shaped IP_3R•IP_3 transport rate disappears with high v_{IP3R} values at low j_1 inflows (Fig 17B). Since experiments clearly show low IP_3R•IP_3 transport rates at low Ca^{2+}_{cyt} concentrations we conclude that an influence of low Ca^{2+}_{cyt} concentrations on IP_3R•IP_3 dissociation can be excluded. The results for case (ii) (influence of high Ca^{2+}_{cyt} on IP_3R•IP_3 dissociation) and case (iii) (no influence of Ca^{2+}_{cyt} on IP_3R•IP_3 dissociation) are qualitatively similar (Fig 17B), i.e., an influence of high Ca^{2+}_{cyt} on IP_3R•IP_3 dissociation cannot be excluded.

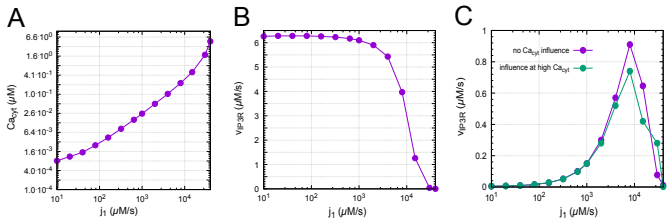

Fig 17. Influences of cytosolic calcium and cytosolic calcium inflow rates j_1 on $IP_3R{\bullet}IP_3$ dissociation and activity. Panel A: increase of cytosolic calcium concentration Ca^{2+}_{cyt} as a function of calcium inflow rate j_1 into the cytosol (independent how Ca^{2+}_{cyt} influences $IP_3R{\bullet}IP_3$ dissociation). Panel B: $IP_3R{\bullet}IP_3$ transport rate v_{IP3R} as a function of j_1 when $IP_3R{\bullet}IP_3$ dissociation is first-order with respect to Ca^{2+}_{cyt}; see (i) in text. Panel C: $IP_3R{\bullet}IP_3$ transport rate v_{IP3R} when $IP_3R{\bullet}IP_3$ dissociation is not dependent on Ca^{2+}_{cyt} (purple curve, condition (iii) in text) or when high Ca^{2+}_{cyt} concentrations only influence $IP_3R{\bullet}IP_3$ dissociation (green curve, condition (ii) in text). Details of these calculations are given in Supporting Information 'S8 Program'.

Oscillations

Although calcium oscillations [108–114] were not our primary focus in this research, we observed that the interaction between cytosolic calcium, PMCA/NCX, capacitative calcium entry and calcium-induced calcium release can lead to sustained oscillations. Remarkably, the period of these oscillations can vary from 2 seconds up to 30 hours! We found that the transport turnover numbers of SERCA (k_{23}), IP_3R (k_{38}), the Ca set-point in the ER (defined by k_{20}, k_{21}), and the inflow rate of calcium into the cytosol (k_1) are the parameters which affect the period most. For larger period lengths the oscillations are of the relaxation-type as shown in the build-up of calcium in the ER and its rapid release into the cytosol (Fig 18). The oscillations become high frequent with smaller amplitudes when k_{23} is increased (see 'S9 Program' for more details). In general, we found that an increased Ca inflow into the cytosol (up to a certain point) promotes (shorther period) oscillations, for example by the leak term $j_1{=}k_1{\cdot}Ca_{ext}$, or by a capacitative Ca entry at low Ca_{ER} levels. On the other hand, locking calcium concentrations in the ER to high values (by changing k_{20} and/or k_{21}) leads to increased period lengths and eventually to the loss of oscillation. Concerning the IP_3 channel oscillations, j_{IP3R}, we sometimes observe a split peak as in Fig 18D. This occurs because of the bell-shaped behavior of the $IP_3R{\bullet}IP_3$ Channel Open Probability (Fig 15). When the cytosolic calcium concentration increases above the pCa_{cyt} peak value (see Fig 15) and then decreases and passes the pCa_{cyt} peak again a double peak in j_{IP3R} is observed.

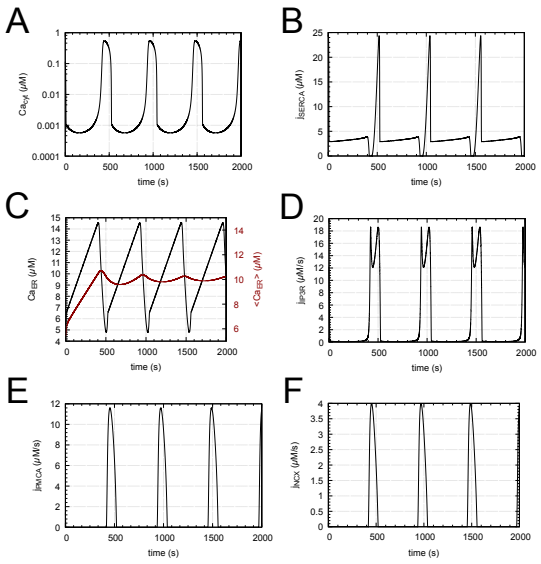

Fig 18. Example of sustained oscillations. The period in this case is 8.6 minutes. The red curve in panel C shows the average Ca_{ER} concentration which oscillates around its set-point (Eq 17), here set to 10 μM. Also note the split peak of j_{IP3R} in panel D. Rate parameters, initial concentrations as well as binaries and the source file are given in 'S9 Program' together with additional calculations showing how parameter values can affect the oscillations with period lengths between a few seconds and up to 30 hours (see 'S9 Program').

It should be noted that the oscillations shown in Fig 18, as well as the above referred 2s and 30h oscillations in 'S9 Program' are *independent* of IP_3. In these calculations the levels of $IP_3R{\bullet}IP_3$ and IP_3 are kept constant by setting the rate constants k_{77} and k_{78} to zero. On the other hand, when the dissociation of $IP_3R{\bullet}IP_3$ and its formation by IP_3R and IP_3 are taken into account, then different IP_3 levels can increase or decrease period lengths by regulating the amount of $IP_3R{\bullet}IP_3$ and thereby regulating the associated flux j_{IP3R} across the ER membrane (see *Influence of IP_3* in 'S9 Program').
Although the oscillations observed in our model could be classified as IP_3 independent [111, 114], the kinetics and cooperativities of PMCA, NXC, leakage terms into the cytosol, and SOCC/STIM are additional factors which are expected to influence and contribute to the oscillations, besides $IP_3R{\bullet}IP_3$ and IP_3. It appears therefore interesting to investigate in further studies how the integration and their kinetics of the various inflows and outflows of cytosolic Ca^{2+} take part in the generation of these oscillations.

Concluding remarks and future aspects

This work aimed at the development of a basic cellular model of Ca^{2+} homeostasis. A model like this poses the problem that certain cellular compounds/parts and their functions will certainly be neglected. In our case the role of mitochondria as an additional

Ca store and regulator was not included, together with transporters such as the RyR's, ARCC's, VOCC's along with sodium and potassium channels. Such neglects certainly limits the applicability of the model. On the other hand, we feel that through the model we have pointed at important regulatory features, such as the hysteretic behaviors of the Ca pumps and the enhanced cooperativity when the $IP_3R{\bullet}IP_3$ channel closes at high Ca_{cyt} levels. The model's astonishing oscillatory capability, which integrates Ca regulatory aspects of the model and is largely unexplored, appears to be an interesting aspect of further research with respect to both ultradian/high frequency [108, 110, 112] and possibly circadian [113] Ca oscillations. We also hope that the source files of the accompanying programs and their compiled binaries may be of interest as starting points for generating more improved models.

Supporting information

S1 Text Model details. List of rate equations, abbreviations, and LSODE Y(i) assignments for the model Fig 3.

S2 Text PMCA kinetic parameters for S2 Program and S3 Program. Description of PMCA rate equations, cytosolic Ca^{2+} set point, and the estimation of PMCA V_{max}, K_M and turnover number.

S3 Text Dicalcic model. Derivation of Eq 22 with n=1 and n=2, and fits to the experimental data by Kaftan et al. (Fig 2 in Ref. [73]).

S1 Program Cytosolic calcium homeostasis in a minimal model. Fortran source file and executables showing results of Fig 2.

S2 Program Modeling the application of ionophore A23187 on erythrocytes. Rate equations, parameters and calculations for Fig 5B.

S3 Program Modeling cytosolic calcium regulation by PMCA in bovine endothelial cells. Rate parameters and calculations for Figs 6B and 6C.

S4 Program Modeling cytosolic calcium regulation by PMCA and NCX in bovine endothelial cells. Rate equations, parameters, initial concentrations, and calculations for Figs 7C and 7D.

S5 Program Modeling cytosolic calcium regulation by PMCA and NCX in bovine endothelial cells. Rate equations, parameters, initial concentrations, and calculations for Fig 8B.

S6 Program Analysis of Ca^{2+}-leakage rates from the ER. Determination of first-order rate constant and Michaelis-Menten as well as hysteretic parameters from the experimental results by Luik et al. [74] and Camello et al. [10], respectively.

S7 Program Calculations leading to Figs 10-12. Calculated capacitative Ca^{2+} inflow rates with concentration dependent cooperativity.

S8 Program Influences of cytosolic calcium and cytosolic inflow rates j_1 on $IP_3R{\bullet}IP_3$ dissociation and activity. The supporting information shows the details leading to Fig 17.

S9 Program Oscillatory responses of the model. Calculations showing the results of Fig 18 and parameter influences on the period.

Acknowledgments

We thank Tormod Drengstig and Kristian Thorsen for comments during the early stages of this project.

References

1. Bianchi CP. Cell Calcium. London Butterworths; 1968.
2. Koutalos Y, Yau KW. Regulation of sensitivity in vertebrate rod photoreceptors by calcium. Trends in Neurosciences. 1996;19(2):73–81.
3. Carafoli E. Calcium signaling: A tale for all seasons. PNAS. 2002;99(3):1115–1122.
4. Krizaj D, Copenhagen DR. Calcium regulation in photoreceptors. Frontiers in Bioscience - Landmark. 2002;7(4):d2023–d2044.
5. Marks F, Klingmüller U, Müller-Decker K. Cellular Signal Processing. Second Edition. Garland Science; 2017.
6. Dupont G, Falcke M, Kirk V, Sneyd J. Models of Calcium Signalling. Springer; 2016.
7. Langley LL, editor. Homeostasis. Origins of the Concept. Dowden, Hutchinson and Ross, Inc.; 1973.
8. Thompson JL, Mignen O, Shuttleworth TJ. The ARC channel—an endogenous store-independent Orai channel. Curr Top Membr. 2013;71:125–148.
9. Prakriya M, Feske S, Gwack Y, Srikanth S, Rao A, Hogan PG. Orai1 is an essential pore subunit of the CRAC channel. Nature. 2006;443(7108):230 – 233.
10. Camello C, Lomax R, Petersen OH, Tepikin A. Calcium leak from intracellular stores—the enigma of calcium signalling. Cell Calcium. 2002;32(5-6):355–361.
11. Bird GS, Hwang SY, Smyth JT, Fukushima M, Boyles RR, Putney JW. STIM1 is a calcium sensor specialized for digital signaling. Current Biology. 2009;19(20):1724–1729.
12. Brandman O, Liou J, Park WS, Meyer T. STIM2 is a feedback regulator that stabilizes basal cytosolic and endoplasmic reticulum Ca^{2+} levels. Cell. 2007;131(7):1327–1339.
13. Schwaller B. The continuing disappearance of "pure" Ca^{2+} buffers. Cellular and Molecular Life Sciences. 2009;66(2):275–300.
14. Schwaller B. Cytosolic Ca^{2+} buffers. Cold Spring Harbor Perspectives in Biology. 2010;2(11):a004051.
15. Brini M, Carafoli E. The plasma membrane Ca^{2+} ATPase and the plasma membrane sodium calcium exchanger cooperate in the regulation of cell calcium. Cold Spring Harbor Perspectives in Biology. 2011;3(2):a004168.

16. Goto Y, Miura M, Iijima T. Extrusion mechanisms of intracellular Ca^{2+} in human aortic endothelial cells. European Journal of Pharmacology. 1996;314(1-2):185–192.

17. Carafoli E. The plasma membrane calcium ATPase: Historical appraisal and some new concepts. In: Chakraborti S, Dhalla NS, editors. Regulation of Ca^{2+}-ATPases, V-ATPases and F-ATPases. Springer International Publishing; 2016. p. 3–11.

18. Di Leva F, Domi T, Fedrizzi L, Lim D, Carafoli E. The plasma membrane Ca^{2+} ATPase of animal cells: structure, function and regulation. Archives of Biochemistry and Biophysics. 2008;476(1):65–74.

19. Prole DL, Taylor CW. Structure and function of IP_3 receptors. Cold Spring Harbor Perspectives in Biology. 2019;11(4):a035063.

20. Radhakrishnan K, Hindmarsh AC. Description and Use of LSODE, the Livermore Solver for Ordinary Differential Equations. Lawrence Livermore National Laboratory Report UCRL-ID-113855. NASA Reference Publication. 1993;1327.

21. Wang Y, Geer LY, Chappey C, Kans JA, Bryant SH. Cn3D: Sequence and structure views for Entrez. Trends in Biochemical Sciences. 2000;25(6):300–302.

22. Fan G, Baker ML, Wang Z, Baker MR, Sinyagovskiy PA, Chiu W, et al. Gating machinery of InsP3R channels revealed by electron cryomicroscopy. Nature. 2015;527(7578):336.

23. Yi TM, Huang Y, Simon MI, Doyle J. Robust perfect adaptation in bacterial chemotaxis through integral feedback control. PNAS. 2000;97(9):4649–53.

24. Wilkie J, Johnson M, Reza K. Control Engineering. An Introductory Course. New York: Palgrave; 2002.

25. El-Samad H, Goff JP, Khammash M. Calcium homeostasis and parturient hypocalcemia: an integral feedback perspective. J Theor Biol. 2002;214(1):17–29.

26. Ni XY, Drengstig T, Ruoff P. The control of the controller: Molecular mechanisms for robust perfect adaptation and temperature compensation. Biophys J. 2009;97:1244–53.

27. Ang J, Bagh S, Ingalls B, McMillen D. Considerations for using integral feedback control to construct a perfectly adapting synthetic gene network. J Theor Biol. 2010;266(4):723–738.

28. Drengstig T, Jolma I, Ni X, Thorsen K, Xu X, Ruoff P. A basic set of homeostatic controller motifs. Biophys J. 2012;103(9):2000–2010.

29. Ang J, McMillen DR. Physical constraints on biological integral control design for homeostasis and sensory adaptation. Biophys J. 2013;104(2):505–515.

30. Briat C, Gupta A, Khammash M. Antithetic integral feedback ensures robust perfect adaptation in noisy biomolecular networks. Cell Systems. 2016;2(1):15–26.

31. Aoki SK, Lillacci G, Gupta A, Baumschlager A, Schweingruber D, Khammash M. A universal biomolecular integral feedback controller for robust perfect adaptation. Nature. 2019;570(7762):533–537.

32. Krishnan J, Floros I. Adaptive information processing of network modules to dynamic and spatial stimuli. BMC Systems Biology. 2019;13(1):1–26.

33. Waheed Q, Zhou H, Ruoff P. Kinetics and mechanisms of catalyzed dual-E (antithetic) controllers. PLoS One. 2022;17(8):e0262371.

34. Shoval O, Goentoro L, Hart Y, Mayo A, Sontag E, Alon U. Fold-change detection and scalar symmetry of sensory input fields. PNAS. 2010; p. 201002352.

35. Drengstig T, Ni X, Thorsen K, Jolma I, Ruoff P. Robust adaptation and homeostasis by autocatalysis. The Journal of Physical Chemistry B. 2012;116(18):5355–5363.

36. Briat C, Zechner C, Khammash M. Design of a synthetic integral feedback circuit: dynamic analysis and DNA implementation. ACS Synthetic Biology. 2016;5(10):1108–1116.

37. Guerini D, Pan B, Carafoli E. Expression, purification, and characterization of isoform 1 of the plasma membrane Ca^{2+} pump focus on calpain sensitivity. Journal of Biological Chemistry. 2003;278(40):38141–38148.

38. El-Jouni W, Haun S, Machaca K. Internalization of plasma membrane Ca^{2+}-ATPase during Xenopus oocyte maturation. Developmental Biology. 2008;324(1):99–107.

39. Hicke L. Ubiquitin-dependent internalization and down-regulation of plasma membrane proteins. The FASEB Journal. 1997;11(14):1215–1226.

40. Thorsen K, Agafonov O, Selstø CH, Jolma IW, Ni XY, Drengstig T, et al. Robust concentration and frequency control in oscillatory homeostats. PLoS One. 2014;9(9):e107766.

41. Thorsen K, Drengstig T, Ruoff P. The effect of integral control in oscillatory and chaotic reaction kinetic networks. Physica D. 2019;393:38–46.

42. Niggli V, Penniston JT, Carafoli E. Purification of the (Ca^{2+}-Mg^{2+})-ATPase from human erythrocyte membranes using a calmodulin affinity column. Journal of Biological Chemistry. 1979;254(20):9955–9958.

43. Niggli V, Adunyah E, Carafoli E. Acidic phospholipids, unsaturated fatty acids, and limited proteolysis mimic the effect of calmodulin on the purified erythrocyte Ca^{2+}-ATPase. Journal of Biological Chemistry. 1981;256(16):8588–8592.

44. Mandal A, Liyanage MR, Zaidi A, Johnson CK. Interchange of autoinhibitory domain conformations in plasma-membrane Ca^{2+}-ATPase-calmodulin complexes. Protein Science. 2008;17(3):555–562.

45. Bradshaw RA, Dennis EA. Handbook of Cell Signaling. Academic Press; 2009.

46. Mrosovsky N. Rheostasis: The Physiology of Change. Oxford University Press; 1990.

47. Placzek S, Schomburg I, Chang A, Jeske L, Ulbrich M, Tillack J, et al. BRENDA in 2017: New perspectives and new tools in BRENDA. Nucleic Acids Research. 2016; p. gkw952.

48. Carafoli E, Zurini M. The Ca^{2+}-pumping ATPase of plasma membranes purification, reconstitution and properties. Biochimica et Biophysica Acta (BBA)-Reviews on Bioenergetics. 1982;683(3-4):279–301.

49. Dode L, Vilsen B, Van Baelen K, Wuytack F, Clausen JD, Andersen JP. Dissection of the functional differences between sarco (endo) plasmic reticulum Ca^{2+}-ATPase (SERCA) 1 and 3 isoforms by steady-state and transient kinetic analyses. Journal of Biological Chemistry. 2002;277(47):45579–45591.

50. Dode L, Andersen JP, Leslie N, Dhitavat J, Vilsen B, Hovnanian A. Dissection of the functional differences between sarco (endo) plasmic reticulum Ca^{2+}-ATPase (SERCA) 1 and 2 isoforms and characterization of Darier disease (SERCA2) mutants by steady-state and transient kinetic analyses. Journal of Biological Chemistry. 2003;278(48):47877–47889.

51. Niggli V, Adunyah E, Penniston J, Carafoli E. Purified (Ca^{2+}-Mg^{2+})-ATPase of the erythrocyte membrane. Reconstitution and effect of calmodulin and phospholipids. Journal of Biological Chemistry. 1981;256(1):395–401.

52. Kubitscheck U, Pratsch L, Passow H, Peters R. Calcium pump kinetics determined in single erythrocyte ghosts by microphotolysis and confocal imaging. Biophys J. 1995;69(1):30–41.

53. Bruce JI. Metabolic regulation of the PMCA: Role in cell death and survival. Cell Calcium. 2018;69:28–36.

54. Blaustein MP. Sodium/Calcium Exchange. In: Bradshaw RA, Dennis EA, editors. Handbook of Cell Signaling. Amsterdam: Elsevier; 2010. p. 949–953.

55. Chen Q, Mahendrasingam S, Tickle JA, Hackney CM, Furness DN, Fettiplace R. The development, distribution and density of the plasma membrane calcium ATPase 2 calcium pump in rat cochlear hair cells. European Journal of Neuroscience. 2012;36(3):2302–2310.

56. Schatzmann H. Dependence on calcium concentration and stoichiometry of the calcium pump in human red cells. The Journal of Physiology. 1973;235(2):551–569.

57. Dagher G, Lew VL. Maximal calcium extrusion capacity and stoichiometry of the human red cell calcium pump. The Journal of Physiology. 1988;407:569.

58. Tiffert T, Staines HM, Ellory JC, Lew VL. Functional state of the plasma membrane Ca^{2+} pump in Plasmodium falciparum-infected human red blood cells. The Journal of Physiology. 2000;525(1):125–134.

59. Sedova M, Blatter L. Dynamic regulation of $[Ca^{2+}]_i$ by plasma membrane Ca^{2+}-ATPase and Na^+/Ca^{2+} exchange during capacitative Ca^{2+} entry in bovine vascular endothelial cells. Cell Calcium. 1999;25(5):333–343.

60. Putney JW. Capacitative Calcium Entry. Chapman & Hall; 1997.

61. Choi HS, Eisner D. The effects of inhibition of the sarcolemmal Ca-ATPase on systolic calcium fluxes and intracellular calcium concentration in rat ventricular myocytes. Pflügers Archiv European Journal of Physiology. 1999;437(6):966–971.

62. Scharff O, Foder B, Skibsted U. Hysteretic activation of the Ca^{2+} pump revealed by calcium transients in human red cells. Biochimica et Biophysica Acta (BBA)-Biomembranes. 1983;730(2):295–305.

63. Frieden C. Slow transitions and hysteretic behavior in enzymes. Annual Review of Biochemistry. 1979;48(1):471–489.

64. Caride AJ, Elwess NL, Verma AK, Filoteo AG, Enyedi Á, Bajzer Ž, et al. The rate of activation by calmodulin of isoform 4 of the plasma membrane Ca^{2+} pump is slow and is changed by alternative splicing. Journal of Biological Chemistry. 1999;274(49):35227–35232.

65. Caride AJ, Filoteo AG, Penniston JT, Strehler EE. The plasma membrane Ca^{2+} pump isoform 4a differs from isoform 4b in the mechanism of calmodulin binding and activation kinetics implications for Ca^{2+} signaling. Journal of Biological Chemistry. 2007;282(35):25640–25648.

66. Foder B, Scharff O. Solitary calcium spike dependent on calmodulin and plasma membrane Ca^{2+} pump. Cell Calcium. 1992;13(9):581–591.

67. Wu X, Bers DM. Free and bound intracellular calmodulin measurements in cardiac myocytes. Cell Calcium. 2007;41(4):353–364.

68. Jurado LA, Chockalingam PS, Jarrett HW. Apocalmodulin. Physiological Reviews. 1999;79(3):661–682.

69. Huang CY, Chau V, Chock PB, Wang JH, Sharma RK. Mechanism of activation of cyclic nucleotide phosphodiesterase: requirement of the binding of four Ca^{2+} to calmodulin for activation. PNAS. 1981;78(2):871–874.

70. Persechini A, Stemmer PM. Calmodulin is a limiting factor in the cell. Trends in Cardiovascular Medicine. 2002;12(1):32–37.

71. Bayley P, Ahlstrőm P, Martin SR, Forsen S. The kinetics of calcium binding to calmodulin: Quin 2 and ANS stopped-flow fluorescence studies. Biochemical and Biophysical Research Communications. 1984;120(1):185–191.

72. Chou AC, Ju YT, Pan CY. Calmodulin interacts with the sodium/calcium exchanger NCX1 to regulate activity. PLoS One. 2015;10(9):e0138856.

73. Kaftan EJ, Ehrlich BE, Watras J. Inositol 1, 4, 5-trisphosphate ($InsP_3$) and calcium interact to increase the dynamic range of $InsP_3$ receptor-dependent calcium signaling. The Journal of General Physiology. 1997;110(5):529–538.

74. Luik RM, Wang B, Prakriya M, Wu MM, Lewis RS. Oligomerization of STIM1 couples ER calcium depletion to CRAC channel activation. Nature. 2008;454(7203):538–542.

75. Michalak M, Milner R, Burns K, Opas M. Calreticulin. Biochem J. 1992;285(Pt 3):681–692.

76. Campbell AK. Intracellular Calcium. John Wiley & Sons; 2014.

77. Zheng L, Stathopulos PB, Li GY, Ikura M. Biophysical characterization of the EF-hand and SAM domain containing Ca^{2+} sensory region of STIM1 and STIM2. Biochemical and Biophysical Research Communications. 2008;369(1):240–246.

78. Stathopulos PB, Li GY, Plevin MJ, Ames JB, Ikura M. Stored Ca^{2+} depletion-induced oligomerization of stromal interaction molecule 1 (STIM1) via the EF-SAM region. Journal of Biological Chemistry. 2006;281(47):35855–35862.

79. Thiel M, Lis A, Penner R. STIM2 drives Ca^{2+} oscillations through store-operated Ca^{2+} entry caused by mild store depletion. The Journal of Physiology. 2013;591(6):1433–1445.

80. Hancock J. Cell Signalling. Oxford University Press; 2010.

81. Grabmayr H, Romanin C, Fahrner M. STIM proteins: An ever-expanding family. International Journal of Molecular Sciences. 2020;22(1):378.

82. Lanner JT, Georgiou DK, Joshi AD, Hamilton SL. Ryanodine receptors: structure, expression, molecular details, and function in calcium release. Cold Spring Harbor Perspectives in Biology. 2010;2(11):a003996.

83. Sanders KM. Invited Review: Mechanisms of calcium handling in smooth muscles. Journal of Applied Physiology. 2001;91(3):1438–1449.

84. McCarron J, Bradley K, MacMillan D, Muir TC. Sarcolemma agonist-induced interactions between $InsP_3$ and ryanodine receptors in Ca^{2+} oscillations and waves in smooth muscle. Biochemical Society Transactions. 2003;31(5):920–924.

85. Suematsu E, Hirata M, Hashimoto T, Kuriyama H. Inositol 1, 4, 5-trisphosphate releases Ca^{2+} from intracellular store sites in skinned single cells of porcine coronary artery. Biochemical and Biophysical Research Communications. 1984;120(2):481–485.

86. Iino M. Biphasic Ca^{2+} dependence of inositol 1, 4, 5-trisphosphate-induced Ca release in smooth muscle cells of the guinea pig taenia caeci. The Journal of General Physiology. 1990;95(6):1103–1122.

87. Bezprozvanny I, Watras J, Ehrlich BE, et al. Bell-shaped calcium-response curves of lns (l, 4, 5) P_3 and calcium-gated channels from endoplasmic reticulum of cerebellum. Nature. 1991;351(6329):751–754.

88. Mikoshiba K. The IP_3 receptor/Ca^{2+} channel and its cellular function. In: Biochemical Society Symposia. vol. 74. Portland Press; 2007. p. 9–22.

89. Taylor CW, Tovey SC. IP_3 receptors: Toward understanding their activation. Cold Spring Harbor Perspectives in Biology. 2010;2(12):a004010.

90. Mikoshiba K. IP_3 receptor/Ca^{2+} channel: From discovery to new signaling concepts. Journal of Neurochemistry. 2007;102(5):1426–1446.

91. Berridge MJ, Irvine RF. Inositol phosphates and cell signalling. Nature. 1989;341(6239):197–205.

92. Serysheva II. Toward a high-resolution structure of IP_3R channel. Cell Calcium. 2014;56(3):125–132.

93. Südhof T, Newton CL, Archer 3rd B, Ushkaryov YA, Mignery GA. Structure of a novel $InsP_3$ receptor. The EMBO Journal. 1991;10(11):3199.

94. Mikoshiba K. The discovery and structural investigation of the IP_3 receptor and the associated IRBIT protein. In: Islam S, editor. Calcium Signaling. Springer; 2012. p. 281–304.

95. Newton CL, Mignery GA, Südhof T. Co-expression in vertebrate tissues and cell lines of multiple inositol 1, 4, 5-trisphosphate ($InsP_3$) receptors with distinct affinities for $InsP_3$. Journal of Biological Chemistry. 1994;269(46):28613–28619.

96. Iwai M, Michikawa T, Bosanac I, Ikura M, Mikoshiba K. Molecular basis of the isoform-specific ligand-binding affinity of inositol 1, 4, 5-trisphosphate receptors. Journal of Biological Chemistry. 2007;282(17):12755–12764.

97. Tu H, Wang Z, Bezprozvanny I. Modulation of mammalian inositol 1, 4, 5-trisphosphate receptor isoforms by calcium: A role of calcium sensor region. Biophys J. 2005;88(2):1056–1069.

98. Bezprozvanny I. The inositol 1, 4, 5-trisphosphate receptors. Cell Calcium. 2005;38(3):261–272.

99. Sienaert I, Missiaen L, De Smedt H, Parys JB, Sipma H, Casteels R. Molecular and functional evidence for multiple Ca^{2+}-binding domains in the type 1 inositol 1, 4, 5-trisphosphate receptor. Journal of Biological Chemistry. 1997;272(41):25899–25906.

100. Ding Z, Rossi AM, Riley AM, Rahman T, Potter BV, Taylor CW. Binding of IP_3 and Adenophostin A to the N-terminal region of the IP_3 Receptor: Thermodynamic Analysis Using Fluorescence Polarization with a Novel IP_3 Receptor Ligand. Molecular Pharmacology. 2010; p. https://doi.org/10.1124/mol.109.062596.

101. Shinohara T, Michikawa T, Enomoto M, Goto JI, Iwai M, Matsu-ura T, et al. Mechanistic basis of bell-shaped dependence of inositol 1, 4, 5-trisphosphate receptor gating on cytosolic calcium. PNAS. 2011;108(37):15486–15491.

102. Nosyreva E, Miyakawa T, Zhengnan W, Glouchankova L, Mizushima A, Masamitsu I, et al. The high-affinity calcium–calmodulin-binding site does not play a role in the modulation of type 1 inositol 1, 4, 5-trisphosphate receptor function by calcium and calmodulin. Biochemical Journal. 2002;365(3):659–667.

103. Zhang X, Joseph SK. Effect of mutation of a calmodulin binding site on Ca2+ regulation of inositol trisphosphate receptors. Biochemical Journal. 2001;360(2):395–400.

104. Taylor CW, Prole DL. Ca^{2+} signalling by IP_3 receptors. In: Balla T, Wymann M, York JD, editors. Phosphoinositides II: The Diverse Biological Functions. Springer; 2012. p. 1–34.

105. Berridge MJ. Inositol trisphosphate and calcium oscillations. Biochem Soc Symp. 2007;74:1–7.

106. Irvine R. 'Quanta' Ca^{2+} release and the control of Ca^{2+} entry by inositol phosphates - A possible mechanism. FEBS Letters. 1990;263(1):5–9.

107. Tipton KF, Dixon HB. Effects of pH on Enzymes. Methods in Enzymology. 1979;63:183–234.

108. Berridge MJ. Cytosolic calcium oscillators. The FASEB Journal. 1988;2:3074–3082.

109. Goldbeter A, Dupont G, Berridge MJ. Minimal model for signal-induced Ca^{2+} oscillations and for their frequency encoding through protein phosphorylation. PNAS. 1990;87(4):1461–1465.

110. Schuster S, Marhl M, Höfer T. Modelling of simple and complex calcium oscillations: From single-cell responses to intercellular signalling. European Journal of Biochemistry. 2002;269(5):1333–1355.

111. Sneyd J, Tsaneva-Atanasova K, Reznikov V, Bai Y, Sanderson M, Yule D. A method for determining the dependence of calcium oscillations on inositol trisphosphate oscillations. PNAS. 2006;103(6):1675–1680.

112. Parekh AB. Decoding cytosolic Ca^{2+} oscillations. Trends in Biochemical Sciences. 2011;36(2):78–87.

113. Enoki R, Ono D, Kuroda S, Honma S, Honma Ki. Dual origins of the intracellular circadian calcium rhythm in the suprachiasmatic nucleus. Scientific Reports. 2017;7(1):1–8.

114. Dupont G, Combettes L, Bird GS, Putney JW. Calcium oscillations. Cold Spring Harbor Perspectives in Biology. 2011;3(3):a004226.